Aus der Fakultät für Biologie, Department II

Anthropology and Human Genetics

Institut der Ludwig−Maximilians−Universität München

Vostand: Prof. Dr. Wolfgang Enard

Biophysics-based modeling and data analysis of local field potential signal

Dissertation

zum Erwerb des Doktorgrades der Naturwissenschaften

an der Medizinischen Fakultät der

Ludwig−Maximilians−Universität München

vorgelegt von

Weiwei Chen

aus

Zhejiang/China

Jahr

2023

Mit Genehmigung der Medizinischen Fakultät
der Universität München

Betreuer(in):	Prof. Dr. Anton Sirota
Zweitgutachter(in):	Prof. Dr. Tobias Staudigl
Dekan:	Prof. Dr. med. Thomas Gudermann
Tag der mündlichen Prüfung:	20. Dezember 2023

Contents

Abstract (English)

Understanding the neurophysiological mechanisms of information processing within and across brain regions has always been a fundamental and challenging topic in neuroscience. Considerable works in the brain connectome and transcriptome have laid a profound foundation for understanding brain function by its structure. At the same time, the recent advance in recording techniques allows us to probe the nonstationary brain activity from various spatial and temporal scales. However, how to effectively build the dialogue between the anatomical structure and the dynamical brain signal still needs to be solved. To tackle the problem, we explore interpreting electrophysiology signals with mechanistic models.

In chapter 2 we first segregate high-coherent brain signals into different pathways and then connect their dynamics to synaptic properties. Based on a state space model of LFP generation, we explore several preprocessing methods to bias the signal to the synaptic inputs and enhance the separatability of pathway-specific contributions. The separated sources are more reliable with the preprocessing methods, especially in highly coherent states, e.g., awake running. With reliably separated pathways, we further studied their synaptic properties and explored the local directional connections in the hippocampus. The estimated synaptic time constant and pathway connection agrees with well-established anatomical studies.

In chapter 3 we explore establishing a simple model to capture the impulse response of passive neurons with detailed dendritic morphology. We validate Green's function methods based on compartmentalized models by comparing them to numerical simulations and analytical solutions on continuous neuron membrane potentials. A parameterized model based on laminar Green's function is further developed and helps to infer the anatomical properties, like the input current distribution and cell position, from their spatiotemporal response patterns. The effect of cell position and template are examed.

Based on the model of chapter 3, we use the biophysical possible impulse response profile to regularize the source separation in the frequency domain in chapter 4. The components from different frequencies are clustered according to the same latent input distributions. The source separation in better-separated frequency bins from the same pathway helps separation in other highly contaminated

frequencies. The optimization is formulated as a probabilistic model to maximize the negentropy as well as spatial likelihood. Similar to dipole approximation for EEG signals, Green's function method provides an effective approximation to capture biologically possible spatiotemporal patterns and helps to guide the separation. We validated the method on real data with optogenetic stimulation.

In chapter 5 we further separate the far-field signals from the local pathway activities according to their physiological properties. We propose a pipeline to reliably separate and automatically detect far-field signal components. Based on this, a toolbox is provided to remove the EMG artifacts and assess the cleaning performance. In the free-running animals, we show that EMG artifacts shadow the high-frequency oscillatory events detection, and EMG cleaning rescues this effect.

Overall, this thesis explored multiple possibilities to incorporate neurophysiology knowledge to understand and model the electrical field potential signals.

Zusammenfassung (Deutsch)

Das Verständnis der neurophysiologischen Mechanismen der Informationsverarbeitung innerhalb und zwischen Gehirnregionen war schon immer ein grundlegendes und herausforderndes Thema in den Neurowissenschaften. Weitreichende Arbeiten zum Konnektom und Transkriptom des Gehirns haben eine Grundlage für das Verständnis der Gehirnfunktion gelegt. Des Weiteren ermöglicht uns der derzeitige Fortschritt in der Aufnahmetechnik, die nicht stationäre Gehirnaktivität auf verschiedenen räumlichen und zeitlichen Skalen zu untersuchen. Wie jedoch die anatomischen Strukturen und die dynamischen Gehirnsignal effektiv zusammen wirken können, muss jedoch noch gelöst werden. Um dieses Problem anzugehen, untersuchen wir die Interpretation elektrophysiologischer Signale mit mechanistischen Modellen.

In Kapitel 2 trennen wir zunächst die hochkohärenten Gehirnsignale in verschiedene Leitungsbahnen und verbinden dann die Dynamik mit synaptischen Eigenschaften. Basierend auf einem Zustandsraummodell zur Erzeugung lokaler Feldpotentiale (LFP) untersuchen wir verschiedene Vorverarbeitungsmethoden, die die Signale bestmöglich auf die synaptischen Eingangsströme ausrichten und die Trennbarkeit von leitungsbahnspezifischen Beiträgen verbessert. Die Trennung der Signalquellen ist durch das Vorverarbeitungsverfahren insbesondere während hochkohärenter Verhaltenszustände (z. B. laufen im Wachzustand) zuverlässiger. Mit zuverlässig getrennten Leitungsbahnen konnten wir die entsprechenden synaptischen Eigenschaften weiter untersuchen und die lokalen gerichteten Verbindungen im Hippocampus untersuchen. Die geschätzte synaptische Zeitkonstante und die Verbindungen der Leitungsbahnen stimmen mit etablierten anatomischen Studien überein.

In Kapitel 3 untersuchen wir die Erstellung eines einfachen Modells zur Beschreibung der Impulsantwort passiver Neuronen mit detaillierter dendritischer Morphologie. Wir validieren Greensche Funktionsmethoden basierend auf kompartimentierten Modellen, indem wir sie mit numerischen Simulationen und analytischen Lösungen des kontinuierlichen Membranpotentials von Neuronen vergleichen. Ein parametrisiertes Modell, das auf der laminaren Greenschen Funktion basiert, wird weiterentwickelt. Es hilft dabei, die anatomischen Eigenschaften - die Verteilung des Eingangsstroms und die Zellposition - aus ihren raumzeitlichen Reaktionsmustern abzuleiten. Die Auswirkung der Zellposition

und des Templates werden untersucht.

Basierend auf dem Modell aus Kapitel 3 verwenden wir in Kapitel 4 das biophysikalisch mögliche Profil der Impulsantwort, um die Quellentrennung im Frequenzbereich festzulegen. Die Komponenten verschiedener Frequenzen werden nach derselben latenten Eingangsverteilungen geclustert. Die Quellentrennung in besser getrennten Frequenzbereichen derselben Leitungsbahn hilft bei der Quelltrennung in anderen stark kontaminierten Frequenzbereichen. Die Optimierung wird als probabilistisches Modell formuliert, um sowohl die Negentropie als auch die räumliche Wahrscheinlichkeit zu maximieren. Ähnlich wie die Dipolnäherungen für EEG-Signale bietet die Greensche Funktionsmethode eine effektive Annäherung, um biologisch mögliche raumzeitliche Muster zu erfassen, und hilft, die Quellen zu trennen. Wir haben die Methode an realen Daten mit optogenetischer Stimulation validiert.

Im Kapitel 5 trennen wir weiter die Fernfeldsignale von den Signalen der lokalen Leitungsbahnen nach ihren physiologischen Eigenschaften. Wir schlagen eine Methode vor, die es erlaubt, Fernfeld-Signalkomponenten zuverlässig von lokaler Aktivitaet zu trennen und automatisch zu erkennen. Es wird eine Toolbox bereitgestellt, die EMG-Artefakte entfernt und die bereinigten Signale bewertet. In Ableitungen von freilaufenden Tieren zeigen wir, dass EMG-Artefakte die Erkennung von hochfrequenten Oszillationen beeintraechtigt, aber nach der Bereinigung des EMG-Signals erkannt werden kann.

Insgesamt untersucht diese Dissertation mehrere Möglichkeiten die elektrischen Feldpotentiale neuronaler Aktivität unter Einbeziehung neurophysiologischen Wissens zu modellieren und zu verstehen.

List of Figures

List of Tables

Chapter 1

Introduction

Our understanding of complex behavior and cognitive function depends on decoding how the information is processed within and across brain regions. The brain activity underlying signal processing could be observed with various recording techniques at different spatial and temporal scales. The last decade has seen a great advance in interpreting the existing measures as well as the development of new recording techniques. For example, with the advancing of large-scale recordings, a huge amount of work has been dedicated to decoding the task information from unit data (Jazayeri & Ostojic, 2021, Cunningham & Yu, 2014), and understanding neuron representation mainly based on signal correlation to different features of tasks.

The function of the brain has more than passively representing information from the environment. The study of the sensory or motor cortex benefit from their position close to explicit sensory information or behaviors. According to the information bottleneck theory, it's reasonable to understand their representation when the areas are close to the inputs and outputs stage, such that one can observe and control the experiments. However, recent works suggest that the brain employs a much more complex architecture to process information through both forward and top-down regularization instead of simply relaying the information to higher-order cortical areas (Rao & Ballard, 1999). This raises the question of how the brain generates hypotheses from the inside and selectively processes sensory information accordingly. These complex nonlinear processing patterns could only be understood by interpreting their spatiotemporal patterns, identifying individual pathways, and studying their dynamic interactions. Electrophysiology signals at different spatial scales with their fine temporal resolution have been employed to capture the fast spatiotemporal response in the brain, among them, high-density space-resolved local field recording has the best spatial resolutions. In this work, I will focus on the biophysical modeling and interpretation of local field potential (LFP) signals. Ultimately, I will discuss how to incorporate the LFP modeling into a multi-objective general mechanistic model that integrates different measures to probe the multiregional activities.

1.1 Biophysics Origin of LFP

LFP has been getting more attention since the advance of multielectrode recording. Compared to the high-frequency unit activity (Koch, 2004), the slower part mainly reflects synaptic activity driven by presynaptic neural populations (Einevoll et al., 2013) and contains information about how these neurons integrate synaptic inputs. Therefore, direct summation of all spikes in the local network has a poor prediction of the generated LFP patterns. Instead, accurate modeling or prediction of LFP has been well explored by detailed neuron simulations accounting for their transmembrane currents (Einevoll et al., 2013, Lindén et al., 2014).

Take the hippocampus as an example, where pyramidal cells are packed in a single layer called stratum pyramidal, while their axons lay in parallel with each other. The synapses targeting postsynaptic populations are clustered in a depth-dependent manner. The input-response of each pathway, therefore, has a specific spatial profile depending on where it comes along the dendritic tree (see detail in chapter 2 and chapter 3). So the question is, how can we quantitatively capture the input-response of neurons?

The impulse response of the neuron's membrane potential has been investigated to study how the signal is processed along dendrites (Cash & Yuste, 1999, Sprusston, 2008). The complex morphology of dendrites allows complicated modulation of input signals (Rall, 2011). Different effects of modulation could be achieved by arranging the cell's branching patterns, active conductance and the site of inhibition (Rall, 2011, Grienberger et al., 2017, Wybo et al., 2015). Analytical solutions of the membrane potential at arbitrary points have been provided for simple morphology (Rall, 2011, Brandwood, 1983, Koch & Poggio, 1985) and largely extended to capture an arbitrary dendritic tree, quasi-active conductance, as well as gap junctions (Abbott et al., 1991, Coombes et al., 2007, Caudron et al., 2012). However, the extracellular potential integrates the electric field generated by all transmembrane currents at any arbitrary position over the whole neuron. This makes the overall integration very complex and hard to implement, especially for a population of neurons with complex dendritic morphology. To resolve this problem, a multi-compartment model approximation will simplify the computation of the membrane impulse response.

Therefore, a computational framework to simulate neuron activity first and then use volume conduction theory to compute the extracellular potentials has been well established (Lindén et al., 2014). Multi-compartment models proved to be adequate and widely used to simulate the membrane potential dynamics of complex neurons with arbitrary dendritic trees (Hines & Carnevale, 2001). In these models, the morphology of dendritic trees confines the spreading of the electrical field in the intercellular conductance by the sparse connectivity matrix between discretized compartments. Ions flow along the dendritic tree according to the electrical field, various active conductance sitting at the membrane and adding

nonlinear effect to the currents, hence the morphology of the dendritic tree has a great impact on the spatial distribution of current density. In simulations, any continuous dendritic trees reconstructed from real data could be approximated by the multi-compartment model, with cable equation describing the dynamics of carrier ions with the equivalent circuit and active conductance fitted to the experimental data (Sterratt et al., 2011a, Dayan & Abbott, 2001, Carnevale & Hines, 2006, Druckmann et al., 2007).

In this framework, transmembrane currents reflect the dynamics of ions distributed across the neural membrane driven by electrochemical gradients. The ionic gradients are maintained mainly by various active transport processes and drive the ion flow when specific ion channels open (Sterratt et al., 2011a). When the synaptic input comes, neurotransmitters bind to specific post-synaptic receptors, which leads to the opening of the post-synaptic ion channels. The corresponding ion flow through the membrane changes the membrane potential. The local change of the membrane potential creates an electrical field, which leads to the spreading of ions across and through the whole neuron tree, which in turn can be modeled by equivalent circuits. This whole process is well established and is the basis for programs such as NEURON (Carnevale & Hines, 2006). The transmembrane currents, as opposed to axial currents flowing within the neuron, take into account any charge flowing across the neuron membrane.

By assuming a quasi-static approximation of Maxwell's equations at low frequencies (Plonsey & Heppner, 1967, Gratiy et al., 2017), the electric field potential could be given according to local extracellular conductivity σ (Butz & Cowan, 1974, Nunez et al., 2006). It's also worth being cautious about the effect of inhomogeneous and frequency-dependent extracellular conductivity (Bédard et al., 2004), the complex tissue-specific conductivity and the boundaries for large-scale head models (Wolters et al., 2006). In these cases, the extracellular conductivity σ_f could be modeled as a $3D$ complex vector at frequency f. Here for simplicity, we only consider the homogeneous and isotropic conductance, which doesn't have a frequency-dependent capacitative effect (Logothetis et al., 2007, Hagen et al., 2016), i.e. the extracellular conductivity σ_f is modeled as a scalar.

The mechanism governing the generation of LFP is relatively straightforward, however, simulating the field potential with thousands of neurons remains time and computation resource-consuming. To simplify the whole process, (Hagen et al., 2016) proposed a hybrid framework to simulate multi-scale networks. In their work, they use spatiotemporal filter kernels to capture the extracellular signals stemming from the synaptic activity for each connection pathway. By convolving with their corresponding population spike rates, the model could accurately predict the spatiotemporal dynamics of ground truth extracellular signals from conductance-based multicompartment neuron networks obtained by numerical simulations (Hagen et al., 2022). This linearized framework accounts for the biophysics of neurons, populations, and recurrent connections and at the

same time largely simplifies computation compared to biophysically detailed network models. We would also use this insight in our work here, discussed in chapter 3 and in our inverse model in chapter 4.

1.2 Inverse Modeling of LFP Signal

The inverse problem attempts to infer the microscopic variables from the macroscopic signals. In the narrative of electrophysiology signals, it usually infers primary current dipoles or current distributions which give rise to the spatiotemporal profile of the volume conducted LFP signal. The inverse modeling of electrophysiology data is generally ill-posed which means multiple different architectures will render the same pattern (Buzsáki et al., 2012, Nunez et al., 2006). It would be useful to separate the inverse problem of the LFP into two steps, namely, to recover at the level of transmembrane currents, or to recover the underlying activity of input currents or in general active currents. Current source density methods aim to solve the first problem, namely estimate the density of transmembrane current sources (CSD) generating the LFP (Nicholson & Freeman, 1975). CSD could be computed by a spatial Laplacian (Nicholson & Freeman, 1975) and it is extended by modeling the plausible waveforms of current sources (Pettersen et al., 2006) and more general the kernel method kCSD (Potworowski et al., 2012). Compared to the spatial Laplacian, the latter method allows for a more smooth estimation of the CSD, allows for flexible channel arrangement, and takes care of missing channels. It also allows for putting prior knowledge about the spatial profile of local currents into account. Furthermore, the inverse modeling framework of CSD incorporates the modeling of smooth temporal dynamics with Gaussian process based gpCSD (Klein et al., 2021).

However, apart from getting rid of volume conduction, the current source density is still a mixture of contributions from different pathways. This is caused by the electrical field spreading inside neurons. For example, both perforant path (PP) coming from the medial entorhinal cortex and Schaffer collateral (SC) from the CA3 region target CA1 neurons and are major inputs to the CA1 region (Fernández-Ruiz et al., 2012). Their synapses of the PP target the stratum lacunosum-moleculare and the synapses of SC target the stratum radiatum. However, the impulse response of PP typically has a current source at stratum radiatum and vise versa because of the cable property of the dendritic tree. To understand the signals, we still need to separate signals into different pathways.

Statistics-based methods are used to segregate the signal into pathway-specific synaptic activities. Unsupervised methods seek to identify pathways with particular statistics-based methods properties. Principle component analysis or factor analysis is used to find latent factors that explain most of the variance in the data. Independent component analysis (Bell & Sejnowski, 1995, Cardoso, 1998, Hyvärinen & Oja, 2000, Korovaichuk et al., 2010), find components most inde-

pendent from each other. Extensions for ICA also consider the nonstationarity of the components (Artoni et al., 2012). Temporal patterns could also be used to segregate oscillation patterns from LFP data (Sirota et al., 2008, Lopes-dos Santos et al., 2018). In spite of the widely used temporal independency, spatial-temporal ICA (Łęski et al., 2010) explores to utilize the spatial sparsity to separate temporally correlated signals on CSD instead of LFP. One problem with the statistical methods is that their independence assumption is often violated since the signals are usually synchronized, especially in the freely moving animals (Sirota et al., 2008). This problem could be mitigated by high pass filtering the data or taking CSD (Schomburg et al., 2014). We would explore methods to deal with this problem in chapter 2.

While all these statistics-based methods are fast and scale well, it requires post-hoc knowledge to interpret the results. The anatomical position of the components usually helps to identify their pathways (Fernández-Ruiz et al., 2012, Schomburg et al., 2014, Herreras et al., 2015). The synaptic content of components could be validated by pharmacological blockage or optogenetic modulation (Benito et al., 2014, Fernández-Ruiz et al., 2021).

Bayesian models have also been employed to model the local networks. Dynamic causal models (Friston et al., 2003, Pinotsis et al., 2017) have been exploited to model the local dynamics and understand the connectivity between principal cells and interneurons. However, the forward modeling of LFP is largely simplified and dendritic morphology is ignored in current models. Besides, the current model usually assumes simple cortical networks and ignores the complex interaction between local sub-networks, which is critical for cortical population dynamics (Mizuseki et al., 2009). These make the results of simple Bayesian modeling hard to interpret. It remains unresolved how to construct an inference model that connects local population dynamics to LFP.

1.3 Cross Regional Connectivity and Large Scale Modeling

Now moving to a different scale, recent years have seen a great advance of large-scale recordings in behaving animals, which allows concepts of brain connectivity to become increasingly prevalent to uncover how computation is carried out in multiple brain regions. Apart from how stimuli are represented in local areas, it has been shown that brain networks communicate and entrain connected regions through oscillations (Fries, 2015, Sirota et al., 2008, Mizuseki et al., 2009).

To understand the communication between regions, functional connectivity has been used to capture cross-regional neuronal interactions (Seth et al., 2015, Bastos & Schoffelen, 2016). Granger causality, based on the idea of the history of cause would help to predict the current state of the effect (Geweke, 1982; 1984),

has been widely used to capture the information processing pattern between brain regions (Seth et al., 2015). Benefiting from regression models, the Granger causality is usually formulated to capture linear dependencies (Barrett et al., 2010), which directly connect to cross-correlation and partial correlation in the temporal domain and cross-spectral density methods in the frequency domain (Barnett & Seth, 2014). Therefore, it usually scales well with high dimensional data and a long recording time. When formulated in general information-theoretic measures, Granger Causality connects to the transfer entropy framework, which is used in interpreting connections between spiking neurons or populations (Barnett et al., 2009, Ito et al., 2011, Palmigiano et al., 2017).

The functional connectivity method is fast and easily scaleable but generally suffers when applied to realistic data. One problem is when the noise is too large, the direction estimation fails in methods like Granger causality. This problem has been mitigated by estimating in the forward and backward temporal direction (Haufe et al., 2012, Vinck et al., 2015). One could also use phase slope index (PSI) methods assuming a constant time lag to determine the direction of pairwise connections (Nolte et al., 2008). Another major problem attributed to the volume conduction of the signal is always a mixture of multiple pathways and noise. This situation is intensified when high-density multichannel recording is applied. Therefore, applying the inverse method and segregating signals is critical to avoid spurious causal connections. This would be explored in detail in chapter 2.

Biophysical modeling based methods have been developed to test hypotheses about neural dynamics and estimate the relevant physiological meaningful parameters (Friston et al., 2003, Moran et al., 2008, Wang, 2022). Neural mass models or dynamic mean field models are employed to characterize how local E-I balance shapes the dynamics of local circuits. In this case, the average activity of local principle cells or interneurons is considered as well as the connection between them. In the Bayesian model framework, the best model fits the given assumption which is picked up by scores like BIC or AIC (Moran et al., 2008, Penny et al., 2011, Chaudhuri et al., 2015, Burt et al., 2018). However, the interpretation of Bayesian models is highly dependent on how the assumptions match the underlying mechanisms. Therefore, a clear understanding of the physics of the recorded signals becomes very critical (Friston et al., 1998, Pinotsis et al., 2017, Einevoll et al., 2013). For modeling LFP recordings, the current dipole is used, however, it has been shown to be inadequate to capture the near field electrical potential (Næss et al., 2021). In chapter 3 and chapter 4 we show that the Green's function or transfer function formulated in the frequency domain would be a candidate to connect synaptic activity to the recorded LFP signal.

Recently, biophysical-based large-scale cortical network modeling surges with the advance of research on anatomical structure. Brain tracing works challenge the conventional low-density interareal graphs view and reveal high-density cortical graphs (Markov et al., 2013; 2014). Long-distance neuronal coherence plays an

important role in multisensory integration, working memory, and selective attention (Wang, 2010). However, resting state functional connectivity (using fMRI) and structural connectivity (using diffusion spectrum imaging tractography) measured in the same individuals revealed that strong functional connections commonly exist between regions with no direct structural connection but indirect connections. While direct structural connectivity, on the other hand, can not explain the variance in functional connectivity, because of interregional dynamics (Honey et al., 2009). Therefore, it is important to understand how long-range feed-forward and feed-back connections integrate into local circuits and constraint cortical computation.

Large scale dynamic mean field model has been developed to explore circuit mechanisms. The interarea connectivity is first approximated by high-resolution cortical connection matrices given by diffusion spectrum imaging (DSI) (Hagmann et al., 2008, Deco & Jirsa, 2012) and later by directed and weighted connectivity provided by brain retrograde tracer (Markov et al., 2014, Mejias et al., 2016). The resultant functional connectivity of model simulation is then matched to empirical functional connectivity (Deco et al., 2013, Chaudhuri et al., 2015). The role of different components and their parameter space in the model could be explored with the constrained model. With this framework, it has been shown that locally constrained feedback inhibition compensates for the excess of long-range excitatory connectivity and is critical to shaping the characteristics of local dynamics (Deco et al., 2014). This emphasizes that we need a more precise calibration for continuously fluctuating local population dynamics and improve predictions of the mesoscopic dynamics models by investigating microscopic dynamics. With the high temporal and spatial resolution, local electrophysiology recording provides a clear picture to investigate how presynaptic inputs integrate into local population dynamics.

These concerns lead us to propose a general framework aiming to synchronize investigations in multiple fields based on their shared biophysical mechanisms in the following session.

1.4 The General Framework of LFP Modeling

Our understanding of the brain has been largely advanced with the development of neurophysiology recording and brain connectome (Sporns et al., 2005, Majka et al., 2020, Wang, 2022). Especially with simultaneous multiregional recordings, cross-regional interactions have been related to different behavior, brain information processing and cognitive functions (Sirota et al., 2008, Bastos et al., 2015, Sporns, 2014, Bohland et al., 2009). However, different measurement methodologies typically come with different spatial and temporal resolutions. It raises an exciting challenge to find a comprehensive way to integrate the knowledge from recordings of multiple brain regions at different scales, and with different

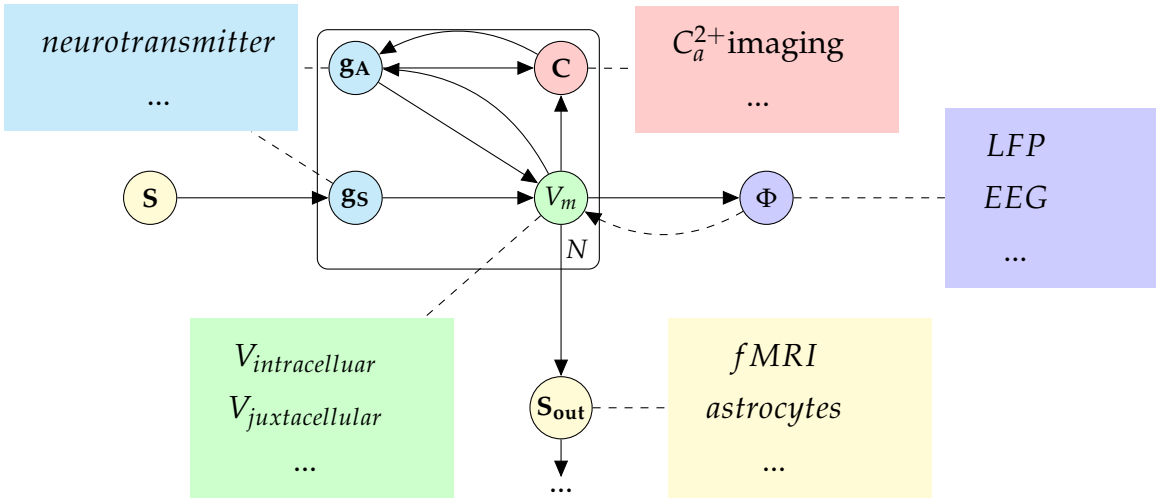

Figure 1.1: Schematic of the microscopic level neural signal generation model. **S** stands for the upstream inputs to local networks. The post-synaptic conductance $\mathbf{g_s}$ responds to their corresponding neurotransmitter and changes the local membrane potential V_m. The change of V_m together with the ion concentration **C** influence a consecutive response of voltage- and ligand-regulated active conductance $\mathbf{g_A}$. Modeled in parallel, the kinetics of active ion currents **C** are much more complicated and usually have a slower time scale compared to passive mechanism (Gold et al., 2006). Neurotransmitters are released according to an action potential, denoted as $\mathbf{S_{out}}$, and link to fMRI signals by neurovascular coupling (Friston et al., 2003) (in yellow). Measures and modeling of the dynamic system come in all levels, macro-scale neuroanatomy like the map of neurotransmitter systems or connection density determined by cellular level retrograde tracing (in cyan) dictates the spatial distribution of $\mathbf{g_s}$ (Hansen et al., 2022, Majka et al., 2020). Similar to neurotransmitters, macro-scale active current conductance density could be measured and come as a prior in dynamic modeling. Ions **C** flow through $\mathbf{g_A}$ and change the transmembrane electrochemical gradient according to Goldman-Hodgkin-Katz formalism. The dynamics of $[Ca^{2+}]$ concentration, one example of **C**, is detected by $[Ca^{2+}]$ imaging (Grienberger & Konnerth, 2012) (in red). The electrical field generated by trans-membrane currents gives rise to local field potential, as well as the macroscopic level far-field EEG signals (Buzsáki et al., 2012) (in blue). LFP influence the membrane potential through ephaptic coupling (Anastassiou et al., 2011). And V_m at a particular position could be recorded directly with intracellular or juxtacellular recordings or patch clamping (in green). The N plates stand for local dendritic integration and they are connected by passive neural dendritic trees.

measurement techniques. Regardless of the signal readout, all measurements basically probe different aspects of the shared underlying biophysical process of brain dynamics. Understanding the system from a generative point of view requires modeling how the latent biophysical process gives rise to the observed signals. Hence the first step is to decide on an appropriate anatomical grid for modeling and then to understand the physical signals over multiple measurement scales which are captured by different techniques.

Here we present a schematic summary of the current views of modeling and how to connect multiple scales (fig.1.1).

To get a mechanistic interpretation of recorded data starts from the microscopic scale, where local neuron populations are studied with all cellular details as well as particular cytoarchitectonic features (Buzsáki et al., 2012). Experimental mapping of neuroanatomical circuitry on the mesoscopic scale to provide comprehensive, brain-wide coverage requires multiregional connectivity measures between groups of neurons (Bohland et al., 2009). Macroscopic is summarising the population activity at the level of entire structural–functional systems and major fiber bundles and is usually used to understand cognitive functions at a coarse grain (Sporns et al., 2005).

Biophysical models have been extensively explored to understand both macroscopic and microscopic level measurements, respectively. Early forward network models are used to understand their oscillatory dynamics and computational functions (Wang, 2010). Recent studies suggest that cortical neuron networks code information in comparably low dimensional manifolds (Cunningham & Yu, 2014). However, the dimension of the subspace also depends on the structure of tasks (Stringer et al., 2019). But there is evidence that projection into a lower dimensional subspace is good enough to capture and decode the task from population dynamics (Pandarinath et al., 2018). This basically asks the question: do we need to model all neuronal details? Or can we capture the neuronal population dynamics with some simple input-response functions instead? If the answer is yes, the lower dimensional latent dynamics of the neuronal population could be conveniently incorporated into the mesoscopic level modeling.

Mesoscopic-level modeling has benefited from the advances in tracing techniques and a large amount of brain connectome data. Biophysically constrained multiscale modeling is built on local population models with interregional connection given by neuroanatomical data (Deco & Jirsa, 2012, Chaudhuri et al., 2015). Control theory or graph theory is further applied on top of the mesoscopic measurements to understand the dynamics or provide efficient control (Liu et al., 2011, Lynn & Bassett, 2019). However, sufficient approximations of the actual underlying biophysical process are desirable to answer biological questions. Experimental evidence of frequency-dependent information channeling (Bastos et al., 2015) has put constraints on population modeling, which is based on the oscillation

frequency of the model (Feedforward and feedback frequency-dependent interactions in a large-scale laminar network of the primate cortex) (Mejias et al., 2016).) Insights about the function of circuit architecture are gained from exploring the parameter space of this line of modeling (Deco et al., 2014). To match simulations to empirical data, mean-field abstraction is used to capture the local network activity (Deco et al., 2013). More sub-networks need to be accounted for, but the latent space is still much lower than the population size (Mizuseki et al., 2009, Jazayeri & Ostojic, 2021). These works about low dimensional approximation again suggest that detailed population models are unnecessary for large-scale modeling. Instead, we need simple and sufficient functional models for the abstract local population impulse response. But how do we find such a model? Considering the number of recording sites and the complexity of mechanisms that regulate the neuron populations, the modeling work faces a considerable parameter space, and its inversion is generally ill-posed.

To bridge the gap, LFP is in a good position to connect different microscopic measurements, helping to understand and confine the input-response of local networks. Down to the physical origin of electrophysiological signals, the multi-electrode recording captures slower subthreshold membrane potential dynamics which reflect multiple latent sources (Buzsáki et al., 2012), as well as spiking activity which code the task-relevant information in a spatially resolved manner (Cao et al., 2021, Gallego-Carracedo et al., 2022) (fig. 1.1 blue). Even though we still don't have a clear understanding of all the sources of LFP, which consists of large synchronized inputs to the local circuits (Benito et al., 2014, Schomburg et al., 2014), and contributions of active conductances, the modeling could be related to postsynaptic activity (Makarova et al., 2011) (fig. 1.1 cyan), $[Ca^{2+}]$ dynamics measured by $[Ca^{2+}]$ imaging (fig. 1.1 red) (Grienberger & Konnerth, 2012), and other latent intracellular processes (Reimann et al., 2013) measured by intracellular recordings (fig. 1.1 green). The magnitude of LFP depends on the cytoarchitecture, geometry of current sources (Fernández-Ruiz et al., 2013), as well as the level of the correlation between current sources. It has been shown that the LFP signal is significantly detectable in most laminar structures like cortical areas and hippocampus (Głąbska et al., 2014, Schomburg et al., 2014, Bastos et al., 2015).

The underlying population activity which leads to the LFP also gives rise to the fMRI signals by influencing the local blood flow by neurovascular coupling (Friston et al., 1998) (fig. 1.1 yellow). Although the connection between the electrophysiological signal and fMRI signal is still under investigation (Goense & Logothetis, 2008), it is helpful to take one step back and first model the underlying brain activity. The population response could be modeled using forward modeling (Wong & Wang, 2006), or by fitting to data either using higher order Volterra functions (Song et al., 2009), nonlinear system identification (Brunton et al., 2016, Rudy et al., 2019) or empirical data constrained neuron

networks (Andalman et al., 2019).

Then the recording signal could be modeled with different signal readout mechanisms (Friston et al., 2003, Einevoll et al., 2013). One advantage of using the LFP is that it shares the same biophysical process as far-field signals like EEG or EcoG and thus naturally connects, and the generation process of electrical fields also generates the signals of MEG recordings (Næss et al., 2021). The relationship could then be simulated by a linear forward model, namely, the lead field (Mechler & Victor, 2012). Constraining the local population response model by LFP would vastly reduce the parameter space. Furthermore, using LFP makes it possible to prob fast-nonstationary integration of population inputs into a local neuron. In chapter 3 we present a linear forward modeling method.

We should also emphasize the point that LFP data, especially with multichannel recordings, captures how the long-distance or local presynaptic activity is projected to the local circuit. This way, on top of coarse-scale tracing data, we have a clear local readout of how the groups of presynaptic neurons are influencing the downstream activity. By first investigating locally how the integration happens, we further suggest that the connectivity weight between areas, currently modeled with anatomical data, could be relaxed and fitted with a probabilistic model. Highly nonstationary and fluctuating brain connectivity would benefit from the identification of circuit architecture (Zhang et al., 2017). This way, the identification of interactions within and between circuits could further benefit from the recent development of graphic models and causal discoveries (Glymour et al., 2019). In chapter 4 we investigate how to separate contributions from different pathways based on their statistics with a biophysical constraint, and this could be further adapted to a Bayesian model fitted to empirical data.

This framework based on biophysics and probabilistic modeling and connected to multi-scales and multiple recording techniques would allow researchers to incorporate modulations to validate brain functions, e.g., optogenetic modulation for local neuronal processes (Fernández-Ruiz et al., 2021, Valero et al., 2022) in the microscopic scale or cross-regional modulation like TMS in mesoscopic scale. One related question would be: do we need to explicitly model the population activity and the link between the latent activity and the observed recording, or is it sufficient to just build a predictive model with neural network to match the recorded signals. Here we suggest to have this biophysical-based generative model, that could be fitted by multiple techniques and we believe this would put more constraints on the model fitting. It is likely that the dimension of population dynamics is still larger than the number of recording sites, especially when we consider the spontaneous activity or when the subject is facing natural stimuli (Stringer et al., 2019). In this way, a linear inversion will fail to give you the whole picture, but joint fitting with multiple measurements will reveal better the underlying process. With all possible parameter spaces to be fitted, it's clear that one can not claim to discover the "true process" of the brain activity, but can

only aim to find an approximation that is as close as possible to the underlying process given all possible recordings. And with the best model one could find, the hope is this would help us to understand the brain and answer interesting questions like how the information is processed, or how dysfunction in different scales affects cognitive functions.

1.5 Preview of the Dissertation

In this thesis, we seek to robustly segregate and model the local circuit in the hippocampus with LFP data. Statistical methods are general, easy to scale, and fast. It generally has very few assumptions on the biophysical mechanisms of the data. Unsupervised learning methods are widely applied to disentangle the pathways of specific activities (Herreras et al., 2015). However, post-hoc knowledge of biophysical mechanisms is still needed to understand and interpret the results, which sometimes fails to unmix the sources when the statistical assumptions are not fulfilled. On the other hand, biophysics-based models typically have particular assumptions on the recorded signal, which limit their usage to specific cytoarchitecture (Einevoll et al., 2007, Gratiy et al., 2011). Here, we seek to improve the separation by utilizing some generic biophysical properties to guide the statistical separations.

In chapter 2, we set off to improve the unsupervised method to separate the sources by biasing data to their high-frequency part. We first show that synaptic input is more localized around the input site at the higher frequencies because of the cable effect of dendritic cable. On the other hand, higher-frequency signals are less affected by slow active processes in the dendrites. We find biasing data to the higher frequencies stabilizes the separation. By applying Granger causality analysis to the separated data, we find stable asymmetric directions found by the analysis match the known MEC-HP circuitry. Besides, we also find a lot of cross-laminar directional connections. This demonstrates it is possible to discover the complex interaction between multiple pathways, including cross-regional connections, with LFP data. Our analysis of the components' time scale also suggests that the LFP involves complex slower conductances. The slower part of LFP affects separation in the real data more than the simulated passive neurons suggest. There is a complex nonlinear process in the real neurons and signal contributed by a rich amount of sources, especially in the slow frequency.

In chapter 3 and 3, we try to find an efficient strategy to model LFP signals and connect them to presynaptic inputs. We re-discover the early work of transfer/Green's function method to capture the membrane potential (Koch, 2004, Abbott et al., 1991), which is later developed to take into account the LFP signal (Gratiy et al., 2011), and we extend it for more general usage. This idea aligns with current kernel-based simulation methods, and the linearization of the population response is nicely demonstrated in current work (Hagen et al.,

2022). The questions we ask are, first of all, how to efficiently capture the impulse response with a known morphology and, secondly, how to deal with recordings where we don't have an explicit reconstruction of cell morphology.

In chapter 3 we present the essential modeling components and show how the simplified Green's function method could generate a LFP signal response for neurons with any given morphology. We connect to the early work of Green's function treatment of membrane potentials (Abbott et al., 1991, Koch & Poggio, 1985, Caudron et al., 2012), and discuss how heterogeneity affects the transfer function. We demonstrate the usage of this model by comparing it to the numerically simulated data, where the prediction is similar, but Green's function method is much faster. With this simple forwarding modeling strategy, we investigate how the population properties affect the LFP. We also show a simple way to parameterize the model. With this model, we are able to tell the position of the current injection and multiple biophysical parameters. To summarize, we demonstrate that the frequency domain Green's function method provides an efficient way to characterize LFP signals systematically.

Based on results from chapter 3, in chapter 4 we propose a model for the inverse problem on LFP multichannel recording data. The idea is to unmix LFP signals with the biophysical-inspired constraint. The logic is when one separates the LFP signals with unsupervised methods, the algorithm is likely to fail because the independence or sparsity of the signal is not fulfilled. However, brain signals are typically highly correlated and barely become sparse when, in this case, the animal is moving (Sirota et al., 2008). Therefore we propose to use biophysical models in chapter 3 to constrain the spatial profile of components. By considering their statistics, parameterization with the Gaussian mixture model allows us to loose the reliance on a detailed, precise knowledge of neuron morphology. We formulate the problem into a maximum likelihood framework and demonstrate that this method improves the source separation in the frequency domain.

When separating sources in chapter 2, a closer look at the frequency patterns not only allows us to probe the local biophysical signals but could also help us to identify the far-field artifacts. These volume-conducted artifacts have been reported to constitute a large portion of electrophysiological recordings, especially at higher frequencies ($> 30Hz$) (Muthukumaraswamy, 2013) Amongst them, EMG artifacts coming from various head muscle activities show an interesting colored (compare to a flat spectrum for white noise) frequency pattern. Utilizing the spatial pattern given by volume conduction theory and the temporal pattern, we present in chapter 5 an ICA-based EMG-removing toolbox that autonomously identifies and removes these types of far-field activity, as well as removes common line noise. We show that the identified far-field noise is taking a significant portion of the high-frequency signals, and by removing it, we improve the separation of biophysically meaningful signals.

I would like to close the introduction with this alike mind:

> "It's one thing to know that something causes something else and why. What more does "function" add to that? – Lauren Ross"

When we set off to answer the why question, then an explicit and carefully quantified picture of the network structure, its dynamics which is constrained by the biophysical network architecture, and the generative model and mechanism behind all these becomes more important than just relating neural activity to particular predefined cognitive functions.

Chapter 2

LFP Model in the Temporal Domain

The local field potential (LFP) is generated by multiple neural transmembrane current sources: synaptic currents, action potentials (Gold et al., 2006), active conductance currents, dendritic spikes, as well as slow non-neuronal sources, such as glia or polarization of blood vessels. Generally speaking, any transmembrane current source would contribute to the extracellular electric field, with distinct sources linearly mixing and giving rise to a complex interference pattern that is what observable LFP is. While the high-frequency part is used to detect the spiking activity of neurons, the slower part referred to as local field potential is biased to sub-threshold transmembrane currents, e.g., dendritic processes and synaptic currents, as well as the gradients of the putative extracellular diffusion current (Gratiy et al., 2017). The latter contributes mostly to the slower frequencies less than a few hertz, and the former is predominate in the physiological frequencies. This provides rich information about local dynamics, far beyond a simple average of local spiking activity, as it is currently mostly utilized.

One of the major contributors to LFP is synaptic input currents. It has been well established in theoretical works (Lindén et al., 2014). The synaptic currents result in large dipoles along the dendrites and the field it generates spreads around the neuron population and depends on their spatial alignment and correlation level (Łęski et al., 2013). Simulations have been used to tell how the extra-cellular field profile is shaped by local populations (Einevoll et al., 2013, Lindén et al., 2014, Hagen et al., 2016).

The study of local network dynamics would be enhanced by incorporating the input signal to the local system. In practice, it's difficult to target precisely the directly connected sender and receiver pair in different brain areas at the same time. However, information carried by synaptic currents resembles the presynaptic activity directly targeting the local network (Einevoll et al., 2013, Pesaran et al., 2018). This would be captured by LFP and mixed with the currents generated by local dynamics. So it would be useful to recover the afferent synaptic currents from the LFP data.

With the LFP reflecting the collective behavior of local and afferent dynamics, we would like to identify the contribution of the underlying synaptic and non-synaptic mechanisms of the LFP. This poses an inverse problem. However, by contrast to the forward problem, the inverse problem is generally ill-posed and doesn't have a unique solution (Buzsáki et al., 2012, Nunez et al., 2006). Methods have been applied at different levels to extract the information. For example, current source density methods aim to estimate the density of transmembrane current sources (CSD) generating the LFP (Nicholson & Freeman, 1975). It starts with spatial Laplacian and is extended by modeling the plausible forms of current sources (Pettersen et al., 2006) and more general kernel method kCSD (Potworowski et al., 2012). Later work also incorporates the modeling of smooth temporal dynamics with Gaussian process based gpCSD (Klein et al., 2021).

On the other hand, unsupervised methods are employed to identify pathways with certain statistical properties. Principle component analysis or factor analysis is used to find latent factors that explain most of the variance in the data. Independent component analysis (Bell & Sejnowski, 1995, Hyvärinen & Oja, 2000, Korovaichuk et al., 2010), find components most independent from each other. Extensions for ICA also consider the nonstationarity of the components (Artoni et al., 2012). In spite of the widely used temporal independency, spatial-temporal ICA (Łęski et al., 2010) explores to utilize the spatial sparsity to separate temporally correlated signals after reducing the volume conduction with CSD methods.

Bayesian models have also been employed to model the local networks. Dynamic causal models (Friston et al., 2003, Pinotsis et al., 2017) have been used to model the local dynamics and understand the connectivity between principal cells and interneurons. However, the forward modeling of LFP and dendritic activities is largely simplified in this kind of model. Especially for high-density LFP recordings, a simple dipole model is not sufficient to capture and make full use of the spatial profile of input responses (Næss et al., 2021).

In this work, we are interested in LFP source separation as well as the inverse problem of LFP. Here we theoretically formulate and emphasize how the dendritic properties would affect the source separation. We provide methods to reduce the cable effect and increase spatial sparsity. We further develop methods to estimate the synaptic properties of each pathway. Then we validate the methods with NEURON simulation. With these methods, we further develop a framework to automatically separate and select reliable components which consistently appear across multiple recording sessions. Our method finds more reliable components across sessions than previous methods. These reliable components generally have meaningful dipole shapes which agree with the anatomy of the known structures in the hippocampus and their receptor types are discussed. We further confirmed the components with multivariate Granger causality assessments. The connections estimated with the method agree with the anatomical connection.

2.1 LFP Dynamics Model

Neurons propagate electrical activity to process information. They are enclosed by an insulating membrane with ion channels distributed across it. Ions flow through these channels, producing transmembrane currents. During synaptic transmission, neurotransmitters released from the presynaptic terminal bind to postsynaptic receptors, which directly or indirectly open ion channels located at the postsynaptic terminal and elicit post-synaptic currents. These change the membrane potential of neurons. So the membrane potential directly corresponds to synaptic input (Sterratt et al., 2011a).

Inferring the synaptic activity corresponding to different pathways is important in understanding the dynamics of neuron circuits. Local electrophysiology data has been recorded to interpret the network dynamics, yet how to disentangle the effluent activity and local network response remains to be elucidated (Einevoll et al., 2013). Once proper functional links between neural physiology activity and the recorded signal (forward models) have been established, for example in LFP modeling (Nicholson & Freeman, 1975, Brette & Destexhe, 2012, Lindén et al., 2014), model inversion has been employed to infer the dynamics of local neuron network (Mazzoni et al., 2008, Moran et al., 2008, Barbieri et al., 2014). State space modeling has been widely used to infer neural network activity. Detailed biophysical models of single neurons have been explored to capture postsynaptic activities in voltage dye imaging (Huys et al., 2006, Pakman et al., 2014). On the other hand, the multichannel extracellular recording provides us with a lower resolution yet powerful tool to simultaneously record LFP and unit data, the extended spatial sampling allows us a closer look at the input activity from effluent pathways. However, biophysical modeling in multichannel recording is still under investigation. Therefore in this work, we built a biophysical proper model with certain simplification to infer pathway-specific contributions in local neural population from LFP recording.

The very basic motivation is, whether we can more precisely monitor the input and output of the local network directly with the help of multi-site recordings, instead of recording and trying to interpret the input and output by patching single neurons or larger imaging methods that ignore the sublayer subtlety such as EEG.

In the following, the realistic biophysical model of LFP is revisited in section 2.1.1, a discretized and simplified model is proposed in section 2.1.2, and our method is explained in detail. In the result section, our method is tested in different scenarios. Conductance-based models and other nonlinear facts will be discussed.

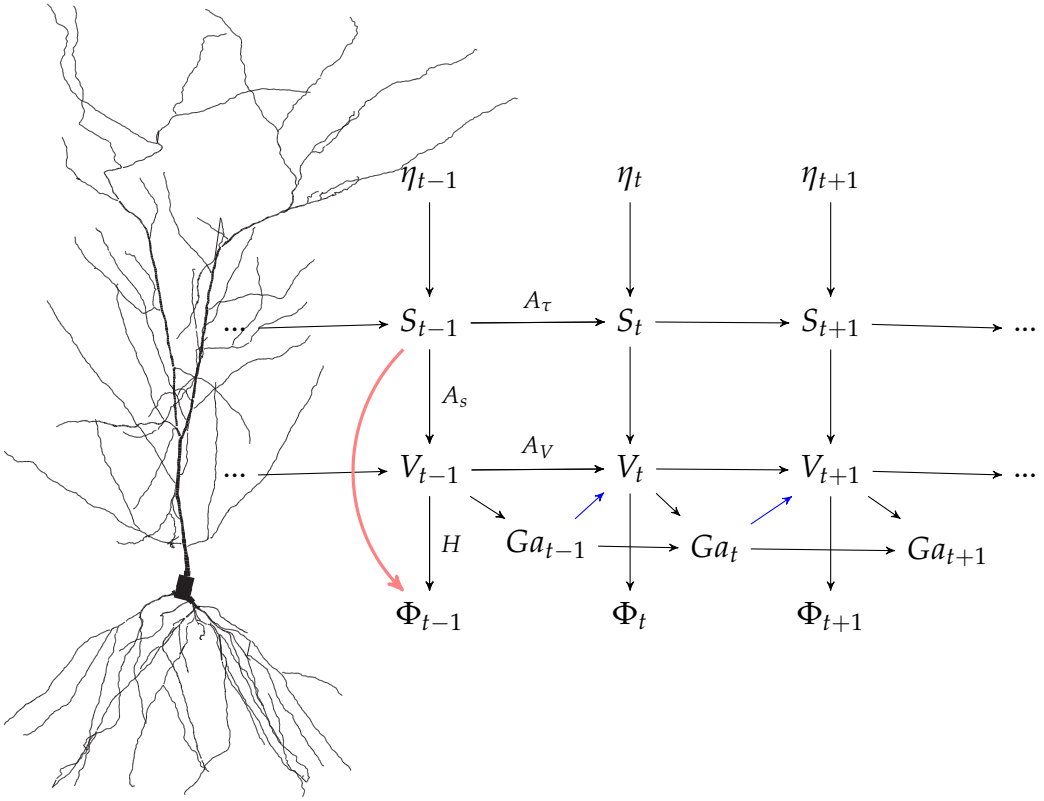

Figure 2.1: The Schematic of LFP Signal Generation through a Dendritic Tree is Depicted as a State Space Model. Pathway-specific inputs $\mathbf{J}$ arrive at their corresponding synapses $\mathbf{S}$ activate synapses according to auto-regressive dynamic systems parameterized by A_τ. When the local synapses are opened, currents flow through synapses according to the synaptic distribution $\mathbf{A}_s$ and lead to the local membrane potential $\mathbf{V}$ depolarization. The currents flow along the dendritic tree with the conductance depicted by $\mathbf{A}_V$. At the same time, the depolarization of $\mathbf{V}$ leads to the opening of various voltage-gated ion channels $\mathbf{G_a}$, and $\mathbf{G_a}$ also have their own, usually slower, kinetics. The transmembrane currents, determined by membrane potential $\mathbf{V}$, generated the local electric field. Therefore, the local field potential Φ is linearly generated by membrane potential $\mathbf{V}$, H denotes their relationship. This chapter tries to separate the contribution of pathway-specific contribution from Φ (red arrow from $\mathbf{S}$ to Φ) by reducing the history dependence contribution according to this state space model.

2.1.1 Forward Model of the Membrane Potential

The neuron cable model is well established to characterize membrane kinetics of dendrites (Dayan & Abbott, 2001, Sterratt et al., 2011a). In a continuous-valued manner, passive membrane properties are modeled using the cable equation, while active channels, as well as synapses, are modeled as nonlinear conductances distributed across the neuron's membrane. $V(x,t)$ (denotes as V for nomination simplicity) is the membrane potential at the location of x along the neuron cable at observation time t, E_l denotes the resting potential. Currents flow within the neuronal cable with the axial conductance g_a, and cross membrane with the passive conductance g_l. The phospholipid bilayer structure of the membrane acts as a capacitor with capacitance C_m. These are the basic passive properties of neurons.

Additionally, k families of inputs project to distinct positions with time-invariant spatial loading $A_i(x)$, whose equilibrium potentials are E_i, respectively. Besides that h different types of active ion channels are located along the dendrites. Their conductances $Ga_j(x,V)$ are modeled as functions of membrane voltage and other dependencies like calcium concentration c_x. The driving force of membrane currents is given by the difference between the current membrane potential and their respective equilibrium potential $E_{Ga,j}$ for each active channel family, which is determined by their ion permission.

According to Kirhoff's law of current conservation, the net current in each dendritic compartment should be zero. Hence, the cable equation is written as:

$$C_m\frac{\partial V}{\partial t} + g_l(V-E_l) + \sum_j^h Ga_j(x,V)(V-E_{Ga,j}) + \sum_i^k A_{si}(x)s_i(V-E_i) - g_a\frac{\partial^2 V}{\partial x^2} = 0. \quad (2.1)$$

A summary of the variables could be found in table 2.2.

The overall currents flow across the membrane is denoted as transmembrane current $I_{membrane}$. The transmembrane current consists of the capacitive current, current flow through channels as well as synaptic currents (e.g. the first line of eq.(2.1)).

According to the current conservation law, we could further write the $I_{membrane}$ as the negative of axial current:

$$I_{membrane} = g_a\frac{\partial^2 V(x)}{\partial x^2}. \quad (2.2)$$

$I_{membrane}$ gives rise to the extracellular potential that we could measure with LFP and EEG (Einevoll et al., 2013), which we would discuss later in the next session.

The synaptic inputs are distributed along the dendritic tree according to a distribution $A_{si}(x)$ for each pathway i. For simplicity, their activity are simulated as an exponentially decay process with pathway-specific inputs η_i. At any point, x the membrane potential $V(x)$ evolves according to equation 2.3. That is,

$$\frac{\partial V}{\partial t} = \frac{-g_l(V-E_l) + g_a\frac{\partial^2 V}{\partial x^2} - \sum_j^h Ga_j(x,V)(V-E_{Ga,j}) - \sum_i^k A_{si}(x)s_i(V-E_i)}{C_m} \tag{2.3}$$

$$\frac{\partial s_i}{\partial t} = -\tau_i s_i + \eta_i. \tag{2.4}$$

An analytical solution of the membrane potential is usually very difficult to achieve (Butz & Cowan, 1974, Abbott et al., 1991, Caudron et al., 2012), we'll discuss this later in the next chapter (see Green's function).

An easier alternative is to discretize the spatially continuous system which leads to the multi-compartmental model.

$$\begin{aligned} V((k+1)T) &= A_V V(kT) + B_V S(kT) \\ S((k+1)T) &= A_{SI} S(kT) + B_S \mathbf{E}(kT), \end{aligned}$$

$$\begin{aligned} \textit{where} \qquad A_V &= e^{C_m^{-1}(G_A - G_l)T} \\ B_V &= (A_V - I)(G_A - G_l)^{-1} A_s \\ A_{SI} &= e^{A_\tau T} \\ B_S &= (A_{SI} - I)A_\tau^{-1}. \end{aligned} \tag{2.5}$$

$A_s \in R^{N\times K}$ is the synaptic distribution of all the pathways. We use $G_A = g_a \nabla \in R^{N\times N}$ to account for the axial currents operator. G_l and C_m is passive conductance and capacity. $A_\tau = diag(\tau_1, ..., \tau_k)$ captures the time constants of the synapses. To keep it simple, we just list the major formulas, and the details of derivation could be found in the appendix A.1. As would be expected with dynamics of a linear system (Gajic, 2003), discrete-time state space models of the membrane potential (equation.2.3) could be captured by a multivariate auto-regressive process.

2.1.2 Model of the Local Field Potential

The LFP is an integration of electrical potential produced by current sources (transmembrane currents) (Einevoll et al., 2013, Nunez et al., 2006). For simplicity, the electric field is regarded as a quasi-static field (Plonsey & Heppner, 1967). (Notice that this assumption is valid at the frequencies typically encountered in nervous tissue, but violated in the very low frequency (Gratiy et al., 2017)). Assuming a purely homogeneous and isotropic ohmic conductivity, LFP is given according to Gauss' divergence theorem.

$$\Phi(t, r_j) = \frac{1}{4\pi\rho}\int \frac{1}{|r_j - r|} I_{membrane}(t, r)dr \tag{2.6}$$

To achieve a numerical solution, we discretized the model and simulate each neuron by n compartments, e.g., $V \in \mathbb{R}^n$. Then equation 2.6 becomes a linear transform of the current sources (Johnston & Wu, 1994, Pettersen et al., 2006), as has been shown in (2.7):

$$\mathbf{\Phi} = \begin{pmatrix} \phi_{1,t} \\ ... \\ \psi_{m,t} \end{pmatrix} = H \times \mathbf{I_{membrane}} = B^* \mathbf{V}. \tag{2.7}$$

$H \in \mathbb{R}^{m \times n}$ resembles a distance-dependent mapping from currents at compartments to recording sites. Here we define $B^* = HG_A$ which uses the axial current operator to obtain the transmembrane currents (eq.2.2) and then map it to the extracellular field. Therefore, $\mathbf{\Phi}$ is a linear transformation of the membrane potential $\mathbf{V}$.

With this, we could combine the eq.2.5 with the linear transform of eq.2.7:

$$\begin{aligned} \mathbf{\Phi}(kT) &= B^* \mathbf{V}(kT) \\ \mathbf{V}((k+1)T) &= A_V \mathbf{V}(kT) + B_V \mathbf{S}(kT) \\ \mathbf{S}((k+1)T) &= A_{SI} \mathbf{S}(kT) + B_S \mathbf{E}(kT), \end{aligned} \tag{2.8}$$

Denote $B_\Phi = B^* B_V$ and $B_\Phi^+ = W_s (G_A - G_l)(A_V - I)^{-1} \tilde{B}_{:m}$ its pseudo-inverse (with $W_s A_s = I_{K \times K}$), the dynamics of LFP could also be captured by a multivariate auto-regressive model:

$$\sum_{i=0}^{2} Z_i \Phi(t+i) + \sum_{j=0}^{1} Z_{*/j} \Phi^{*/}(t+j) = \mathbf{E} \tag{2.9}$$

$$\begin{aligned} \textit{where} \quad Z_2 &= B_S^{-1} B_\Phi^+, \\ Z_1 &= -B_S^{-1}(B_\Phi^+ A_{\Phi,:m} + A_{SI} B_\Phi^+), \\ Z_0 &= B_S^{-1} A_{SI} B_\Phi^+ A_{\Phi,:m}, \\ Z_{*/1} &= -B_S^{-1} B_\Phi^+ A_{\Phi,m+1:}, \\ Z_{*/0} &= B_S^{-1} A_{SI} B_\Phi^+ A_{\Phi,m+1:} \end{aligned}$$

which directly links the LFP to the presynaptic inputs.

Assume the number of inputs is at least the same as recording sites, then B_Φ has an inverse matrix $B_\Phi^\circ = B^*(A_V - I)(G_A - G_l)^{-1} A_s = B_\Phi$. So we would further

have:

$$\Phi(kT) = \sum_{j=1}^{2} Z_j \Phi((k-j)T) + \sum_{j=1}^{2} Z_{*/j} \Phi^{*/}((k-j)T) + B_E E((k-2)T) \quad (2.10)$$

$$\begin{aligned} \textit{where} \quad Z_1 &= (A_{\Phi,:m} + B_\Phi^\circ A_S B_\Phi^+), \\ Z_2 &= -B_\Phi^\circ A_S B_\Phi^+ A_{\Phi,:m}, \\ Z_{*/1} &= A_{\Phi,m+1:}, \\ Z_{*/2} &= -B_\Phi^\circ A_S B_\Phi^+ A_{\Phi,m+1:} \\ B_E &= B_\Phi^\circ B_S, \end{aligned}$$

where $\Phi^{*/}$ span the orthogonal complement space of Φ. Details could be found in appendix A.2.

2.2 Methods

2.2.1 Simulation

Here we use the LFPy toolbox (Lindén et al., 2014) to simulate the local field potential. The detailed neuron model we used, the early brunching CA1 pyramidal neurons, is downloaded from ModelDB.The soma of the pyramidal cell locates at 0um. All the passive parameters are kept the same as previous work (Grienberger et al., 2017).

To be comparable to the real data, we modeled the two profoundly studied hippocampal pathways: the Schaffer collateral path and the perforant path. The Schaffer collateral path is the projection from CA3 to the CA1 radiatum layer(rad.). So we modeled it as synapses targeting the oblique dendrites. While the perforant path is the input coming directly from layer III of Entorhinal cortex (ECIII) and it targets the apical dendrites (locunosum moleculare (l.m.) layer). We simulate the input loading in a distance-dependent manner centering at the middle of the radiatum or l.m. layer. To model the distribution of the laminar synapses, the whole cell is binned into n input layers. The total number of synapses is assigned according to the depth of the layer. Afterward, the number of synapses is distributed according to the surface area of each compartment within the layer.

We model the neuron to study the dynamic pattern of its input-response, therefore, the input activity is generated as a random spike train with a non-stationary Poisson process and the spike time is been saved as the ground truth activity.Afterward, a binary spike train is constructed, and then the ground truth synaptic currents *stim* are generated with the given synaptic time constant τ. In the simulation, the synaptic kinetics are modeled as AMPA receptors with double-exponential functions (rising $\tau = .01$ms and decaying $\tau = 2$ms. We also simulated the inhibitory components around soma at $[-20, 50]\mu$m according to

the realistic synaptic distributions given in (Jaffe & Carnevale, 1999). The GABA receptors are modeled as double-exponential functions with a rising time constant of 1ms and a decaying time constant of 12ms.

In the theta-modulated simulation, signals are modulated by an $f_\theta = 8$Hz theta signal with a phase shift for each pathway. The mean firing rate is modeled as a gamma frequency burst sitting on theta baselines (fig.2.2). The theta phase of each pathway is shifted for radiatum, l.m., PV cell (IN) inputs at $[120, 0, 240]$ degrees, and their gamma oscillation frequency is modeled as $[70., 100., 125.]$ Hz, respectively.

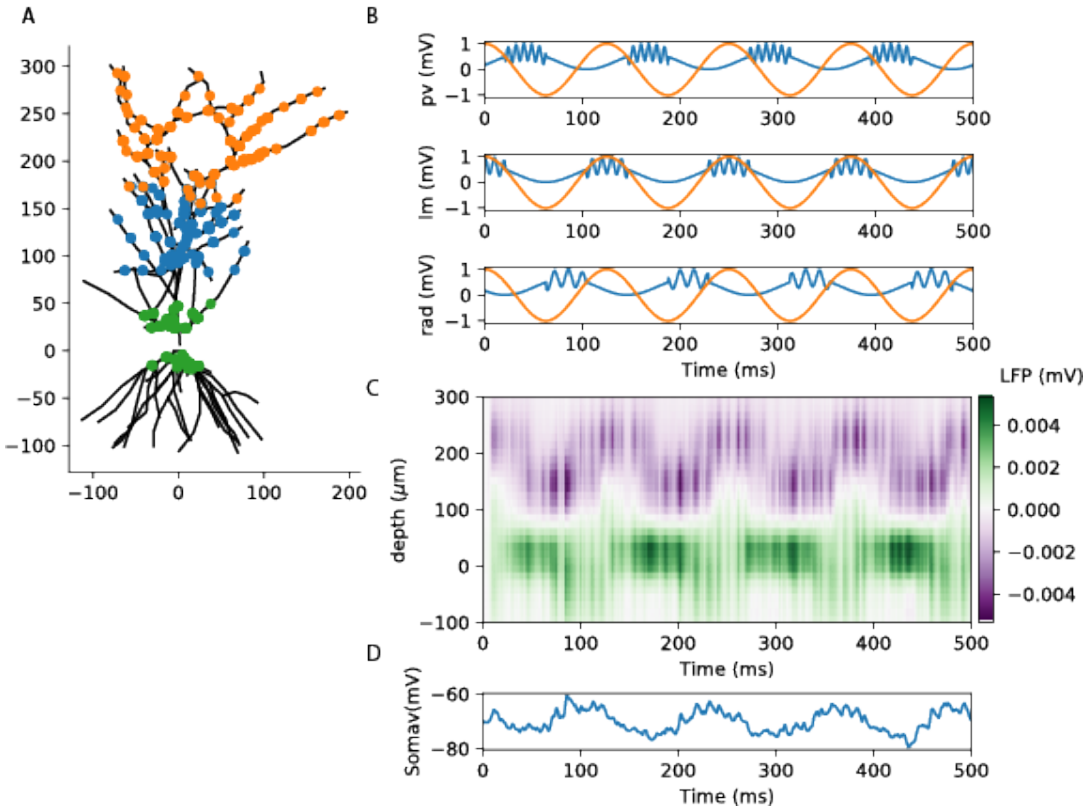

Figure 2.2: Theta modulated simulation. A. Example for the distribution of synapses along the neuron: PV interneuron input on the soma (pv, green), CA3 Shaffer-Collateral input to str. radiatum (rad, blue) and MEC layer 3 perforant path input to locunosum moleculare (lm, orange) B. Firing rates of the presynaptic cells (blue). Plot with a common theta wave as coordinate (orange). C. Generated LFP signals. D. Membrane potential at soma.

2.2.2 Recording

The adult Long Evans rat was housed together with other Long Evans rats at standard conditions. All experiments were in accordance with the European Union guidelines on the protection of vertebrates used for experimentation (Directive 2010/63/*EU* of the European Parliament and of the Council of 22

September 2010). They were performed under the German Law for Protection of Animals (TierSchG) and approved by the local authorities ($ROB - 55.2 - 2532.Vet_0 2 - 16 - 170$). The rat was trained on a T-maze alternation task. After the conclusion of the training the animal was returned to ad libitum water access and at 10 month of age, weighing 460 gram the rat was chronically implanted with depth electrodes. Subsequently, a miniature stainless steel screw (0.86 mm diameter, Antrin Miniature) was implanted above the cerebellum to serve as the ground. Craniotomies were performed above the right Olfactory bulb as well as over a trapezoid right hemispheric area, extending between ca. -3 and -6 mm AP and between ca. 0.5 and 5 mm ML. After durotomies, the craniotomies were each covered with a sheet of pre-polymerized 1 : 10 PDMS (Sylgard 184, Dow Corning), and the borders were sealed with tissue glue (Vetbond, 3M) and UV curing dental cement (Tetric EvoFlow, Ivoclar). Three 64-channel silicon probes (linear arrangement of 20 um spaced recording sites, H3, Cambridge Neurotech) which had been mounted on custom-made microdrives to allow for postsurgical depth adjustment and probe recovery were painted before implantation with fluorescent DiIC (Invitrogen) to facilitate post-mortem visualization of electrode tracks. In addition probe shanks were coated with water-dissolvable polyethylene glycol (PEG, average mol wt 8000, Sigma Aldrich) to mechanically stiffen them for insertion through the PDMS polymer. Atlas-derived insertion coordinates were rescaled based on measured bregma-lambda distance (8.5 mm). With help of a robotic stereotaxic apparatus (Stereodrive, Neurostar) the probes were inserted at or close to the target depth. The probe targeting the medial entorhinal cortex was inserted at -4.8 mm AP, $+4.7$ ML, with an insertion angle of 43 anterior-to-posterior and an insertion depth of ca. 50 um beyond LFP phase reversal in superficial layers of MEC). The probe targeting the dorsal hippocampus was inserted at -3.5 mm AP, 1.8 mm ML, and 3 mm DV. The sleeves of the recoverable microdrives were cemented to a 3D printed support structure, the implant was covered with a 3D printed protective cap and the animal returned to its home cage. After a 7-day recovery period, the animal was put on a water restriction schedule identical to the one used in the training phase and recordings were performed in the T-Maze alternation task described above.

Before the first post-surgical recording the anatomical position of the probes was inferred from ongoing recordings with help of known physiological landmarks and probe depth adjustments were done using the microdrives to optimize coverage of the structures of interest. Electrical signals were recorded in a tethered configuration using the eCube recording system (WhiteMatter) and a headstage (HS-640) with 4 headstage modules stacked to acquire data from the 3 depth probes as well as the EEG channels. Signals were amplified ($200x$) and digitized at 25 kHz. Ground and reference were shorted together and connected to a cerebellar stainless steel screw. During preprocessing the electrophysiological data was downsampled from 25 kHz to 1250 Hz to simplify the analysis of LFP patterns.

After the conclusion of the experiments, the rat was deeply anesthetized with Pentobarbital and transcardially perfused with PBS followed by 4% paraformaldehyde (PFA). The brain was carefully mechanically extracted from the skull and stored in 4% PFA for post-fixation overnight. Subsequently, brain slices of 70μm thickness were made on a vibratome (OTS 5000, FHC Inc.), the slices mounted in Mounting Medium with DAPI (VECTASHIELD, Vector Laboratories) on glass slides and borders sealed with nail polish. Slices were then preselected for candidate DiI stained fluorescent electrode tracks with help of an epifluorescence microscope and regional targeting of the fluorescent silicon probe tracks was verified using a confocal microscope. (Leica TCS SP5).

Anatomical layers were identified in the recordings with help of known physiological landmarks: The center of the CA1 pyramidal layer was defined as the channel with peak ripple power. Subsequently, the dendritic input layers of CA1 and Dentate Gyrus were defined with the help of the spectral profile, and theta-gamma modulation profiles of LFP across depth as well as sharp-wave-ripple (SWR) and theta-triggered CSD pattern and the spatial distribution of gamma burst modes after spatially resolved gamma burst detection. In some cases, a combination of features was used to define a layer most consistently across sessions. CA1 oriens was defined using depth profiles of spatially resolved gamma burst detection and identified with the burst mode directly neighboring the CA1 pyramidal layer in the direction of the neocortex. This corresponded to the border between the CA1 pyramidal layer and CA1 oriens being located about midway through the superficial CA1 sharp-wave source in SWR-triggered CSD profiles. CA1 stratum radiatum was taken to cover the space between the upper and lower zero-crossings of the sharp wave sink in SWR-triggered CSD profiles. The fissure between CA1 stratum lacunosum moleculare and the outer molecular layer of Dentate Gyrus was assumed to run between the dorsal $\frac{2}{3}$and ventral $\frac{1}{3}$ of the ventral CSD source of the SWR associated sharp-wave.

In sessions where dentate spikes were detected, this corresponded to the dorsal border of the main sink associated with Dentate Spike Type 1. The space between such defined CA1-DG fissure and the lower border of CA1 radiatum was labeled as CA1 stratum lacunosum moleculare. Dentate Gyrus (DG) outer molecular layer was defined as the space between the Fissure and DG middle molecular layer with the DG middle molecular layer being taken to encompass the channels with the strongest mode of theta modulation of high gamma ($100 - 200$ Hz) power in DG. In sessions with Dentate Spike detection, this corresponded to the location of the main CSD sink associated with Detate Spike Type 2. Finally, DG inner molecular layer was being located via the most dominant DG sink in average ripple-triggered CSD profiles.

Brain states were labeled as awake theta, awake non-theta, slow wave sleep (SWS), and REM sleep with the help of motion tracking derived head speed as well as using LFP power in dorsal CA1 stratum oriens in the delta ($2 - 4$ Hz), theta

(5 − 9.5 Hz) and alpha-beta (10 − 25 Hz) bands as well as 160 − 200 Hz power in the olfactory bulb EEG. First active behavioral periods were distinguished from inactive periods as displaying head speeds exceeding 50 mm/s. To detect theta states we defined a theta reference channel in the CA1 stratum oriens ca. 100μm dorsal of the center of the CA1 pyramidal layer. Theta states were then detected automatically using the ratio of the power in the theta band (5 − 9.5 Hz) to the power of neighboring bands (2 − 4 Hz, 10 − 25 Hz) on this channel. The ratio threshold separating theta from other states was set empirically in each animal after visualization of the spectrograms and state separation results. High voltage spindle (HVS) periods were detected independently with help of EEG signals and excluded from candidate theta periods. Candidate theta periods separated by less than 2 seconds were merged, and candidate theta periods shorter than 2 seconds were skipped. Slow wave states (SWST) were defined as periods when the theta reference channel integrated power in the 2 − 4 Hz and 10 − 25 Hz bands exceeded an empirically set threshold during non-Theta, non-HVS periods. Theta periods occurring during inactivity were defined as REM when they directly followed slow wave states. The remaining theta periods were considered awake theta. Slow wave sleep (SWS) was defined as slow wave states during motor inactivity and with 160 − 200 Hz power in olfactory bulb EEG being below an empirically set threshold. SWS candidate periods shorter than 20 seconds were skipped. All remaining periods and SWST periods outside SWS were considered awake non-theta states.

2.2.3 State Space Model Estimation and Source Separation

As we have shown in the last session (eq.2.10), dendrites integrate synaptic currents and, therefore, LFP depends linearly on its own previous values and on a stochastic term. What's more, it also depends on the representation of the membrane dynamics in it's null space. This brings about the spatial-temporal dependency of the response pattern (Sterratt et al., 2011b). That means the spatial pattern flattens out with time because of cable effect 2.3. This pattern could be easily appreciated in simple neuron cables. The analytical solutions in the level of membrane potential have been well developed mainly with Green's function methods (Butz & Cowan, 1974, Abbott et al., 1991).

Because the inputs dominate the LFP signals, it is possible to segregate the signals contributed by different pathways when they are independent enough (Hyvärinen & Oja, 2000, Makarova et al., 2011, Schomburg et al., 2014, Fernández-Ruiz et al., 2021). But the estimation would be affected by the history-dependent part of the signal. However, when the correlation of the signal increases, the dependency would accumulate with time and affects the separation of the signal.

Therefore, we develop different ways to reduce the history dependency of LFP signal and enhance the pathway separation. First of all, according to eq.2.10,

the LFP could be captured by a MAR(2) model. Therefore, we fit a MAR model according to the following:

$$\underset{\{Z_i\}}{argmin} \qquad L = \sum_k \left\| \Phi(kT) - \sum_{j=1}^{2} Z_j \Phi((k-j)T) \right\|_2^2. \tag{2.11}$$

We apply ICA on the residue data after we remove the history-dependent part of the signals. We denote the preprocessed data as $rLFP$ and the result of this method as $rLFP - ICA$.

However, MAR model fitting has its limitations. In the underlying mean-field model, all neurons are assumed to be homogeneous. Furthermore, the non-stationary inputs would affect the estimation of the MAR model. On the other hand, the order or MAR model would change when the input spectrum is not white, i.e., the inputs from the presynaptic activity have some particular temporal structure. Therefore, in practice, we use MAR model fitting to reduce the effect of history integration.

On the other hand, a simple temporal derivative could also help to reduce the effect of temporal integration. We call the temporal derivative of LFP $dLFP$ and this method $dLFP - ICA$. In practice, we always compare the result from $dLFP - ICA$ and $rLFP - ICA$ because the former is more robust to noise but the latter largely reduces the temporal integration effect and tracks the fast events of inputs. Clearly with this simple operation, here we made the least assumption of the data generation model, yet reduced the temporal dependency. Compared to the original LFP, $dLFP$ is largely dominated by the synaptic inputs to the local network. $dLFP - ICA$ preserves the temporal information of the wideband signal while compensating the $P \propto 1/f^{\alpha}$ power-law spectrum by taking the derivative of the time series. The activity of the source is integrated back to approximate the original LFP patterns.

It has been widely recognized that the temporal power spectrum of an arrhythmic LFP signal follows a $P \propto 1/f^{\alpha}$ shape (Buzsaki, 2006, Mitra & Pesaran, 1999). This is called a "power-law" distribution, and the exponent α is linked to cognitive functions (Buzsaki, 2006, He, 2014). It has been pointed out by multiple modeling works that α would be related to membrane time scales, including synaptic conductance (Gao et al., 2017) as well as membrane conductance (Pettersen et al., 2014). We also notice that active conductance will contribute to the power-law shape. Overall, the power-law shape in the high frequency here represents the dendritic and synaptic integration of the input signal. With our formulation in eq.2.10, the power-law spectrum would naturally be explained by the vector auto-regressive model. This observation indicates that temporally whitening data with auto-regressive models would reduce the integration effect and yield better separable signals (Mitra & Pesaran, 1999). Therefore, we also include the whitened data as $wLFP$ and the method as $wLFP - ICA$.

The separation on orignal LFP data and high-passed (>30 Hz) LFP data is labeled as $LFP-ICA$ and $btLFP-ICA$, respectively.

2.2.4 Independent Component Analysis

Independent component analysis is a blind source separation tool widely used to separate mixed signals, so the components are statistically independent or as independent as possible. In the commonly used linear settings, it assumes the signal X is constructed by a linear mixture of multiple signals $S=[s_1,...,s_i]^T$ with specific spatial loading $A=[A_1,...,A_i]$. Writes:

$$X=AS. \tag{2.12}$$

while its inverse, the unmixing of the signal, would be written as $S=WX$.

Statistical independence is defined as the joint probability of any two signals being separable, that is,

$$p(s_i,s_j)=p(s_i)p(s_j), \tag{2.13}$$

assessed with information theory, is defined by their mutual information as equal to zero. The concept of independence (Comon, 1994) and information-maximization (Sejnowski, 1996) was proven to be equivalent to maximum likelihood (Cardoso, 1997), optimize non-gaussianity (Hyvarinen, 1999), and the higher order moments based separation (Cardoso, 1999). In this work, we use the maximum likelihood-estimation-based fast kernel ICA (KDICA) to separate the independent sources (Chen, 2006) for its fast and stable performance and probabilistic likelihood estimation.

Without diving too much into the details, the KDICA separates independent components by maximizing log profile likelihood. This is achieved by minimizing the negative log profile likelihood function J using Laplacian kernel density estimates which renders a fast kernel density estimation of the source distributions.

Suppose each source activity s_i has a density function r_i, then $p(X)=|det(W)|\prod_{i=1}^{m}r_i(W_ix)$, is the likelihood function of observations of X. Then replacing r_i with the k kernel density estimators $\bar{r}_{W_i}(s)=\frac{1}{nh}\sum_{i=1}^{k}K(\frac{W_iX-s}{h})$, here the Laplacian kernel is used for density estimation. Then the log profile likelihood is given as:

$$l_p(W)=\frac{1}{n}\sum_{t=1}^{n}\sum_{i=1}^{m}log\bar{r}_{W_i}(W_iX(t))_log|det(W)|. \tag{2.14}$$

and hence W is optimized to minimize $J\sim -l_p(W)$. We also use J to assess the performance of separation. Even though it's not directly generalizable over different data sets, it indicates how well the separation explains the data.

2.2.5 Cross Frequency Coupling

The cross-frequency phase-amplitude coupling is measured by modulation index (Tort et al., 2008) and mean vector length (Canolty et al., 2006). The cross-frequency coupling measures are compared with surrogate sequences where we keep the phase data but shuffle the amplitude of higher frequency with random time lag similar to (Tort et al., 2010). This way, we keep the temporal structure as well as the marginal distribution of both sequences.

2.2.6 Component Time Constant Fitting

Here we separated the LFP signals into pathway-specific IC components, naturally, we asked the question of whether we can tell more about the synaptic properties of each component. In the linear system, the presynaptic spike-trains first pass through an auto-regressive model is then filtered by the neural dendrites. In the frequency domain, these two processes, together with the dynamics of the presynaptic activity are multiplied. That means, any dynamical pattern, even when narrow band oscillations, will have a baseline shaped by the synaptic kinetics and neural dendrites. And among these two filtering effects, the slower synaptic kinetics will dominate the slow frequency part of the spectrum (see the impulse response pattern of passive neuron dendrites in the next chapter).

Here we consider the slow frequency baseline response produced by synaptic kinetics. Instead of a double-exponential function, we fit an exponential decay to capture the decay time constant of the receptors for simplicity. The spectrum of a synapse with time constant τ is written as:

$$\frac{dx}{dt} = -\frac{x}{\tau} + \delta \Rightarrow j\omega X(\omega) = -\frac{X(\omega)}{\tau} + 1 \tag{2.15}$$

Therefore, the *log* power spectrum of the signal is fitted to:

$$\underset{\tau, c\star}{argmin} |2log(\Phi(f)) - (c\star - log(\frac{1}{(2\pi\tau)^2} + f^2))| \tag{2.16}$$

2.2.7 Evaluate the Components

Reliability

To assess the stability of the ICA parameter estimation, we look at the reliability of the components in two levels. Firstly, we estimate the reliability of the estimation within each session, by employing the resampling method (Meinecke et al., 2002). In each session, we generate the surrogate data by bootstrapping. Since the number of potential independent sources could be larger than the recording dimensions and ICA is a method of finding local minima (Hyvärinen & Oja, 2000), we need to limit the algorithm to search for the local minima close to the

original estimation. A simple trick to control the searching is to project data to the subspace spanned by the original ICA estimate first, then estimate a new rotation matrix on the resampled data. With this, we only consider small deviations from the original unmixing matrix, so the search would converge much faster and the new estimation would be better interpretable. One latent assumption of this method is the ICA components are rotated to improve the independence between each pair of the components in the bootstrap samples. Therefore, instead of measuring the square error estimate of the mixing or unmixing matrix, or the similarity of each of n new estimated component with regard to the original component, here we decompose the rotations into $\frac{n(n-1)}{2}$ elementary rotation angles by taking the matrix logarithm .

$$\hat{\alpha}^{*b} = ln(\hat{R}^{*b}) \tag{2.17}$$

Here, each component $\alpha_{ij}$is the angle of a rotation in the $i-j$ plane. And then the separability matrix is given by:

$$\hat{S}_{ij} = \sqrt{\frac{1}{B}\sum_{b=1}^{B}(\hat{\alpha}_{ij}^{*b})^2} \tag{2.18}$$

Therefore, $\hat{S}_{ij}$ measures how unstable the component i is with respect to a rotation in the $i-j$ plane. It measures how well the components i and j are separated. In practice, the components belonging to the same subregion would generally render a higher $\hat{S}_{ij}$, forming an independent subspace, indicating they are contaminated due to nonlinear interactions within the same neuron population. Independent sources or inputs from the upstream are typically easier to separate and have a lower $\hat{S}_{ij}$. We implement following the steps in (Meinecke et al., 2002), the full derivation could be found in section III of this paper.

Apart from testing the reliability in each session, we also need to group and realign the data across sessions. To cluster the components and assess the significance of the cluster, we use ISCtest (Hyvärinen, 2011) designed by (Hyvärinen, 2011) for testing the inter-subject mixing matrix consistency. This algorithm considers two components to be similar if the corresponding spatial pattern (loading of the mixing matrix) is similar. A significance test is conducted against the null hypothesis under which the independent components are random orthogonal components in the whitened space. In other words, here in the null hypothesis, components from different sessions have no intersession consistency in their spatial loading. In contrast to that, the components we are interested in usually have well-defined spatial patterns due to the anatomical wiring. During the cluster assignment, each cluster would contain only one component from each session. The ISCtest also controls the false positive rates of the detected clusters of components (equ.B.9), and the false discovery rates of joining components to the clusters (equ.B.8). In the appendix B.4 we summarize the basic idea about isctest.

In experiments, the recording shank is moved deeper across days to access signals across layers. In the hippocampus, the channels with the largest ripple power are detected as pyramidal cell layers and aligned accordingly.

Pairwise Mutual Information

The separation performance of ICA is given by the negative profile likelihood J. However, we also want to check how independent is each pair of signals separated by the ICA. Therefore we also use mutual information to evaluate the separation of signals. The mutual information is estimated with a histogram-based method, where the marginal distribution of signals is first transferred into a uniform distribution and then binned into optimized numbers of bins (Moddemeijer, 1989). This provides a robust entropy estimation of any arbitrary distributions.

Causality

Granger causality is widely used to determine the direction of information flow in the field of brain signal analysis, especially in electrophysiology signal processing (Granger, 1969, He et al., 2019). It conceptualizes the "causality" with two fundamental components: the past of one time-series Y_t contains information that helps to improve the prediction of X_t and if this information is contained in no other series in the predictor, then Y_t is said to cause X_t. Here we use the linear implementation of Granger causality, i.e., Multi-Variate Granger Causality (MVGC (Barnett & Seth, 2014)). The connection strength is assessed by the Geweke's measure (Geweke, 1982; 1984), which compares the predictability with or without Y_t, which is written as:

$$F_{Y_t \to X_t | \mathbf{Z}} \equiv \ln\left(\frac{\Sigma_{\epsilon_t}}{\Sigma_{\epsilon'_t}}\right) \tag{2.19}$$

where Σ_{ϵ_t} is the prediction residue without Y_t, and $\Sigma_{\epsilon'_t}$ is the prediction residue with the past of Y_t. This definition is closely related to the nonlinear causal measure of transfer entropy (Barrett et al., 2010), especially in the linear Gaussian model case, they are equivalent to each other.

A frequency domain factorization of Granger causality is also applied to understand where information transition happens (Geweke, 1982, Chen et al., 2006). For a linear system that we consider here, we assume the frequency domain transfer function of the system can be written as: $H(\omega)\Sigma H(\omega)^* = S(\omega)$, with $S(\omega)$ being the cross-spectral density matrix for a multivariate signal $\mathbf{X}$ at frequency ω, and Σ represents the AR model prediction residues. The frequency domain Granger causality can be computed as:

$$f_{Y_t \to X_t}(\omega) \equiv \ln\left(\frac{|S_{xx}(\omega)|}{|S_{xx}(\omega) - H_{xy}(\omega)(\Sigma_{yy} - \Sigma_{xy}^2/\Sigma_{xx})H_{xy}(\omega)^*|}\right) \tag{2.20}$$

which has been proved by (Geweke, 1982) that:

$$\frac{1}{2\pi}\int_{-\pi}^{\pi} f_{Y_t \to X_t}(\omega) d\omega = F_{Y_t \to X_t} \tag{2.21}$$

In the multivariate case, the Granger causality is naturally extended by fitting a multivariate AR model where the causal residue then been factorized in the frequency domain to see the causal connection happen within each frequency band (Barnett & Seth, 2014).

To avoid high variance and bias caused by independent VAR model fitting, the MVGC toolbox fits the full model and extracts reduced model parameters from the full model via factorization of the spectral density matrix (Chen et al., 2006, Dhamala et al., 2008).

In freely moving animals, the functional connectivity variate depends on the behavior of the animal. Therefore, we compute Granger Causality in periods from the whole session. Considering the causal strength would change in different periods, the directional estimation is conducted by comparing the causal flow in both directions. Statistical significance is assessed by a two-sided Wilcoxon sign rank test corrected for multiple-comparison by Bonferroni correction.

2.3 Results

2.3.1 Separation in Simulation Data

To appreciate the cable effect, we first simulate the LFP response to a single str.radiatum input. Even when there are no active channels and the synaptic currents keep the same spatial pattern, the spatial pattern of the LFP is changing due to the cable filtering effect (fig.2.3 A). The spatial profile is narrower at the raising phase while getting stable afterward. This slower stable pattern largely dominates the whole time series and would be detected as the principal component as well as the rad. component, as would also be easily appreciated in (Makarova et al., 2011). On the other hand, the $dLFP$, $wLFP$, and the $rLFP$ are largely dominated by the raising phase of the signal, they respond quickly to the input and fall back to the baseline afterward (fig.2.3 A, B, C, D). This enables $dLFP$, $wLFP$, and the $rLFP$ to track the fast-changing signal.

The capacitive current reduces the amount of current produced by the synaptic input and changes the spatial loading of the response patterns. We didn't specifically fit the capacitive currents here, but the temporal fitting largely reduces the spatial spreading patterns (fig.2.3 C). In practice, we find the $rLFP$ and $dLFP$ give very similar separation performance, but $dLFP$ is model-free and integration back to the LFP time scale would preserve the original power law spectrum pattern. We use the $dLFP$ to demonstrate the benefit of reducing temporal dependency in separation in the following analysis.

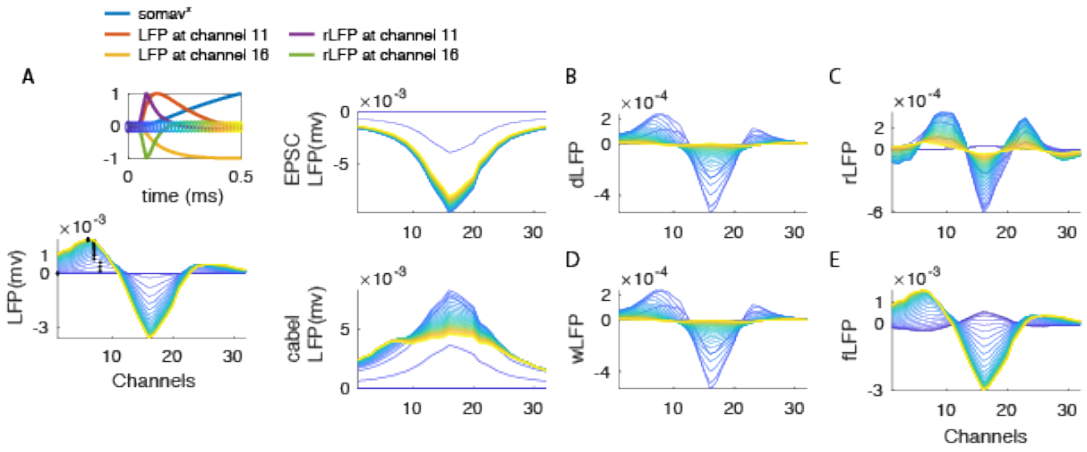

Figure 2.3: Cabel effects and preprocessing methods. A. Dendritic impulse response to radiatum input. The LFP recorded parallel to the somatodendritic axis on the lower left panel is displayed in the other three views. The spatial profile of the response pattern is plotted at each sampling time, their order is depicted by their color and shared with all the other subplots. The color map is shown in the upper-left inset. The upper-left inset shows the time series at multiple recording sites, notice the peak time varies according to their distance to the input. The LFP recording is further separated into the contribution from EPSC and the cable currents. The cable effect alleviates the fast and localized instantaneous effect of inputs. B. The same signal after pre-processing with temporal-derivative ($dLFP$). C. The same signal after removing the MAR model fitting ($rLFP$). D. The same signal after temporal whitening ($wLFP$). E. The same signal after high-pass filtering above 30 Hz ($fLFP$).

In the simulation, we applied ICA to $dLFP$ and LFP. Here we introduce a low correlation signal and the firing rate is modulated by a slow band theta wave (fig.2.2). As suggested by previous works (Makarova et al., 2011), ICA still separates the components under low correlation levels and recovers the dynamic patterns of the pathways (fig.2.4B, PSD).

However, we find contamination in the slower frequencies, especially in the LFP components. This could directly be appreciated from the time series (fig.2.4E). The LFP components show a higher pairwise mutual information (2.4 A). The radiatum component and l.m. components are better separated in especially higher frequencies but contaminated in the slower frequencies (fig.2.4B, C). With the Granger Causality estimation, we would see a spurious causal link from the rad. stim to l.m. component in LFP data, but this is reduced in the dLFP data (fig.2.4 G inset). On the other hand, the rad. comp also has a significant influence on the IN component, because the driving forces of the GABAergic inputs would be highly influenced by the nearby excitatory pathways.

We next test the ICA methods on different co-incidence levels. Inputs are projected to different depth layers. Amari distance measures how similar the mixing matrix is compared to the ground truth. In the lower correlated data, LFP ICA usually separates the signal well except for a few very close input pairs (fig.2.5 A, B). In this case, however, $rLFP$ and $wLFP$ components are not very reliable, likely due to the model estimation.

When the correlation is large, LFP ICA would converge into local minima and gives spurious components(fig.2.5A). The estimation sometimes converges into different local minima and becomes less reliable over multiple estimations (a larger S in fig.2.5 A, especially when the inputs are close to each other (fig.2.5 C). However, $dLFP$ always has a reliable separation (fig.2.5 B, C).

We also checked the Granger Causality between stimulation sequences and the components. A better separation leads to a better Granger Causality estimation. In the high correlation level, LFP components contaminate each other and show a high causal strength in the wrong direction (fig.2.5D, E, left column). While the $dLFP$ components have a better separation and GC estimation except for a few concatenated inputs.

Overall, the temporally sparser signal enabled a better separation in highly synchronized scenarios and this would provide a better signal for connectivity estimation.

2.3.2 Synaptic Time Constant Fitting

We next investigated the synaptic properties for each pathway by fitting the time constant to the power spectral density baseline of each component (fig.2.6 A). Notice the spectrum is multiplicative, which means the contribution from the

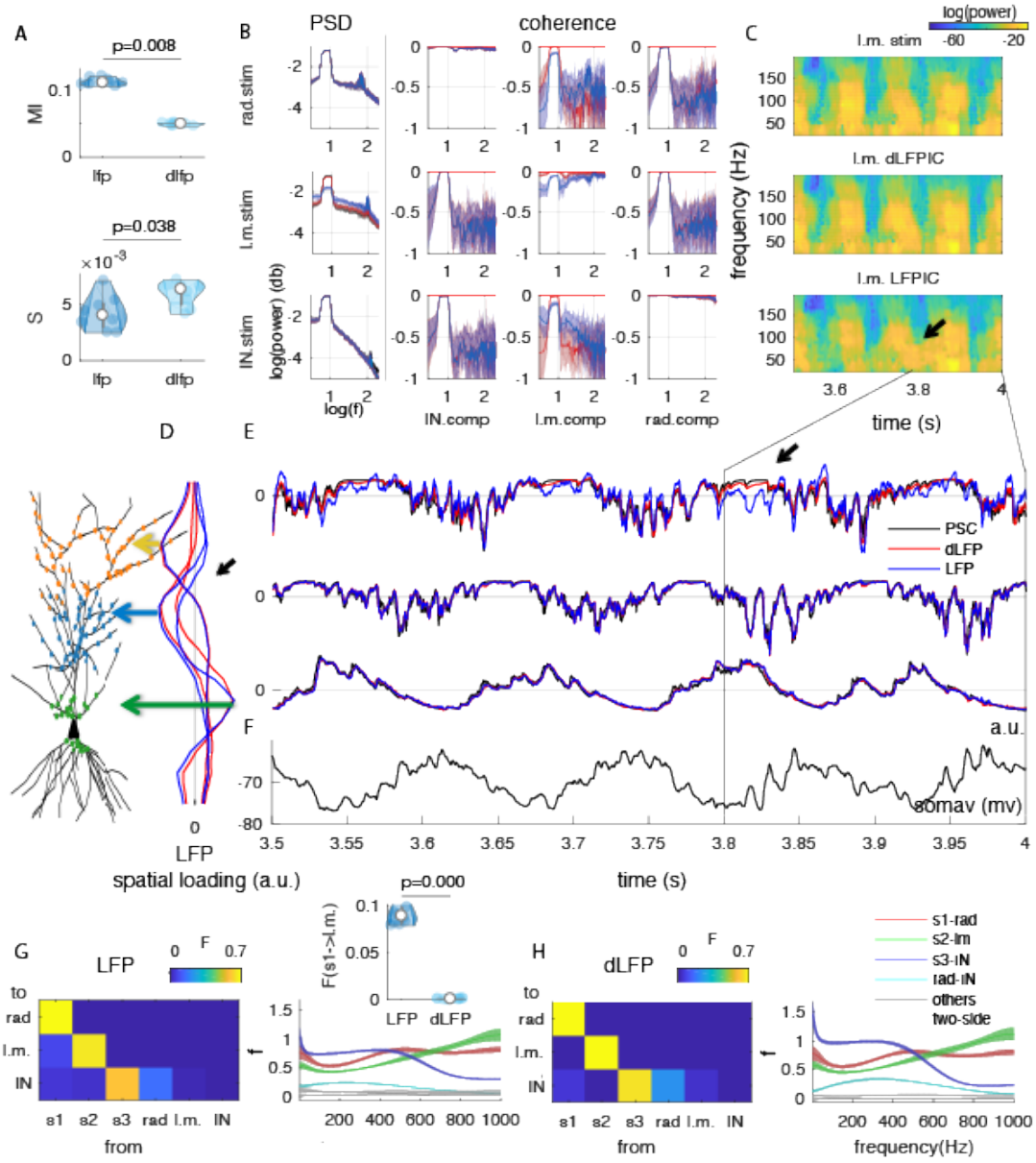

Figure 2.4: ICA separation in simulated theta modulated periods. A. upper: median pairwise mutual information cross sessions; down: separability S across sessions. B. power spectral density of synaptic currents(stim, black) overlapped with IC.dLFP(red) and IC.LFP(blue) on the left and coherence on the right between stim and IC.dLFP/ IC.LFP in red and blue, respectively. all the plots are in log-log scale. C. Example spectrogram of the l.m. components. D. Spatial loading of the dLFP IC components (red) and the LFP IC components(blue). E. Example activity of the components. F. Membrane potential at the soma. G. Granger causality (F) of stims and LFP components (left) and its frequency domain decomposition (f, right). Inset compares the Granger causality from s1 (rad. stim) to l.m. component estimated, the spurious estimated connection due to separation contamination, with LFP IC or dLFP IC components. H. same as G but for dLFP IC components.

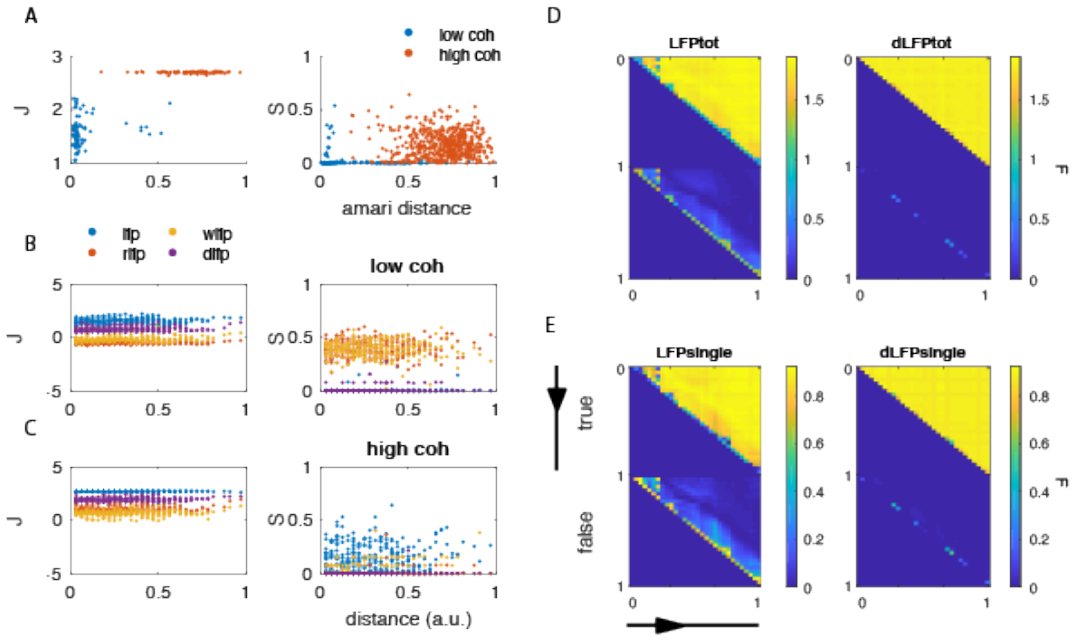

Figure 2.5: ICA separation with regard to distance and correlation level. A. Separation performance measured by Amari distance from ground truth versus negative profile likelihood J for LFP component on the left and Amari distance verses separatability S on the right. B. J (left) and S of separation measured by layer distance at low coherence level simulation. C. J (left) and S of separation measured by layer distance at high correlation level simulation. D.E. separation performance at a high correlation level. D. Total GC is explained by true stim in the upper panel versus explained by the wrong stim in the lower panel. Right GC and wrong GC are separated by dotted lines. GC is computed for each pair of inputs coming at different layers. We only plot the upper triangle of the matrix because the input at layer i and layer j are symmetric to scenarios with input at layer j and layer i. E. Smallest value of true GC pair on the upper panel and largest wrong GC pair estimated from the same simulation.

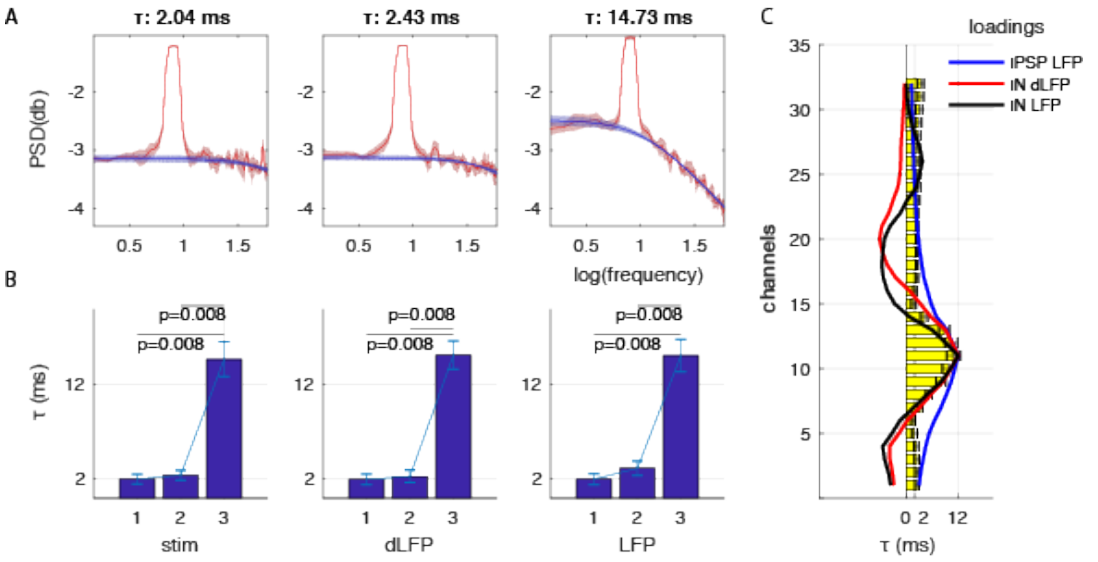

Figure 2.6: Synaptic time constants estimated from power spectral density. An Example time constant estimation from stims' power spectral density(red, in log-log scale). Blue indicates the fitted baselines. B. Estimated time constants for each component. C. Time constant estimated with the LFP data at each recording channel. Blue is the ground truth LFP profile of IPSC, red is the dLFP IN component, and black is the LFP IN component. Ground truth 2ms for AMPA-based rad. component and l.m.component and 12ms for GABA based IN component is marked in each case.

Table 2.1: Time constant estimation for simulated pathways.

Pathways	Stim	dLFP IC	LFP IC	Ch_{max} LFP	Ch_{max-2} LFP
str. rad.	2.04± 0.50	1.99 ± 0.58	2.01±0.58	2.41±0.28	2.38±0.25
str. l.m.	2.43±0.53	2.31±0.66	3.17±0.76	2.48±0.67	2.46±0.67
IN	14.73±1.85	15.16±1.50	15.10±1.71	10.37±1.58	7.54±1.16

input temporal pattern and from synaptic integration will add up linearly in the log scale. Therefore, it's possible to separate the baseline pattern contributed by synaptic kinetics from the input spectral when the latter exhibits oscillatory patterns (Donoghue et al., 2020). In spite of the large theta band power, the estimated time constant for *stim* matches the simulated AMPA and GABA receptor kinetics (table 2.1, fig.2.6 B). In this case, the time constants estimated by both LFP and $dLFP$ components match the ground truth.

On the other hand, the time constants estimated by the raw LFP signals show a mixture of both AMPA and GABA receptors. For channels close to the center of the input target region, the spectrum and time constant are dominated by one single pathway (table 2.1 Ch_{max} LFP). While LFP in other channels reflects a mixture of synaptic response from all the pathways (table 2.1 Ch_{max-2} LFP, fig.2.6 C).

Overall, we show the possibility to establish the synaptic properties in each afferent pathway with simulation. Estimations based on the mixed signal in LFP recording will likely lead to misinterpretation of local synaptic organization, especially when multiple pathways with different synaptic properties converge into the same neuron population. While source separation and parameter fitting for each pathway renders biophysically meaningful interpretation and relieved this problem.

2.3.3 Identify Robust Components Corresponding to the Pathway Topology

We apply ICA to data collected in freely moving animals. During the running period, LFP has strong theta band synchronization and is largely dominated by slower frequencies (Sirota et al., 2008, Schomburg et al., 2014, Buzsaki & Mizuseki, 2014). We preprocess the data and apply ICA to LFP, $fLFP$, $wLFP$, $rLFP$, and $dLFP$ data. After ICA separation, we first look at the reliability of the separation.

Similar to simulation data, $fLFP$, $wLFP$, $rLFP$, and $dLFP$ components have much smaller pairwise mutual information both in the hippocampus and MEC (fig. 2.7 A, B). The components are also more reliably separated with pre-processing

(fig.2.7 C, D).

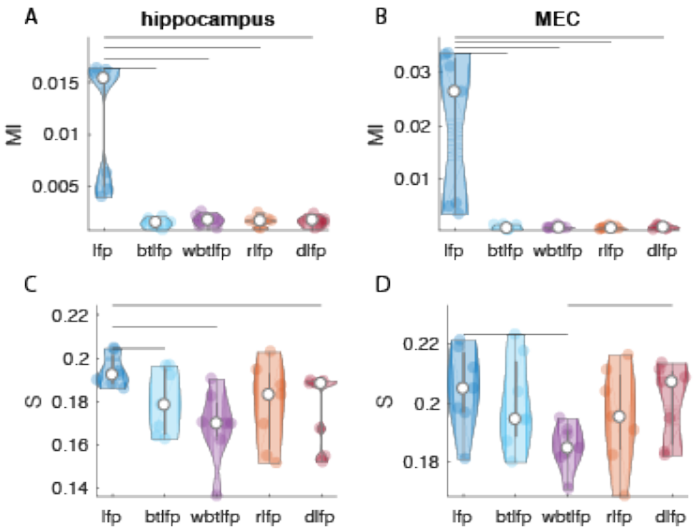

Figure 2.7: Reliability of hippocampal LFP separation. A. The average pairwise mutual information (MI) for components separated from hippocampal CA1 high-density recording data with different preprocessing methods at each session ($n = 7$). Bar indicates significant $p < 0.05$. Lower mutual information indicates a better separation. B. Same as A but for MEC data. C. The average separability for CA1 components (equ. 2.18). A lower S usually indicates reliable separation and less contamination. D. Same as C but for MEC data.

Next, we cluster the components according to their spatial profiles. Clusters would depend on the smoothness of the current source kernels 2.8, when the kernel width is small, the result would be affected by noisy channels and imperfect separation. On the other hand, when the kernel width is too large, the large current kernels give spurious current sources (Potworowski et al., 2012). Here we choose 4 channels which sum up to $\sim 90\mu m$ as the kernel width to preserve a good amount of spatial detail.

In the hippocampus, we consistently observe 8 clusters with $dLFP - ICA$ (figure 2.8 B first row and figure 2.10) with consistent spatial loading and cross frequency modulation. Most of the components explain $< 10\%$ of the total power of $dlfp$ except for one flat component (also observed in other methods, fig. 2.9 A clu.3 and B clu.4). This component surprisingly has consistent spatial loading where little spikes sitting on the nearly flat baseline may reflect channel impedance noise. The flat component also corresponding to the far field signal volume conduction doesn't have a clear cross-frequency modulation compared to other hippocampal components, but contributes mostly to the total power (49%, especially in the high frequency (figure 2.12 B clu.3, D clu.3)). Interestingly, we also find a similar component in MEC shank, which takes 46% of the total $dlfp$ power (fig. 2.10 B clu.5). The coherence between these two components shows a clear power in the high-frequency range (fig. 2.11 C). This motivated us to design a toolbox to remove the far-field noise from the data, which will be introduced in chapter 5.

The rest of the consistent components all have meaningful spatial profiles and

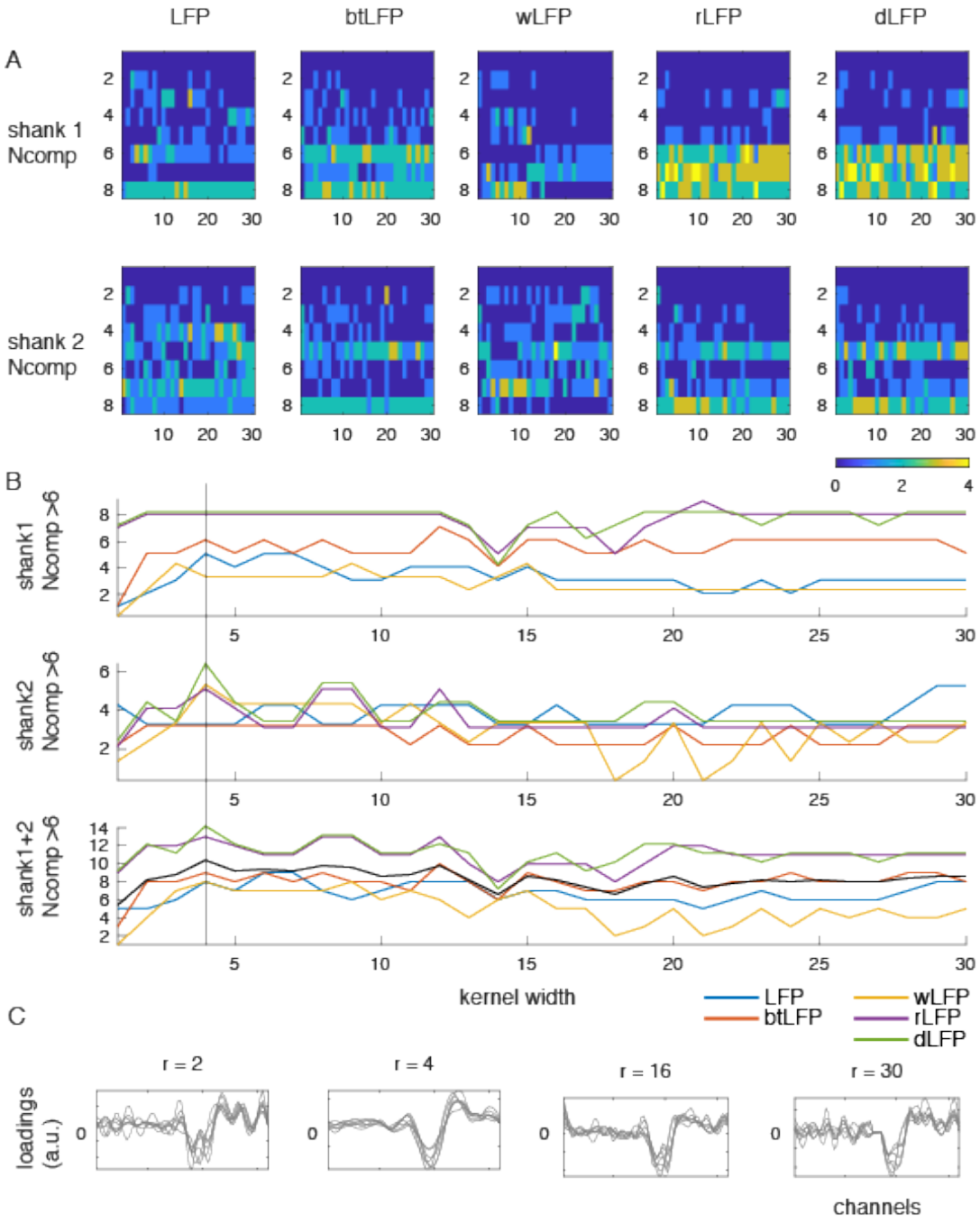

Figure 2.8: Consistent clusters cross sessions with different pre-processing steps. A. The clustering results across sessions, the x-axis is the kernel width measured by minimum channel distance, the y-axis is the number of sessions whose component shows up in each cluster (N_{comp}), color indicates how many clusters have N_{comp}. B, The number of clusters appears over 75% of data. The line indicates $r = 4$, which is used in the later analysis. C, examples of clusters (MEC layer II component of $dlfp - ICA$) given by choosing given kernel width.

consistent dynamic patterns. The cross-frequency coupling appears to be consistent across sessions, especially in the preprocessed data (fig 2.9 A for wide band LFP data and B for high passed preprocessed data, fig. 2.10 shows the $dlfp - ICA$ result).

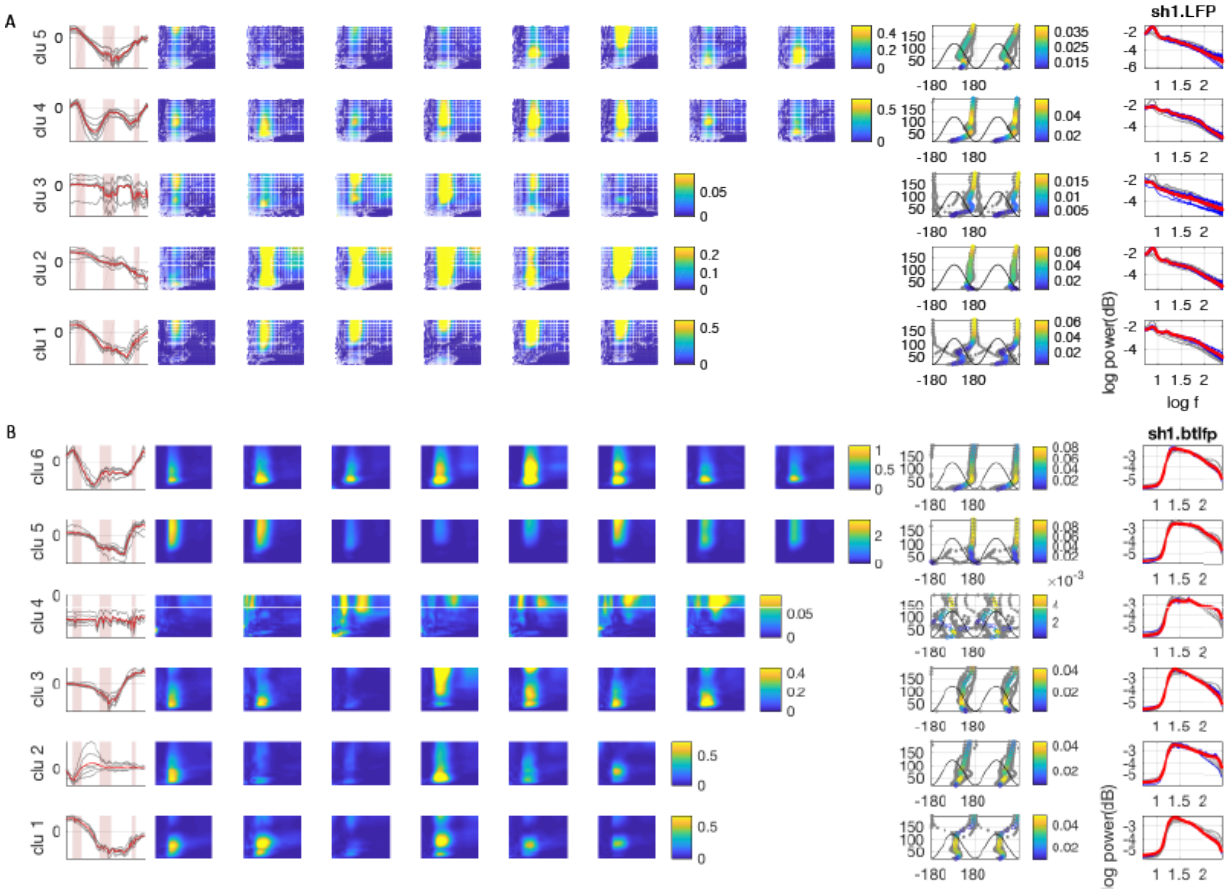

Figure 2.9: Cluster results of hippocampal LFP and btLFP components. A. The hippocampal LFP components. 1 LFP spatial loading of the components. 2. cross-frequency coupling of each component measured with modulation index ($x10^{-3}$) in each session. 3. Theta modulation is measured by phase locking value. X axis is the phase of theta, and the color indicates the resultant length at each gamma frequency. We also show the preferred theta phase at each frequency from each session in gray. The black line indicates theta waveform.4. The normalized power spectrum density in log-log scale. B. The hippocampal btLFP components. Same arrangement as in A.

One component with the largest current loading at the middle molecular layer (DG mmol) and characteristic strong theta modulation in high gamma frequency above 100Hz at the trough of theta cycle (mean=165.7 $\pm$ 8.6, $p < .0001$ with Rayleigh's test) is consistently separated with all the methods (figure 2.9 A clu.1, B clu.5 and figure 2.10 A clu.8). This is consistent with the previously described perforantal path projecting from MEC layer II to dentate gyrus middle molecular

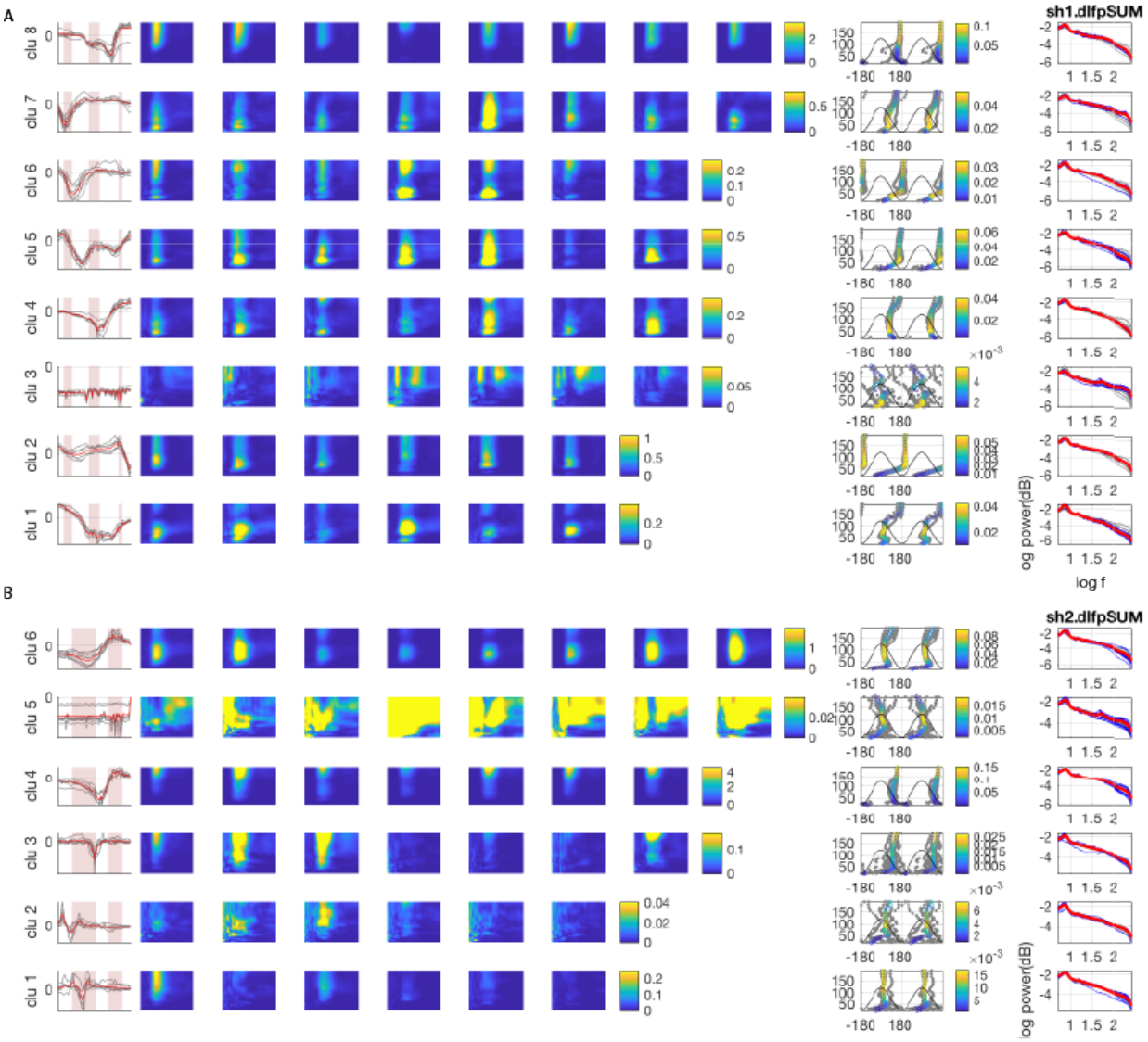

Figure 2.10: Cluster results of dLFP. The analysis is applied to the integrated activity. A. The hippocampal components. 1 LFP spatial loading of the components. 2. cross-frequency coupling of each component measured with modulation index ($x10^{-3}$) in each session. 3. Theta modulation is measured by phase locking value. X axis is the phase of theta, and the color indicates the resultant length at each gamma frequency. We also show the preferred theta phase at each frequency from each session in gray. The black line indicates theta waveform.4. The normalized power spectrum density in log-log scale. B. The MEC components. Same arrangement as in A.

layer (Benito et al., 2014, Fernández-Ruiz et al., 2021).

Another strongly theta-modulated component is the hippocampal stratum lacunosum moleculare layer component (str. l.m. 2.10 clu.1). It shows a strong modulation at 100Hz around the peak of hippocampal pyramidal layer theta (mean $= 16.8 \pm 15.7$, $p < 0.001$ with Rayleigh's test, figure 2.9 B clu.1 figure 2.10 A clu.1). The separation in wide band LPF data shows a spatially consistent component with similar spatial loading (2.9 A clu.5) but is highly influenced by the DG mmol component.

Apart from the perforantal pathway, we also find components with a large sink at stratum radiatum, corresponding to the Schaffer collaterals (Fernández-Ruiz et al., 2012, Schomburg et al., 2014). It contributes 7% to the total power in $dlfp$ and is best modulated by theta at 164 ± 15 around 56 ± 28 Hz (fig. 2.10 A clu.5, also in fig. 2.12 A clu. 4 B clu. 6). Both band-pass filtered ICA and the dlfp-ICA show the best theta-gamma modulation at slow gamma range ($30 - 80$Hz), which agrees with previous works (Schomburg et al., 2014) while wide band LFP shows a wider coupling range.

We have one component located below the DG mmol component, due to the span of the recording shank, we don't know where exactly is the center of the current source (fig.2.10 A clu.2). It contributes 2% to the total power, with the best theta modulation around 60Hz at the trough 207 ± 11, similar to the CA1 Schaffer component. We hypothesize that this component reflects the commissural pathway projecting to the inner dentate granular layer (Fernández-Ruiz et al., 2021).

The other component with high theta modulation at a slow gamma range is located at the deep end of the CA1 pyramidal layer (fig. 2.10 A clu.7). It contributes 3% of the $dlfp$ power. The best theta gamma modulation, however, is at the descending phase (61 ± 29) of pyramidal theta. We term it the alveus component.

Above this component is the hippocampal pyramidal layer component (Pyr. comp, fig. 2.10 A clu.6). It contributes 2% of the total $dlfp$ power and has a typical high theta gamma modulation in the high gamma range (> 120 Hz) around 197 ± 14.

The last cluster 4 in the hippocampus has a spatial profile, which agrees with the LEC projection target, the Dentate Gyrus outer molecular layer current sink, and is modulated by theta at 48Hz around the theta trough 176 ± 50 (p=0.02, fig. 2.10 A clu.4, fig.2.9 B. clu.3). It contains 8 of the total $dlfp$ power.

In the MEC, we consistently observe $3 - 6$ components, 3 of them corresponding to the superficial layer activity, and the rest is located at deep layers (figure 2.12 F). Despite the EMG component, superficial components contribute most to the power in the entorhinal cortex. These components also show strong coherence with components in the hippocampus (fig. 2.11 A, B).

Robust cluster 6 at MEC has a large dipole spanning layer I to layer III. This cluster contributes 21% of the $dlfp$ signal power and has the best theta modulation at the middle gamma range 83 Hz around theta peak 34 ± 11 ($p < 1e-4$). Cluster 4 at MEC belongs to layer II and contributes 9% of the total MEC $dlfp$ power. It has the best theta modulation at a high gamma range before the theta trough 135 ± 3 ($p = .0001$), which agrees with the MEC II neuron population firing (Mizuseki et al., 2009).

Here wide-band ICA gives the least separable stable estimation cross sessions under the same statistical criteria $\alpha_{clu} = .05$ (significance corrected by FPR), $\alpha_{comp} = .05$ (significance corrected by FDR), which implies a failure of clean separation. This could be due to the strong slower frequency oscillation that entrains the local network dynamics (Sirota et al., 2008, Mizuseki et al., 2009), which increases the dependence between components. The other cause of this could be the frequency dependence of the corresponding dipole shapes (Gratiy et al., 2011), which we will discuss in detail in the next session. As we can see from the cable equation, the neuron membrane performs a low pass filtering, which leads to a broader average dipole shape in the slower frequency and a more localized one in the higher frequency. This also leads to a higher spatial overlapping, which would be critical in separating the highly synchronized components, especially in the wake theta state. Apart from the passive membrane properties, the active conductance is most prominent in the slower frequencies. Various active conductance alleviates fast changes in dendrites (Magee, 1998), contribute to dendritic resonance (Hu et al., 2009), and introduce input-dependent nonlinear integration (Spruston, 2008).

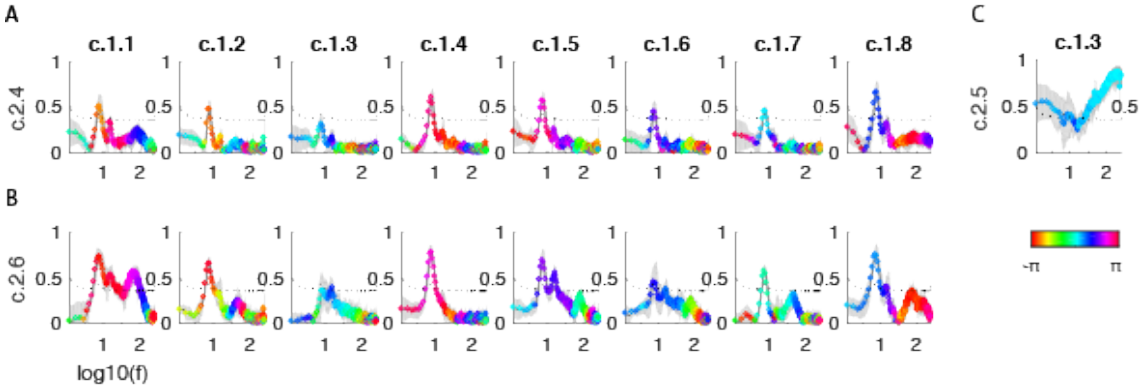

Figure 2.11: Coherence Between Hippocampus and MEC superficial layer components. A, Coherence between Hippocampus and MEC layer II component. B, Coherence between Hippocampus and MEC layer III component. C, Coherence between Hippocampus and MEC EMG components. Color code phase shifts. The black line is the variance of shuffled surrogate data coherence. Phase = phase(MEC) - phase(Hippocampus)

Overall, we show the LFP components with proper separation are stable, and

we group them over the sessions. Pushing the data into a sparser regime would enhance the separation. This probably is due to less contamination from the slower frequency band, where most of the nonlinear process and slow frequency modulation happen. In the next session, we set out to study the interaction between the consistently separated components.

2.3.4 Reliable Causal Direction Estimation

One of the major advantages of utilizing LFP is to tell about the connectivity within and between areas. In other words, we aim to obtain a faithful estimation of the information flow between interested LFP sources. Firstly, we can see large coherence between MEC superficial layer components and hippocampal components, mainly in theta band (fig. 2.11A, B, fig AppendixB.5). However, many are significant, and we can not exclude the possibility of indirect connections. Therefore, here we propose to use causal discovery and inference methods (Peters et al., 2017) as a measure indicating good separation. The causal relationship will be contaminated if the components are not well unmixed. But on the other hand, a good separation of the mixed signal will improve the MAR model estimation.

The components extracted with the independent component analysis naturally fit into the Ganger causality framework and have multiple benefits. The fast electrical response of the membrane potential gives rise to return currents spreading through the whole neuron and gives rise to a dipole shape. This creates instantaneous interactions between recording sites which would affect modeling and causal inference, volume conduction also adds to this problem (Barnett & Seth, 2015, Bastos & Schoffelen, 2016). Applying source separation beforehand and obtaining spatially meaningful components, however, would reduce the noise, take care of the return currents, and get rid of far-field volume conducted signals.

The causal information flow between robust components reveals major pathways in the hippocampus (Andersen et al., 1971). We observe two major connections between the MEC and the hippocampus. Firstly, we find a strong unidirectional information flow from the MEC layer II component to the DG mmol component which agrees with the anatomical connection. The unidirectional information flow mainly happens in the gamma band (figure 2.12 A MEC clu.4 to HP clu.8, C, figure 2.13 I).

The str. l.m. component, with a slightly slower peak theta-gamma modulation than the MEC III component, is mainly influenced by the MEC layer III component at the middle gamma range (figure2.13 H) significantly slower than the MEC layer II projection in the perforant path.

Interestingly, we find the CA1 str. l.m. component receiving layer III projection from MEC is highly regulated by both the Schaffer component and the alveus

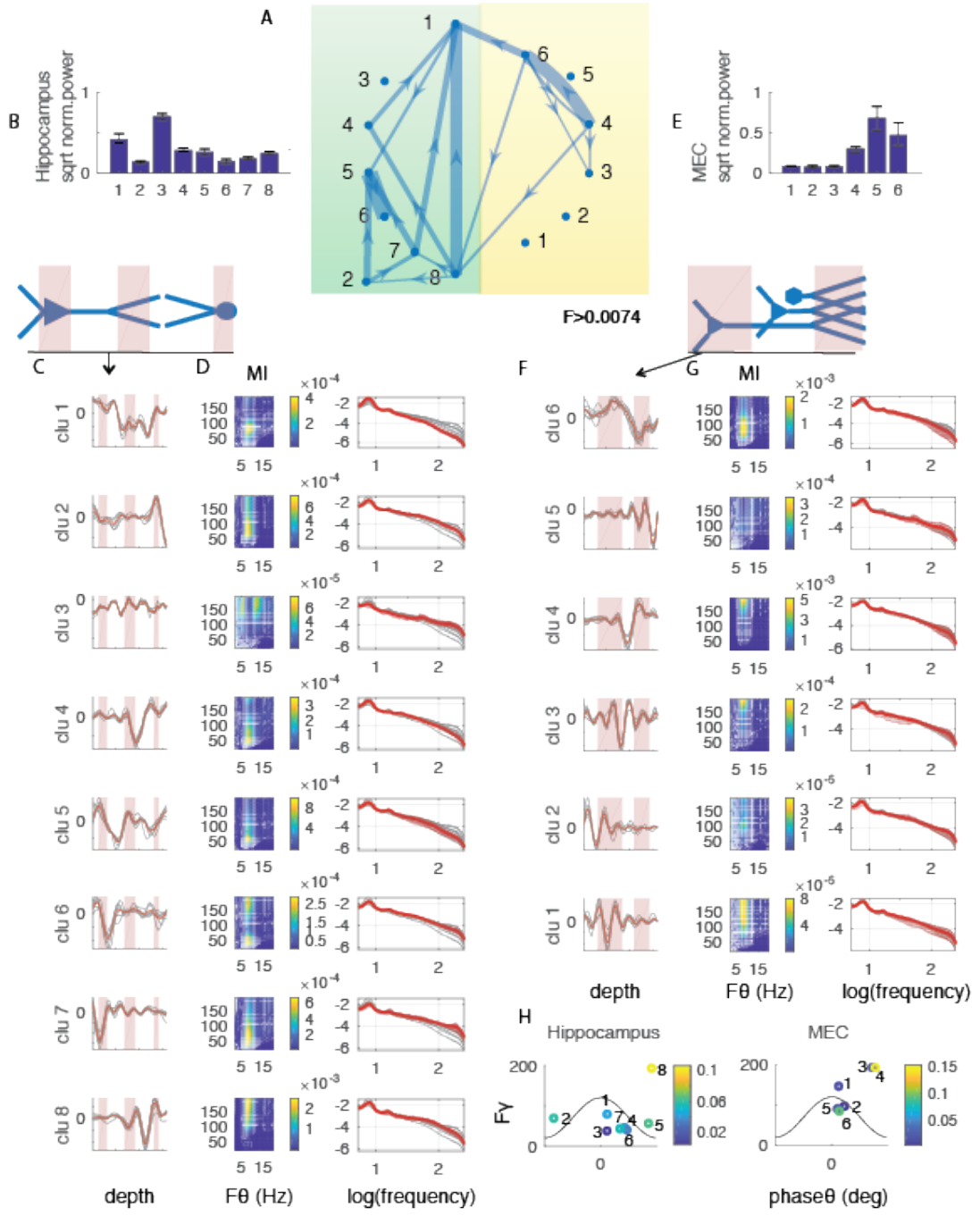

Figure 2.12: the estimated connection between stable components. A, connectivity graph. Greens indicate components from the hippocampus, and yellow indicates components from the medial entorhinal cortex (MEC). B. Depth profile of Hippocampus, which maps into the components spatial profile in C. From left to right, patches indicate the pyramidal layer, stratum lacunosum moleculare (l.m.) layer, and the granule layer in the dentate gyrus, respectively. C. current sources density spatial profile of all the consistent hippocampal components. D, color map on the left is the average modulation index cross sessions($x10^{-3}$). On the right, we show the normalized power spectrum density of each component (in red), compared to all the other components (in gray) in log-log scale. E, the depth profile of MEC superficial layers, which maps into the components' spatial profile in F. From left to right, patches indicate layer III and layer I, respectively. F, current sources density spatial profile of all the consistent MEC components. G, same as D but for MEC components.

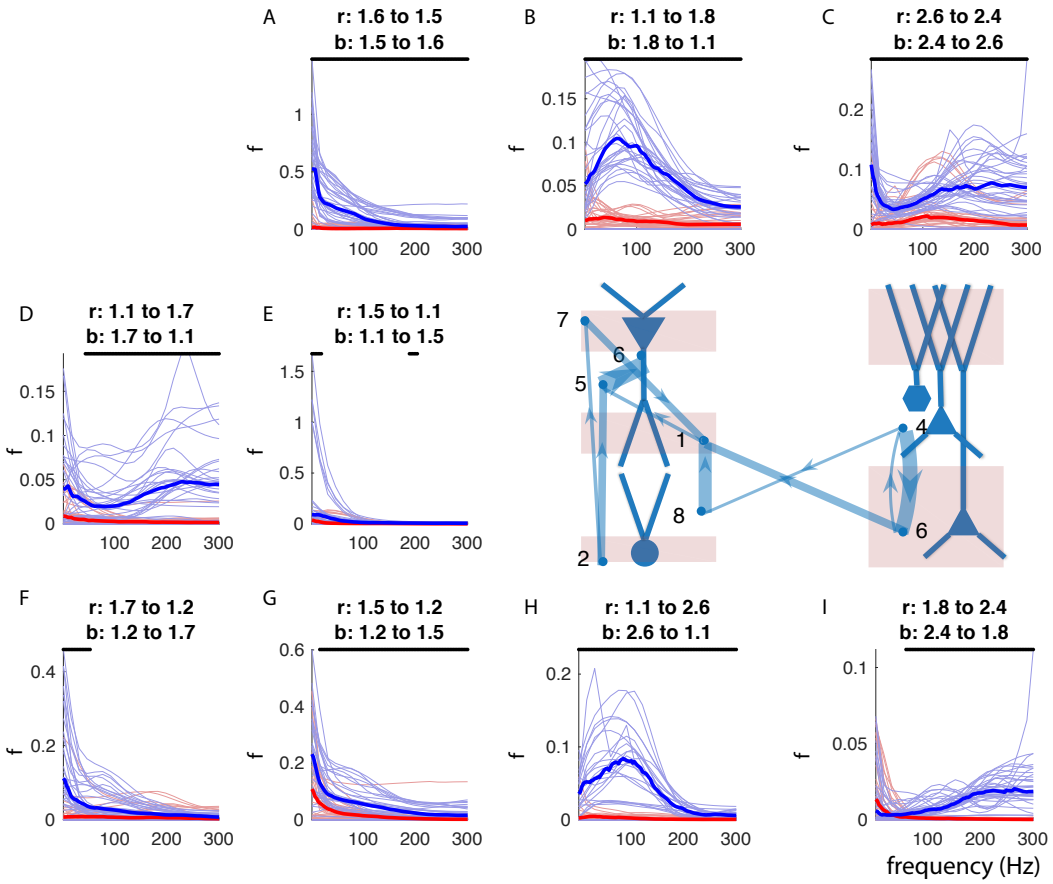

Figure 2.13: Perforant Path and Schaffer collaterals revealed by the frequency domain Granger causality (GC). A, frequency domain GC between shank1 component 6 (1.6) (pyramidal layer component) to shank1 component 5 (1.5) (stratum radiatum). The shadowed line is the frequency domain Granger Causality value from each period cross all sessions. The darker line is average $F(\omega)$. Black dots indicate a significantly higher influence in one direction, two-sided Wilcoxon sign rank test p<.05 corrected by Bonferroni correction.

component at both slow frequency and the gamma band (fig.2.13 D, E). This indicates that apart from being located at the distal dendrites, the hippocampus uses more complex mechanisms to regulate the MEC layer III input in local computations (Mikulovic et al., 2018, Leão et al., 2012). While layer II projection from MEC is less influenced by other hippocampal pathways.

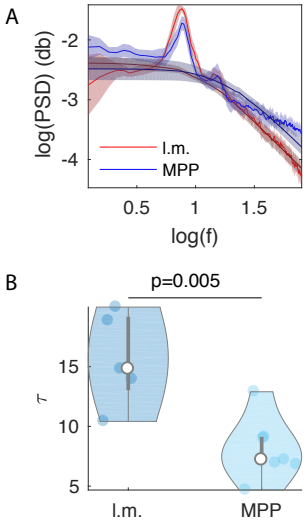

Figure 2.14: Perforant path time constants estimated at $[1,80]$ Hz. A, power spectrum density of str. l.m. component and DG mmol component plotted in log-log scale for each session. The solid line indicates the median value at each frequency and the shadowed area indicates one standard deviation. B. Compare the estimated time constant of the components across sessions. p=.005 given by the Wilcoxon rank sum test.

Within the hippocampus, we observe a strong influence from the Schaffer collaterals onto the pyramidal layer component (fig.2.13 A), and the Schaffer component also gates the information from MEC to the pyramidal layer (fig.2.13 E and A, fig.2.12 A), mainly at the slower frequency band. The Schaffer component receives information from the comm. the component at the inner molecular layer of the Dentate Gyrus. Instead of a direct anatomical connection, this link is more likely due to their common cause: the CA3 neurons. This also emphasizes the importance of combining our knowledge of anatomical connections (Andersen et al., 1971, Tecuatl et al., 2021) to the causal link estimation. Instead of purely relying on the causal inference methods to study the connections between regions, the causal inference could help to detect the non-stationary functional connection strength at anatomical connections (Zhang et al., 2017).

In the MEC, we observe a strong mutual influence between layer II and layer III components (fig.2.13 C). This is also inherited by the DG mmol component and CA1 str. l.m. component (fig.2.13 B). This indicates MEC layer II and III population dynamics highly influence each other through both principle cells and inter-neurons, and they are the common cause of components in MEC and hippocampus (Mizuseki et al., 2009, Winterer et al., 2017).

Besides the connections, here we also estimated the synaptic response time constants of the PP pathway component2.14: l.m. (comp.1): 14.8 ± 2.9 ms, mmol (comp.8): 7.2 ± 1.6 ms (fig.2.14 A). None of them show a pure AMPA receptor-modulated pattern. Instead, they are a mixture of faster and slower synaptic and dendritic mechanisms. The l.m. component contains a larger amount of slower mechanisms compared to the DG mmol components (fig.2.14 B $p < 1e3$ Wilcoxon

rank sum test), which qualitatively agrees with the previous calibrated NMDA receptor distribution on the apical dendrite. A larger $NMDA/AMPA$ ratio has been found in dentate LPP synapses compared to MPP synapses, while the ratio in CA1 Schaffer pathway is similar to the LPP synapses and generally smaller than str. l.m. synapses (Otmakhova et al., 2002, Nicholson et al., 2006, Min et al., 1998). It has also been reported that during anesthetization l.m. component is significantly reduced during pharmacological intervention with bicuculline while the mmol component is less affected (Benito et al., 2014). Our analysis confirms the large contribution of NMDA receptors in l.m. component in freely moving animals.

Overall, we find the directional connections between pathways within and projecting to the hippocampus could be estimated by applying Granger causality to independent components. Our estimation from the freely moving animals agrees with anatomical findings. This is one step further than the common correlation-based analysis. Previous studies suffered from high volume conduction and nonlinear mixing of pathway-specific sources (López-Madrona et al., 2020). We release this problem by pushing the components separation to the sparser higher frequency regime, hence improving the separability of the signals. With the PP path as an example, we show the possibility to infer the synaptic properties from the component spectrum in real data. The resulting components capture rich information on pathway-specific dynamics.

2.4 Discussion

2.4.1 Impacts of Cable Model

In this chapter, we discussed how the cable effect of dendritic filtering affects the LFP signal unmixing. In the nonindependent regime, ICA separates components based on their temporal sparsity. Therefore, we propose to release this problem by pre-processing LFP data by taking the temporal derivative or temporal whitening (Mitra & Pesaran, 1999), and bias it to the sparser high-frequency regime, It helps to improve the separation when simulated inputs are highly dependent. In the real data, this pre-processing step also reduces the impact of nonlinear dendritic interaction (Spruston, 2008) and removes the colored spectrum bias, without which the high power slower frequency signal will dominate the separation. With it, we obtain stable clusters of pathway-specific components over multiple recording days. The activity of the components tells about their pathway-specific synaptic properties. By applying Granger causality methods on the activities of the components, we obtain consistent uni-directional connections from the entorhinal cortex to the hippocampus revealing the perforant path and agreeing with anatomy.

Here we introduced multiple strategies to remove the cable-induced history

dependency of the LFP signal. With the linear MAR model formulation, the immediate idea would be to remove the history dependency with a linear model, which we implement as *rLFP*. But in practice, we encountered a couple of problems with this method. First is induced by the curse of dimensionality. MAP model estimation performs well with a variable number lower than 10, but with the increase of recording sites, the number of coefficients to be estimated in the MAR model scales with n^2. With a lower dimensional latent space, namely, when the dimension is less than recording sites, the model is identifiable. However, it's not easy to recover the high dimensional latent space.

Here we have a high dimensional model, i.e., the multicompartment model with noise coming at each compartment, together with Kirhoff's law of current conservation and fast axial conductance, the transfer matrix A_V in equ.2.5 is dominated by the capacitive effect. When V_m maps to the observational recording data, it projects the high dimensional V_m data to the lower dimensional Φ data in a distance-dependent manner. Therefore, whitening by fitting an AR model would largely account for Z_1 and Z_2 in equ.2.10. The regression model might also benefit from knowing the shape of the MAR coefficient and some reasonable parameterization.

Here we also would like to emphasize the benefit of operating event discovery in the re-scaled or temporally whitened time series. Oscillation detection has been known to suffer from the power-law-shaped spectrum (Mitra & Pesaran, 1999). Previous works have employed whitening to remove the effect of power-law baseline for better oscillation detection (Sirota et al., 2008). In the frequency domain, methods have been developed to explicitly separate narrow band oscillatory signal from baseline power-law shape (Donoghue et al., 2020) in the spectrum. But notice the fact that all these methods are based on fitting a linear model to remove the history-dependent part of the data as shown in equ.2.10. In practice, the model fitting is ambiguous, especially in high-density recording data. Fitting a single AR model with an arbitrary channel would work for the purpose of revealing the high-frequency pattern. However, the same AR model won't capture the true coefficient at each recording site, which could also be seen by the change of power law slopes across the recording sites (Gao et al., 2017). However, if we fit an AR process for each and every recording site, the potential synaptic or membrane property information is lost with whitening [1].

Therefore, we use temporal differential data for the analysis in this chapter. Other pre-processing methods help to improve the sparsity of the signal and enhance the separability, but they distort the time series of data, even when some distort in a predictable way. Whitening with one single channel generally preserves the relative temporal pattern between channels, and it largely enhances

[1] But notice the argument about AR model difference applies only in local signals. In terms of contribution from far-field signals, the difference between recorded channels should be negligible (see chapter 5).

the separability in some of the very difficult sessions. Fitting the MAR model also helps in some of the very difficult scenarios, but in general, we are at risk of losing some temporal information. Temporal differential data, on the other hand, is model-free and easy to apply. It could also be compared to extracting large synaptic events with Haar wavelets (Fernández-Ruiz & Herreras, 2013).

An alternative would be to fit the entire LFP generation model like in equ.2.10. This could be performed as a state space model (SSM), where the low dimensional source space is first mapped into the high dimensional multicompartment membrane potential space and then reduced into the observational LFP recording space. However, the identification of the SSM depends on the independent sampling of the source, without which the model would be much more complex and need to incorporate more steps. The identifiability of the system depends on how much the model matches the data generation process. Resolving it in the temporal domain appears to be complicated. Therefore, in the simplified linear regime, we seek to capture the impulse-response of the linear system in the following chapter 3 and 4.

2.4.2 Identifying Inter-neuron

In the simulation, we show the potential to separate the inhibitory synapses and identify their synaptic content by the typical slower GABAergic time scale. This benefits from our simulation settings. Here we consider GABAergic synaptic inputs arriving at the given theta phase (Mizuseki et al., 2009). Because of the chloride gradient in neurons established by the potassium chloride co-transporter KCC2 (Payne et al., 2003), in the hippocampus of adult animals, the reversal potential E_{GABA} is usually maintained below or equal to the resting membrane potential, leading to membrane hyper-polarization (Ben-Ari, 2002, Klyachko & Stevens, 2006) or shunting inhibition (Bartos et al., 2007), respectively. In terms of shunting inhibition, the membrane potential pattern would be heavily affected by excitatory input, which makes them generally inseparable. Therefore we only consider GABAergic inputs, which cause inhibitory postsynaptic currents that hyper-polarize neurons.

However, identifying interneuron components is much more complex in real data. First of all, the time scale of the GABA receptor is 20 ms, sitting within the range between the excitatory $AMPA$ and $NMDA$ receptor, which is 2 7 ms and 60 ms, respectively (Grienberger et al., 2017). And the time constant of excitatory pathways is further modulated by I_h current (Magee, 1998). So it's impossible to decide which synapse without further information.

Moreover, future work should simulate the inhibition in a network to validate the separation of the afferent synaptic inputs from the local oscillation. Although in our setting, manually injecting the correlated inputs with a constant delay is more statistically dependent and theoretically should acerbate the situation.

That means if the inhibitory input is successfully separated in this case, it should be easier to separate in the real case. However, we still need to validate the recurrently connected network and see if causal direction analysis would apply.

2.4.3 Analysis of Local Pathway Dynamics

Here we separate and analyze the basic dynamics of each component. Unlike other large-scale recordings, the high-density probe parallel to the somato-dendritic axis provides a closer look at the dendritic processes. Analyzing the LFP profile allows for an intermediate step to connect microscopic synaptic distribution to the macroscopic time scale analysis with fMRI signals (Gao et al., 2020) by fast spatially resolved LFP signal. Proved with the simulation data, the mixed signal at each recording site consist of a mixed time response from all the nearby pathways. Unmixing reveals the dynamics of a single pathway and it's easy to infer the synaptic properties when the pathway activity contains only one type of synapse, The large time constant observed in the l.m. component, compared to all the other hippocampal components, indicates a longer integration time likely contributed by a large $NMDA/AMPA$ ratio and balanced by I_h currents (Otmakhova et al., 2002, Magee, 1998). Further analysis would include exploring the impact of different dendritic conductance and reconciling the abundant research on dendritic integration with the extracellular recordings.

The unmixing of signals also allows for the assessment of connections between areas carried by each pathway. The closer the component time series resemble the input time series, the better we can tell the directional connections projecting to local circuits. When the components are contaminated by cohesive input or nonlinear dendritic integration, it leads to spurious directional connections. Interestingly, in the simulation data, where only passive conductance is considered, the spurious causal direction is not symmetric and is biased to the radiatum input towards the l.m. component, which means the activity of radiatum input helps to predict the time series of l.m. component response. This might due to radiatum inputs has higher activity and stands in the way of currents passing from distal dendrites toward the soma. On the other hand, we find no directional connection from radiatum input towards the l.m. component in the passive neuron simulation with $dLFP$ based separation, which agrees with ground truth and indicates less cross-contamination. However, in the real data, the connection shows up from the l.m. component towards radiatum (fig.2.12 clu.1.1 to clu.1.5). Together with this, we find both the radiatum and l.m. component, representing the post-synaptic dynamics, is influenced by a fast, in terms of its synaptic time constant, and orient-located component, which receives input mainly from the CA3 component (fig.2.12 clu.1.2). This might reflect the inhibitory regularization by multiple different CA1 inter-neurons, including VIP cells regulated disinhibition on basket cells as well as OLM cells (Turi et al., 2019). Since this is the first time this pathway is revealed by LFP causal analysis, further validation by

manipulation is needed in the future.

The strong connection from the m-mol layer component to the str. l.m. component raises multiple concerns about the causal analysis in local recordings. First, one needs to keep in mind that the components reflect the transmembrane currents in the population, which says many of them come from synaptic origin. The whole local information processing system (fig.1.1), could be simplified into a graph (fig.3.9), as we will mention in the next chapter. That means when a directional link is established, it means information that comes to the upstream area is processed and projected to the downstream area. However, at the same time, there is no clue whether the downstream neuron would fire or be effectively recruited by the upstream area. The connection is established because of the physical synaptic connection, which might go through certain plasticity but would generally always be there during the recording. This is also shown by the wide band directional connection, e.g., from EC layer III to l.m. component (fig.2.13 1.1 to 2.6) and many others. To study the connection between areas, instead of talking about frequency band limited cross-regional interaction, it would be beneficial to separate the whole process into 2 steps, namely the synaptic projection and the dendritic integration.

Secondly, the causal analysis always benefits from including potential components to the data (Peters et al., 2017). Therefore, a consistent discovery of the components over sessions is important, and one needs to be cautious about components thrown out from the analysis. Here we benefit from simultaneous recording in both the entorhinal cortex and hippocampus and discover the clear uni-directional connection from the entorhinal to the hippocampus from LFP, which agrees with anatomy data (Mizuseki et al., 2009). However, we also find a strong directional connection from the m-mol component to the l.m. component. This connection is not explained away by including EC layer II and III components or the CA3 component. This indicates that the interaction between the hippocampal projecting population in the entorhinal cortex is not fully captured by their major dendritic inputs. The connections through other mechanisms, e.g., through inter-neuron in the same layer (Winterer et al., 2017) would be reflected in their output, which would be later captured by the synaptic currents at m-mol layer and CA1 distal dendrites. Previous work has reported a small subset of EC layer III pyramidal cells fire in phase with EC layer II population and shows the strongest theta phase-locking (Mizuseki et al., 2009). The connection from the EC layer III component to the m-mol component might resemble the projection from EC layer II cells to the EC layer III subnetwork, while neurons from the same population also project to the DG m-mol layer. One further possibility is the link resembles the feed-forward inhibition from layer II island cell that activates the interneurons targeting distal dendrite and conjugates layer III inputs (Kitamura et al., 2014). Whether this synchronization comes from the input level strong mutual connection (fig.2.13 2.4 and 2.6), or if other mechanisms are involved

could be further explored. By jointly conditioning on all the components seen in the local circuit, we find the interaction happens at different levels, be it dendritic mechanism or population-level perisomatic interaction. Another very interesting direction would be to involve the population activity analysis in the causal inference, similar to what we do in the simulation data. This way, we could easily have a fine-grained understanding of how the dendritic integration works over multiple areas in freely behaving animals.

Finally, we want to emphasize that even when both pre- and post-synaptic population firing could be recorded, it's still helpful to combine LFP into the analysis. LFP not only provides information about the synaptic property, as we have shown here, but it also allows a simple and close to a linear readout of the cross-area influence, while causal influence at the level of population activity could be nonlinear with synaptic integration and local oscillation, and these processes are modulated by behavior states in a much more complex manner. Moreover, a lot of causal analyses suffer from reciprocal connections (Peters et al., 2017). Tell apart the synaptic input from the population activity would help to infer cross-regional connectivity.

Table 2.2: Summary of Cable Parameters.

variable	meaning	size
Basic scales:		
N	number of compartments	
M	number of recording sites	
K	number of pre-synaptic pathways	
h	number of classes of active channels	
Membrane Properties:		
$V(x)$ or $\mathbf{V}(kT)$	membrane potential	scalar at x or $N \times 1$
$I_{membrane}(x)$ or $\mathbf{I_{membrane}}$	transmembrane currents	scalar at x or $N \times 1$
g_l or $\mathbf{G}_l$	passive membrane conductance	scalar at x or $N \times 1$
C_m or $\mathbf{C}_m$	capacitive effect	scalar at x or $N \times 1$
g_a	axial conductance	scalar at x
Synaptic inputs:		
$\{Ga_j(x,V)\}$	active conductance type j	scalar at x
$\{Ai(x)\}$	synaptic distribution of pathway i	scalar at x
A_s	synaptic distribution	$N \times K$
η or $\mathbf{E}(kT)$	Presynaptic activity	$K \times 1$
$\{\tau_i(x)\}$ or A_τ	synaptic time constants of each pathway i	scalar at x or $K \times K$
LFP parameters:		
$\Phi(x)$ or $\mathbf{\Phi}(kT)$	local field potential	scalar at x or $M \times 1$
H	distance dependent mapping from $I_{membrane}$ to LFP	$M \times N$
B^*	mapping from $\mathbf{V}$ to LFP	

Chapter 3

Impulse Response of Passive Neuron

With the high-density recordings developed in recent years, we are able to characterize the spatial profile of local field potential. In the last chapter, we've shown the advantage of separating pathway-specific contributions from LFP data. A stable separation would help to understand better the pathway dynamics. However, selecting biophysical meaningful components from ICA generally requires expertise in LFP analysis. When the components are contaminated, the unsupervised method cannot tell a physiologically plausible component from the others, even though sometimes its spatial profile is clear according to the anatomy of the recording arrangement. The spatial profile of LFP is determined by the morphology of local neurons (Sterratt et al., 2011b). Therefore, in this chapter, we ask the question: how could we efficiently model the LFP patterns? Especially the LFP impulse response of the local population when some of the neural morphology information is given.

Detailed biophysical modeling helps to understand and characterize the extracellular fields generated by neural dynamics. The forward modeling framework with multi-compartment modeling is well-studied (Hagen et al., 2016) and applied to inverse modeling of current generators underlying recorded signals (Einevoll et al., 2013, Pesaran et al., 2018, Ness et al., 2015, Głąbska et al., 2016, Gratiy et al., 2011, Cserpan et al., 2017).

The impulse response of neuron membrane potential highly depends on the geometry of the dendritic tree structure. Modeling work based on cable theory closely resembles neuronal membrane dynamics (Rall, 2011, Carnevale & Hines, 2006). Numerical modeling as a forward model is an effective way to simulate complex dynamical interactions between different factors, e.g., synapses, active conductance, and so on. However, it's difficult to make the inference with the feed-forward simulation (Pesaran et al., 2018). Current inverse problems typically study the transmembrane current distribution that generates the local field potential (Pettersen et al., 2006, Buzsáki et al., 2012), without considering the constraints brought by the dendritic morphology (but see (Gratiy et al., 2011,

Buccino et al., 2018, Cserpan et al., 2017)).

When passive membrane properties are considered, analytical solutions could be conducted using Green's function method (Butz & Cowan, 1974, Koch & Poggio, 1985, Abbott et al., 1991, Gratiy et al., 2011). It simplifies the integration process of membrane potential dynamics into a linear convolution with a time-invariant filter. Green's function is widely used to characterize the dendrite computation on different tree structures, or coupling by gap junctions (Timofeeva et al., 2013). The passive membrane condition could be further extended to the quasi-active membrane, i.e., with resonant membrane dynamics (Coombes et al., 2007).

Previous work connecting the cell morphology to extracellular potential mainly focuses on the extracellular action potential (EAP). The wave-shape of recorded EAP appears to depend on the location of recording sites (Gold et al., 2006). Therefore, EAP contains information about the size and location of dominant current sources located around the soma. The inverse problem is been modeled with the point neuron model (Chelaru & Jog, 2005, Kubo et al., 2008) or dipole model (Mechler & Victor, 2012, Mechler et al., 2011). Recent works solve the inverse model with detailed modeling and deep neural networks to account for complex spatial-temporal patterns (Lueckmann et al., 2017, Buccino et al., 2018). However, compared to the shape and discrete events of the action potential, in LFP modeling, we are facing continuous signals capturing the slower and noisy presynaptic inputs. Therefore we need to find an easy way to characterize their temporal properties.

Here the aim is to establish a framework for modeling the LFP spatial-temporal pattern with known neuronal morphology. This work is aiming to prove the concept, therefore, we constrain ourselves to the passive cable. We discuss a flexible yet efficient way to capture the heterogeneous population response. We show the multi-compartment-based feed-forward simulation (MFF) catches the membrane impulse response dynamics and is comparable with other analytical solutions. A simple parameterized model is provided, and a lower dimensional representation of the LFP component based on the model is discussed. Finally, we show the model inversion. These demonstrate the frequency domain representation effectively bridges the cell morphology with its dynamics. This could be a good candidate for developing pattern recognition methods for LFP data.

3.1 Greens Function

3.1.1 Greens Function: Impulse Response in the Frequency Domain

The impulse response of neurons is described by the neural cable theory (Rall, 2011). According to Kirchhoff's current law, The cable equation is written as ref.

(Dayan & Abbott, 2001, Sterratt et al., 2011b, Carnevale & Hines, 2006):

$$2\pi\omega C_m \frac{\partial V}{\partial t} = g_l(E_l - V) + g_a \frac{\partial^2 V}{\partial x^2} + \mathbb{I}_j, \tag{3.1}$$

When a passive membrane is considered, the dendritic responses would be linear and time-invariant.

As one can appreciate from the cable equation 4.1, the spatial pattern of the neuronal response evolves with time. In other words, here, the space and time are not independent (Gratiy et al., 2011), instead of the commonly assumed spatial-temporal independent response pattern (Makarov et al., 2010) or spatially fixed rank-1 response pattern (Einevoll et al., 2007) (signal X_i could be composed by rank-1 vectors A_i, S_i, written as $X_i = A_i' S_i$. The dependency is induced by the interplay of axial current (spatial Laplacian) and trans-membrane resistor–capacitor-currents.

On the other hand, when transformed into the frequency domain, the convolutionary neuronal response becomes multiplicative, which means in the frequency domain, the impulse response is a rank-1 matrix of space and time. This could be seen in the frequency domain cable equation:

$$i2\pi\omega C_m \tilde{V} + g_l \tilde{V} - g_a \frac{\partial^2 \tilde{V}}{\partial x^2} = \tilde{I}_j, \qquad s.t. \qquad \tilde{V} = (i2\pi\omega C_m + g_l I - g_a \nabla^2)^{-1} \tilde{I}_j. \tag{3.2}$$

With the linear operation, the frequency domain impulse response directly captures the return current pattern of the neuron given any arbitrary input distribution. Because of the inversion, the spatial pattern in the right-hand side of equation3.2 varies across frequency. This corresponds to the time-dependent spatial pattern in the temporal domain. It would also induce a low-pass effect of membrane signal to add to the power-law effect observed in extracellular recording (Pettersen et al., 2014, Gratiy et al., 2011).

Here we set out to capture the LFP signal with Green's function method. Green's function is the impulse response of the neurons given the close-end condition of dendritic trees and initial conditions. Due to the linearity of the passive cable equation, the input is a sum of delta functions, and so the resulting LFP pattern would be the superimposing of Green's function response to the input delta functions.

To characterize how the responses of neural membrane potentials are affected by the morphology of the dendrite tree, Green's function methods have been utilized (Butz & Cowan, 1974, Abbott et al., 1991, Coombes et al., 2007). Based on the analytical solution of current injection in the infinite long cable, Green's function of membrane potential impulse response at any given recording point along the arbitrary dendritic tree has been well established. Recently, Green's

function methods have been extended to gap-junctions (Timofeeva et al., 2013), and network dynamics (Yihe & Timofeeva, 2016).

Instead of continuous temporal domain analytical solutions of membrane potential, here we stay in the complex frequency domain for it's more flexible to model extracellular fields, especially when there are multiple inputs. The goal is to establish Green's function as the basis for inverse modeling of LFP recordings. We first describe Green's function formulation of both transmembrane current source and local field potential based on multi-compartment models. Then we introduce multiple simplifications and parameterize the system for further inverse modeling.

3.1.2 Green's Function for Homogeneously Distributed Inputs

Membrane potential modeling with Green's function has long been proposed to study the effects of dendrite morphology before numerical methods based on multi-compartment models took its place. However, the modeling of local field potential appears to be much more complicated. To get the membrane potential, one needs to solve the linear system described by the cable equation. But to calculate the extra-cellular potential, we need to further integrate over the continuous membrane with the inverse of its distance with regard to the recording sites. Meanwhile, utilizing the idea of a multi-compartment model, as proposed early in (Koch, 2004) and later work by Gratiy (Gratiy et al., 2011) simplified this problem by descritizing the neuron and resolve Green's function as in a linear system, getting the membrane potential response as well as the trans-membrane currents response at each compartment, and calculate local field potential by standard LFP methods. In the frequency domain, this appears as just another linear operator adding on top of the membrane potential Green's function. Here we employ the same idea to build the base functions used in a general inference framework.

By discretizing the dendritic tree, the membrane potential impulse response (Green's function) is easily achieved for the linear system. Here we start with the frequency domain Green's function in response to the unit δ input at a given depth.Along with the Neuron simulation, we could adopt the same tree structure in both numerical simulation and Green's function reconstruction. In the detailed neuron model, the dendrites of the neuron are subdivided into smaller segments to enhance the precision of numerical integration (Carnevale & Hines, 2006, Cuntz et al., 2010). For many interested brain areas, the passive parameters of cells with detailed morphology reconstruction could be found in online open-source libraries like NeuroMorpho (http://neuromorpho.org/).

The input is modeled as a current injection. Notice that the resonant (quasi-active) current could also be modeled in the same manner (Koch & Poggio, 1985). Starting from the simplistic scenario, suppose that we have a single compartment

that receives a uniformly distributed unit current impulse δ. This will lead to an abrupt change in the local membrane potential, and the difference in electrical potential will drive the ions into the neighboring compartments.

In the frequency domain, the corresponding Green's functions of transmembrane currents at any segments $\tilde{\boldsymbol{G}}\boldsymbol{h}$ could be estimated by a linear system simplification:

$$i2\pi\omega C_m\tilde{V} + g_l\nabla^2\tilde{V} = \tilde{\mathbb{I}}_j, \qquad \tilde{I}_m = -M\tilde{V}, \tag{3.3}$$

$$\tilde{\boldsymbol{G}}\boldsymbol{h}(\omega) = \tilde{I}_m(\omega) = M(Y(\omega) - M)^{-1})\tilde{I}_s = M(Y(\omega) - M)^{-1})\tilde{\mathbb{I}}_j(\omega), \tag{3.4}$$

where $M = \nabla^2$. Here $Y(\omega)$ is the passive membrane property which depends on frequency ω.

After we get the Green's function of transmembrane currents, the Green's function of LFP produced by this segment at frequency ω could be written as:

$$\tilde{\boldsymbol{G}}(\omega) = B\tilde{\boldsymbol{G}}\boldsymbol{h}(\omega), \qquad \forall\omega. \tag{3.5}$$

Here we could use point approximation or line source approximation to generate LFP, and B denote the field potential generated by I_m at each compartment (Holt & Koch, 1999). The mapping B is linear, and it is determined by the relative position c of the cell with regard to the recording shank (see figure3.1 C). The information of the neuron population thus could be inferred from B, which we will discuss in the following session.

Notice here the LFP signal recorded at any arbitrary site is approximated by a homogeneous resistive extracellular field (Nicholson & Freeman, 1975, Lindén et al., 2014), but the inhomogeneous extracellular impedance (Pettersen et al., 2006) or frequency filtering effect of extracellular field (Bédard et al., 2004) could also be captured by this model. In this case, we need to measure the impedance of the extracellular space and then replace the B with a complex impedance matrix Bi. For simplicity, we limit our discussion here to an isotropic conductance-based extracellular environment.

The single neuron frequency domain Green's function could be easily extended to the population level. Assuming the inputs from specific pathways i will target the postsynaptic population in a depth-dependent manner, e.g., with a spatial distribution $\mathbf{y}$, we could model the mean field response of the population transmembrane currents as a linear summation of all the inputs.

To simplify the modeling, we assume the current is distributed according to f within each laminar perpendicular to the recording shank and distributed according to y_i dependents on the depth i parallel to the recording shank. Similar to the current source bases kernel current source density method, we can go one step further, forming the laminar Green's function bases for currents injected into given depth layer i (fig.3.1 A). Given a input base l_i, the corresponding Green's

function bases of CSD $\tilde{\boldsymbol{G}}\boldsymbol{c}_i$ is:

$$\tilde{\boldsymbol{G}}\boldsymbol{c}_i = \sum_j l_j \tilde{\boldsymbol{G}}\boldsymbol{h}_j, \qquad l_i = \begin{cases} f(z_j) & j \in layer_i \\ 0 & otherwise \end{cases} \tag{3.6}$$

where f could be any function describing the input synaptic distribution. The overall LFP produced by the column of neurons is the summation over all the laminar $\tilde{\boldsymbol{G}}\boldsymbol{c} = \sum_i y_i \tilde{\boldsymbol{G}}\boldsymbol{c}_i$ is discussed in the next section.

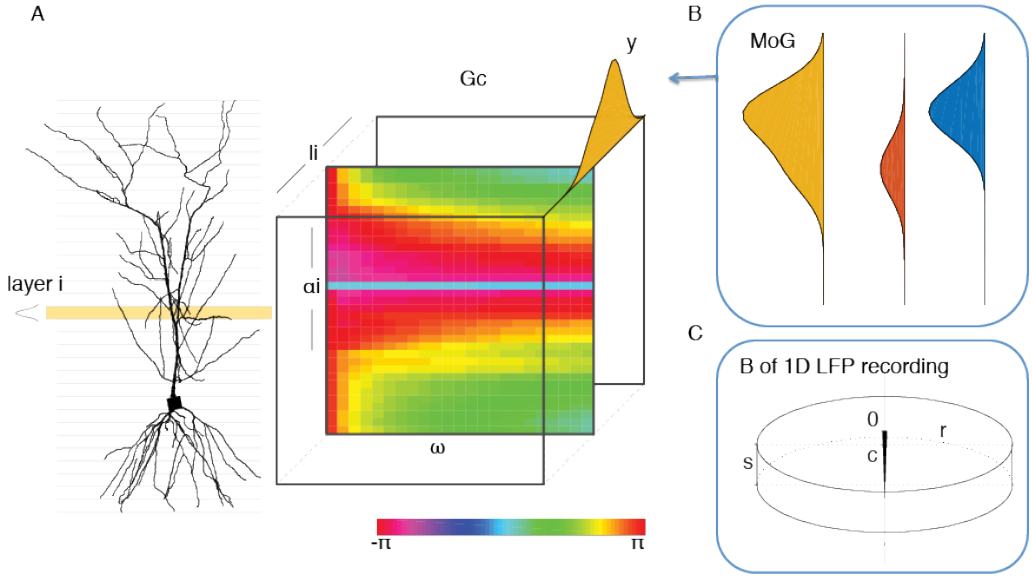

Figure 3.1: Green's Function Model of the impulse response of a neuron. A. The Green's function of a given cell with a given input pattern y. The Green's function is presented as a 3-dimensional tensor with regard to the frequency ω in the horizontal axis, the recording depth in the vertical axis, and the input distribution y in the 3rd dimension. Color map indicates the phase of the Green's function basis G_c at input layer i. B. Parameterization of the input current distribution as a mixture of Gaussians. The yellow input pattern is linearly constructed by the red and blue gaussian shapes. C. Parameterization of the B matrix in the 1D recording. The 1D recording shank is assumed to be placed in the middle of a neuron column and the top channels of the shank are regarded as 0 depth. The neuron column with length S is placed at c. Its radius is r.

3.1.3 Infer the Input Current Distribution

In the previous session, we described how to construct the Green's function for a given afferent pathway. In this session, we consider the inverse problem, i.e., how to infer the input pattern as well as the cell property when observing an LFP pattern. Starting with the 1D recording, we ask the question: if the cell morphology and the relative position of the cells to the recording site are given or measurable, can we infer the input distribution from the data?

We formulate the inference as a maximum likelihood problem. Assuming that the evoked pattern $\tilde{\Phi}_n$ is the ideal impulse-response pattern $\boldsymbol{G}_n$ with some Gaussian noise $N(0,\sigma)$, the likelihood would thus be:

$$p(\mathbf{A}_n) = \bar{A}_n \prod_{\omega} exp(-\frac{\left\|\tilde{\Phi}_n(\omega) - \boldsymbol{G}_n(\omega)\right\|}{2\sigma^2}), \tag{3.7}$$

where $\bar{A}_n$ is the scaling factor. Then frequency domain response $\boldsymbol{G}_n$ is matched to the observed measurements $\tilde{\Phi}_n$.

Here, $\boldsymbol{G}_n$ is parameterized as current input y placed at a unit-length homogeneous neuronal column, which is then scaled with s and shifted with an offset c regarding the unit length linear probe (see figure.3.1). Given the geometry of the recording probe, the goal is to simultaneously infer the parameter of the neural ensemble, including the relative location of the neurons, the length, and offset of the neurons, and the synaptic distribution, as well as the power in all the frequencies. To do this, we first model the laminar current source density (fig.3.1 G_{ci} in equ.3.6) in response to input layer $i : i \in 1,...,N$, as described in the last session (fig.3.1 layer i). Then the total CSD pattern is a linear summation over all the input layers weighted by the synaptic distribution $y = [y_1,...,y_N]^T$:

$$\boldsymbol{Gc} = \sum_{i}^{N} y_i G c_i \tag{3.8}$$

Notice the spatial pattern, unlike the power of activity, is assumed to be constant in all the frequencies.

To simplify the input inference and enhance the smoothness of the input shape, we use a mixture of N_g Gaussian kernels to model the input shape $y := \sum_{i=1}^{N_g} w_i N(\mu_i, 1/\beta_i)$ since Gaussian mixture is widely used to model arbitrary smooth distributions.By using loglikelihood, the loss function is equivalent to the Euclidean Norm of the difference between the fitted from the observed pattern and henceforth the problem could be written as:

$$\begin{aligned} argmin_{\Theta} \quad & L = \textstyle\sum_{\omega} \left\|\tilde{\Phi}(\omega) - \boldsymbol{G}(\omega)\right\|, \\ \text{subject to} \quad & y > 0 \\ & c < 1 \\ & \textstyle\sum w_m = 1 \end{aligned} \tag{3.9}$$

where the $\boldsymbol{G}(\omega)$ is computed as:

$$\boldsymbol{G}(\omega) = B * (\sum_{i}^{N} Gc_i(\omega) y_i). \tag{3.10}$$

$$B = B(x,s,r,c) \tag{3.11}$$

$$\mathbf{y} = \sum_{m}^{Ng} w_m * exp(-(l-\mu_m) * \beta_m) \qquad with \qquad l = linspace(0,1,N) \tag{3.12}$$

$$and \qquad \sum_{m}^{Ng} w_m = 1 \tag{3.13}$$

According to equ.2.6, B is fitted with relative length s and offset c compare to the known electrode (figure 3.1). In the 1D case, the contribution of current sources layer i at the recording site at x it could be written as:

$$B = B(x,s,r,c) = \frac{\Delta}{2\sigma}\left(\sqrt{(c+\alpha_i s - x)^2 + r^2} - |c+\alpha_i s - x|\right) \tag{3.14}$$

In this work, the current source layer α is chosen to preserve the same segmentation as the input current layers l (see figure3.1 A). Pattern fitting with equation 3.9 could be conducted in the real domain or complex domain.

3.2 Simulation Methods

3.2.1 Numerical Simulation

The multi-compartmental simulation is performed within NEURON (Carnevale & Hines, 2006). We use the time step of $dt = 0.02$ms.The intracellular resistivity was set to $R_i = \Omega cm$ and the membrane resistance was set to $R_m = 15k\Omega cm^2$. The membrane capacitance was set to $C_m = 1\mu F cm^2$. The reversal potential for leaking current was set to $V_{leak} = -65mV$.

Its morphology is shown in fig.3.2 A. The membrane potential V_m and transmembrane currents I_{mem} at each segment are recorded for further analysis.

The impulse response of NEURON simulation is the deconvoluted version of the membrane potential V_m or transmembrane currents I_{mem}. Since convolution is multiplication in the frequency domain, the deconvolution is achieved by Fourier transform of V_m or I_{mem} divided by Fourier transform of input currents I_{in}.

3.2.2 Temporal Domain Green's Function Methods

To connect to theoretical approaches for studying the dynamics of the neuron membrane potentials, here we also compute the temporal domain Green's function of the same simple passive cable model as in the NEURON simulation, shown in fig.3.2 A.

Here we applied the sum-over-trips method (SOT, or path integration method) first introduced to resolve the membrane potential in arbitrary branching dendrites (Abbott et al., 1991) and simplified later with optimized trip selection and matrix-based methods (Cao & Abbott, 1993, Caudron et al., 2012). The core of the method is to use a Feynman-Kac representation of the solution in terms of random walkers on a dendritic tree of arbitrary geometry (Abbott et al., 1991). In other words, the method represents Green's function as a sum over all the possible "trips" along the dendritic tree starting at one given point x on segment i (e.g., input site), cross over and ends up at y on segment j (e.g., recording site). The traveling rule at terminals takes care of the boundary conditions.

The SOT will converge to the true Green's function $G_{x,y}$ When all the possible trips are considered. With a finite number of trips in the sum, Green's function will be dominated by the shortest path through x to y. However, in the long time limit, SOT will converge to ground truth (Abbott, 1992). It's worth mentioning that Green's function here is computed for each pair of input-recording sites (interchangeable due to the symmetry of the dendritic tree) because the trips are determined by the location of the pair.

Later works include systematically optimizing the integration of trips (Abbott, 1992, Cao & Abbott, 1993, Caudron et al., 2012). The matrix method of (Caudron et al., 2012) is used here for the simple model in fig.3.2 A. Briefly, the idea is to group all the trips according to their lengths. A modified direct edge adjacent matrix could be used to compute the sum of coefficients of trips of a given length. Then adding trips is nothing more than a multiplication of the edge-adjacency matrix. Detail of this algorithm could be found in (Caudron et al., 2012) section Matrix Method.

To compare with the frequency domain Greens function forward model, the impulse response of the analytical SOT method is obtained by Fourier transform of the time domain spatial-temporal pattern. Same to the NEURON simulation, the deconvolution is achieved by Fourier transform of V_m or I_{mem} divided by Fourier transform of input currents I_{in}.

3.2.3 Greens Function with Neuron Reconstructions

Green's functions of any given neuron are based on multi-compartment models with anatomically reconstructed morphology. Passive capacitors C and resistors R could be computed accordingly (Sterratt et al., 2011b) or directly by the standard NEURON implementation (Carnevale & Hines, 2006). Here we provide two alternative ways to reconstruct the neuron, based on python simulation and the NEURON toolbox (Hines & Carnevale, 2001, Lindén et al., 2014) or the MATLAB-based TREEs toolbox (Cuntz et al., 2010).

The reconstruction with NEURON is based on the parameters computed and used

in the numerical simulation. For multi-compartmental model with anatomical reconstructions, to ensure good numerical precision and capture the transient membrane response, we use the $lambda\_f(100)$ rule in NEURON to determine the number of segments (Hines & Carnevale, 2001). The compartmentalization was done so that no dendritic compartment was larger than $1/30$ of the electronic length at 100Hz. The mapping from transmembrane currents to LFP recording with line-source approximation or point-source approximation could be obtained from *LFPy* simulation. In the comparison between the NEURON simulation and Feed-Forward modeling, we use the point-source approximation in both situations.

The MATLAB-based TREEs toolbox could also effectively reconstruct the multi-compartmental geometry of the dendritic trees with the same $d - lambda$ rule at 100 Hz. The detailed dendrites segmentation is slightly different from NEURON reconstruction (Cuntz et al., 2010), but clamping at the same lambda frequency forces the algorithm to optimize the geometry to render a competitive electrical response. Therefore, these differences would barely affect multi-electrode extracellular recording. With all the passive parameters, the impulse response of a neuron is calculated according to equ.3.4 and equ.3.5 at each given frequency. Afterward, the current-LFP matrix B is generated with point source approximation. The Greens' functions of heterogeneous hippocampal neurons are obtained with this method.

3.2.4 Multi-compartment based Forward Simulation

With the passive membrane assumption, we can easily simulate the impulse response of a given neuron or a homogeneous neural population with frequency domain feed-forward simulation. Here in the forward modeling, the system impulse response is modeled by its Greens' function multiplied by the Fourier transform or wavelet transform of the input $I(\omega)$. This is possible because, in the linear system, the convolution in the temporal domain is equivalent to multiplication in the frequency domain. This technique is frequently used in temporal convolutions or filtering because it simplifies the recursive multiplication to a linear operation.

3.3 Results

3.3.1 Frequency Domain v.s. Temporal Domain Green's Function

To validate Green's function-based feed-forward simulation, we compare it with well-established analytical solutions and numerical solutions in a simple dendritic tree model. The model illustrated in fig.3.2 is constructed based on the dendritic system studied in (Butz & Cowan, 1974, Abbott et al., 1991). Here we create two levels of symmetric brunching to explore: 1. how the branching affects the

membrane voltage 2. how the voltage evolves with regard to the relative distance from the input site. Considering the cyclical symmetry, the input is injected at the middle of primary, secondary, and tertiary dendrites as an instantaneous delta impulse current(fig.3.2), or a sinusoidal wave (fig.3.3). The membrane potential and transmembrane currents are recorded at each segment in NEURON simulation and the frequency domain-based forward simulation (FF). With the SOT method, the membrane potential is recorded at two sites, one at the middle of the secondary branch and the other at the tertiary branch(fig.3.2A, r_1,r_2).

The membrane potential spreading in the dendritic cable and the peak membrane potential at each segment decreases as a function of distance from the input site(fig.3.2B, C). Both Neuron simulation and the FF modeling based on the frequency domain Green's function captures the flow of ions. The largest peak appears less than 0.1ms, and the power decreases fast because of leaking currents. The largest discrepancy between NEURON and FF simulation appears at .1ms, due to high-frequency transient response, especially around the input segment. The membrane potential in the two recording sites has similar responses (fig.3.2E), which could be summarised in the frequency domain (fig.3.2 F and G).

Then the SOT analytical solution for each input-recording pair is also computed. To guarantee that the SOT solution converges, we compute Green's function for $k = 4 \times 10^{[0:4]}$ trips. Here the difference is measured by the area between curves normalized by the area under the membrane potential response of $k = 4 \times 10^4$. Because the trips in the matrix method are selected based on the basic four classes of trips (Abbott et al., 1991), which is much more effective than randomly selected trips, the algorithm converges fast, and the error is close to 0 when the number of trips is larger than 1000 (fig.3.2 E inset). We use $k = 4 \times 10^4$ in the following analysis. Multi-compartment-model based simulations, frequency domain based forward (FF) simulation, and SOT generally match each other.

The largest disagreements between the SOT of both NEURON simulation and FF modeling appear around 0.1ms(fig.3.2D). This could partially be due to the not perfect delta impulse input current used in the multi-compartment model. But the impulse response functions are still close to each other (fig.3.2E).

To have a closer look at the spatial-temporal pattern of Green's functions, we also transfer the SOT and NEURON simulation into the frequency domain and compare to the frequency domain FF model, both amplitude and phase at two recording sites are shown in fig.3.2 F and G respectively. The Green's functions at each recording site match each other, especially in the slower frequency. While recordings obtained from different sites are distinguishable from each other. We also observe the error increase with frequency. For frequency above 2000Hz, there appears to be a large difference between the Green's functions. This also contributes to the difference of transient response in fig.3.2D.

To assess the difference between multi-compartmental model-based modelings to

the analytical SOT solution, we compute the amount of mismatch normalized by SOT response, as $D_{SOT} = \frac{Area_{mismatch}}{Area_{SOT}}$ in fig.3.2H. The amount of D_{SOT} of NEURON simulation is similar to FF modeling. Due to numerical integration, NEURON fits better when the recording sites are close to the input ($R2$). While the distant recordings $R1$ in FF have similar precision as the close one $R2$ (fig.3.2 left). The average D_{SOT} is comparable between these two methods.

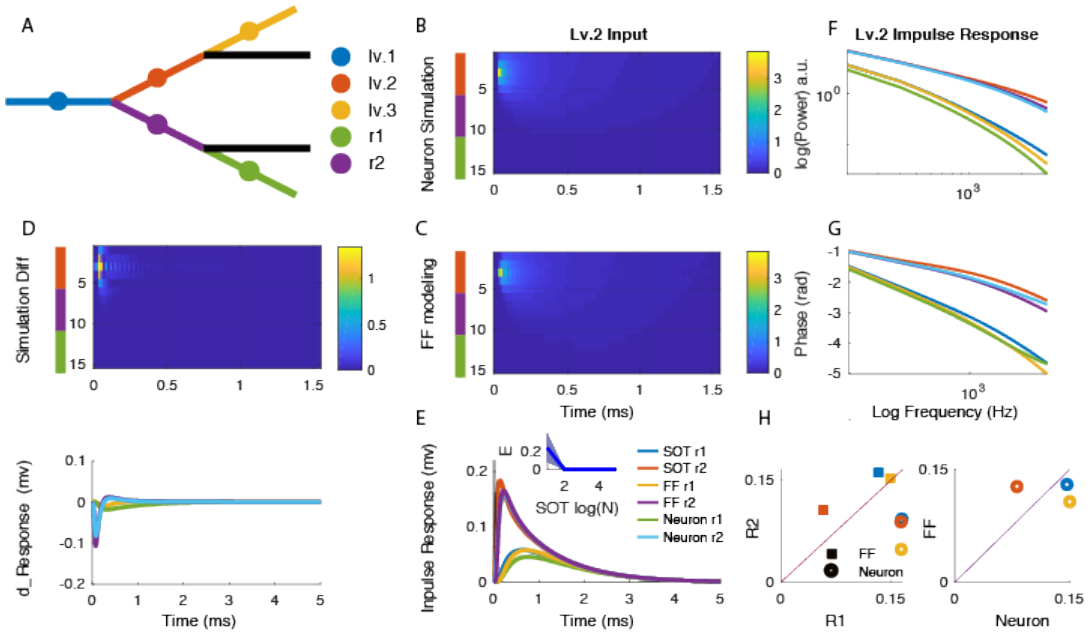

Figure 3.2: Comparison of Green's function methods. A: Model schematic. The color indicates inputs and recording sites at different branching levels. B. Example impulse response with NEURON simulation. Input at lv.2 brunch and membrane potential recorded at three connected brunches, including the input brunch and two recording brunches, indicated by color on the left. C. Same as B but for frequency domain based forward (FF) simulation. D. Difference between NEURON and FF simulation. Upper: Difference of impulse response in B and C, Lower: NEURON and FF recordings each compare to Sum-Over-Trips solutions. Color code is the same for E, F, and G. E. Temporal domain impulse-response recorded at r1 and r2. Inset is the convergence performance of SOT Green's function pattern when the number of trips increases. F, G Frequency decomposition of impulse response in F power and G phase, respectively. H. D_{SOT} NEURON and FF simulation compare to the SOT solution. Left: D_{SOT} for each method at proximal recording site R2 and distal recording site R1. Right: for all the input sites, compare average D_{SOT} obtained by NEURON and FF method.

Next, we look at the transmembrane currents' response to oscillatory inputs. LFP is generated by the transmembrane currents (see equ.2.9 and section.2.1.2), and blurred with volume conduction The transmembrane currents' spatial-temporal response from the NEURON simulation is similar to the FF simulation (fig.3.3B).

The injected current is considered part of the transmembrane current in the FF model but not so in the NEURON simulation, so we didn't plot the transmembrane current at the input segment in FF simulation (white line). The phase lag from the input current increases with distance from the input (see appendix fig.C.1). Again take the $lv.2$ input site as an example, the recording site at adjacent brunch $r2$ shows a small phase lag while $r1$ at the distal brunch has a much larger phase lag (fig.3.3C). Here the histogram of the demodulated phase shows only one peak. The phase lag estimated by FF simulation indicated by the red cross agrees with the mode of demodulated phase. Summarized in fig.3.3 E, the resultant length of the phase difference between demodulated phase and FF phase is close to 0 and smaller in the closer $r2$ than the more distal $r1$. The wavelet transform of the transmembrane current illustrates the spectral profile of the response, both simulations again follow the inputs, but the power of FF at $r2$ is smaller than the NEURON simulation, similar to the results of impulse response (fig.3.3 D).

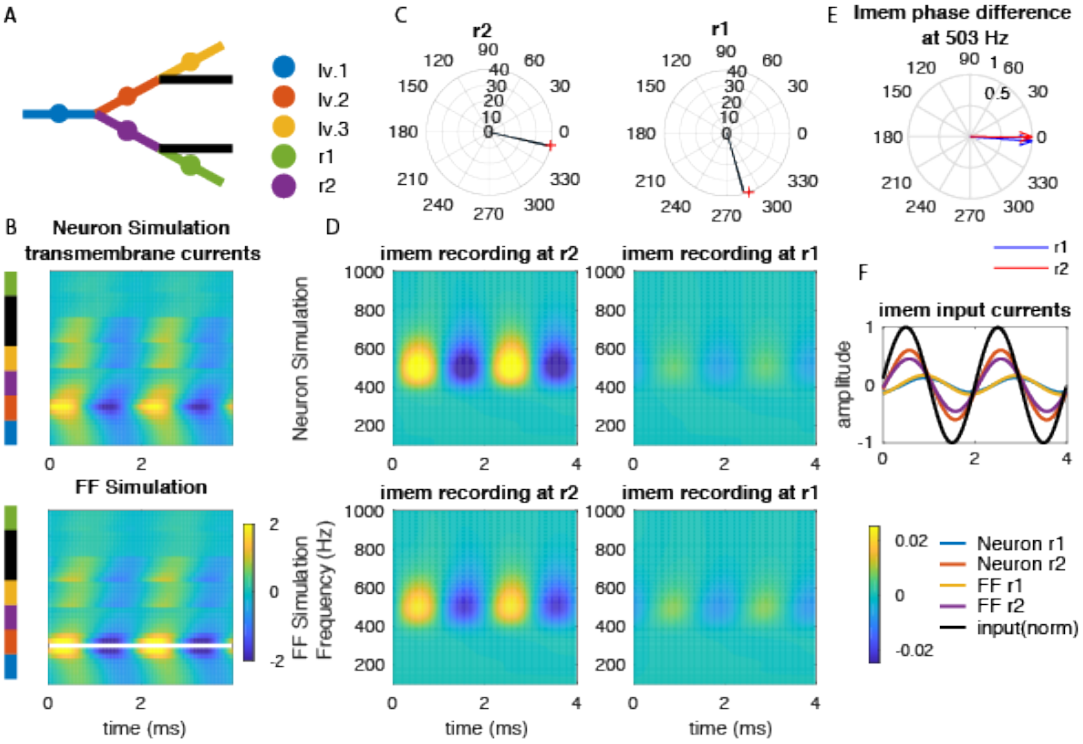

Figure 3.3: Comparison of Simulation with Oscillatory Inputs. A. Model schematic, B. Trans-membrane current(i_{mem}) for NEURON (upper) and Frequency domain based Forward simulation (lower) at all the segments sorted by their brunching level on the left. Same color scale. C. The demodulated phase around input frequency was recorded at $r2$ and $r1$. D. Wavelet transform of the i_{mem} at $r2$ and $r1$. E. Phase difference between FF estimation and demodulated NEURON simulation. Same color scale. F Recorded temporal trace plot against input current.

In the complex multi-compartment model, we could also use the frequency domain Forward modeling to establish a fast LFP response pattern 3.4. We simulate a realistic CA1 pyramidal neuron with random inputs in NEURON. In neuron simulation, the inputs are simulated with a conductance model (synaptic conductance) instead of the current injection in a linear system. This means the driving force of the synaptic current would be influenced by the membrane potential change. We compare the NEURON simulation with the frequency domain Forward simulation. To obtain the temporal domain LFP pattern of the FF model, we first compute the frequency domain complex wavelet transform of synaptic conductance, multiply it with the Green's function (fig.3.4B), and then use inverse wavelet transform ($[60, 2000]$Hz) to get the temporal domain LFP trace.

The linear FF simulation generally matches the nonlinear conductance-based model (fig.3.4D). However, we also notice the FF simulation responds faster to the inputs while the conductance model is slower, therefore smoother than the FF model (fig.3.4C). This is due to the change of driving force in the conductance-based input model. Same as in the simple model, here Green's function also shows a larger portion of return currents at the distal apical dendrites in high frequency compared to the slow frequency (fig.3.4B) due to the linear cable filtering effect. We also observe that FF simulation has a larger return current locally in the distal dendrites compared to the NEURON simulation. This could be caused by compartmentalization or numerical integration and should be explored more when applied to realistic scenarios.

Overall, we demonstrate here the FF simulation closely matches the NEURON simulation, and the Green's function from all the methods matches each other. Green's function estimated in the frequency domain is fast and provides an easy way to summarize the spatial-temporal pattern dictated by dendritic morphology. In this section, we study in fine detail whether the membrane potential at each segment generated by each method matches each others. While in the following analysis, we will look at a relatively coarser measure: the LFP signals. Furthermore, the discussion here could be of interest for cell localization on high-density EAP recording. However, how active conductance adds to the impulse response needs to be established in further works. We'll discuss this at the end of this chapter.

3.3.2 Similarity under Heterogeneity

Next, we use the FF Green's function to study the LFP pattern generated by different morphology. For this purpose, we use a CA1 pyramidal cell data set from `http://neuromorpho.org` (adult male Sprague-Dawley rat hippocampus, Achieve Name: Chen, $n = 47$). The digital reconstructions were performed with Neurolucida (MBF Bioscience Williston, VT, USA). We choose this data set

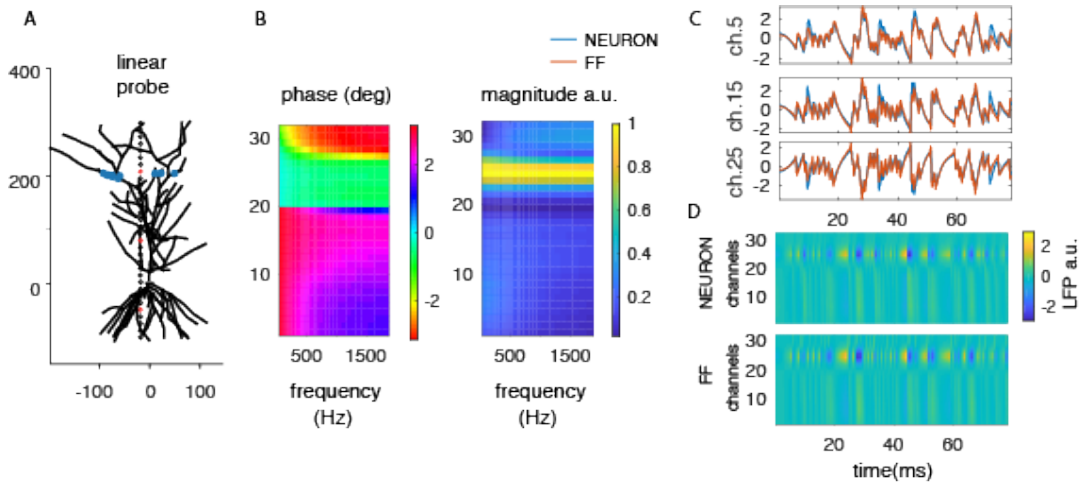

Figure 3.4: Realistic multi-compartment model simulation. A. Schematic of the multi-compartment model. Blue dots label synapse-targeted branches. Red dots on the linear probe indicates the location of channel 5,15,25 in C. B, The frequency domain Green's function in phase and magnitude. C. Normalized LFP trace ([60,2000]Hz) generated by NEURON or FF simulation from three channels. The trace is normalized by their variance. D, Normalized LFP traces ([60,2000]Hz) cross channels.

because of the large number of cells and the complete dendritic tree reconstruction.

Green's function is computed for all the reconstructed cells. Here we assume a passive membrane with a resistance of $50000\Omega cm^2$, axial resistance of $150\Omega cm$, and a membrane capacitance of $1\mu Fcm^2$. LFP is approximated by assuming transmembrane currents homogeneously distributed within each depth layer in a $50\mu m$ column. To assess the similarity of Green's function profiles, the input is distributed according to the depth parallel to the neuronal dendritic tree axis.

We find that the LFP Green's function profile is determined by the input depth. Fig.3.5A shows two examples of neurons with different morphology. The magnitude of impulse response will always peak around the input layer. Their LFP GF response is similar for especially basal and proximal inputs. When the input is located at distal dendrites, we find a larger return current towards soma in cell 2, which has more proximal branches. But the return currents tend to be more local in higher frequencies in all the scenarios.

To assess how much the heterogeneous morphology affects the GF profile, we look at the similarity between GF from different cells (fig. 3.5B, C). For each frequency, the phase and magnitude of Green's function from each cell are compared to others with the same input layer. Results across all the input layers are summarized in B and C for phase and magnitude, respectively. The phase is more sensitive to morphology change while the magnitude pattern is very close

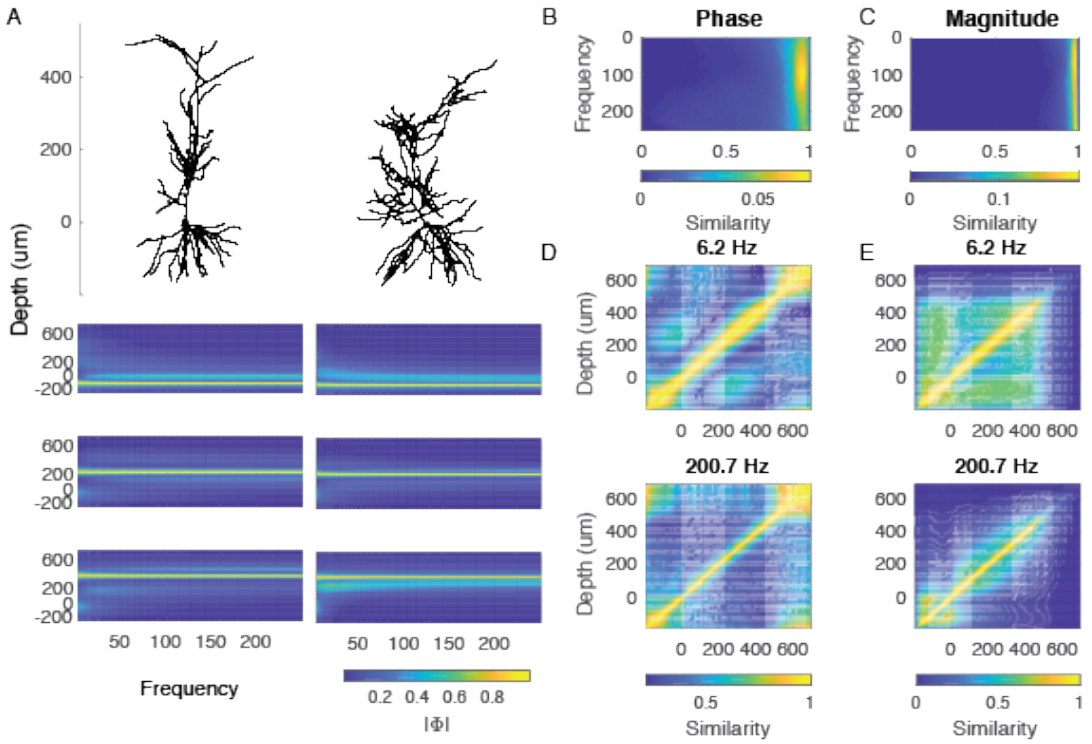

Figure 3.5: Comparison of Green's function from Heterogeneous Population. A, Green's function of two example pyramidal neurons. Lower panel: input currents are injected at $-105\mu m$, $145\mu m$, and $295\mu m$. The color plot shows the normalized magnitude of LFP Green's function profile at each frequency band. The y-axis indicates the recording depth. B, Histogram of the pairwise similarity of LFP response patterns from the different neurons. The Phase of Green's function from each cell is compared to others with the same input layer at a given frequency. Each frequency row sums up to one. C, Same as B but for magnitude. D, Average phase similarity between Green's function response with different input layers at 6.2Hz(upper) and 200.7Hz(lower). E, Same as D but for magnitude.

to each other. This is because of the large peak around the input site and the low-pass spreading pattern of the neural dendrites. Magnitude is dominated by the input site, while phase captures the "spreading" pattern of the current flow, which is influenced by the branching patterns especially when the frequency is low (fig.3.5B). But they are generally similar to each other, and the similarity is close to 1.

The Green's function response from different layers, on the other hand, tends to be different from each other(fig.3.5D, E). Compared to the high similarity within layers, the similarity between layers is much lower depending on the distance between the input layers. In lower frequencies, sometimes the input above and right below the soma layer could have a similar dipole shape because of the return currents (notice in this analysis we don't distinguish the dipole sign). But this tendency again shows less in the high-frequency data because of the locality of return currents. The magnitude of the GF also shows a sharper peak in high frequency due to the low-pass filtering of neuronal cable. The block on the upper right corner ($> 400\mu m$) is due to a few dendrites extending to this distance. This would give little magnitude similarity and no phase difference.

Green's function representation of LFP allows an easy grasp of how the other parameters affect the response (fig.3.6). Here to see how the heterogeneity of cell morphology affects the LFP response and how the effect dependents on the distance of recording shank with regard to the neuron ensemble, we simulate the Green's function of each at each depth layer. The corresponding Green's function is then normalized to unit variance and projected to the first 3 principle component of the generated data set(fig.3.6A). The real part of their Green's function is shown in fig.3.6 B. Input depth, indicated by color in fig.3.6A, is the major dimension that contributes to the distribution of LFP patterns. The difference brought by heterogeneous morphology is almost orthogonal to the difference caused by input depth. When we step away from the center of the ensemble, the pattern at the edge of the ensemble is still very similar to the center(fig.3.6A 2nd column). When the distance is more than 1mm, the contribution of the spatial heterogeneity is almost ignoble, however, the input layer depth still could bring difference(fig.3.6A 3rd and 4th column). Plotting all the components together shows the effect of input depth(fig.3.6C). The far-field signal could contribute to recordings in neighboring areas, this contribution could be simplified by the current dipole approximation.

Another example is to use Green's function to study how the geometry of layers affects the LFP signal. Here we simulate the grid recording of Dentate Gyrus, which is known to have a curved layered configuration (Fernández-Ruiz et al., 2013). Dentate Granular Cell(GC) from previous mice study (Schmidt-Hieber et al., 2007)(Achieve Name: 95960, *cell*_10 is used for simulation for it has complete morphology) and only the dendritic tree is considered here. Input is injected at the inner, middle, and outer parts of the dendritic tree to resemble the

CA3 commissural input, MEC layer III, and LEC layer II impulse respectively. To demonstrate the concept, we implement a simple symmetric architecture with two parallel layers and a half circle connecting them at $x = 0\mu m$. GC cells are distributed at the gray circles indicated in fig.3.6 E, $1 - D$ LFP and CSD is recorded at 5 positions to resemble the multi-shank recordings (left side indicates the current sink, and the right side is the current source). When the recording shank crosses the dentate structure, the amplitude is about 40 fold larger than the first shank. The amplitude of LFP response is amplified by the symmetric architecture of the layer (Fernández-Ruiz et al., 2013), and we find they are further amplified by the irregular dentate curvature. A simple second-order derivative along the linear probe close to the curvature (fig.3.6 E, 3rd shank,$x = 20\mu m$) shows a much larger current sink than at the parallel layer (fig.3.6 E, 4th shank,$x = 180\mu m$). This calls for caution when analyzing the LFP pattern in irregular structures.

To summarize, here we use Green's function to illustrate how the heterogeneity of cell morphology affects the LFP pattern they generate. The detailed morphology affects the LFP pattern generated by a single cell, especially when the recording sites are close to the cell. However, the input layer depth explains more of the variance of the LFP pattern than the cell morphology fig.3.6. This suggests that we could use Green's function as a template to distinguish pathway response terminating at different laminar depths, which we would use in the next chapter. We also demonstrate the utility of the frequency domain method to explore the influence of complex layer geometry. This method is fast and the result is comparable to the NEURON simulation. It could provide an easy first understanding of the signal and could be easily adapted to modeling and inference. With this, we demonstrate one way to parameterize the model and infer useful properties in the next section.

3.3.3 Model Inversion with Frequency Domain Green's Function

We fit the FF simulated LFP profile with our model. The ground truth LFP profile is generated with the frequency domain forward model. Here the model fitting is nonlinear, it consists of two major parts: input current fitting and the CSD-LFP mapping matrix: B matrix fitting for cell location(fig.3.7). To assess the performance, we directly look at the square error of the field potential profile. The fitted pattern is a significantly better match to the ground truth($median_{error} = 0.036$) than the shuffled null distribution($median_{error} = 0.248$, fig.3.7A). With the same Green's function template, the algorithm could recover exactly the true input distribution and the position of the cell, even when the cell is small compared to the recording shank(fig.3.7A, B).

Next, we ask how would different biophysical properties contribute to the model fitting. We set off to see the influence of the template on model inversion. From

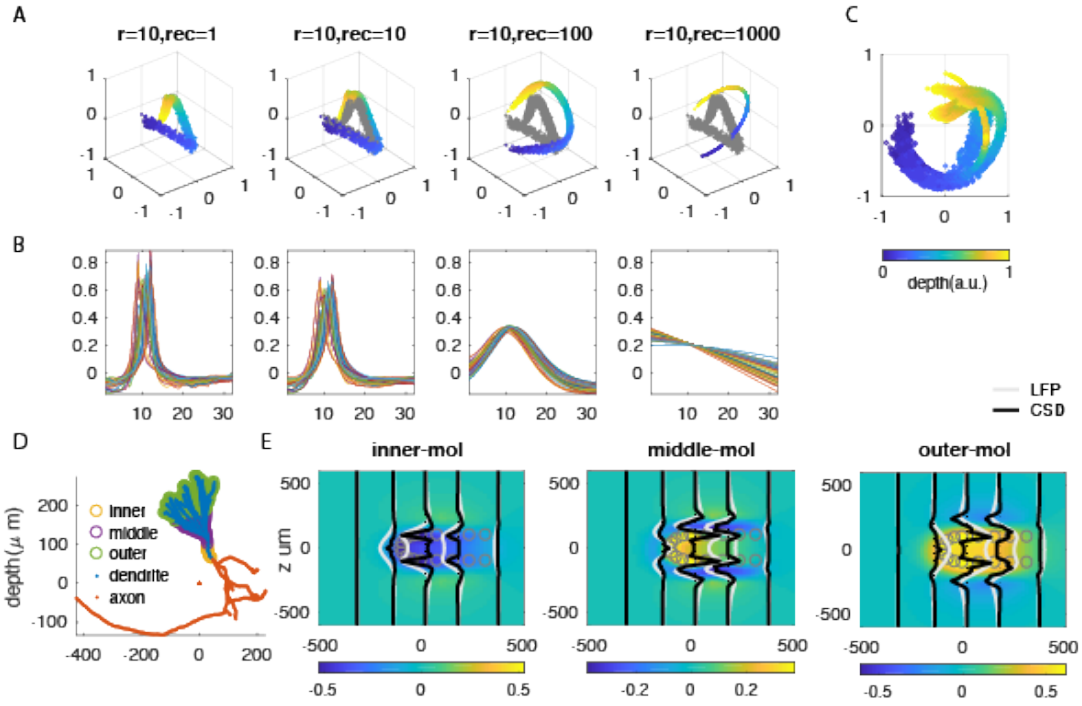

Figure 3.6: Green's Function Based Representation of heterogeneous impulse-response. A. Effect of the distance between recording sites and neural column. To study how the spatial profile change with input depth and neuromorphology, we plot the normalized Green's function of laminar current injection from an online dataset. The components are estimated by assuming a random average on $x-y$ plane. LFP is generated by a neural column ($r = 10\mu$m) within which currents are homogeneously distributed in the $x-y$ plane for each cell and each laminar injection. The recording shank are locate at the center ($rec = 1\mu$m), boundary ($rec = 10\mu$m), and outside ($rec = 100\mu$m or $rec = 1000\mu$m) of the column. The color indicates the depth of the current injection. All the impulse response profiles are projected to their first 3 components. The gray manifold on later subplots is the distribution of ($rec = 1\mu$m) and is plotted for contrast. B. The example real part of components from A, generated by laminar injection at 10. C. Plotting manifolds together shows heterogeneity has a smaller effect when the recording distance is large. But there is a dimension that components distribution varies according to the injection depth. D. Simulation of Dentate Gyrus populations. The current distribution according to the somatodendritic axis is plotted on an example Dentate Granule cell. DG curvature is modeled as two parallel layers and a half circle connecting them at $x = 0\mu$m. 2 D LFP profile is indicated by color. 5 linear shanks are put at different positions of the DG curvature. The recorded LFP is plotted in gray, and the current source density by spatial Laplacian is plotted in black.

the last section, we proved that population LFP Green's function profile within the same cell category is generally similar even when the detailed morphology is different. But how would this affect the model inversion? To answer this question, we fixed the cell location and generated target LFP patterns with randomly distributed weights from all Green's function patterns with the input depth. We fit sample patterns with the average template(fig.3.7D) or the Green's function from the last cell in the data set, denoted as the single cell template. Fitting with one cell or average template captures the current distribution, while the average template match closer to the target randomly constructed cell patterns. The fitted current lying around the diagonal indicates that the peak of fitted currents matches the ground truth. The fitting based on the average template appears to match better narrow input current pattern(fig.3.7E lower). In general, the fitting with the average template ($E(loss) = 0.027$) fits better than the single cell template($E(loss) = 0.049$, $p < .001$ Wilcoxon signed rank test). Furthermore, when single cell template is considered, the performance depends on how closely the template resembles the ground truth while the average template is usually close enough to the ground truth that release this dependence (fig. 3.7 F). However, we could see that the model inversion suffers most from the extreme distal inputs regardless of which template is chosen (fig.3.7F). Therefore, in practice, it would be helpful to use a template as close as possible to the generator of the target LFP pattern, but a template with similar morphology could already give a fair first estimation.

Next, we look at how the cell position affects model inversion. Here we find when the whole cell is within the recording range, the fitting generally matches the ground truth(fig.3.8C, D). However, the error rate is significantly larger when the cell crosses outside the recording range(fig.3.8D, $p < 0.001$ Wilcoxon rank sum test). We find simultaneously fitting the Green's function from multiple frequency bins improves the fitting (fig.3.8B). It reduces the depth of spurious local minimum in the complex energy landscape (fig.3.8E a:1 bin, b:16 bins). Within the recording range, pattern fitting normally has a nice global minimum (fig.3.8E.c). But when the cell is too far from the recording shank, it's difficult to reconstruct the current(fig.3.8E.d). This also indicates for cells aligned with but much deeper than the recording shank, it would be difficult to determine precise cell scales, a current dipole approximation could be used here.

Overall, we demonstrate here Green's function model inversion and how the different aspects of the model affect model inversion. We find the fitting does not heavily depend on the exact cell morphology, an arbitrary cell from the same category could be used to fit the model. But a better fitting would be achieved with an average neuron response pattern. Instead of fitting with one frequency band, we find simultaneous fitting with multiple frequency bands would help to improve model inversion. This method works best when the neuron is within the recording range, and the performance decreases when the cell is outside the

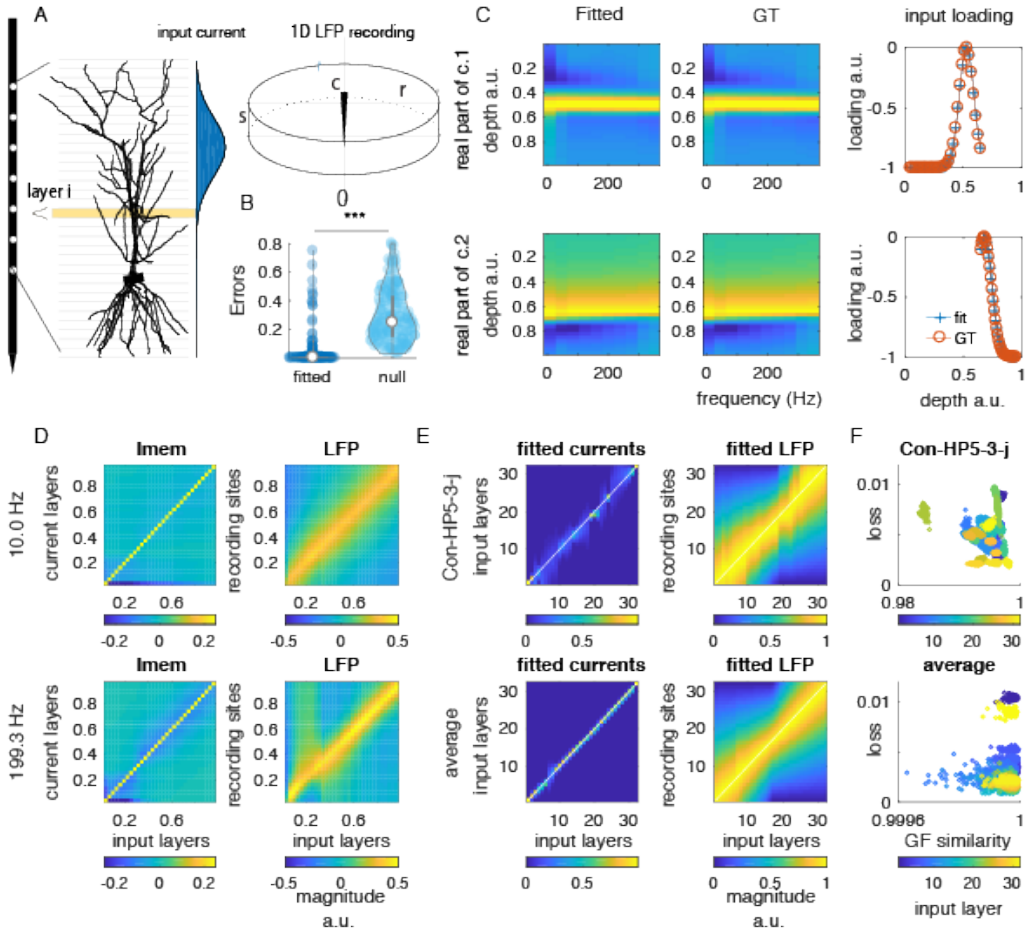

Figure 3.7: Demonstration of Green's Function Fitting: Effect of the Cell Template. A: Schema of frequency domain forward modeling. The current input target at a unit length neuron according to the depth in the somatodendritic axis. Afterward, the neuron is mapped to a recording probe according to the right inset. Right inset: The position and the scale of the neuron are parameterized according to a unit length recording linear probe. B. The error of Green's function fitting is less than the error given by unit variance gaussian current injection at random depth ($n = 100, ^{***} p < 10^{-10}$ Wilcoxon signed rank test). C. Example fitting performance. The FF simulation is fitted with the same cell template, emulating the situation when cell morphology is accessible. The color map depicts the real part of the fitted profile (Fitted) and the ground truth (GT). The fitted (cross) current distribution and cell position match the ground truth (circle). The fitting is plotted w.r.t. the unit-length recording probe with markers depicting input layers in A (see method 3.1.3). D. Fitted transmembrane currents and LFP Green's function w.r.t. input at each input layer at low (top, 10.0 Hz) and high (bottom, 199.3 Hz) frequency. Green's function is normalized to a unit norm at each input position, and the real part is plotted. The transmembrane currents' LFP profile is much more localized at higher frequencies. ($n = 100$) E. Fitted input currents distribution and its contribution to LFP with regard to input at each input layer. The FF simulations ($n = 100$) consist of randomly weighted neurons from the same dataset at $r = 1000\mu$m (unscaled) and are fitted with a single cell template or the average cell template. Both the input current distribution and its LFP profile are normalized to a unit norm at each input position. F. The fitting error plot against the similarity between the template used for fitting and the randomly mixed Green's function. Color depicts the input layer of FF simulation.

recording range because more alternative solutions would give rise to similar LFP recording patterns.

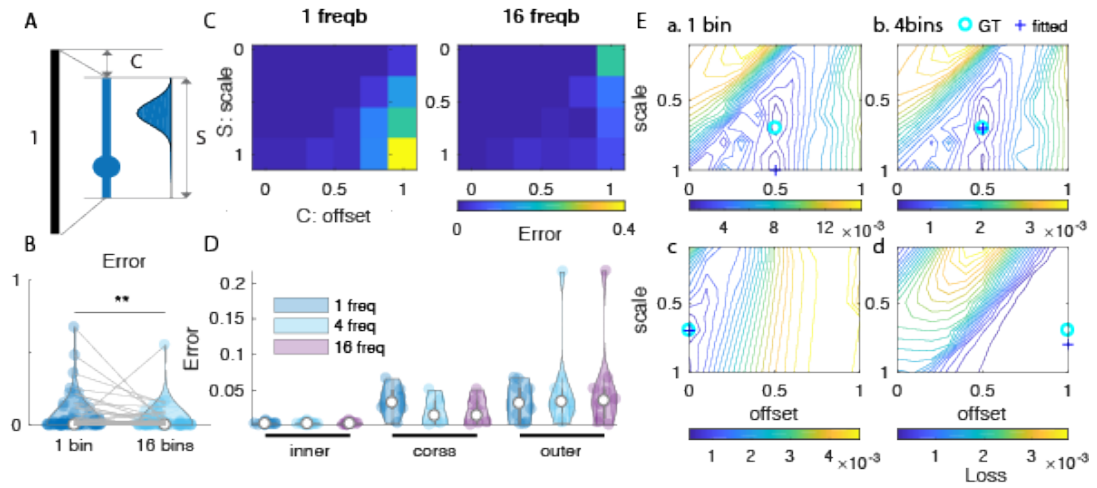

Figure 3.8: Demonstration of Green's Function Fitting: Effect of Cell Positions. A. Schematic of how to parameterize the current distribution by unit length current scaled with S and shift with offset C, w.r.t. unit length linear probe. B. Error of fitting with one frequency band is compared to fitting with 16 frequency bands ($n = 24$, $^{**}p = 0.019$). C. Fitting errors with single or multiple frequency bands are shown according to the offset and scale of FF simulation. D. Fitting error with different frequency bins grouped by cell position within, crossing, or outside of the unit length probe reporting range. E. Example optimization landscape for 1 frequency bin (a) or 4 frequency bins (b-d). a, b. Example fitting of FF simulation crossing the recording range. Fitting with one frequency bin in (a) has multiple local minimal, while fitting with 4 bins in (b) reduces the spurious local minimal. c. There is a clear global minimal when the input profile is within the recording range. d. When the input profile is outside of the recording range, the fitting fails because the optimization landscape is too flat.

3.4 Discussion

To summarize, we revisit the compartmentalized Green's function method for multi-compartment model forward simulation. By implementing and comparing different forward modeling methods, both on the level of membrane potential and LFP, we demonstrate that compartmentalized Green's function method effectively captures the spatiotemporal response pattern of the passive neural dendritic tree. Alongside the linear separatable properties in the frequency domain, the feed-forward Green's function framework would also speed up simulation by replacing the integration with frequency domain linear multiplication. Replacing the dendritic integration with some simpler kernel formulation has been developed and discussed recently (Hagen et al., 2022). In practice, it provides an easy and

fast estimation of how complex cytoarchitecture affects recorded LFP signals. One step further than forward modeling, we proposed a model to infer anatomical properties and distribution of input currents from impulse response based on laminar Green's functions.

The question we are interested in is how to effectively construct a biophysical model that connects the synaptic integration with laminar LFP recording for the purpose of probabilistic inference. We have demonstrated the utility of Green's function model in passive neuron settings. Amongst all the factors modulating synaptic integration, distance-dependent resistance change and capacitance change could bring interesting local effects. However, as a linear effect, it could be directly accounted for by the Green's function (Tuckwell, 1988). The progressive increase in synaptic conductance with distance from the soma could also be directly formalized into the linear multiplicative weight of synaptic distributions (Magee & Johnston, 1997).

However, it has been suggested that multiple active mechanisms participate in signal processing along dendrites (Magee, 2000). In the following section, we'd briefly discuss their impacts and suggest how to further incorporate them into modeling.

3.4.1 Nonlinear Effects

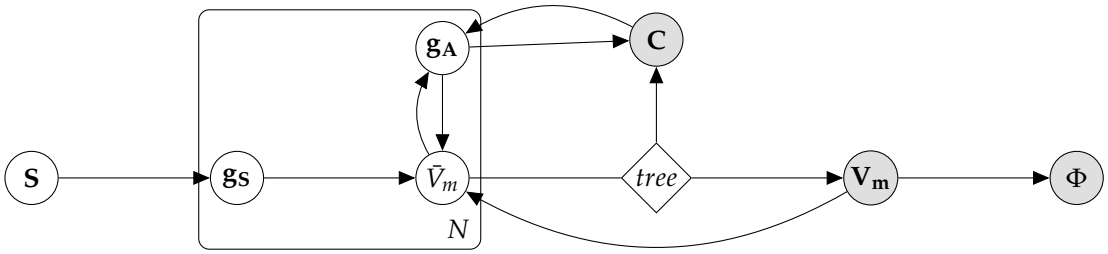

Figure 3.9: Schematic of the simplified mechanistic LFP model based on the microscopic level neural signals. **S** stands for the upstream inputs to local networks. The post-synaptic conductance $\mathbf{g_S}$ response to their corresponding neurotransmitter and changes local membrane potential V_m. The change of V_m together with the calcium concentration **C** influence a consecutive response of voltage- and ligand-regulated active conductance $\mathbf{g_A}$. The calcium concentration **C**, also confined by the intercellular mechanisms, is much more complicated and usually has a slower time constant compared to the passive mechanism, hence being modeled in parallel. The N plates denote the compartmentalization by common inputs. The $\bar{V}_m$ is introduced here for computational convenience. LFP Φ is then generated by the transmembrane currents, which is determined by membrane potential V_m.

Active Na^+ and K^+ dependent conductance play important roles in shaping

the dendritic computation (Magee et al., 1998, Cash & Yuste, 1999). Here we just name a few with typical spatial profiles affecting the electrical response patterns of the dendrites. Na^+ channels are uniformly distributed throughout the dendritic arbor (Magee, 2000). Besides voltage-gated channels, the ratio between the fast AMPA receptor and the slower voltage-dependent NMDA receptor variate according to the distance from the soma, regulating the dendritic excitatory postsynaptic potentials (EPSP) response pattern (Nicholson et al., 2006). On the other hand, the impact of active Na^+ channels is compensated by active K^+ channels (Cash & Yuste, 1999). The density of A-type K^+ channels on dendrites increases according to the distance from the soma, generating outward current and regularizing the dendritic excitability (Hoffman et al., 1997). I_h current, produced by Hyperpolarization-activated cyclic nucleotide-gated (HCN) channels, also increases from the soma to the distal apical dendrites in CA1 pyramidal neurons as well as cortical pyramidal neurons (Magee, 1998). It acts as a slow component to dampen dendritic excitability (Magee, 1998) and plays an important role in dendritic resonance (Hu et al., 2009, Stark et al., 2013).

The function of active channels in shaping the EPSP profile depends on the precise channel distribution of the cell, and it could be modeled as current inputs on top of passive neuronal dendritic trees (fig.3.9). In practice, many of the active currents could be linearized, which yields a quasi-active description of active channels (Koch, 1984, Wybo et al., 2015). While in general, resonance, which also takes a large part of nonlinear cell response, could be implemented by a bandpass linear filter term in each compartment, as far as the density is known, and this could be further fitted as an extra term (Coombes et al., 2007, Hutcheon & Yarom, 2000, Cook et al., 2007).

The Ca^{2+} is another important mechanism that regularizes signal processing in dendrites (Gasparini et al., 2004). The Ca^{2+} signals are mediated by influx through both NMDA receptors and voltage-gated Ca^{2+} channels (VGCCs). It regulates multiple active conductances, participate in synaptic plasticity (Magee & Johnston, 1997, Bi & Poo, 1998), and nonlinear dendritic processing, e.g., associate with local dendritic Na^+ spikes when inputs are concurrently activated. The intracellular Ca^{2+} homeostasis is regularized and compartmentalized by endoplasmic reticulum (Karagas & Venkatachalam, 2019), which makes the modeling much more complex (Borg-Graham, 1999, Hay et al., 2011).

Increasing evidence has converged to show that functional relevant compartmentalization (Losonczy & Magee, 2006, O'Hare et al., 2022, Otor et al., 2022) determined by channel distribution and dendritic morphology serve as computational units. Therefore, we propose to process these active conductances in functional dendritic subunits (Polsky et al., 2004), denoted by the N plates with local membrane potential $\bar{V}_m$, and potentially in some slower time scale compared to the passive dendrites, while modeling their LFP contribution according to the passive dendritic tree with $\mathbf{V_m}$. Membrane potential dynamics for each plate in

this nonlinear case could be very complicated, but the LFP pattern would likely be captured by a limited number of kernels (Głąbska et al., 2016). Volterra series or Gaussian process methods could also account for higher-order nonlinear terms in the impulse-response transfer function (Wybo et al., 2015, Turner & Sahani, 2014). In terms of biophysical parameter fitting and compartmentalization, previous works have demonstrated the usage of a multi-objective cost function to reduce the dendritic compartments while keeps multiply key features of their somatic and dendritic firing (Keren et al., 2005). How to optimally compartmentalize the neuron dendrites would be a very interesting topic in the future.

Chapter 4

Biophysics Based Source Separation

Local field potential, compared to EEG recordings, shows a spatial profile shaped by the morphology of local neurons, the ion distribution, and their synaptic distribution next to the recording sites (Gold et al., 2006, Einevoll et al., 2013, Łęski et al., 2013, Næss et al., 2021). The feed-forward model of LFP generated by the local neuron population is comparably well studied (Lindén et al., 2014).

In the previous chapter, we present a model that connects the microscopic postsynaptic activity to the macroscopic population level local field potential. The model is based on the frequency domain transfer function of the passive neural membrane cable model. That is to say, the model aims to capture the fast first-order linear response of the neural membrane, which means, compared to a simple dipole model describing the far field potentials, this model will effectively capture the dipole shape field potential generated by current injection at any arbitrary point of dendrites.

Motivated by the previous chapter, we explore the possibility of adding the biophysical constraints as a prior into the probability model of LFP and helping to separate the sources in the frequency domain. Frequency domain signal separation is widely applied, especially in the signal processing community (Adali et al., 2008, Anemüller et al., 2003). As with many other methods, it comes with blessings and curses. In general, frequency domain time-frequency representation or spectrogram formalization allows for spatial-temporal pattern recognition. It connects to the temporal patterns separation, e.g., empirical mode decomposition (Huang et al., 1998, Lopes-dos Santos et al., 2018, Mijović et al., 2010), spatial-temporal ICA (Głąbska et al., 2014) or probabilistic time-frequency analysis (Turner & Sahani, 2014, Song et al., 2021), which resolves the underdetermined source separation problems, where recording sites is less than the potential number of sources. But at the same time, accurate estimation of time-frequency representation is still an unresolved problem due to Heisenberg–Gabor uncertainty principle (Moca et al., 2021), and noise (Mitra & Pesaran, 1999). Grouping components from different frequency bands requires prior knowledge

about the wave-shape and signal patterns (Anemüller et al., 2003, Sirota et al., 2008). But since time-frequency representation allows for sparse and unbiased signal representation (as we'll discuss in the following sections), and it's easy to incorporate the prior knowledge of dendritic transfer function, we set off formalizing signal separation in the frequency domain.

Biophysical constraints help to separate highly correlated signals by utilizing the spatial profile separated in independent frequency bands. We propose a method to cluster the components with the help of biophysical modeling. We further formalize the biophysical constraints into a probabilistic model and show how to separate components by maximizing the neg-entropy. In the simulation of passive neurons, it helps to cluster and refine the components. In the real data, we show frequency domain LFP components clusters represent pathway-specific signals.

4.1 Source Separation Model

4.1.1 LFP Source Mixing in Frequency Domain

The impulse response of neuron is described by the neural cable theory (Rall, 2011). According to the Kirchhoff's current law (Dayan & Abbott, 2001, Sterratt et al., 2011b, Carnevale & Hines, 2006), The cable equation is written as:

$$2\pi\omega C_m \frac{\partial V}{\partial t} = g_l(E_l - V) + g_a \frac{\partial^2 V}{\partial x^2} + \mathbb{I}_j, \tag{4.1}$$

When passive membranes are considered, the dendritic responses would be linear and time-invariant.

As one can appreciate from the cable equation4.1, the spatial pattern of the neuronal response evolves with time. In other words, here, the space and time are not independent (Gratiy et al., 2011), instead of the commonly assumed spatial-temporal independent response pattern (Makarov et al., 2010) or spatially fixed rank-1 response pattern (Głąbska et al., 2016) (signal X_i could be composed by rank-1 vectors A_i, S_i, written as $X_i = A_i' S_i$. The dependency is induced by the interplay of axial current (spatial Laplacian) and trans-membrane resistor–capacitor-currents.

On the other hand, when transformed into the frequency domain, the convolutionary neuronal response becomes multiplicative, which means in the frequency domain, the impulse response is a rank-1 matrix of space and time. This could be seen in the frequency domain cable equation:

$$i2\pi\omega C_m \tilde{V} + g_l \tilde{V} - g_a \frac{\partial^2 \tilde{V}}{\partial x^2} = \tilde{I}_j, \qquad s.t. \qquad \tilde{V} = (i2\pi\omega C_m + g_l I - g_a \nabla^2)^{-1} \tilde{I}_j. \tag{4.2}$$

The spatial pattern in the right-hand side of equation4.2 varies across frequency. This corresponds to the time-dependent spatial pattern in the temporal domain. It

would also induce a low-pass effect of membrane signal to add to the power-law effect observed in extracellular recording (Pettersen et al., 2014, Gratiy et al., 2011).

The frequency domain formulation resembles the linear separation of ICA $X = AS$, where the mixing matrix A correspond to the spatial input-response pattern and S to the input activity $\tilde{I}_j$. On the other hand, brain communication usually exhibits specific frequency patterns (Mizuseki et al., 2009, Bastos et al., 2015).Therefore we are seeking to separate the signals in the frequency domain.

The separation in the frequency domain is a general result, and it applies to both membrane potentials as well as extracellular recordings. As we have shown in equation 3.5 in the Green's function section, the extracellular potential, generated by the trans-membrane currents, is a spatial-dependent linear transform from the membrane potential. That means it's also just a linear combination of input-response patterns in the frequency domain and could be separated into $\tilde{\Phi} = \sum \tilde{\Phi}_j \tilde{I}_j$.

4.1.2 Complex ICA use Entropy Bound Minimization

To perform the decomposition, we first need to select a proper cost function (Comon, 1994). There's plenty of evidence showing the neuronal activity in the brain is skewed (Buzsaki & Mizuseki, 2014). Therefore we use independent component analysis to explore the non-Gaussian nature of the signal (Hyvärinen & Oja, 2000).

Complex ICA is closely related to real ICA but has a richer family of possible probability density functions. ICA based on maximum-likelihood estimation, information maximization, negentropy, or non-Gaussianity maximization is intimately related (Cardoso, 1998, Adali et al., 2008). Still, the performance would depend on the nonlinear functions used in density matching. Therefore here we use the complex ICA by entropy bound minimization (ICA-EBM) (Xi-Lin Li & Adali, 2010), which is based on the principle of maximum entropy. The pdf of a complex random variable is defined through the joint density, consider the mapping $\mathbb{C}^N \mapsto \mathbb{R}^{2N}$ such that $\bar{s} = \bar{W}\bar{x}$ where $\bar{x} = [x_R^T, x_I^T]^T$ and $\bar{W} = \begin{bmatrix} W_R & -W_I \\ W_I & -W_R \end{bmatrix}$ since $W = W_R + jW_I$. By the computation of Jacobian as

$$p_X(x) = |det(\bar{W})| p_S(Wx) \tag{4.3}$$

where $p_S(Wx) = p_S(s) = p_S(s_1, s_2, ..., s_N)$. Therefore, the mutual information is given as equation 1 in (Xi-Lin Li & Adali, 2010):

$$I(s_1; ...; s_N) = \sum_{n=1}^{N} H(s_n) - log|det(\bar{W})| - H(X) \tag{4.4}$$

where according to the definition, $det(\bar{W}) = det(WW^H)$ makes $log|det(\bar{W})| = 2log|det(W)|$. $H(x) := -E(log(p(x_R, x_I)))$ stands for the entropy of x.

In the complex ICA-EBM, entropy is estimated by bounding the entropy of estimates. Instead of directly estimating the $H(s)$, it is approximated by finding the maximum entropy distribution as the entropy bound. Henceforth, maximizing the independents is obtained by minimizing mutual information between independent sources s_n to minimize the entropy bound we found in the first step. The maximum entropy estimation finds the best approximation for the underlying distribution, and the entropy bound minimization pushes the sources as independent as possible.

Two types of entropy bound is used, accounting for two widely used families of bi-variate distributions. In the Entropy Bound I, a linear decomposition $[s_R, s_I]^T = W[u, v]^T$ is considered, where W is a 2×2 nonsingular matrix, and $[u, v]$ are a pair of zero mean random variables since s is zero mean. The upper bound for $H(s)$:

$$\begin{aligned} H(s) &= log|det(W)| + H(u, v) \\ &\leq log|det(W)| + H(u) + H(v) = H^{[bound,I]}(s, W) \end{aligned}$$

where the equation holds iff u and v are statistically independent and the bound is uniquely determined by B. In the Entropy Bound II, the decomposition $[s_R, s_I]^T = W[u, v]^T = Wr[cos\theta, sin\theta]^T$ is considered where r and θ are the magnitude and the argument of $u + jv$, respectively, leads to the entropy bound:

$$\begin{aligned} H(s) &= log|det(W)| + H(u, v) \\ &= log|det(W)| + E[logr] + H(r, \theta) \\ &\leq log|det(W)| + E[logr] + H(r) + H(\theta) \\ &\leq log|det(W)| + E[logr] + H(r) + log(2\pi) \\ &= H^{[bound,II]}(s, W) \end{aligned}$$

where the first equality hods iff r and θ are statistically independent, and the second one holds if θ is uniformly distributed in $[-\pi, \pi)$, i.e., $u + jv$ is circular. The $H^{[bound,II]}(s, W)$ again is uniquely determined by W.

To determine the bound for $H(u)$, $H(v)$, and $H(r)$, similar to the idea of variational inference, complex ICA-EBM seeks to find a distribution q best describes the underlying distribution from a wide range of bi-variate distributions summarized by a set of functional forms. By whitening and constraining the demixing vector for each source to be unit length, i.e., $E[u] = E[v] = 0$, $E[u^2] = E[v^2] = 1$, $E(G_1^I(u)) = \mu_{G_1}^I$ and $E(G_2^I(v)) = \mu_{G_2}^I$, where $G_1^I(u)$ and $G_2^I(v)$ are the measuring functions captures the higher order moments of non-Gaussian distributions. Since $q(s_R, s_I) = \frac{1}{det(W)} q(u)q(v)$, the maximum entropy distribution q of Entropy Bound I could be constructed in the general form of $q(u) = A_1 exp[-a_1 u^2 - b_1 u - c_1 G_1^I](u)$

and $q(v) = A_2 exp[-a_2 v^2 - b_2 v - c_2 G_2^I](v)$. The Entropy Bound I is thus written as:

$$\begin{aligned} H^{[bound,I]}(s,W) =& log|det(W)| + log(2\pi e) \\ & - V_1^I \left\{ E\left[G_1^I(u) \right] \right\} \\ & - V_2^I \left\{ E\left[G_2^I(v) \right] \right\} \end{aligned}$$

where $V_1^I \left\{ E\left[G_1^I(u) \right] \right\}$ and $V_2^I \left\{ E\left[G_2^I(v) \right] \right\}$ are neg-entropy, they could be numerically calculated and would never be negative. The optimization of Entropy Bound I is a weighted linear combination of two statistical independent variable u and v, hence the distribution it gives belongs to the family of weighted linear combination distribution (Johnson & Tenenbein, 1981). Similarly the Entropy Bound II is also defined with a $q(r)$ whose $E(r) = 1$, $E(r^2) = 2$ and $E(G^{II}(r)) = \mu_G^{II}$, therefore $q(r) = A_3 r exp[-a_3 r^2 - c_3 G^{II}(r)] I(r \geq 0)$. The bound would be

$$\begin{aligned} H^{[bound,II]}(s,B) &= log|det(W)| + log(2\pi e) - V^{II}(\mu_G^{II}) \\ V^{II}(\mu_G^{II}) &= 1 + log A_3 - 2a_3 - c_3 \mu_G^{II} \end{aligned}$$

Among all these possible entropy bounds, the tightest one is used as the final estimate of $H(s)$, i.e.,

$$\begin{aligned} H_{k_1,k_2}^{[bound,I]}(s) &= \min_W H_{k_1,k_2}^{[bound,I]}(s,W) \\ H_k^{[bound,II]}(s) &= \min_W H_k^{[bound,II]}(s,W) \\ \hat{H}(s) = min(\min_{1 \leq k_1,k_2 \leq K^{[I]}} & H_{k_1,k_2}^{[bound,I]}(s), \min_{1 \leq k \leq K^{[II]}} H_k^{[bound,II]}(s)). \end{aligned} \tag{4.5}$$

The entropy bound is given by comparing the density matching over several potential families of distributions (analog to functional in variational methods, see Appendix), which accounts for various possible distributions.

Complex ICA is performed on wavelet-transformed data. In contrast to sources in EEG or MEG recording (Anemüller et al., 2003), LFP is dominated by local dipoles. Assuming a slow plasticity rate of the synapses results in a static spatial loading and a consistent change of components' spatial loading according to their frequency bands. In other words, each local component will have a share in all the frequency bands, and the spatial loading at each frequency band is similar, as illustrated in figure 2. Here in the simulation, the source activity tiles the entire spectrum, and the corresponding LFP components appear in all the frequency bands. But in reality, the source activity usually reflects large local synchronized activities and thus typically oscillates within specific frequency bands (Sirota et al., 2008). Complex ICA could be applied to each frequency band independently and grouped with post-hoc clustering methods (Anemüller et al.,

2003). If one assumes a constant frequency pattern, which implies a constant ratio across all the frequency bands, then frequency-embedding could be applied on windowed data (Sirota et al., 2008). Here we want to keep the method as flexible as possible such that 1) it deals with continuous activity and 2) it doesn't assume any temporal pattern apriori. Henceforth due to the frequency-dependent term in the input-response4.2, we decide to decompose the signal at each frequency and, at the same time, optimize the components coming from the same pathways according to the reconstructed Green's function, which would be discussed in the following section.

4.1.3 Complex Component Extraction Regularized by Biophysical model

Here we propose to bring the biophysical model to bridge the components in different frequency bands. Briefly speaking, we are trying to find for each frequency f_i a set of complex components $S^{fi} = W^{fi}X^{fi}$ that are independent of each other and match a set of input current distributions y_j that are shared in all frequencies. This writes as:

$$L = \sum_i (I(s_1^{fi};...;s_N^{fi}) + \sum_j^N \alpha |A_j^{fi} - \tilde{G}_j|_{Fro}^2) \tag{4.6}$$

$$= \sum_i (\sum_{n=1}^N H(s_n^{fi}) - \gamma log|det(\bar{W}^{fi})| - H(X^{fi}) + \alpha \sum_j^N |A_j^{fi} - \tilde{G}_j|_{Fro}^2) \tag{4.7}$$

The independence of components at f_i is obtained by minimizing mutual information I^{fi} between independent sources S^{fi} according to equ.4.4. For the biophysical model, we assume for the source activities we want to separate, and there exists more than one observable frequency band F_I (in terms of discrete frequency bands in spectrogram) that they are independent or their occurrence is sparse. Notice the assumption is normally fulfilled in electrophysiology recordings where information is transferred in broad frequency bands. On the other hand, this assumption is, in fact, a necessary but not sufficient condition for independence in temporal domain (Zhang & Chan, 2006), which has been explored to enhance the sparsity of signal separation by extracting subband independent components when the Independence assumption is not fulfilled with adaptive filter (Cichocki & Amari, 2002, Tanaka & Cichocki, 2004, Zhang & Chan, 2006) or wavelet decomposition (Kisilev et al., 2003). Notice here the assumption of the adaptive filter doesn't hold since the mixture matrix depends on frequency because of the cable effect. Therefore, we separate signals on each frequency band of the wavelet transformed coefficient, respectively.

In the second part, we use biophysical models as a constraint to group components from different frequencies and enhance separation on dependent frequency

band F_D. Blind source separation in biomedical data typically faces the problem of feature selection and overfitting, which would hopefully be helped by incorporating biophysical models as constraints (Makeig et al., 2012). As discussed in the last chapter, we propose to use Green's function of multi-compartment cells as a prior of the mixing matrix.

The concerns come in two folds. First of all, the impulse response of neurons typically has a multi-pole shape due to the cable effect, which would be easily captured by linear operation with Green's function basis. The basic Green's function basis is easily adaptable to any brain areas of interest by finding example cells in the target region from the online neuromorphic dataset. Then there comes the second concern, because of the heterogeneity of neurons, which will almost surely bring variation to the impulse response. To keep the method as general and robust as possible, we don't want to rely too much on Green's function basis of selected neurons. Therefore, we add this as a regularization term instead of using Green's function basis to fit the signal like in previous work (Gratiy et al., 2011). This regularization term is guaranteed to be positive, except for when the input is exactly generated by some linear transform of the Green's function basis. In that case, this regularization term is guaranteed to be zero. Another advantage of this formulation is to separate the optimization of temporal independence from approximating the component with a potential biophysical plausible pattern. This way, the loss function L could easily be optimized in a parallel manner.

The other way to look at the biophysical-based constraint, as we design it, is to think of that in a constrained optimization problem, where:

$$min \qquad L = \sum_i I(s_1^{fi};...;s_N^{fi}) = \sum_i (\sum_{n=1}^{N} H(s_n^{fi}) - \gamma log|det(\bar{W}^{fi})| - H(X^{fi}) \tag{4.8}$$

$$s.t. \qquad A^{fi} = inv(\bar{W}^{fi}), \qquad \forall j, \exists \tilde{G}_j, \qquad s.t. \quad A_j^{fi} = \tilde{G}_j \tag{4.9}$$

Which says the whole signal is assumed to be a mixture of some components or pathways with impulse response $\tilde{G}_j$, whose inverse $\bar{W}^{fi}$ will unmix the signal and render the most mutually independent activities for each of the pathways. With this formulation, it's clear that equ.4.6 is just the Lagrangian function of equ.4.8 where α is the corresponding Lagrange multiplier.

Apart from the biophysical feasibility of the template, we also have some technique concerns when we design the constraint term. Like the real domain ICA, the complex domain ICA also suffered from the indeterminate phase of the component. We use the squared Frobenius norm between normalized components and their aGFs. On the one hand, it measures the difference between each normalized component A_j^{fi} and the best possible approximate Green's function $\tilde{G}_j$ (aGF) by fitting to the cluster of components, respectively. We could easily see that this measure is equivalent to the log-likelihood of observing A_j^{fi} with the

generative model of:

$$A_j^{fi} = \tilde{G}_j + \epsilon, \qquad where \qquad \epsilon \sim \boldsymbol{CN}(0, \sigma I_n) \tag{4.10}$$

Since the entropy of each source is $H(S_j) := -E(log(p(S_j)))$, then to add the spatial prior of S_j is $-log(p(\epsilon)) = \gamma |A_j^{fi} - \tilde{G}_j|_{Fro}^2$, where $\gamma > 0$ is a constant that also accounts for the effect of noise variance σ. On the other hand, the squared Frobenius norm could also align with the complex ICA neg-entropy optimization algorithm and could be easily optimized based on Wirtinger calculus (Adali et al., 2008).

In previous ICA works, adding regularization to the ICA has been used to incorporate prior knowledge to the blind source separation (Cichocki & Georgiev, 2003). This is also closely related to the regularizes used in dictionary learning, but normally the prior is put on every entry of the mixing matrix, like l_1 or l_2 or more complex l_{1-2}. Our prior is composed of biophysically plausible models, which are inherently characterized by their dipole shape and smooth loading. Notice, here again, we are just proposing one potential way to compute the spatial prior, or kernel of the LFP transfer function, but this could also be achieved by simulation (Hagen et al., 2018; 2022).

In practice, the gradient of the spatial constraint is calculated as the following. Considering the entropy estimator is given in equ.4.6 and the constrain that $|\bar{W}_n^{fi}| = 1$, the cost function leads to the following constrained optimization problem,

$$min \qquad L = \sum_i (\sum_{n=1}^{N} H(s_n^{fi}) - \gamma log|det(\bar{W}^{fi})| - H(X^{fi}) + \alpha \sum_j^N |A_j^{fi} - \tilde{G}_j|_{Fro}^2) \tag{4.11}$$

$$s.t. \qquad ||\bar{W}_n^{fi}|| = 1. \tag{4.12}$$

where $s_n = w_n^H x$. The detailed derivative of the gradient of entropy bound could be found in complex-EBM algorithm (Xi-Lin Li & Adali, 2010), here we simply list out the gradient of the biophysical constrain $L_p = \sum_i \sum_j^N |A_j^{fi} - \tilde{G}_j|_{Fro}^2$ as in equ.4.11.

$\frac{\partial L_p}{\partial \bar{W}^{fi*}}$ is written as follow:

$$\begin{aligned}
\frac{\partial J}{\partial \bar{W}^{fi*}} &= \frac{\partial tr((A^{fi}-\bar{G})(A^{fi}-\bar{G})^H)}{\partial \bar{W}^{fi*}} \\
&= \frac{\partial \left[tr(A^{fi}A^{fiH}) - tr(\bar{G}A^{fiH}) - tr(A^{fi}\bar{G}^H)\right]}{\partial \bar{W}^{fi*}} \\
&= \frac{\partial \left[tr(A^{fiH}A^{fi}) - tr(A^{fiH}\bar{G}) - tr(\bar{G}^H A^{fi})\right]}{\partial \bar{W}^{fi*}} \\
&= \frac{\partial \left[tr(\bar{W}^{fi-H} iP^{fiH} A^{fi}) - tr(\bar{W}^{fi-H} iP^{fiH}\bar{G}) - tr(\bar{G}^H iP^{fi}\bar{W}^{fi-1})\right]}{\partial \bar{W}^{fi*}} \\
&= \bar{W}^{fi-H}\left[iP^{fiH}(A^{fi}-\bar{G})\right]\bar{W}^{fi-H}
\end{aligned} \tag{4.13}$$

where iP^{fi} is the inverse of the Eigen matrix given by PCA of the original covariance matrix. H indicates the complex conjugate transpose. Henceforth, we have $A^{fi} = iP^{fi}\bar{W}^{fi-1}$, and it maps lower dimensional signal space back to the original space. Here we ignore the ω for convenience.

4.2 Algorithm and Results

4.2.1 Overview of the Biophysically Constrained Method

In fig.4.1 we show the workflow of the algorithm. The algorithm takes multi-electrode recording time series as input (fig.4.1 B).

We first apply complex wavelet transformation (CWT) to each channel and get a 3 way tensor of the size $N_{channel} \times N_t \times N_\omega$, where $N_{channel}$ is the number of recording sites on the linear shank, N_t is the number of time points, and N_ω is the number of frequencies. Complex ICA is then applied to each frequency, and here we get the unmixing matrix $W_{\omega i}$ and mixing matrix $A_{\omega i}$ for each frequency ωi (fig.4.1 D). We then cluster all the components from the mixing matrix $A_{\omega i}, i \in 1,...,N_\omega$ into N_clus clusters, written as $A_n^\omega, n \in 1,...,N_{clu}$ (fig.4.1 E). As we will discuss later, it's critical to find clusters with meaningful spatial loadings, especially in real data. We then fit the Green's function $\tilde{G}_n$ to each cluster A_n^ω, respectively. N_{clu} is generally larger than the number of components in each frequency, and we keep clusters with small average fitting lost (fig.4.1E red square).

The loss function contains the neg-entropy of the entropy classes and the loss of Green's function fitting (equ. 4.13). The mixing matrix is updated according to the loss function (equ. 4.11). If the change of the loss function is smaller than a given precision, then the best mixing matrix A_ω and unmixing matrix W_ω are kept, and the unmixed signal at each frequency is computed.

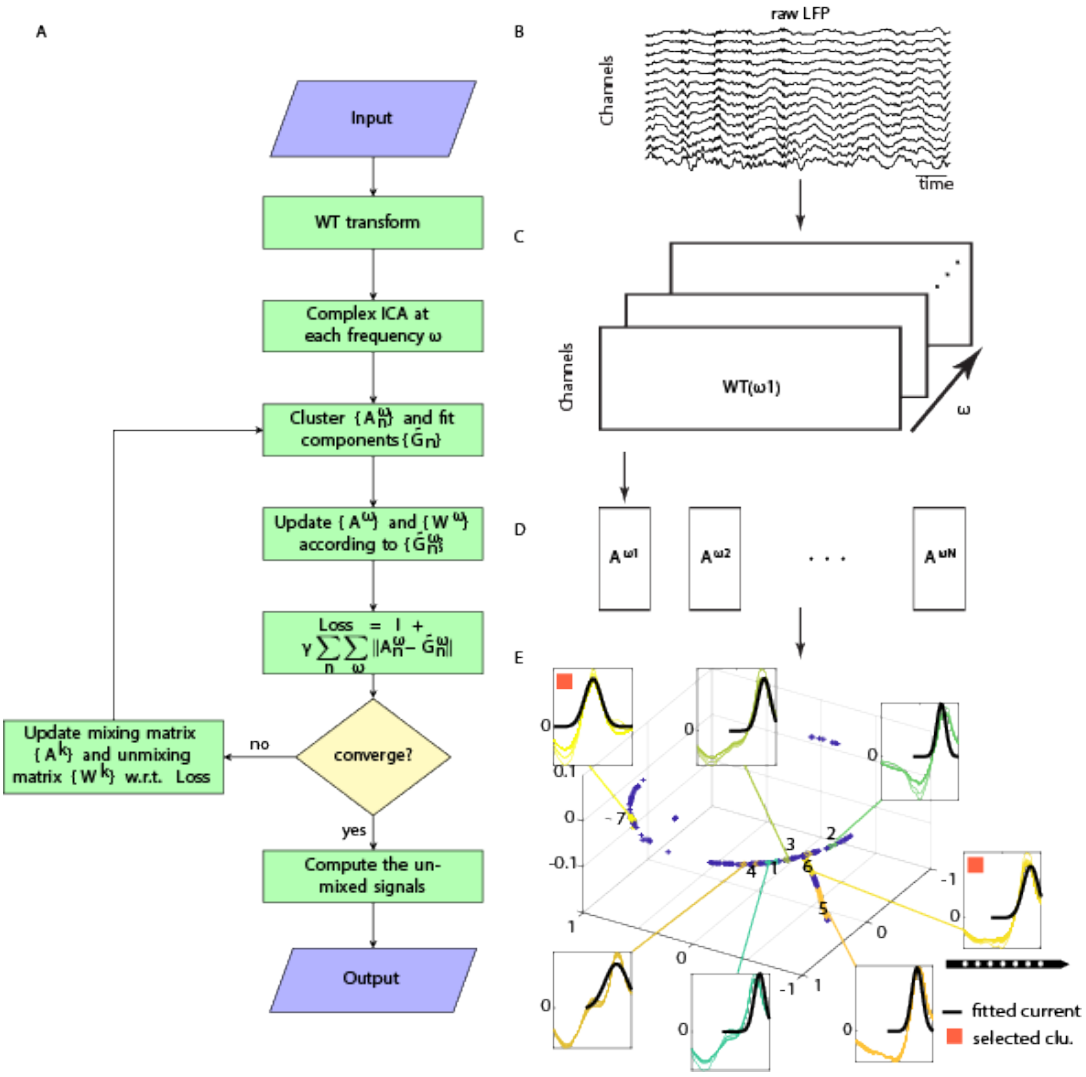

Figure 4.1: The workflow of the template-based complex ICA (tcICA) of the LFP signals. A. The workflow. A-D. The separation procedure was applied to raw LFP traces simultaneously recorded by a high-density multichannel silicon probe across the hippocampal CA1 layers in a single recording session. First, the complex morlet wavelet transform is applied to data B. Then, the wavelet signals C at each frequency ω were decomposed by EBM complex ICA in D. Components from all frequencies are pooled together and form clusters in E, each cluster has at most one component from each frequency. A Green's function $\tilde{G}_n$ is fitted to each cluster. Then every component is assigned to one cluster according to its spatial profile. After the assignment, the loss is computed according to equ.4.13, and the gradient is computed. When the separation fails at some frequencies, the component will be reinitiated with the fitted clusters. The process continues until it converges.

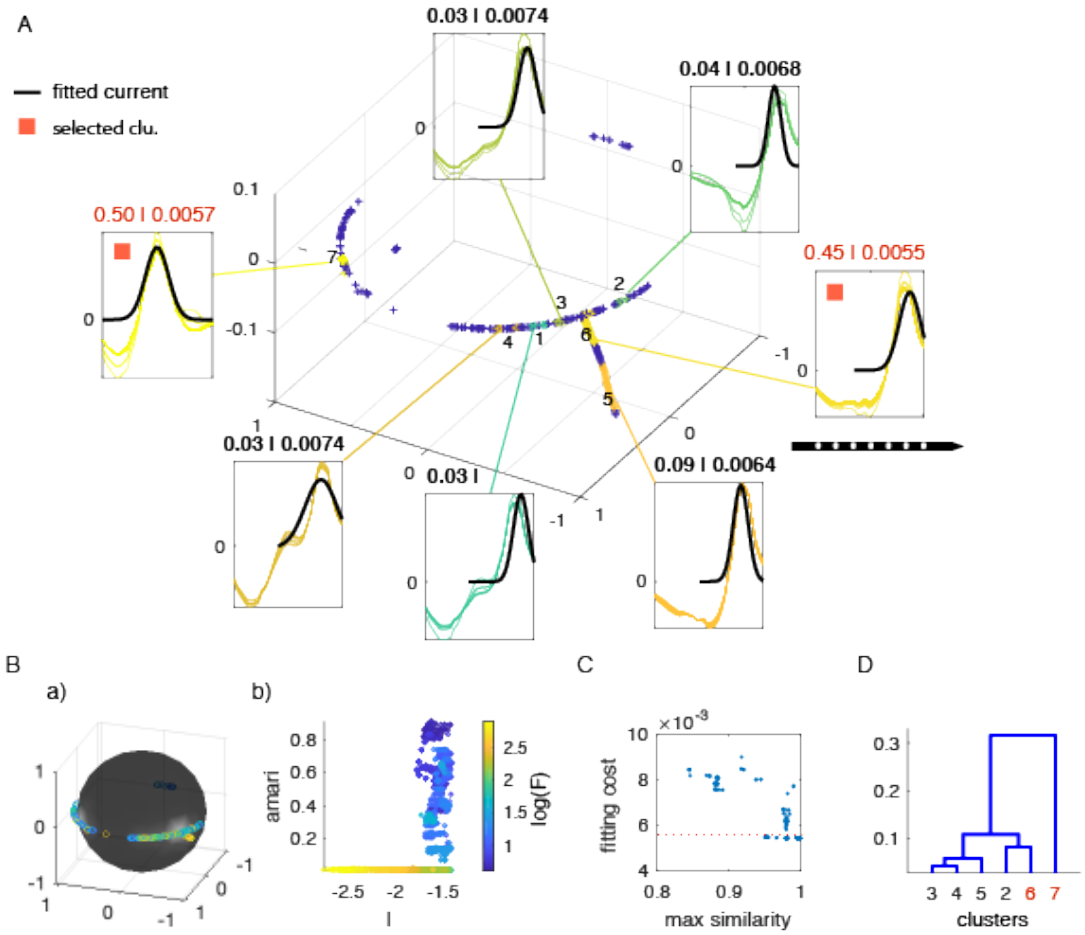

Figure 4.2: Clustering of complex components. A. The real part of normalized and aligned components are projected at their first 3 principal components. The indexes of the clusters shown next to them are the same as in D. Color indicates the result of clustering on the components. Their spatial profile is shown at the inset next to each cluster. The black line indicates the model fitting to the components. The red square shows the selected clusters. The number on the title of insets indicates $R_i|fittingcost$, where $R_i = \frac{N_i}{N_\omega}$ is the amount of frequency bands have components from this cluster i. B. a) The distribution of components' spatial profile. The probability density of the spatial profile on the ball is re-scaled according to its maximum value and colored on a grayscale. The original components is plotted on top of it, and the color indicates the frequencies they come from. b) The neg-entropy I plotted against the resulted Amari distance to the ground truth at each frequency, respectively. a) and b) share the same frequency scale. C. Clustering is reinitialized for 10 times, and the average model fitting cost for each of them is plotted against the similarity of each cluster to their closest ground truth component. The red dotted line is the threshold we use (.0058). D. Hierarchical clustering based on the distance between their centroids of the 7 clusters shown on A.

4.2.2 Clustering and Distribution of Spatial Patterns

Grouping components from different frequency bands have been an unsettled problem in the complex ICA studies (Anemüller et al., 2003). Here we cluster the components according to their spatial loadings (fig.4.2). All the components are normalized to unit variance and are rotated according to the largest absolute loading site. As we discussed in the last chapter, the impulse response of a passive dendrite is generally spatially localized around the input site, especially in the higher frequencies range. But notice this assumption would be violated if the synapses from the same input cover more than half of the membrane surface or if there is some special arrangement of membrane conductance. In terms of active conductance, when it's large enough to over-dominate the input currents, it would be classified into active local processes and treated as another source, e.g., action potentials around soma far away from the dendritic inputs.

There is generally three properties that define the LFP impulse response at each frequency, aka response kernel, the spatial pattern, the amplitude, and the phase. The input response to a unit step input is usually considered in a linear system. However, to simplify the computation, we use the normalized spatial pattern, i.e., normalizing the components' spatial loading to unit variance.

By normalizing the spatial loading, we are able to focus on the spatial pattern produced by the dendritic trees. And interestingly, we could capture the distribution of smooth impulse response by projecting them into a unit ball spanned by the first 3 principle components (fig.4.2 B.a) grayscale indicates the probability, here it's scaled by the largest probability). In the passive scenario, for example, the components show clear local peaks corresponding to pathways targeting different dendritic locations (fig.4.2 B.a) two peaks corresponding to the two selected components in fig.4.2 A, scatter plots shows $A_{\omega i}, i \in 1, ..., N_\omega$, the color of the scatter plots indicates ω according to the color bar shared in fig.4.2 B.b)). As discussed in the previous section, components from higher frequencies are more localized and cluster around the peak. The contaminated components sit between the clusters and share less probability because they are most likely not so consistent across frequencies as the independent ones. Nevertheless, when inputs are not independent, the spurious components will appear across multiple frequency bands and could even form small clusters (fig.4.2 A).

Components usually separate better in higher frequencies (fig.4.2 B.b)). The components are sparser and more separable in higher frequencies, resulting in smaller neg-entropy. But when it comes to lower frequencies in highly co-activation scenarios, lower neg-entropy doesn't necessarily indicate a better separation. Optimizing the entropy would result in contaminated components. However, clusters close to the ground truth usually better fit the biophysically based templates (fig.4.2 C). Therefore, we only keep component clusters below a threshold (.0058) of average fitting costs (threshold of fitting cost is possible

because we use the normalized components).

In practice, components form large contaminated clusters when inputs are highly co-activated, therefore we select clusters as separable as possible. To achieve this, we apply hierarchical clustering to the centroid of clusters (fig.4.2). Then a given number of clusters is selected according to their distance from each other.

To summarize, we propose multiple criteria to ensure stable clustering over multiple frequency bands. We cluster components A^{ω} based on the normalized spatial loading. The average cost of fitting and hierarchical clustering are used afterward to select meaningful components.

4.2.3 Sources Separation in Simulated Data

We then apply the algorithm to the simulation data, where the Schaffer collateral path and the perforant path are projected to the passive CA1 dendritic trees. To illustrate the result, we present an example separation in fig.4.3. The inputs are generated as a Poisson process with $coincidence = 0.2473$. The stimuli time series S_{stim} are then computed by integrating the binary spike trains with a time constant of $\tau = 2ms$ to proximate the synaptic currents used in NEURON simulation, which is generated by the double exponential function of $\tau_1 = .01ms$ and $\tau_2 = 2ms$ (fig.4.3 A). The Schaffer collateral path starts $500ms$ earlier than the perforant path.

The components separated by the ICA are contaminated in the high coincidence scenario (fig.4.3 B). We could also appreciate the contamination from the spatial profile of the separated components (fig.4.3 D. blue trace in lower panel) But the template-based method helps constrain the components' spatial loading and reduce the cross contamination (fig.4.3 C, E). It also vastly improves the separation of complex ICA by clustering the components and optimizing with spatial constraint (fig.4.3 F). The cross-contamination is computed as the IC activities explained by the integrated stimuli, i.e., $\frac{cov(\hat{S},S_{stim})}{cov(S_{stim},S_{stim})}$. This means for the perforant path ICA component, for example, apart from the stimuli of the perforant path, the Schaffer collateral path also helps to explain the activity with a coefficient of 0.3283. While for the perforant path tcICA component, apart from the perforant path stimuli, the Schaffer collateral path only helps to explain the activity with the coefficient of 0.0183. Therefore, each pathway's activities are mainly explained by its own stimuli.

tcICA reinitializes components according to their clusters and then optimizes with constraints according to the loss function (equ.4.6). To understand how the regularization affects the solutions, we apply tcICA with different hyper-parameters. The regularization hyper-parameter γ of $\gamma log|det(W)|$ is chosen from $\gamma = 10^{-3}, 10^{-2}, 10^{-1}, 1$. The regularization hyper-parameter α of $\alpha|A_j^{fi} - \tilde{G}_j|_{Fro}^2$ is chosen from $\alpha = 10^{-2}, 10^{-1}, 1, 10$. We simulated data with an average spike

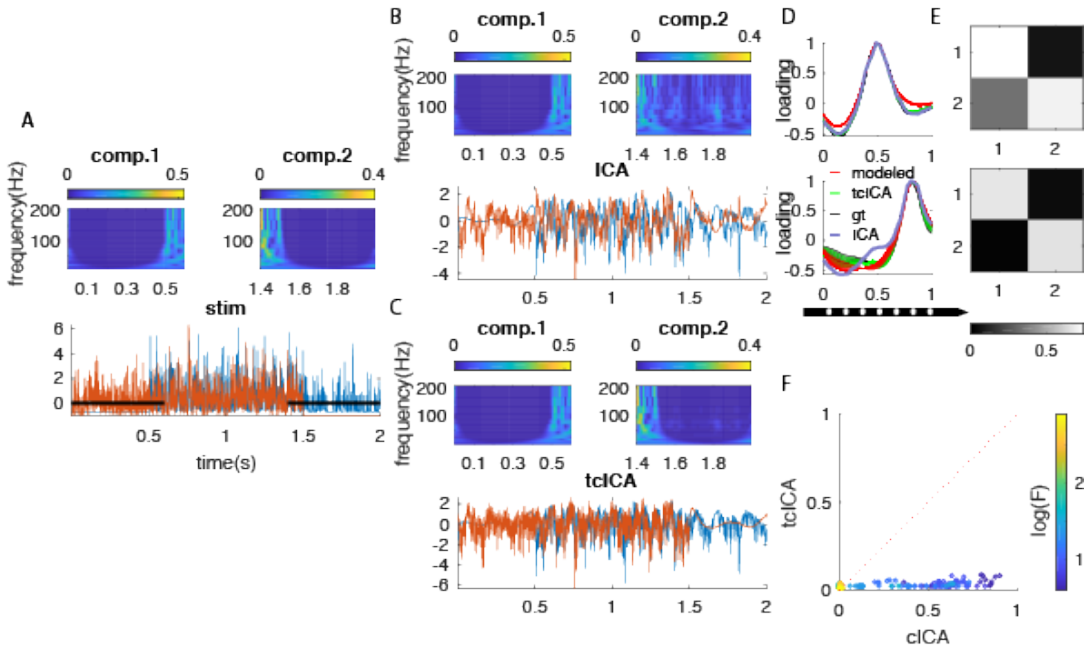

Figure 4.3: Comparison of ICA methods. Example separation on highly co-activated ($coincidence = 0.2473$) data. A. time series of two stimuli, the input of Schaffer collateral starts $500ms$ earlier than the perforant path and ends $500ms$ earlier as well. Their continuous wavelet transform (CWT) of the time series at the beginning and end of the simulation is shown on the upper panel and indicated by the thick black line on the lower panel. B. the time series of the independent components given by ICA, the components are flipped so that the largest absolute value loading is always positive. The components are aligned to the ground truth by their spatial loading. CWT of the two components is shown on the upper panel. C. same as B but with template-based complex ICA. D. The spatial profile of the components. Schaffer collateral component on the upper panel and perforant path component on the lower panel. The components at multiple evenly sampled frequency is shown. Red: model fitted to the tcICA components, green: the tcICA component, black: the ground truth, blue: the ICA component. E. the cross-contamination of the components. Upper panel: ICA, reads: $\begin{bmatrix} 0.7403 & 0.0597 \\ 0.3283 & 0.6991 \end{bmatrix}$ lower panel: tcICA, reads: $\begin{bmatrix} 0.6708 & 0.0409 \\ 0.0183 & 0.6591 \end{bmatrix}$. F. the Amari distance of ICA unmixing matrix with regard to ground truth at each frequency indicated by color. $x - axis$ is components by plain complex ICA, $y - axis$ is components by tcICA. dotted line indicates $x = y$.

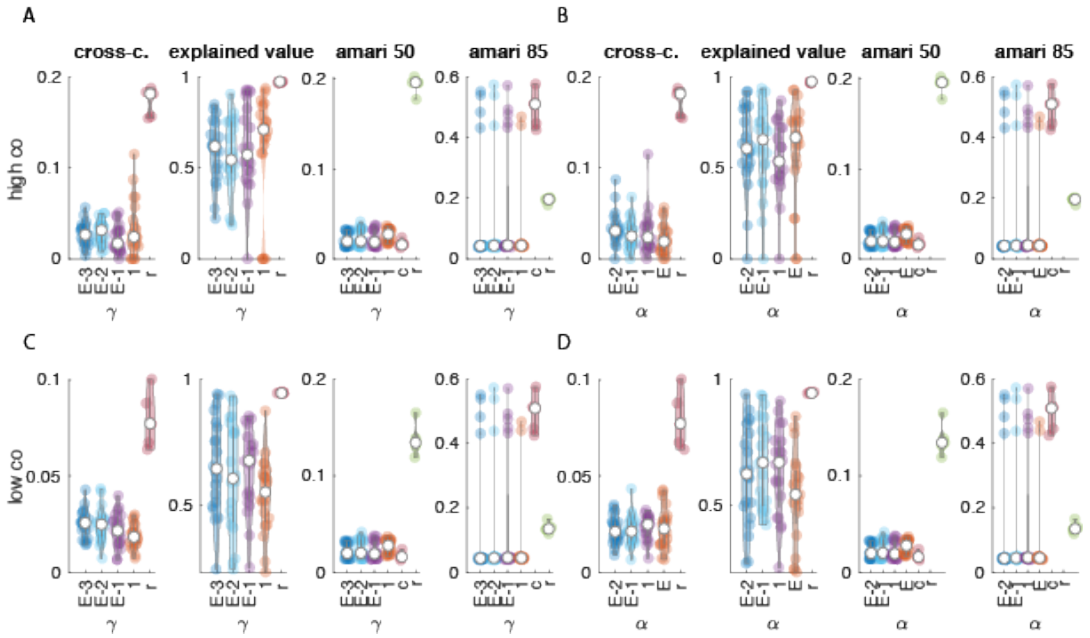

Figure 4.4: Optimization depends on the weighting of regularization. A, C.Effect of $\gamma log|det(W)|$ over pooled result for all the $\alpha|A_j^{fi} - \tilde{G}_j|^2_{Fro}$ for A: high co-activated data and C:low-co-activated data. To characterize the distribution, we plot the cross-contamination, the explained value by reconstructed inputs, and the 50% and 85% Amari distance of components over all the frequencies for each trail. The results of temporal ICA are plotted along with tcICA and labeled as "r" for "real". Amari distance for complex ICA is also plotted with "c". B,D. Effect of $\alpha|A_j^{fi} - \tilde{G}_j|^2_{Fro}$ over pooled result for all the $\gamma log|det(W)|$ for B: high co-activated data and D:low-co-activated data. The subplots are arranged the same as in A.

coefficient of 0.1750 ± 0.0096 for high-coincident data and 0.1003 ± 0.0165 for low-coincident data (fig.4.4). We find much less cross-contamination of tcICA compared to the temporal ICA (fig.4.4A-D, cross-c.). But at the same time, the explained value by the reconstructed stimuli is not as good as temporal ICA, partially due to the transfer between temporal and frequency domain (fig.4.4A-D, explained value.). The Amari distance, on the other hand, confirms that tcICA helps to reduce cross-contamination, especially in frequencies bands challenging to separate (fig.4.4A-D, Amari 50% for "easy" compared to Amari 85% for "difficult|. Temporal ICA r stays the same.). This shows the general effect of moving the components according to their clusters.

Apart from the clustering, the weights of regularization also affect the solutions depending on the input coincidence levels. We find that in the high-coincidence scenario, a larger α would help to add the impact of the spatial constraint (fig.4.4B). Slightly reduced $\gamma log|det(W)|$ would also allow the components to release the orthogonality constraint (fig.4.4 A). But in the low-coincidence scenario, orthogonality helps to reduce the cross-contamination (fig.4.4 C). According to the results, we choose $\gamma = 10^{-1}$ and $\alpha = 10^{-2}$ in the real data.

4.2.4 Source Separation in Real Data

We validate the complex ICA on the real data where optogenetic stimulation is given at contra-lateral CA3 areas.

Applying tcICA to the real data, we first need to decide the number of components. The real data is much more complex than the simulated passive neurons (fig.4.2B.a) two clusters). In the slower frequencies, low-pass filtering of the neural membrane and various slow nonlinear active processes like $[Ca^{2+}]$ increase the contamination of mixed signals. While in the higher gamma-range frequencies, the dimension of data is spanned on around $7 - 15$ components (fig.4.5A.b.). In other animals, we also observe similar lower-dimensional manifolds. The components found by temporal domain PCA also suggest about 8 components (fig.4.5A.c.). In the frequency domain, to determine the number of clusters, we plot the spatial profile of components to a unit ball spanned by their first 3 principle components, as discussed in the previous chapter.

Components of various origins dominate in different frequency bands respectively (fig.4.5 C.). In the lower frequencies, the dendritic components are prominent. The str.l.m.component (fig.4.5 B, C, D. red cluster) stably appears in all the frequencies. With Its spatial loading getting contaminated in the cICA components in higher frequencies, we can see that l.m. input is closely related to the CA1 pyramidal cells(Fernández-Ruiz et al., 2017). The peak has the same polarity as the l.m. sink, indicating a depolarization instead of a hyper-polarization when the l.m. inputs arrive. This component shows the strongest theta-gamma modulation at around $80 - 100Hz$ before the optogenetic stimuli are applied. On the other hand, the

pyramidal layer component (fig.4.5 B, C, D. yellow cluster) has less share below $100Hz$ and consistently appears in higher frequencies, especially in the ripple frequency band. It shows theta-gamma modulation at around $100-200Hz$. The other prominent component is the str. rad. component (fig.4.5 B, C, D. green cluster). This component, as we expected, is highly influenced by the correlation of pathways and other nonlinear effects of dendritic integration (fig.4.5 C, D).

With the complex ICA, we also find another two components. One has a peak at the end of the CA1 area (fig.4.5 B, C, D gray cluster). In contrast to the other components from the CA1, it has a strong real part but doesn't show a complex spatial pattern at CA1, which is usually produced by currents flowing in the dendritic tree. The lack of imaginary part indicates that this component doesn't come from CA1 neuron but volume conducted from the Dentate Gyrus (DG), which is reported to be large in power because of the folded cytoarchitectonic feature of DG granular cells(Fernández-Ruiz et al., 2013).

Another cluster of components shares a similar complex pattern that appears to be spatially flat and rarely theta modulated (fig.4.5 B, C, D blue cluster). This component is more prominent in higher frequencies compared to lower frequencies (fig.4.5 C blue cluster). Its imaginary part is almost zeros at any recording site. We attribute this component to EMG noise or other far-field noise sources which volume-conducted to the local recordings. We've discussed this component in temporal domain ICA in chapter 2, and in chapter 5 we developed a toolbox to detect and remove this component automatically.

The complex ICA components bring input-response temporal information directly into the components' spatial profile. We then ask the question of how to group them across frequencies. The simple clustering provides evidence that components appear across contiguous frequency bands (fig.4.5 E). But we also find high contamination between components (e.g., fig.4.5 D red cluster). Smoothing in single frequency domain harms the sparsity in both spatial and temporal dimensions, especially in the high coherence scenarios like awaking states(Sirota et al., 2008). Therefore, we use tcICA to optimize components over all frequency bands simultaneously.

In tcICA, we punished the dependency of components and encourage a unitary unmixing matrix (unitary rotation after first PCA whitening) by $\gamma log|det(W)|$, at the same time punish the inconsistency of the components spatial loading over frequencies by $\alpha|A_j^{fi} - \tilde{G}_j|_{Fro}^2$. As an example realization, the clusters usually start with spatially similar components (fig.4.6 D, initiate). But each cluster has components not perfectly separated in some frequency bands. The contaminated components lead to large cost values at the beginning of optimization (fig.4.6 A, summarized optimizations, the cost value above 10^4 are cutoff for illustration. Also B for one realization). During the optimization, components will move towards the selected centers of clusters or peaks of distributions (fig.4.6 C).

When the algorithm converges, we find similar clusters around the centroid of cICA components clusters (fig.4.5 D black line). These components are qualitatively similar to the temporal domain ICA (see appendix D.2). Transferring back to the temporal domain, we find the str. rad. component shows the most significant stimuli-triggered response to contra-lateral CA3 simulations (fig.4.6 D. component 7 c and d). The peak of str. rad. component triggered response is about one magnitude larger than all the other components. With the triggered-average spatial profile, we can see a current sink appear at $6ms$.

The str. l.m. component (fig.4.6 D.component 4) has the largest power (68.2% of total power) and has the most significant theta-gamma modulation before the stimuli, same as simple cICA (fig.4.5 E), and the theta-gamma modulation decreases after stimuli stopped. The ripple band modulation of the pyramidal layer component (fig.4.6 D.component 6) also shows a decrease after the stimuli.

Interestingly, we also observe an increase in the imaginary content of the components in the real data compared to the simulation with passive dendrites. The imaginary part, after shifting the phase to make the largest loading of the component to its real part, indicates how the spatial-temporal pattern change within the oscillatory cycle. In our setting, the imaginary part shows how the peak loading "spread" along the somatodendritic tree (see appendix D.1 for a detailed simulation and discussion). We use $\eta_A = \frac{A_i}{A_r}$ to capture the rich temporal evolution of the spatial profile. In the passive simulation, we find a ratio of 0.0364 ± 0.0432 and 0.0864 ± 0.0938 for the str. rad. component and the str. l.m. component, While in the real data the ratio increased significantly, making it 0.1598 ± 0.0109 ($p < 10^{-3}$ Wilcoxon rank sum test) and 0.1929 ± 0.0161 ($p < 10^{-3}$ Wilcoxon rank sum test), respectively.

To summarize, we separate the components in the frequency domain with tcICA and validate with optogenetic stimulation. Frequency domain patterns appear to be richer and more complex in the realistic data compared to passive neuron simulation. The algorithm yields interesting spatiotemporal spreading patterns which could not be captured by temporal domain ICA that assumes spatial-temporal independence. These observations suggest active conductance is involved in dendritic integration. We'll further discuss this point in the discussion.

4.3 Discussion

In this chapter, we present a method that combines prior knowledge of spatial profiles with statistics-based source separation by utilizing the input response of dendritic trees. The method is designed aiming to provide a simple and fast approximation of response patterns confined by smoothly distributed current sources transferring through dendrites. Similar to a dipole model for EEG data, our model is for LFP recording. Unlike previous works, we first separate the

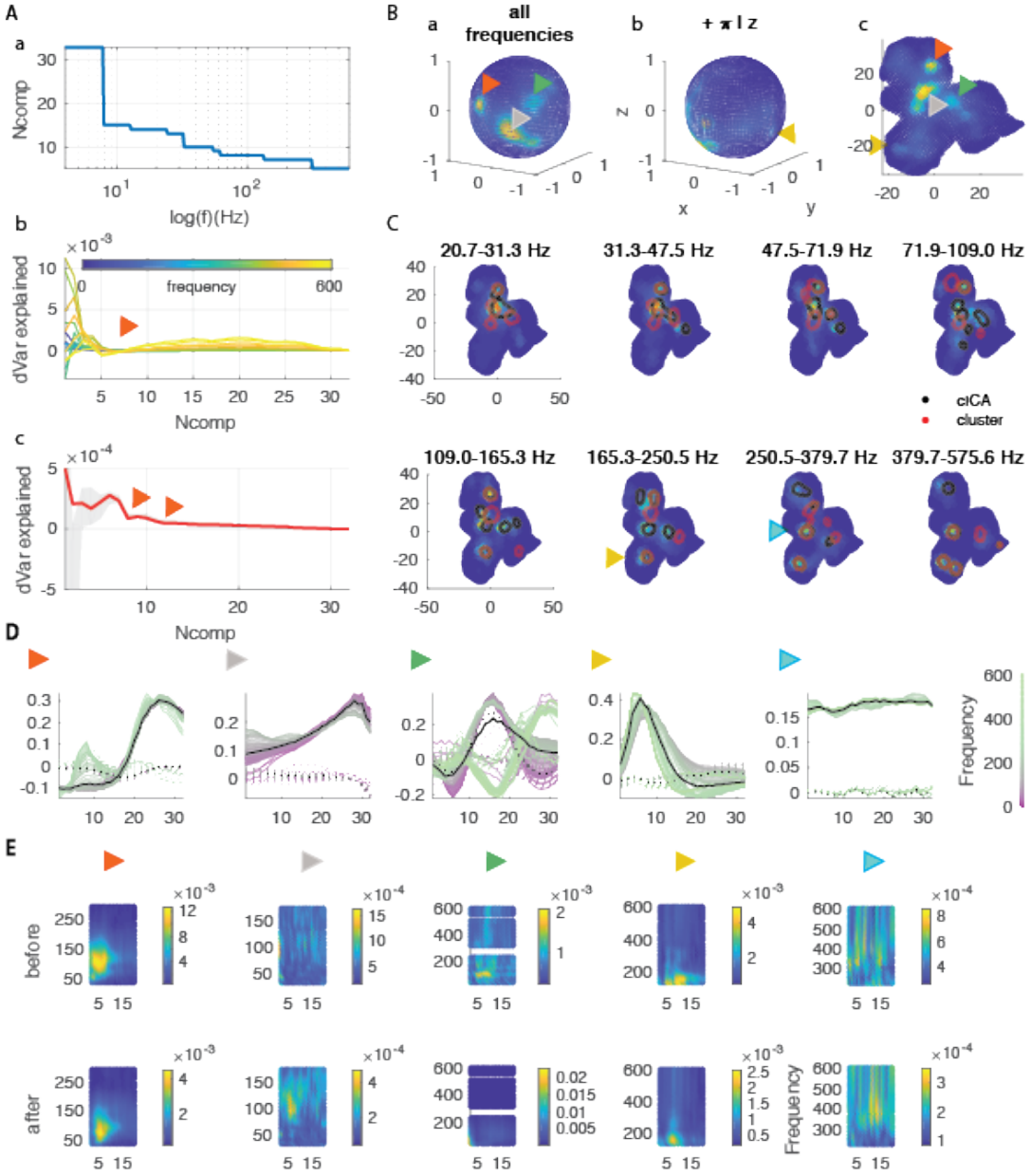

Figure 4.5: Complex ICA in real data in high frequencies. A. The number of dimensions variate across frequencies.a, number of components shared by all the periods. b. *dVar* of explained variance over all the periods for each frequency. c. *dVar* of explained variance for temporal domain data. B. Clustering of components on the unit ball. a. the distribution on a unit ball. b. the same unit ball as in a but rotate π along the z axis. c. the unit ball spanned onto the $2D$ space with tSNE. C. the distribution of clusters of components over different frequencies band. Shown on the same $2D$ space as in B. The red circle indicates the result of clustering, the black circle indicated the top 95% most likely regions. D. example consistent components. red: str.l.m.component; gray: LEC inputs. green: str. rad. component yellow: deep str. pyr. component. blue: EMG noise component. E. Theta gamma modulation in terms of MI. before. after. contra-lateral CA3 stimulation

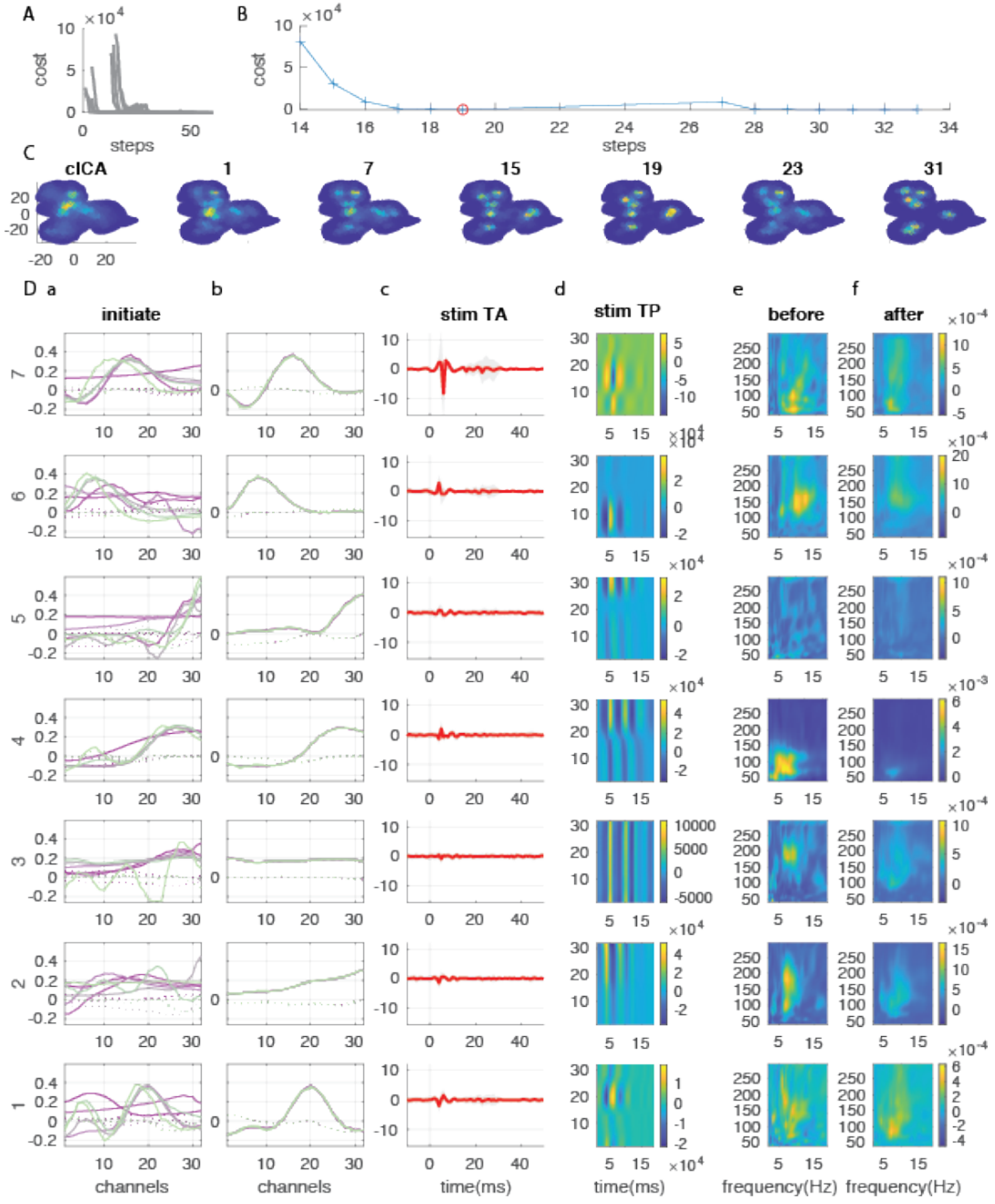

Figure 4.6: Template-based optimization of complex ICA in real data. A. Example random trails of optimization. B-D. Example trail of optimization. B. The cost function. C. The distribution of components' spatial profile evolves with the optimization. The first subplot shows the distribution of complex ICA across all the frequencies (see fig.4.5). The number above each following subplot indicates the step of the optimization. D. The best result achieved at step 19. a. the initial clusters at step 1. The spatial profile is flipped as the largest loading is positive. b. the final clusters' spatial loading. c. the average activity triggered at contra-lateral CA3 stimulation. The stimuli are given at 0ms. d. The spatial profile of the stimuli triggered average. e,f. Theta gamma modulation in terms of MI. e. before, f. after contra-lateral CA3 stimulation

components and fit the response with a Gaussian input pattern. This way, we constrained the input distribution to be local and smooth. But the pattern still depends on the statistical independence or sparsity of the components. The framework includes both spatial and temporal objectives, hence is not a convex optimization problem. Here we discuss some technique and biophysical-modeling-related concerns that call for further exploration.

4.3.1 Concerns about the Component Separation

Since we don't have further prior knowledge of input locations, finding the right clusters of components is the most critical step. When the input is highly correlated, finding the right cluster and re-initialize the optimization usually bring the optimization out of the local minimal corresponding to contaminated components. The major problem is that it's hard to decide which one to keep when multiple clusters all correspond to the same pathway (for example, in 4.2). Therefore, we use the distance between the centroids as well as the fitting cost as criteria. We also tried to select clusters by the distance between the input currents distribution fit at each cluster, but it didn't improve the selection.

Here the current distribution is fitted at every step, but the clusters are not fixed. We redo the cluster every N steps ($n = 10$ here) because components are better separated, and new components join and form better clusters as the optimization proceeds. This way, we can learn the patterns in an unsupervised manner. A further prior of input current distribution might be used in the future, and optimization would be initialized close to the optimum imposed by the experimenter. It might sacrifice the freedom of the algorithm but speed up the convergence.

Currently, there are still many problems to be solved. The first is how to select the correct number of components. The components would be contaminated when we give the wrong number of clusters. However, the number of strong components varies with frequency. We use the gamma band where the components are most consistent (fig.2.8). Another solution would be to embed all the frequencies and separate them based on the amplitude of components (Sirota et al., 2008). The rationale for this would be that synaptic input or active currents come with some spectrum pattern, like gamma burst. Then the general power change of each pattern could be captured by a $1 \times N_t$ time series. If the phase is considered, then the time series doesn't have a clear meaning unless a time series is fitted at each frequency band.

The other problem is it takes a long time to separate components. This is because components are jointly optimized at multiple frequencies. When the number of components increases, it takes much longer for the algorithm to converge. We reduce the time of joint optimization by initiating the components with cICA independently applied at each frequency. Further engineering at gradient would

be helpful. Another possibility would be to down-sample the frequency bands because the frequency domain change is generally smooth, and many of the further analyses could be conducted directly in the frequency domain, even though transferring back to time domain might be problematic.

4.3.2 Concerns about the Biophysical Models

In real data, we find the component profile can not be fully explained by passive conductance. For example, in the CA1 l.m. component, We find a generally larger imaginary part at CA1 rad. layer compared to the passive setting. Linear cross-contamination could not explain this large imaginary part because its response to contra-lateral CA3 stimulus is much less than both CA1 rad. component. The large imaginary part of l.m. component towards the soma implies facilitation of the inputs from distal dendrites. One possible explanation is that it reflects the nonlinear effects, e.g., the Ca^{2+} dynamics, that enhance the dendritic integration, especially for the distal dendrites (Nicholson et al., 2006, Jarsky et al., 2005). It would be interesting to validate the mechanisms involved in the process. After all, decomposition in the frequency domain allows us to extract the spatial-temporal pattern of LFP input response that has been ignored by linear temporal domain source separation.

4.3.3 Extension to LFP Probability Model

In this chapter, we explored how to implement the biophysical constraints to the statistics-based component separation. The regularization comes in two folds, the first is to calibrate the components in the same cluster and fit a shared current input to them, and then is to optimize according to the shared pattern.

The second optimization step is generally stable. The fitting depends on the weights of the spatial and temporal penalty. But the optimization works in a wide hyperparameter range (fig.4.4). Another concern is how much the fitting should rely on the template. Our experience is when the components are severely contaminated, a fitted pattern will improve the separation because of the sparse input location constraint, especially fitting the current distribution with only one Gaussian kernel. The fitting is fast, not necessarily precise, but useful in cluster selection and forcing the components to jump out of previous local minimal. But when it comes to fine-tuning the spatial profile, it's better to allow the components in the cluster to follow their centroids, respectively. Optimization with a fitted pattern usually slightly harms the high-frequency pattern in our passive neuron simulation, while fitting with independence criteria is enough in the highly sparse region. Therefore, we can control how much the optimization relies on the constructed LFP basis. In future work, it might be useful to design the optimization landscape using the template to create a smoother large sink while the likelihood or entropy as a narrower and deeper one sitting on it.

The problem generally comes from cluster assignment and selection, especially during the first several iterations. Here we provide multiple criteria to select clusters, aiming to find biophysically meaningful clusters from the unsupervised learned components. This whole process could be optimized further. An alternative would be to use non-parametric hierarchical Bayesian methods, where the components' number and frequency range could be parameterized and modeled (Bishop, 2006). Experimenters could use further assumptions of both the spatial profile and temporal distribution. For example, the abundant works about channel density distribution along the somatodendritic axis, as well as anatomical studies about pathways, would be useful in constructing the priors (Migliore & Shepherd, 2002, Spruston, 2008). Moreover, for example, the whole system could be modeled by a probabilistic time-frequency analysis (Turner & Sahani, 2014, Klein et al., 2021) or dynamic causal models (Pinotsis et al., 2017). Our formulation for complex impulse response based on the principle of maximum entropy would be helpful in the probability formulation. This could be explored in future work.

Chapter 5

EMG Artifacts Removing

5.1 EMG Noise in Electrophysiology Recordings

Intracranial extracellular recording has been widely used to probe the microscopic level of local neural network dynamics. Multi-site high-density electrophysiology recording has the advantage of monitoring large-scale unit activity, and sub-threshold neuronal activities in high spatial and temporal precision (Buzsáki et al., 2012). However, local field potential, like EEG, is often contaminated by various artifacts. These artifacts with neural or non-neural origin also inevitably affect the interpretation of local signals. Some commonly observed artifacts have a special spatial or temporal profile in extracellular recordings. In this chapter, we explore characterizing and correcting multiple non-local artifacts in LFP recordings with the help of their spatial-temporal properties.

One significant artifact visible from the LFP recording is the far field signal generated by electrical signals in the nearby brain areas and spreading over through volume conduction (Sirota et al., 2008). They would mainly reflect the mean field activity of neurons in the source area. These volume-conducted signals would be picked up by local field recording and affect the interpretation of the local signals. When the channel map is known, these types of signals could be reduced by applying current source density analysis (Potworowski et al., 2012). However, when the channel map is not given, these noises would remain and add to the baseline of the local signal.

Another major physiological noise comes from the electromyographic (EMG) artifacts of the animals, especially when they are moving or chewing. The activity of muscles in the scalp, face, and neck, activities associated with respiration, and the muscles related to blinking et al., would be read from the intracranial recording via volume conduction (Attiah et al., 2017, Watson et al., 2018). Like human EMG artifacts, the muscle activity has a spectrum highly overlapped with gamma band local neural signal (Attiah et al., 2017, Muthukumaraswamy, 2013, Van Boxtel, 2001, Shackman et al., 2009, Watson et al., 2018).

The shape and amplitudes of EMG noise in EEG or MEG data are nonstationary and depend on the muscle contraction. But generally, EMG sources are assumed to be linearly mixed signals which allow for linear segregation of these artifacts from physiological signals (Muthukumaraswamy, 2013, Urigüen & Garcia-Zapirain, 2015). Regression or electroocular (EOG) correction denoise ocular artifacts with the help of simultaneous recording of reference electrodes or EOG channels (Gratton et al., 1983, Croft & Barry, 2000). While empirical mode decomposition (EMD) and wavelet ICA are employed to separate artifacts from single-channel recordings (Mijović et al., 2010), blind source separation based methods have been proposed to remove the stochastic muscle activities with distinguishing spatial profiles (Jung et al., 2000, Delorme et al., 2007, Urigüen & Garcia-Zapirain, 2015). However, the extracted artifacts come from distributed muscle contractions and sometimes are ambiguous. Recent works explore features of various artifacts sources and develop strategies to improve the classification of artifacts from the physiological signals (McMenamin et al., 2010, Mognon et al., 2011, Chaumon et al., 2015, Li et al., 2021).

Compared to the EEG and ECoG recording (Hipp & Siegel, 2013, Chaumon et al., 2015), where the electrodes are placed at the skin or scalp, the myogenic artifact observed in the LFP recording is still visible (Watson et al., 2018) but has less spatial information and generally has different power contain than the extra-cranial recordings (see equ.5.3). Though we don't reconstruct a 3D head model of muscle distribution with regard to the extracellular recording site, the large distance compares to the distance between recording sites smooths out the spatial variation of myogenic sources. Similar to the far-field sources, we expect a flat local component with minimal spatial information. This allows us to detect EMG artifacts based on their spatial profiles.

Other artifacts include power line noise. The power-line noise originates from utility company equipment. It usually is caused by a spark or arcing across some power-line-related hardware or current flows between two conductors in a gap. Previous works employed notch filtering (Luck, 2014) or spectrum estimation to remove the power-line band signal (Mitra & Pesaran, 1999). On the other hand, since the power line noise is generally additive, it is therefore well suited to be detected as an independent noise component (Barbati et al., 2004, Delorme et al., 2007, de Cheveigné & Parra, 2014). LFP recording sits close to the physiological generators compare to EEG data. Hence we expect a more significant signal-to-noise ratio in extracellular recording and better separability of equipment noise sources. Therefore, we also explore removing the power-line artifact using its independent nature in LFP data.

Here we propose a method based on ICA that automatically identifies and removes EMG artifacts and far-field signal contamination. We first show the workflow of EMG-denoising and propose flatness as a criterion for automatic EMG noise detection in local field potential recording. Then we discuss the

properties of EMG artifacts in LFP recording and show the advantage of detecting EMG components on the artifacts-enriched data. Multiple methods are designed to enhance the EMG noise component separation. Finally, we apply this method to LFP recordings to separate gamma band signals from noise. In addition, we also remove the line noise artifacts during the preprocessing. The preprocessing pipeline could be found in an open source EMG denoising toolbox at `https://github.com/YY535/EMG_removing.git`

5.2 Method

5.2.1 Electromyographic Artifacts Detection by ICA

Here we assume the electromyographic artifacts or other far-field volume conductive signals have a fixed spatial pattern and denote as Φ_{EMG}. The recorded LFP is modeled as a mixture of linearly superimposed local neural activity with the EMG component activity and other noise sources Φ_{noise} with loading A_{noise}, which are independent of the physiological signals. The general model writes as:

$$\Phi = A_{neural}\Phi_{neural} + A_s\Phi_{EMG} + A_{noise}\Phi_{noise} \tag{5.1}$$

In reality, Φ_{neural} is usually high dimensional, which is contributed by multiple pathways as well as high dimensional local activities. These could be seen from the unstable source estimation across different periods or the continuously decreasing Eigen spectrum of LFP data (Stringer et al., 2019). Generally speaking, this is an overcomplete ICA problem (OICA), namely, the number of the sources is more than the sensors (Hyvärinen & Oja, 2000). In this case, the classic ICA algorithms pre-processing with PCA or whitening would pick up a subset of components according to their power. The following unmixing will then depend on the independency or non-Gaussianity of the source activity. When the signal sources have sparse (super-Gaussian) marginal distributions and are approximately uncorrelated ("quasiuncorrelated"), that is, they are roughly orthogonal to each other, then they would be identified with ICA. Therefore, once the component is independent of others and picked up by the algorithm, it is possible to remove it from the data. The task here would be to enhance the possibility of picking up the artifact components.

The EMG components we deal with are generally considered independent from the local intracranial signals with a long-tail spectrum. On the other hand, their spatial loading usually lacks dipole shape and is easily distinguishable from the local components (Watson et al., 2018). These properties make EMG components separatable from the rest of the local signals. However, they are usually hidden by the large slow-frequency activities, which share a linear spatial loading. And the separation is also contaminated by the large local events, which generate a large oscillatory baseline. Therefore, to improve the discovery of the EMG component,

the key step is to find the EMG enriched period and reduce the amount of neural activity sharing in the data $\hat{\Phi}_{neural}$. We'll discuss this in the following subsection.

To separate the EMG components, we apply non-Gaussian fastICA (Hyvarinen, 1999) to $\hat{\Phi}_{neural}$. The rationale is this algorithm would iteratively find independent components from the rest of the data, and it's enough to separate noise components from the subspace of neural activity. This would also allow the algorithm to be easily scaled with a larger dataset. After the mixing model is found, we apply a post-hoc feature selection and find the component that best fits the spatial pattern of the far-field signal.

For any electric charge Q far away from the recording sites, the spatial decay of the field is close to linear and flat:

$$\frac{\mathrm{d}\Phi}{\mathrm{d}r} = -\frac{Q}{4\pi\sigma r^2} \overset{r\to\infty}{\to} 0 \tag{5.2}$$

And for a system where the current sink and source are balanced, the dipole term dominates in the far-field approximation (Nunez et al., 2006):

$$\begin{aligned} & \Phi(R) && = && \tfrac{C_{monopole}}{R} + \tfrac{C_{dipole}}{R^2} + \tfrac{C_{quadrupole}}{R^3}... \\ where \quad & \tfrac{C_{dipole}}{R^2} && = && \tfrac{1}{4\pi\sigma}\tfrac{|p|cos\theta}{r^2} \\ therefore \quad & \tfrac{\mathrm{d}\Phi}{\mathrm{d}r} && = && -\tfrac{1}{2\pi\sigma}\tfrac{|p|cos\theta}{r^3} \overset{r\to\infty}{\to} 0 \end{aligned} \tag{5.3}$$

Therefore, we propose a flatness score to capture the spatial pattern of the far-field signal. There are various ways to measure flatness, here we combine two of them. The first is to fit a $1D$ affine function to the spatial loading, that is:

$$SRE = \min_{\alpha,\beta} \left\| A_i - (\alpha \overrightarrow{x} + \beta) \right\| \tag{5.4}$$

where $\overrightarrow{x}$ is the given recording channel map. The inverse of the SRE (squared residue error) is computed and used as the first criterion. Notice we use an affine function here and allow for a non-zero slope α.The slope is designed to capture the inclined shape of the volume conducted field signal in the nearby region. The component generated by nearby areas typically shows a linear decay instead of a dipole shape (Herreras et al., 2015, Krull et al., 2019).

To avoid picking up components reflecting large dipoles, we multiplied the inverse of SRE in equ.5.4 by the absolute value of the vector sum:

$$flatness_i = \frac{|A_i|_1}{SRE_i}. \tag{5.5}$$

where $\|A_i\|_2 = 1$ is the mixing matrix normalized to unit $l2$ norm. It can be shown that the $l1$ norm of A_i (the $|A_i|_1$) is maximized when the component is flat, namely, when every entry of A_i is equal to $\frac{1}{\sqrt{n}}$ (see B.3.1).

The flatness score is expected to be very high because of the small SRE after fitting. We threshold the flatness with the number of channels because when the components are flat $|A_i|_1$ would be proportional to the square root of channel number $\sqrt{n}$. Usually, only one component stands far beyond the threshold (see figure.5.3 A,B). This component would be picked up as an EMG component. In practice, when the component with the largest flatness is too close to the threshold, the small flatness score usually indicates a small effect of EMG artifact in the period. The components extracted in those periods would be spurious.

After the EMG component is identified, the EMG activity is obtained by projecting the original wide band to the component. In the *EMG_removing* toolbox we provide, EMG components are fitted in concatenated long periods. It takes care of data non-stationarity. The ICA components are undetermined with scale, so we compute the unit-variance activity EMG_au and their variance is accounted by mixing matrix A_s or unmixing matrix W_s. So the contribution of EMG components could be written as:

$$\Phi_{EMG} = A_s \Phi_{EMG\_au} \qquad where \qquad \Phi_{EMG\_au} = \bar{W}_s \Phi \tag{5.6}$$

and then the cleaned signal is given by:

$$\Phi_{clean} = \Phi - \Phi_{EMG}. \tag{5.7}$$

To put the fitted EMG segments together, which could be used in further analysis, we could project the uni-variance EMG activity EMG_au back to the original data space of Φ:

$$\Phi_{EMG} = A_s \Phi_{EMG\_au} \qquad \Rightarrow \qquad \bar{\Phi}_{EMG} = \bar{A}_s \Phi_{EMG\_au} \tag{5.8}$$

and the average EMG artifact over all the channels of Φ_{EMG} is given by $\bar{\Phi}_{EMG}$. Notice although the sign of ICA component loading is indeterminate, the projection back to the original space will cancel out the indeterminacy and have a determined sign. To collect data from all the periods, we compute the average EMG contribution over all the channels, which is equivalent to multiplying the uni-variance EMG activity EMG_au with the mean of its spatial loading $\bar{A}_s$ and the average signal is saved for further analysis (right-hand side of equ.5.8).

5.2.2 High Muscle Tone Period Detection

To achieve reliable EMG components, we apply multiple pre-processing steps to enhance the power content of the EMG artifacts in the model training data. These include temporal whitening of the data and a pre-selection of high EMG artifact-contaminated periods.

EMG signal covers a wide frequency range and heavily overlaps with local neural activity (Attiah et al., 2017, Muthukumaraswamy, 2013, Watson et al.,

2018). However, it has been shown that EMG contains the data much more severely in the higher frequency, 10− to 200−fold differences in the power of frequencies above 20Hz (Whitham et al., 2007). Therefore, we keep the wide-band signal while enhancing the high-frequency part of the spectrum by temporally whitening the data (Mitra & Pesaran, 1999). The whitening is done by fitting an AR(2) autoregressive model to the data and removing the signal fitted by the autoregressive model. This procedure largely leaves out the slower frequency synchronized activity and enhances the EMG share in the data.

The high EMG period is selected according to the local signal power and correlations between distant channel pairs. High EMG periods typically coincide with arousal states where the general spectrum power is high(fig.5.1 B, C). But rapid-eye-movement (REM) sleep and large events like a spindle or sharp wave ripple in non-REM sleep also have large baseline power generated by the local physiological activity. At the same time, the EMG artifacts should be minimal in these periods. Applying ICA to sleep periods usually generates spurious components (see fig.5.1 C). Therefore, we must tell high EMG contaminated periods from the high local activity period.

To do this, we consider the correlations between distant channel pairs within consecutive time windows $16ms$, similar to EMG extraction in (Watson et al., 2018). However, instead of selecting channel pairs in different shanks in the paper, we use the total covariance between randomly selected channel pairs within one shank. The aim is to find the periods with large power as well as large pairwise correlation. We use ICA to rotate the joint distribution of total variance and pairwise correlation and set a threshold to get high EMG periods (see fig.5.3).

After detecting the high EMG period, ICA is applied to whitened data in these periods to fit the EMG components. Notice we are pretty conservative in high EMG period selection to guarantee the existence of EMG artifacts. But it doesn't affect the periods we finally remove the EMG artifacts. Instead, the removal of EMG artifacts is performed on the whole session of the wide band or high-pass filtered data (a high-pass filter is an option in the toolbox. The slow frequency of local activity would add to the baseline of LFP data and sometimes contaminate the flat EMG component. We suggest leaving the slow frequency signal unaffected and removing the EMG signal in the higher frequency band above 20 or 30 Hz).

5.2.3 Line Noise Detection

Line noise components could also be detected and removed by ICA. However, the spatial pattern of line noise depends on channel impedance and other conditions and is generally not predictable over animals (see fig.5.3 C). Therefore, we don't have any presumption about its spatial pattern. Instead, we use the definition of line noise and select components based on the average spectrum power ratio within harmonics of local power-line frequency F_{line} ($\{f_{line}\} \in$

$[F_{line} \times n - 5, F_{line} \times n + 5]$ Hz, for all $n = 1,...$ where $F_{line} \times n$ is lower than Nyquist frequency) compare to all the other frequencies, written as follow:

$$R_{line} = \frac{E_{i \in \{f_{line}\}}(P_i)}{E_{j \notin \{f_{line}\}}(P_j)}. \tag{5.9}$$

The power-line noise is removed before we fit the EMG component because the spatial pattern of line noise could also be comparably flat, affecting the EMG component detection. Unlike EMG artifacts, the power-line noise is barely affected by the animal behavior, so the detection is applied to the whole data. When there is strong power line noise, R_{line} would be more than 10 folds. We detect the line noise components only when the power ratio R_{line} is higher than the threshold set arbitrarily as 1.8 (see figure.5.3 D).

However, the line noise would depend on the electrical connection and other factors. Sometimes there is no component passed the threshold, which indicates a small influence of the power-line noise. In this case, the separated components would share a fair amount of neural signals. So We suggest not removing these components but keep them for further analysis or remove with spectrum estimation (Mitra & Pesaran, 1999).

5.3 Results

5.3.1 Nonstationary EMG Content

To test and optimize the EMG correction algorithm, we use multi-electrode recording data in the rat (RS1218) LFP was recorded via a 16-tungsten wire bundle (insulated $12\mu m$ diameter, California Fine Wire, Co.) attached to a 200 μm diameter optic fiber (optrode), implanted above dCA1. The spatial arrangement of the recording sites (resulting from a diagonal cut) enabled coverage of the entire CA1 region in depth (from stratum oriens to stratum lacunosom moleculare). The LFP data is down-sampled at 1000 Hz. We use theta band ($[6.5, 13]$Hz) to non-theta band ($[2, 6.5) \cup (13, 20]$ Hz) power ratio to indicate different brain states (Sirota et al., 2008).

The theta band signal in the pyramidal layer is related to the arousal level of animals. During running, the pyramidal layer signal typically shows a large theta power ratio, while in the slow wave sleep (SWS) period, the spectrum is left with slower oscillation. During shorter rapid eye movement (REM) sleep periods, the theta ratio is also high, while the muscle tone is highly reduced during this period(fig.5.1 E).

To assess the reliability of EMG detection, we first extract EMG components in every 17s window. In each window, we perform fastICA separation on wideband signal and find the flattest component according to equ.5.5. We repeat this process

for 10 times and collect all the flat components.

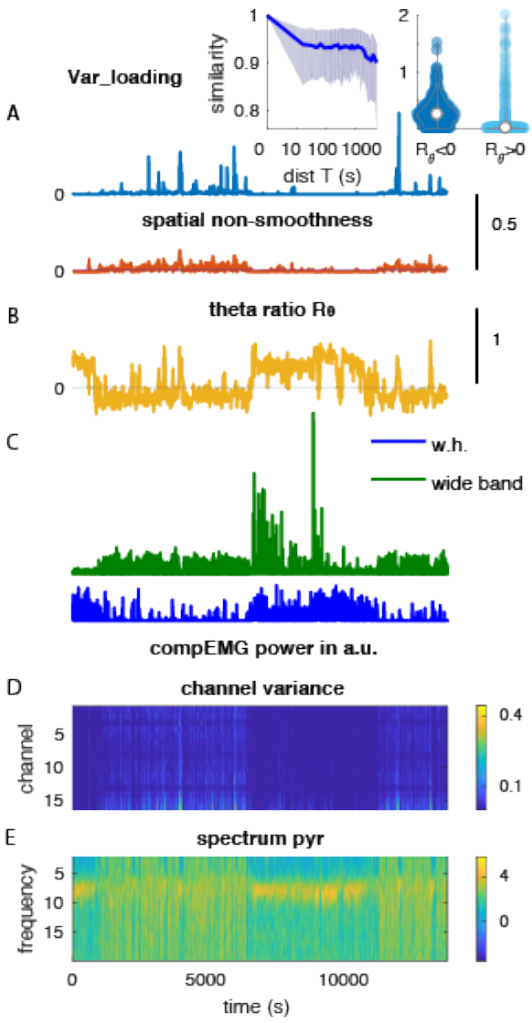

Figure 5.1: State dependency of EMG Components. A. Variance of flat components estimated in sliding windows, inset: left: the similarity of components plot against temporal distance, right: the violin plot for the $Var_{loading}$ at different theta states, i.e., $R_\theta > 0$ or $R_\theta < 0$, respectively. Spatial non-smoothness is the L1 norm of spatial Laplacian. B. Theta to non-theta (< 20 Hz) power ratio at pyramidal layer R_θ. C. EMG components power in wideband signal(w.b.) or whitened high passed signal(w.h.). D. Variance of estimation at each channel. E. Spectrogram of pyramidal layer channel.

The variance of the flat components at each channel across the time windows is summarized as loading variance $Var_{loading}$ in fig.5.1 A. $Var_{loading}$ tells whether ICA always finds the same flat component. $Var_{loading}$ keeps a low level during most of the strong theta period while the variance increases when the theta band signal is lower(fig.5.1A inset right). Interestingly, during the short strong theta period between SWS periods, we also observe large $Var_{loading}$. Since the EMG noise detected here comes from various origins, the large $Var_{loading}$ could be accounted for by the REM sleep period, where muscle tone is reduced.

Deeper channels close to the dentate gyrus show a larger spatial variance compares to the superficial CA1 channels (fig.5.1 D). The components also have more spatial structures(fig.5.1 A spatial non-smoothness), which is brought by local neural signals, Where the signals in deeper channels are amplified by the symmetric spatial arrangement of granular cells (Fernández-Ruiz et al., 2013). In contrast to sleeping periods, the spatial loading of components is flatter in awakening periods, especially when there is more high-frequency muscle tone (fig.5.1

A, B, D). This suggests detecting the EMG components from high muscle tone periods, especially during awakening, instead of training in the whole data session.

A simple threshold-based method is developed and described in the method session to select a high muscle tone period (fig.5.3E, F for the method and G for detected high EMG period in an example time window). This method seeks periods with heavy activity (large variance) across all the channels with little spatial structure (large co-variance between randomly selected large-distance channel pairs). This method is comparable to the EMG detection in (Watson et al., 2018).

To further check the reliability of EMG components during the awakening period, we compute the similarities between components as a function of their temporal distance(with log scale up until 5000ms, fig.5.1 inset left). Only the periods with $R_\theta > 0$ are included in the analysis. The shadowed area indicates the 25 and 75 percentile of the similarity for all time window pairs with a given temporal distance. The similarity is close to one for nearby EMG estimation. However, when the distance is long, the similarity drops. Therefore, we chunk the whole data session into smaller periods to fit EMG components (example shown in the appendix fig.E.1).

Next, we ask whether decomposition in the EMG noise dominant high-frequency data A_h would be different from the one in wide-band signal A. To do this, we first temporally whiten the signal with $AR(2)$ model (Mitra & Pesaran, 1999) and then high-pass above 100Hz. The separation is applied to high theta periods, and the first two flattest components from each training set are shown in fig.5.2, the left column from the wide band and the right column from EMG enriched signal, respectively. The flattest component in EMG enriched signal $f_{Ah1} = 307$ (fig.5.2 B) is slightly flatter than wide band signal $f_{A1} = 196$ (fig.5.2 A). The cleaned wide band signal obtained by subtracting the contribution from each component with (equ.5.6 and equ.5.7) are shown in fig.5.2. The large artifacts at 80s are removed With the flat component from EMG enriched signal. However, projecting to the wide-band trained component only partially reduces the artifact.

5.3.2 Spatial Spreading of EMG Components

To check the spreading of the EMG signal, we use animals with two high-density linear probes, one in the Medial-Entorhinal Cortex (MEC) and the other in the hippocampus. The animal is recorded for 8 consecutive days, and the analysis is performed independently for each day only in awake periods. In addition to whitening, we also enhance high-frequency signals with two other methods: regression ($rLFP$) or taking the derivative of signals ($dLFP$, see section2.2.3). The power spectrum of the components' activity and the coherence between MEC and Hippocampal flat components are computed for each session. To emphasize

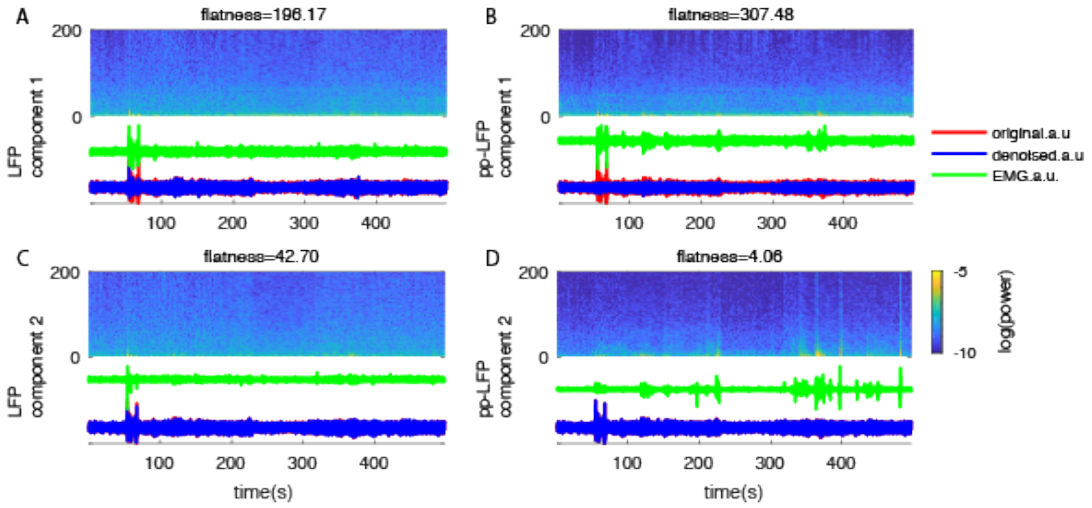

Figure 5.2: EMG removal example with wideband and preprocessed LFP. A. Denoising by removing the flattest component separated from wideband raw lfp. Bottom: The normalized activity (EMG a.u.) of the component with the highest flatness score (green line) is plotted parallelly to the normalized raw and denoised LFP signal from one channel. The denoised signal is obtained by subtracting the component share from the normalized raw LFP. The color map is the spectrogram of the denoised signal for the same period. B. Denoising by removing the flattest component separated from the preprocessed lfp. The component activity is obtained by projecting the raw LFP to the separated component. The same channel is used to demonstrate the performance. C. same as A but for the 2 nd flattest component from raw LFP. D. same as B but for the 2 nd flattest component from preprocessed LFP.

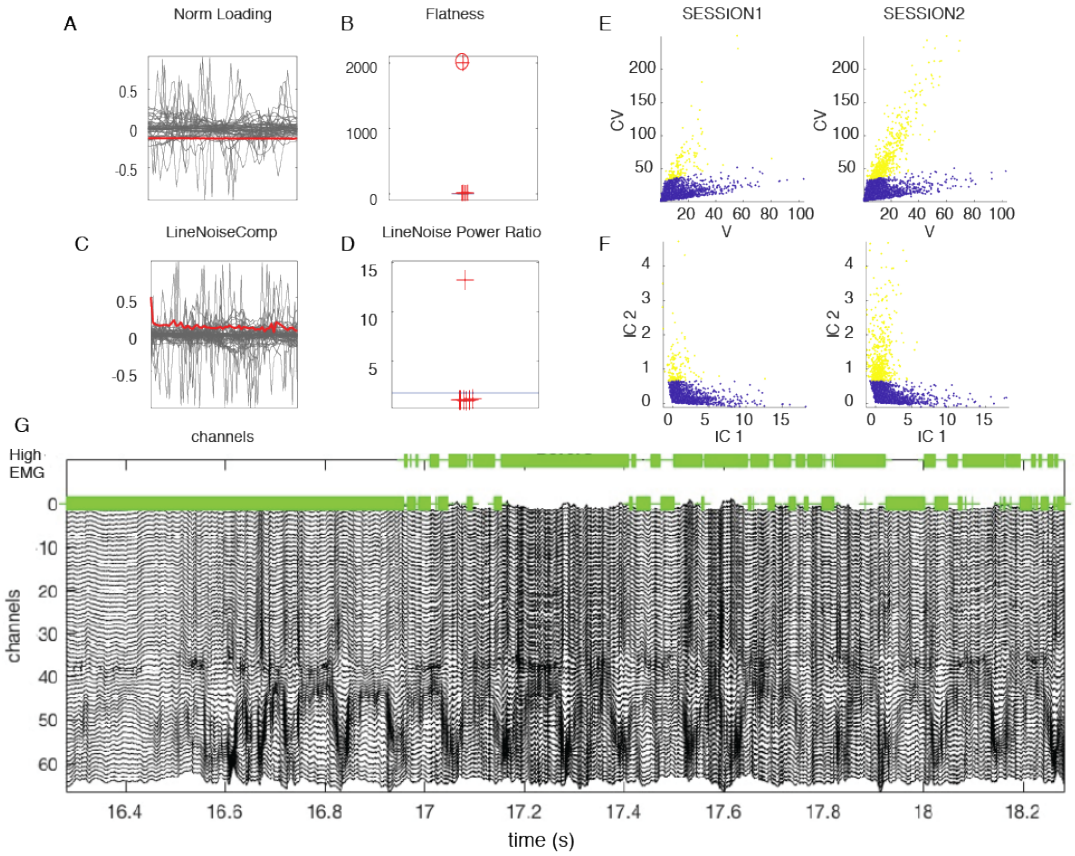

Figure 5.3: EMG and LineNoise artifacts extraction. A. Unit norm spatial loading of all the components in one session. The Red line indicates the EMG component. B. Flatness score of all the components in A. circle indicates the EMG component the algorithm selected. Linear shank here has 64 recording/channels. Most components have small flatness scores and sit less than the threshold. C. Unit norm spatial loading of the Line-Noise component in the same session. D. Power ratio of all the components in C. E. The variance and average co-variance between channel pairs in each sliding window for two randomly picked sessions. The yellow color indicates the period clustered into high EMG periods. F. The variance and co-variance plot in E is projected to the first 2 ICA components of each session. G. Example LFP recording linear profile for high EMG period detection. 0 is close to the CA1 orient layer, and channel 60 is in the dentate gyrus. Green crosses indicate clustering result: green crosses sit on the upper line indicates the period is high EMG period. (rat: APP3)

the high-frequency bias of $wLFP$, the components are not projected back to the original LFP but stay with the whitened signal. But this would not affect the coherence estimation since it's normalized at each frequency band. Because the component power contains variate cross days, we separate them into two clusters: lower contains when the explained variance is less than 20%, and otherwise high contains, plot them in fig.5.4A, C or B, D respectively.

All the flat components have a fair amount of high-frequency share(fig.5.4C,D,F). However, when the power of the component is larger, those from high frequency enhanced data show an even larger gamma band share compared to slower band signal(fig.5.4E), while LFP components show the opposite trend, namely more theta than gamma(fig.5.4E, blue). This indicates the LFP component intends to pick up more slow-frequency activity than high-frequency ones.

Even though the two shanks are recording at different areas, their EMG activity is highly coherent with each other(fig.5.4A, B). When the EMG signal is large, the phase difference is close to 0 in $wLFP$, especially for higher frequencies, suggesting a mainly resistive extracellular conductivity there (Einevoll et al., 2013). Coherence is large for the high-frequency enhanced data, especially in the gamma band(fig.5.4A, B wLFP), but it never reaches 1, which indicates the component activity might be a distance-dependent mixture of multiple muscle sources. The coherence shows a similar frequency bias as in the spectrum. While the whitened signal also has high coherence at a slower frequency, the theta-to-gamma ratio is significantly larger in the LFP components ($p = 0156$). This again indicates a better separation in higher frequency with $wLFP$ compare to separation in original LFP data.

To summarize, we find the EMG components are not stable and are often contaminated by slow local activities. One must be cautious about EMG-slow wave contamination during training, especially in freely moving animals. We find temporal whitening and separation at a high muscle tone period improve the separation. A pre-processing pipeline is developed accordingly (see algorithm 1). The process of correcting EMG noise in the toolbox can be summarised in figure5.5.

5.3.3 EMG Component Validation

In LFP recording, we usually don't have a ground truth of EMG artifact. Additional EMG electrode was used by many to indicate the share of artifacts in EEG or MEG recordings (Li et al., 2021, Gross et al., 2013). However, since the LFP signal receives an electrical field generated by widely distributed muscle contractions, any one channel outside would hardly capture all the contributions. So in the toolbox, we decided to validate the components from their spatial and temporal characteristics, as discussed in previous sessions.

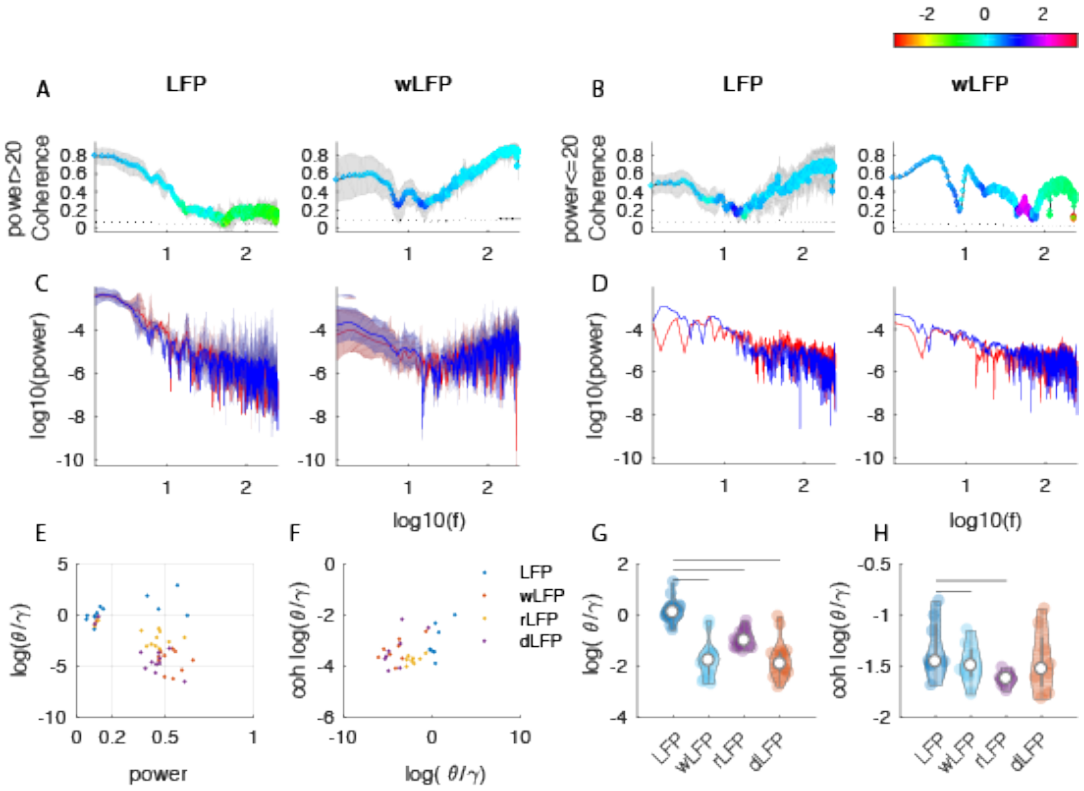

Figure 5.4: EMG components from two shanks. A, B Coherence between EMG components from the hippocampal shank and MEC shank, color indicate phase in $[-\pi, \pi]$ C, D spectrum for EMG components from hippocampal shank in red and MEC shank in blue, respectively. A, C is for sessions EMG components power accounts for more than 20% of the total power. C, D is for sessions EMG components account for less than 20% of the total power. For A-D left is based on the LFP signal, and the right is on wLFP. E. log Theta (θ [4,12] Hz) to Gamma (γ [40,200] Hz) band power ratio plot against component power.F. log $\theta - \gamma$ coherence ratio plot against the log $\theta - \gamma$ power ratio. G. Distribution of log $\theta - \gamma$ power ratio. The black line indicates $p < .0005$ by Wilcoxon signed rank test. H. Distribution of log $\theta - \gamma$ coherence ratio. The black line indicates $p < .05$ by Wilcoxon signed rank test.

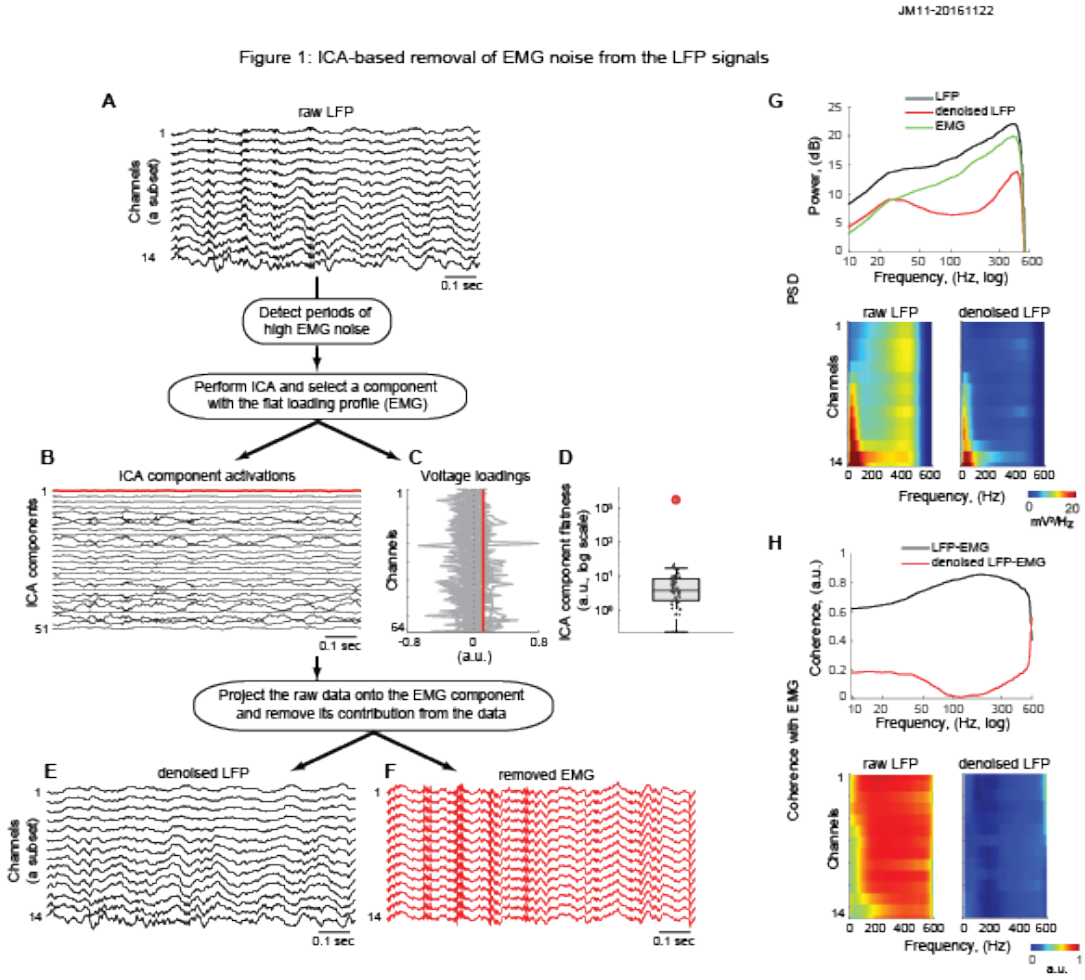

Figure 5.5: General workflow of the ICA-based removal of EMG noise from the LFP signals. A-F. The denoising procedure was applied to raw LFP traces simultaneously recorded by a multichannel silicon probe across the hippocampal CA1 layers in a single recording session A. First, global periods with an elevated occurrence rate of EMG noise in the session were detected. Then, the LFP signals from these periods were decomposed by an independent component analysis (ICA) resulting in a set of ICA components each with a temporal activation B and spatial voltage loading C. We quantified the flatness of voltage loading profiles of all ICA components D. and identified the one with the highest flatness (in red) as the EMG component. Eventually, we reconstructed the denoised LFP signal E. by removing the EMG component from the raw data. The removed EMG traces reconstructed from only the EMG component are shown in F. G. Top, power spectra for the example raw (black) and denoised (red) LFP traces and the removed EMG (green) from the channel $l - 3$ in A, E, and F. Bottom left, a color-coded joint distribution of spectral power as a function of frequency and channel calculated for the raw LFP traces. Bottom right, same as in the middle, but for the denoised LFP traces. Note the reduced power in the high (> 100 Hz) frequency range, corresponding to the removed EMG noise. H. Top, coherence between the raw LFP and the EMG traces (black) and between the denoised LFP and the EMG traces (red) from the channel $l - 3$ in A, E, and F. Bottom left, a color-coded joint distribution of coherence between the raw LFP and the EMG traces as a function of frequency and channel. Bottom right, same as in the middle, but for the denoised LFP and EMG traces. Note the reduced coherence in the high (> 100 Hz) frequency range, corresponding to the removed EMG noise.

First reporting figure is generated by *EMG_rm_report.m* for each periods(fig.5.5, see appendix for reporting fig.E.1). First, the EMG component's spatial loading is shown against all the other components in fig.5.5 D. Its flatness is emphasized by a red circle. At this step, a single and large flatness score indicates good separation. The power spectrum density (PSD) of a selected channel is shown in fig.5.5G Top, together with the PSD of denoised signal and EMG noise. A good separation would typically have a higher power in the gamma band, agreed with experimental reports (Whitham et al., 2007). The cleaned signal would normally have less high-frequency content than the original signal. General optimization of non-Gaussian or independence measures would not guarantee independence in frequency domain decomposition. However, we would expect little coherence in all frequencies. This becomes our next validation plot fig.5.5 H Top, which tells how much the coherence between the original signal and EMG activity is reduced by removing the artifact with our method. Lastly, We also plot the spatial loading and R_{line} in equ.5.9 of the line-noise component.

With *EMG_rm_viewnoise.m* we plot an example period of high EMG noise contained LFP signal in black and the cleaned signal in red (see appendix for reporting fig.E.2). The detected high EMG contamination periods are also shown in green.

In *EMG_rm_viewspec.m* one could find all the frequency domain summaries of detected EMG components of all the channels (see appendix for reporting fig.E.3). The PSD, as well as the coherence between EMG to raw or denoised data, is computed for all the channels to show their spatial profiles (fig.5.5 G Top, H Bottom right). Inspired by the observation and suggestion of (Muthukumaraswamy, 2013), the spectrogram of the original LFP signal, detected components, and the denoised LFP signal are plotted, respectively.

5.3.4 Removing of the High-frequency Artifacts in Gamma Detection

Then we use the EMG removing toolbox to denoise the 32 channel linear recording signal in freely running animals. In contrast to frequency band limited oscillation patterns, the EMG component appears to be the major contributor to the broadband high-frequency activities5.6. The large stripes and "patchy" looking response in the spectrogram (5.6 A), usually caused by animal movements, are corrected by the toolbox (5.6 B), and the physiological signals become visible afterward (5.6 C).

The EMG components are reliably detected in awakening animals. To avoid overfitting, we applied EMG detection only to the awake period. Among 53 sessions of 13 animals, on average, 60% of the awaking period is detected as a high EMG period and used in component fitting (fig.5.7 D). To assess the goodness of the separation, we compare the flatness of the EMG-related components

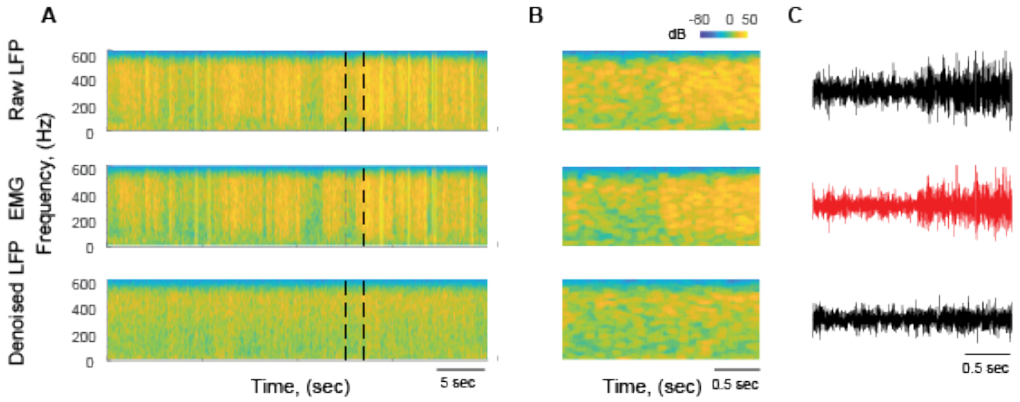

Figure 5.6: Spectrograms for the example LFP segment before and after EMG noise removal. A. Top, example spectrogram of the raw LFP signal, revealing the presence of high-frequency EMG noise. Two vertical black dashed lines depict a 2-sec long segment shown in an expanded format in B. Middle, same as at the top, but for the EMG component removed from the raw LFP trace at the top as a result of denoising. Bottom, same as at the top, but for the denoised LFP. Note the reduced power in the high (> 100 Hz) frequency range, corresponding to the removed EMG noise. B. Top, expanded spectrogram of the 2 sec long segment marked with the black vertical lines in A. Middle and bottom, same as at the top, but for the EMG component and the denoised LFP. C. Top, raw LFP trace from the 2 sec long segment marked with the black vertical lines in A. Note the increased amplitude of high-frequency EMG noise at the end of the trace. Middle and bottom, as at the top, but for the EMG component and the denoised LFP. Note that the high-frequency EMG noise present at the end of the raw LFP trace is now gone.

to non-EMG ICA components. The detected EMG-related components have a significantly higher flatness score ($median = 170.9$) than the non-EMG ICA components ($median = 1.8$,Wilcoxon rank sum test $p < 0.001$. fig.5.7 A). The average power spectra of the EMG component is generally increasing with the frequency (fig.5.7 C) and by removing the EMG component, the largest power reduction happens in high frequency, especially in the ripple band (fig.5.7 D).

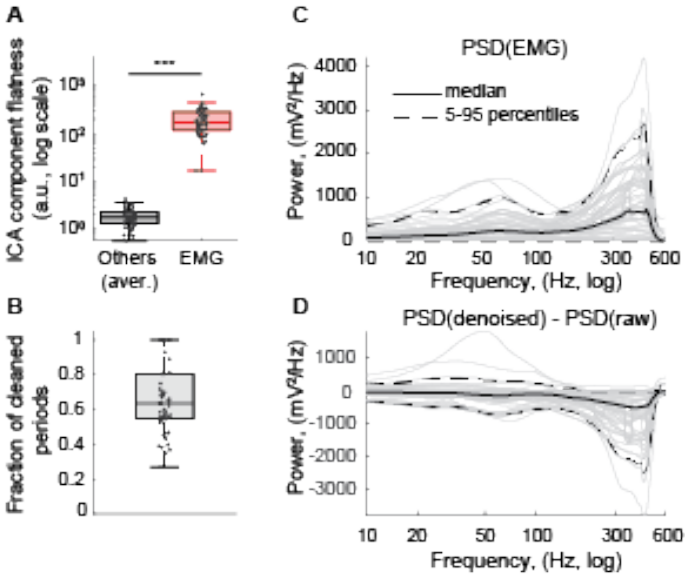

Figure 5.7: Group statistics on the effect of EMG noise removal. (A) Averaged flatness of the EMG-related ICA component (median=170.9) was significantly higher than that of all other (non-EMG) ICA components (median=1.8) (n=53 sessions from 13 animals, Wilcoxon rank sum test, Z=-8.8714, ***p<0.001). The flatness of all non-EMG ICA components was averaged first across all such components within the individual sessions and then – across the sessions. On each box plot, the central mark indicates the median, and the bottom and top edges of the box indicate the 25th and 75th percentiles, respectively. The whiskers extend to the most extreme data points not considered outliers, and the outliers are plotted individually using the '+' marker symbol. (B) Averaged fraction of time within individual sessions, which was actually denoised (median=0.63, IRQ = 0.37-1.00, n=53 sessions from 13 animals). (C) Session-specific (gray lines) and the averaged (black solid line) power spectra of the EMG component (median and interquartile range, n=53 sessions from 13 animals). (D) Same as in (C), but for the difference between power spectra of the denoised and raw LFP signals (median and interquartile range, n=53 sessions from 13 animals).

Next, we ask how EMG removal affects gamma burst detection. Gamma burst has been shown to implicate the time window of long-range coupling between

areas (Sirota et al., 2008). Here we detect gamma burst events as isolated local maximums in the $N_{channel} \times N_{frequency} \times N_t$ $3D$ spectrogram. The bursts too close to each other (threshold of $[nchannel, n_{frequency}, n_t]$ is [3,5,8]) are excluded to avoid double detection. To our surprise, the occurrence rate of bursts at frequencies ($> 150Hz$) is increased after the EMG noise removal (fig.5.8 A, B). It can be explained by the fact that after we remove the high-power far-field contamination, the bursts detected in the denoised LFP are better localized in the time-frequency-anatomical layer space and, correspondingly, more bursts passed our selection criteria (for example, in fig.5.7).

On the other hand, the burst power distributions computed for the raw (but not for the denoised) LFP clearly diverged at frequencies above 100 Hz between the sleep states (SWS, REM) and the locomotion state (RUN) (fig.5.8 C. top). The power of the preserved bursts after the EMG noise removal becomes, however, lower and comparable with the power of bursts recorded during the sleep states. Given the number of detected bursts increases with, on average less power, we ask whether the detected bursts are physiologically meaningful.

We use cross-frequency coupling to validate the physiological property of the detected gamma bursts and observe a general increase in theta-gamma modulation (fig.5.8 D). Theta–gamma coupling (TGC) is a neurophysiologic measure associated with organizing local oscillation within the information processing time window provided by theta cycle (Sirota et al., 2008, Mizuseki et al., 2009, Schomburg et al., 2014). Note the increased theta modulation strength of, for example, the CA1pyr bursts at $150 - 200$ Hz and CA1lm bursts at $70 - 100$ Hz after the EMG noise removal (fig.5.8 D Bottom).

The EMG noise removal consistently improves high-frequency oscillation burst detection. Here we plot the impact of EMG removal in a frequency-resolved manner at each session for different layers (fig.5.9 A for CA1 l.m. layer and appendix fig.E.4 for all layers). The denoising process generally positively impacts detecting gamma bursts with better theta-gamma modulation. Instead of showing a lower TG.mod. strength which would be expected from a lower signal-to-noise power ratio, we find a better theta modulation when the average burst power is largely reduced(fig.5.9 B), which implies a large reduction of EMG-related far-field signals. Interestingly, the difference in burst power correlates with an increase in the theta-gamma modulation (fig.5.9 B) when the power difference is small. We further explore the spatial and frequency domain profile of the improvement of gamma burst detection in the denoised data. Rescuing more of the smaller power gamma bursts significantly correlates with a better average theta modulation in the ripple band, especially around CA1 pyramidal layer and Dentate Gyrus (spearman rank correlation, fig.5.9 C).

Overall, we find more spatial-temporally localized gamma bursts in the EMG-denoised data. These bursts were shadowed by the large EMG noise. By removing

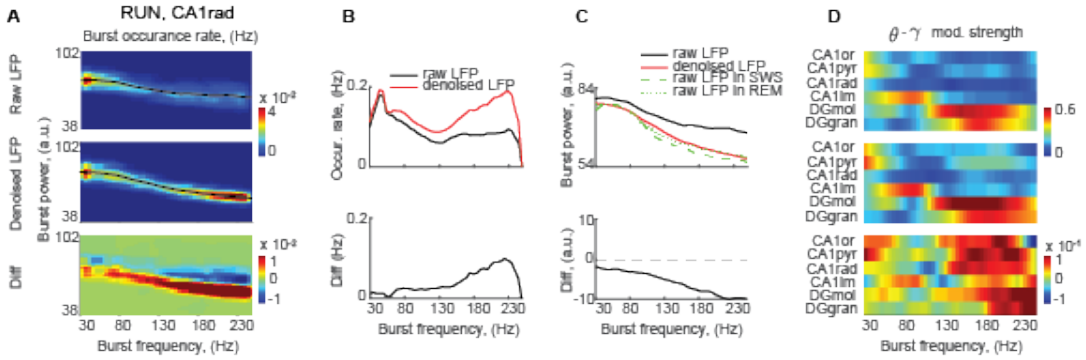

Figure 5.8: Effect of the EMG noise removal on high-frequency oscillation (HFO) bursts for an example session. A. Top, for example, the color-coded joint distribution of the HFO burst occurrence rate (Hz) as a function of burst frequency and power calculated for bursts detected in the raw LFP from the CA1 str. radiatum during the RUN state recorded in a single session. Red and blue colors indicate the maximum and the minimum rate values correspondingly. The solid black line depicts the mean burst power as a function of burst frequency. Middle, same as at the top, but for the bursts detected in the denoised LFP. Bottom, the color-coded difference between the two joint distributions above, computed for the raw and denoised LFP. B. Top, example distributions of the HFO burst occurrence rate (Hz) as a function of burst frequency calculated for the same bursts as in (A), detected in the raw (black) and denoised (red) LFP. Bottom, the difference between the two distributions above, computed for the raw and denoised LFP. Counterintuitively, the occurrence rate of bursts at frequencies > 150 Hz increased after the EMG noise removal. (C) Top, example distributions of the HFO burst power as a function of burst frequency calculated for the same bursts as in (A), detected in the raw LFP during RUN (solid black), denoised LFP during RUN (solid red), raw LFP during SWS sleep (dashed green), and raw LFP during REM sleep (dotted green). All the distributions were normalized by their integral. Bottom, the difference between the two distributions above, computed for the raw and denoised LFP during RUN. (D) Top, example color-coded joint distribution of the strength of HFO burst locking to the theta phase as a function of burst frequency and anatomical layer calculated for the bursts from the same session as in (A), detected in the raw LFP. Red and blue colors indicate the maximum and the minimum rate values correspondingly. The strength of theta phase locking was quantified by the length of Rayeigh's resultant vector (see Methods). Middle, same as at the top, but for the bursts detected in the denoised LFP. Bottom, the color-coded difference between the two joint distributions above, computed for the raw and denoised LFP.

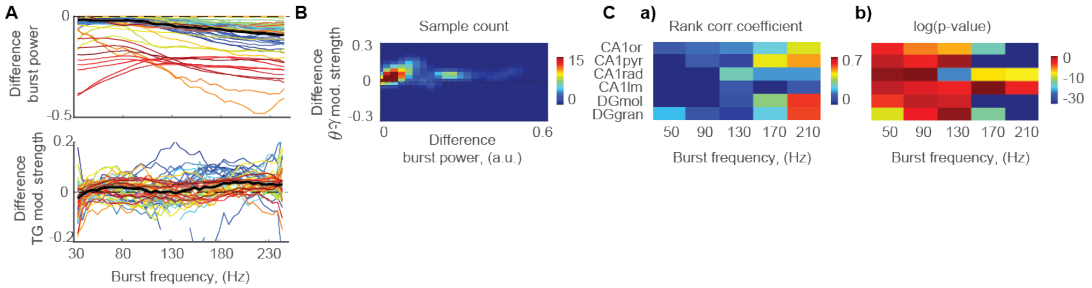

Figure 5.9: Effect of the EMG noise removal on high-frequency oscillation (HFO) bursts. A. Difference between the frequency-resolved burst power (a.u.) profiles (top) or the theta phase modulation (TG mod.) strength profiles (bottom) computed for the denoised and raw LFP (solid black – the averaged (median) profile, different colors – the raw session-specific profiles). The burst power difference is normalized by the power of raw data for pooling across sessions. Same as in the appendix (fig.E.4) where different rows show data for different hippocampal layers. This example comes from the CA1 l.m. bursts. B. Example color-coded joint probability distribution of the profile samples from A top and bottom collected across the sessions ($n = 53$ from 13 animals) as a function of the absolute change in burst power and change in burst theta phase modulation strength after the EMG denoising. This example map was computed for the CA1 l.m. bursts with the frequency of $150 - 190$ Hz. Color depicts the number of profile samples in each map bin (blue - minimum, red – maximum values). C. a) Color-coded map of the rank (spearman) correlation between the absolute change in burst power and change in theta phase modulation strength after the EMG denoising, computed for the bursts from the given anatomical layer and from the given frequency bin. The rank correlation coefficient was computed for the sample pairs collected across the sessions (n=53 from 13 animals). Color depicts the correlation strength (blue - zero, red – maximum values). b) Same color-coded map as in a), but for the p-values (log), corresponding to the rank correlation values in a).

noise, the smaller power gamma burst is rescued, especially in the ripple band near the somata layer. Including them leads to better theta phase modulation, which confirms their physiological origins. Removing EMG with our toolbox helps to improve the physiological signals.

5.4 Discussion

In summary, we explored EMG cleaning with blind source separation in freely moving animals. We find that low-frequency local brain activity affects the detection, and training the components in the high-frequency enhanced data would help to improve the noise separation. Similar to previous observation (Artoni et al., 2012), training EMG detection in high noise periods would improve the separation. Therefore we train the detection only in the awake periods with high correlations between randomly selected channels. With these processes, we are able to separate EMG-related far-field signals and reduce the influence of slow physiological oscillations or large global events like sharp waves (Buzsáki, 2015).

Taking advantage of local high-density recording, we propose the flatness score as a criterion for automatic component selection and provide a toolbox for noise detection and removal. In practice, we find a better flatness score usually indicates the existence of large EMG noise, and the separated component is less contaminated by the large synchronization in local areas. We provide various reporting figures for the users to assess the separation performance. As a general pre-process toolbox, power line noise removal is also included in the toolbox.

With the freely moving animal experiments, we show that EMG noise constantly presents and dominates the high-frequency signal bands (Sirota et al., 2008). By removing the EMG-related far-field component, we are able to rescue the over-shadowed local physiological signals. This way, we also save the signals which would otherwise be discarded in practice due to high EMG noise contamination. We find that automatic detection works reliably in awake animals. This could be used as a pre-processing toolbox for high-density recordings (Buzsáki, 2004, Jun et al., 2017).

5.4.1 Non-stationarity and Reliability of Artifacts Extraction

In practice, ICA based method suffers from cross-contaminations, especially from spatially similar components. This is also a problem we face in real data, especially when there are large global synchronizations or when the EMG noise is negligible, e.g., in head-fixed animals. In these cases, the flattest component will also be selected, but normally, the flattest components estimated over nearby time windows are not stable compared to periods with EMG artifacts (fig.5.1 D). This could be developed into a local criterion for the users to decide whether to

discard the component.

Apart from the large local synchronization, we sometimes find contamination from the local slow signals, indicated by the coherence power of denoised LFP signal and EMG signal at slow frequencies, especially lower than 20 Hz. They could come from general theta oscillation in the Dentate Gyrus, whose power overdominance the CA1 recordings (fig.5.1 D). Removing the signal will introduce spurious signals, especially in the hippocampal recording sites. Besides, the slower frequency band signal is hardly affected by the EMG noise (Muthukumaraswamy, 2013). Therefore, in practice, we suggest performing EMG removal on the signals above 30 Hz.

5.4.2 Flat Components vs. CSD

An alternative method to remove the far-field components, or in general volume conduction, is to compute the current source density (CSD) of LFP data (Nicholson & Freeman, 1975). As pointed out by later works (Pettersen et al., 2006), the CSD computed by simple or smoothed spatial Laplacian is limited by the noise in the recording. Therefore, recent works use a smooth current source basis to fit the underlying current sources, like inverse CSD or kernel CSD (Pettersen et al., 2006, Potworowski et al., 2012). However, this way, the method also introduces the smoothness assumptions into the data. Moreover, noise from a short period of broken channels could influence the interpretation of CSD without careful examination. Our method, on the other hand, focuses on removing far-field volume conducted signals and utilize the assumption that EMG-related far-field signal should be independent of the local signals. The EMG component is generally independent of any other noise sources with localized spatial profiles. By removing the component, we get rid of a flat component that shares the least dependence with any of the rest components and the signal space spanned by them. And Compared to removing the spatial average of the signal, ICA components could adapt to current data and account for small differences in the channel impedance.

Our method also removes large stripe-like noise (fig.5.6) as well as line noise which doesn't have a stereotypical spatial profile (see in appendix fig.E.1)). The EMG-removal toolbox could be used as a pre-processing step before applying CSD analysis.

Another problem is whether this method is useful in other recordings, for example, tetrode assembly (Nguyen et al., 2009), where there is no clear pairwise distance between recording sites. In this case, we hypothesize our method should still be useful because the spatial difference within the same bundle is small, and the phase difference between recording shanks appears to be generally very small (fig.5.4). The other problem is how to detect high EMG periods, which appears to be critical in finding the right component. Recordings in the same layer

could be enrolled in low-frequency oscillations (Sirota et al., 2008). But this step could be improved by using recordings from other areas or setting up an EMG recording channel. Therefore it's worth further validating whether extracting a "flat" component from these data would help to clean the data.

Algorithm 1 EMG removing

Input: data x, size $nchannel \times nt$, line noise ratio threshold $line_thrd$
Output: denoised data x_{new} and unit variance EMG activity EMG_au, as well as its mixing and unmixing matrix A_s and W_s
STEP 1: Cluster Periods: detect high EMG period EMG_thrd with $EMG\_Cluster\_s.m$ and chunck the long data session into n sug_period.
Denoise: Initialized the denoised data with $x_{new} = 0$, with high density probe channels:
for $i = 1$ **to** n **do**
  Temporal whiten the signal and get the whitened signal wx
  STEP 2: Power Line Noise:
  Detect the line-noise A_rm_line with largest $power\_ratio$ on wx
  if $power\_ratio > line\_thrd$ **then**
    Remove line noise from both x and wx.
  end if
  STEP 3: EMG Noise:
  High pass filter wx and get hx
  $[A, W] = fastica(hx)$
  Select EMG_comp with largest flatness equ.5.5, denote its mixing and unmixing matrix as A_s and W_s.
  if $denoise\_frequency\_lowerbound > 0$ **then**
    $EMG\_au = filter(x \times W_s', denoise\_frequency\_lowerbound, 'highpass')$.
  else
    $EMG\_au = x \times W_s'$.
  end if
  Smooth the EMG traces at the ends of each period.
  Remove EMG noise from x by $x_{new} = x - EMG\_au \times A_s$
end for
Copy all the other channels to x_{new} and save data to $.lfpd$.
Save A_rm_line, W_rm_line, A, W and EMG_au into a separate $.mat$ file.
Generating report figures.

Chapter 6

Discussion

Understanding the dynamics of the brain and the communication between brain areas has been a fundamental question in neuroscience. With the recent advance in neuroanatomy, it has become possible to ground the functional connectivity on the structure connectivity (Honey et al., 2009). LFP is an intermediate stage for connecting the macroscopic scale signal to microscopic neuron-level dynamics. This thesis aims to provide solutions to bridge the biophysics and the electrophysiology recording and combine the anatomical-prior to signal interpretation.

In Chapter 2, we start with the unsupervised segregation of pathway-specific LFP. Deriving from the cable equation, we demonstrate that temporal derivative or linear model fitting reduces the capacitive effect and biases the LFP signal to its input. We find that operating on the temporal differential data emphasizes the high frequency where the signal is sparser and better localized to its synaptic inputs, leading to a more stable separation while preserving the broadband temporal structure. This approach also reveals high-frequency patterns hidden by the dominant low-frequency signals. With the broadband signal, we fit the average synaptic response time constant to the spectral baseline. The longer time constant observed on pathway target at the apical dendrites could be explained by a higher $NMDA/AMPA$ ratio. Multiple hippocampal components exhibit high coherence with entorhinal superficial layer components (fig.2.11). We find directional connections that agree with previously known anatomy by applying Granger causality to remove the confound of the indirect influences. Interestingly, the directional connection within the hippocampus or entorhinal cortex shows strong slow frequency content, meaning the slower frequency of the signal is better predicted by inputs from the same region. However, we find the cross-area long-range connection shows a strong peak at the higher frequency.Compared to high-frequency oscillations, causality strength in the slower frequency range is highly influenced by short-range (local) connections, indicating that instead of being a pure afferent copy from the upstream area, slow frequency components of the oscillatory signal also relie on local mechanisms and involve local nonlinear integration.

Next, in chapter 3 we propose a simple parametric model to capture the input-response of passive morphologically detailed neurons. Instead of studying membraine integration using multicompartmental numeric simulation, this model aims to establish a simple and fast approximation of the input current's impulse response at any arbitrary dendritic site and, effectively, provides a closed-form solution of the cable equation for a specific neuron. The model captures the dendritic filtering effect and provides an easy solution allowing one to explore how the cytoarchitecture of neuron population affects the LFP spatial profile. We show that the laminar impulse response of a heterogeneous population could be captured better by its average laminar Green's function, but when the actual cell morphologies are not accessible, it could still be captured with an arbitrary pyramidal cell morphology with less precision. This analytical framework sets the foundation for our model-based blind source separation approach.

Based on the modeling in chapter three, we propose a biophysical model regularized frequency domain source separation framework. This method cluster components across frequencies into different pathways. It uses the laminar approximations to fit a biophysical plausible spatiotemporal profile for each cluster in the more independent or sparser frequency range and then rescues the component separation in the slower and more contaminated frequencies. We validate the method with optogenetic stimulation and find this method captures interesting spatiotemporal dynamics of CA1 distal dendrites. However, this method is still slow and needs to be optimized for practical usage. Nevertheless, it shows the potential to build a physiologically inspired probabilistic model capturing the spatiotemporal pattern of the LFP.

Finally, throughout the analysis, we find strong EMG noise contamination, especially in the high frequency (> 100 Hz). Therefore we developed an EMG-removing toolbox that automatically detects and removes EMG and power-line noise for high-density recording. The method discovers the EMG component by separate sources in noise-enriched data segments. Inspired by previously found EMG signal frequency profile (Muthukumaraswamy, 2013), we enhance the EMG content by temporal whitening the data.According to the far-field nature of EMG noise, we propose flatness as a measure to automatically detect the noise component. This method works reliably in freely moving animals and greatly improves analysis of the high-frequency oscillatory activity.

Beyond the current stage of the Green's function based LFP model, there is a large space for improvement. Here I name a few of them. First, besides the current pyramidal neuron models in the hippocampus CA1 area, we need to extend Green's function laminar basis with more cell types in other regions, including granule cells and stellate cells. The granule cell in the Dentate Gyrus has a characteristic cone-shaped tree of spiny apical dendrites. This would lead to a different dipole shape from the typical pyramidal cell dipole shape, especially around the soma. The stellate cells in the entorhnial cortex typically have a

star-like shape formed by similar-length dendrites radiating from the cell body. This type of dendritic tree hardly forms a large dipole that could be detected afar, but they will contribute to the local electrical field (Tang et al., 2014, Gratiy et al., 2011).

Second, when we consider the LFP recording across multiple regions, there are some other concerns. In this case, if the independency or sparsity is fulfilled, the temporal independence will help separate components. Our fitting would still work since it has already parameterized the scale and offset of the latent neurons for each cluster, respectively (see chapter 3.1.3). However, when different cell types are included, the cell type selection needs to be implemented with sparsity or with a categorical distribution for the probabilistic model. But the situation could be more complex when we consider arbitrary cytoarchitecture, e.g., the folding of dentate gyrus (Fernández-Ruiz et al., 2013). In this case, both blades of the Dentate Gyrus should be modeled, and a ratio of synaptic distribution should fit the suprapyramidal blade to the infrapyramidal blade axis. Another concern is the highly overlapped dendritic trees in the cortical superficial layers. Take the entorhinal cortex as an example: while the cell body of layer II and layer III pyramidal cells are spatially segregated, their dendritic trees both extend to layer I, making it very hard to separate them from each other. Future work could explore whether including prior knowledge of the cell anatomy might help the separation and identification of superficial layer LFP components.

Furthermore, various inhibition patterns play an important role in information processing in local networks, regulate local oscillations (Fishell & Kepecs, 2020, Wang, 2010), and the postsynaptic currents induced by inhibitory synapses also contribute to LFP (Teleńczuk et al., 2017). But due to their dendritic profile and cell body alignment, the contribution of the interneuron dipole is usually ignored. Further work could also explore how to involve them in the modeling framework properly.

Our analysis in chapter 4 also depicted a general involvement of active conductance in LFP signals. We need to validate the nonlinear mechanism underlying these component dynamics by pharmacology and chemical manipulation of presynaptic nuclei in the future (Benito et al., 2014). The subthreshold nonlinear conductance should be carefully treated in constructing the LFP impulse-response kernels. Besides, it would be interesting to explore in future work how much the spatio-temporal profile from source separation could tell about the active conductance properties, especially in the state-dependent manner (Hasselmo & Stern, 2014).

In chapter 2, we have used the hippocampus example to show the potential of separating afferent pathways from local recurrent circuits and study their interaction with causal analysis. It will be essential to validate the component identity and the directional link with experiments in future work. Optogenetic

perturbation, including MEC and LEC perturbation, could be applied to validate the identity of the afferent pathway, as well as the cross-regional connection (Fernández-Ruiz et al., 2021). The casual discovery reduces the effect of indirect connections and, therefore, generally tells more than simple coherence analysis. But our current analysis is based on a multivariate linear model that might suffer from nonlinear interactions, for example, the nonlinear dendritic integration. It would also be interesting to tell apart how much of the local oscillations come from afferent copies of the upstream dynamics versus from the local recurrent E-I network (Schneider et al., 2021) Rigorous validation of the causal inference with the above-mentioned experiments would be important.

Lastly, we want to put a few more words about how can our LFP analysis help to mediate the dialogue between the study of microscopic scale cellular-level processes and macroscopic scale circuits-level neurodynamics. Various network has been explored to map the cellular-level processes to macroscopic scale recording systems (Wang, 2022). However, considering the complex processes involved in local neuron level and network level integration, the inverse problem is generally ill-posed, and the activity accounted for by current models is still limited. Here we propose a model-matching framework to simplify the complex system with a mechanistic model, which can be explored in future work. Generally speaking, the point is to separate the dendritic integration from the point neuron model and simplify the former by compartmentalized integration modules. This way, a mean-field model with compartmentalized dendritic modules defined by the synaptic target profile could directly incorporate structure information, with the compartment segmentation informed by the receptor expression and the synaptic efficacy modeled as a function of neural modulation. The modeled variables could be read out and therefore matched by multiple mesoscopic level recording techniques, like LFP and calcium imaging (fig.6.1).

This framework aims to integrate many advances in neurobiology. In more realistic situations, nonlinear process plays an important role in the dendritic integration (Magee, 2000), to make it more complex, the channels are modulated by the brain state (Delmas & Brown, 2005, Arnsten et al., 2012, Hasselmo & Stern, 2014, Shine et al., 2019) with complex spatiotemporal patterns (Lohani et al., 2022). This requires adding the neuromodulator systems and their signaling pathways to the model. Here we use a hierarchical Bayesian framework to illustrate the idea.

Instead of assuming two homogeneous cell classes and including variables or channels directly in the mean-field neuron mass model, the model needs to take care of the heterogeneity of local populations informed by their intrinsic properties and structure connectivities (Cembrowski & Spruston, 2019). This could be achieved by incorporating anatomical priors and calibrating the model by adding these intermediate steps, like modeling the LFP profiles. Recent works provide various useful neuroanatomy knowledge like the spatial profile of Cyto-, myelo-,

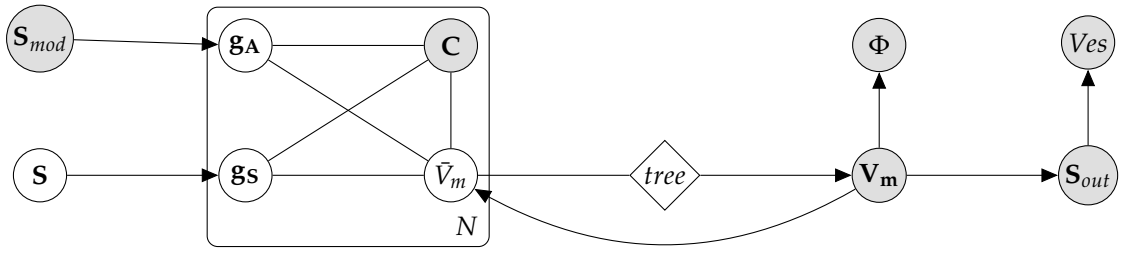

Figure 6.1: Schematic of the simplified mechanistic modeling framework. **S** stands for the upstream inputs to local networks. The post-synaptic conductance $\mathbf{g_S}$ response to their corresponding neurotransmitter and changes local membrane potential V_m. Here we mainly consider the calcium-related second messager system. The change of V_m together with the calcium concentration **C** influence a consecutive response of voltage- and ligand-regulated active conductance $\mathbf{g_A}$, which is further regulated by the neuromodulator systems $\mathbf{S}_{mod}$. The N plates denote the compartmentalization of dendritic integration by common inputs and intracellular calcium buffering, and the complex and slower calcium concentration **C** is modeled in each module accordingly. The $\bar{V}_m$ for local membrane potential, with a mean field approximation, is introduced here for computational convenience. The membrane potential V_m is then computed by $\bar{V}_m$, and action potential is generated accordingly, denoted as S_out. LFP Φ is determined by membrane potential V_m. Neurovascular coupling then links the transient neural activity S_out to the subsequent change in cerebral blood flow V_{ves}, which leads to the fMRI signals. Every component here is vector-based, and the dark notes mark the observable variables (table 6.1).

receptor- and synaptic architecture within local region (Palomero-Gallagher & Zilles, 2019, Shine et al., 2021, Gao et al., 2020, Cembrowski et al., 2018) and the structure connectivity (Honey et al., 2009, Majka et al., 2020) between regions and combined (Harris et al., 2019). LFP spatial patterns would naturally pick up the synaptic connection and the receptor profile, and the receptor kinetics could be modeled into their impulse response spatio-temporal patterns confined by dendritic morphology. To capture the nonlinear input integration, we need to consider the intercellular signaling, including Ca^{2+} dynamics and the second messagers systems (fig.6.1 plates). It should be quantitatively validated in future works how much of the compartmentalization by synaptic distribution would agree with the compartmentalization by the intercellular process like Ca^{2+} (O'Hare et al., 2022). When proper compartmentalization is found, then their dynamics would be further captured by a few analytical functions (Brunton et al., 2016, Rudy et al., 2019, Hasani et al., 2022). Various neuromodulators $\mathbf{S}_{mod}$ also influence the local dynamics by modulating the active conductances. With these steps, we could model how the multiple inputs **S** to the local network are integrated, which would be read out by the electrophysiology signals (fig.6.1). Then

Table 6.1: List of Observation techniques.

Variable	Observation Techniques
V_m: membrane potential	juxacellular recording (Pinault, 1996)
Φ: field potential	LFP (Buzsáki, 2004), EEG (Nunez et al., 2006)
$\mathbf{S}_{out}$: population activity	Utah arrays (Dickey et al., 2009), Neuropixels (Jun et al., 2017)
Ves: vesicular coupling	fMRI (Logothetis, 2008)
C: $[Ca^{2+}]$	calcium imaging (Grienberger & Konnerth, 2012)
$\mathbf{S}_{mod}$: $[Neuromodulators]$	Genetically encoded sensors imaging (Sabatini & Tian, 2020)

the output: the elicited population firing $\mathbf{S}_{out}$, with another layer of dynamical modeling from $\mathbf{V}_m$, could also be detected by electrophysiology measurements, and they would further lead to the subsequent change in cerebral blood flow, which causes the signals measured by fMRI recording (table 6.1). Overall, the idea is to integrate the anatomical information and fit the model with multiple objectives calibrated by different recording techniques (fig.6.1 and table 6.1).

Grounded on the microscopic level priors, the model will help to understand how different mechanisms jointly modulate brain circuits at the mesoscopic scale. With the explicit mechanistic modeling of the local circuits, we can capture the fast time scale nonstationary coupling of neural populations, which helps to understand the flexible brain cognitive functions (Fries, 2015). Since the recordings generally sample in different spatial and temporal scales, a detailed simulation framework would suffer from a great amount of computation. Therefore we turned to summarize the system response steps with a few spatio-temporal patterns. Formulating the general multi-objective model with simpler impulse-response filters of proper compartmentalization at different levels or even conducted in the frequency domain might be interesting to explore in the future.

Appendix A

Linear model discretization

Here we derive the details of discretizing the state space model.

A.1 State Space Model of Membrane Potential

According to equation 2.3 we first discretize the continuous membrane model into the multi-compartment model:

$$\begin{array}{rcl} \frac{\partial \mathbf{V}}{\partial t} & = & C_m^{-1}\left(-G_l\mathbf{V} + G_A\mathbf{V} - \sum_j^h Ga_j(x,\mathbf{V})(\mathbf{V} - E^*_{Ga,j}) - \sum_i^k A_i(x)s_i(\mathbf{V} - E_i^*)\right) \\ \frac{\partial \mathbf{S}}{\partial t} & = & -\tau_i\mathbf{S} + n_i. \end{array} \tag{A.1}$$

where at each compartment, $\mathbf{V_i} = V_i - E_l$, and $\{E^*_{Ga,j}\}$ and $\{E_i^*\}$ are relative reversal potentials of each channel type compare to the E_l.

Here we only consider the low synaptic inputs scenario. Therefore, we consider only the linear part of the system and drop the effects of active channels. The synaptic currents are also considered as current injections in the region of the low synaptic inputs. The full matrix form of equation A.1 could be reduced to:

$$\frac{\partial \mathbf{V}}{\partial t} = C_m^{-1}(-G_l\mathbf{V} + G_A\mathbf{V}) + C_m^{-1}A_s\mathbf{S} = C_m^{-1}(G_A - G_l)\mathbf{V} + C_m^{-1}A_s\mathbf{S},$$

$$where \quad V_t = \begin{pmatrix} V_{1,t} \\ ... \\ V_{n,t} \end{pmatrix}, \quad S_t = \begin{pmatrix} s_{1,t} \\ ... \\ s_{k,t} \end{pmatrix}, \quad A_s = \begin{bmatrix} | & & | \\ A_1, & ... & A_k \\ | & & | \end{bmatrix} \tag{A.2}$$

Considering of the slower changing of the synaptic conductance compared to the

fast membrane conductance, for a small period T, we have:

$$\begin{aligned}
\mathbf{V}(T) &= e^{A_x T}\mathbf{V}(0) + \int_0^T e^{A_x(T-t)}C_m^{-1}A_s\mathbf{S}(t)dt \\
&= e^{A_x T}\mathbf{V}(0) + e^{A_x T}\int_0^T e^{A_x(-t)}C_m^{-1}A_s\mathbf{S}(t)dt \\
&= e^{A_x T}\mathbf{V}(0) + e^{A_x T}\int_0^T e^{A_x(-t)}dtC_m^{-1}A_s\mathbf{S}(0) \\
&= e^{A_x T}\mathbf{V}(0) + e^{A_x T}(-e^{-A_x T}A_x^{-1} + A_x^{-1})C_m^{-1}A_s\mathbf{S}(0) \\
&= e^{A_x T}\mathbf{V}(0) + (e^{A_x T} - I)A_x^{-1}C_m^{-1}A_s\mathbf{S}(0) \\
\textit{where} \quad A_x &= C_m^{-1}(G_A - G_l)
\end{aligned} \tag{A.3}$$

the third line is because synaptic conductance $S(t)$ changes much slower than the membrane conductance so we could assume it to be constant during the interval from 0 to T.

Due to system time invariance the same expressions are obtained for any time interval from kT to $(k+1)T$, the discretized model of membrane potential could be written as:

$$\begin{aligned}
V((k+1)T) &= A_V V(kT) + B_V S(kT) \\
\textit{where} \quad A_V &= e^{C_m^{-1}(G_A - G_l)T} \\
\textit{and} \quad B_V &= (A_V - I)(G_A - G_l)^{-1}A_s
\end{aligned} \tag{A.4}$$

$A_s \in R^{N\times K}$ is the synaptic distribution of all the pathways.

The synaptic activity could also be discretized in the same way:

$$\begin{aligned}
S((k+1)T) &= A_{SI}S(kT) + B_S\mathbf{E}(kT), \\
\textit{where} \quad A_{SI} &= e^{A_\tau T} \\
\textit{and} \quad B_S &= (A_{SI} - I)A_\tau^{-1}.
\end{aligned} \tag{A.5}$$

Here A_τ represents the time-constant matrix of the synapses. $\mathbf{E}$ stands for the pathway-specific inputs.

A.2 Auto-Regressive Model of LFP

The LFP is the observable variable of the system, in the multi-compartment model, for simplicity here, we ignore other noise current sources and only consider the pathway contributions. The LFP signal could be derived from membrane potential as:

$$\Phi_{kT} = H\nabla V(kT). \tag{A.6}$$

To derive the state space equation of LFP, i.e., Φ_{kT}, we multiply both sides of equation A.4 with $B^* = H\nabla$:

$$\begin{aligned} B^*V((k+1)T) &= B^*A_V\tilde{B}\begin{bmatrix} B^* \\ B^{*/} \end{bmatrix} V(kT) + B^*B_V S(kT) \\ \textit{namely} \qquad \Phi((k+1)T) &= B^*A_V\tilde{B}\begin{bmatrix} \Phi(kT) \\ \Phi^{*/}(kT) \end{bmatrix} + B^*B_V S(kT) \end{aligned} \tag{A.7}$$

where B^* maps membrane potential to LFP. But remember that $B^* \in R^{m\times n}$ so it is full row rank, we define $B^{*/}$ to span the orthogonal complement space of B^* and for any $B^{*/}$, we have a $\tilde{B}$ to make sure that $\tilde{B}\begin{bmatrix} B^* \\ B^{*/} \end{bmatrix} = I_{N\times N}$.

From A.7 we could also find that parts of the information span in $B^{*/}$ and captured by $\Phi^{*/}(kT)$ is lost due to the down-sampling of the space.

We could write A.7 as:

$$\Phi((k+1)T) = A_\Phi\begin{bmatrix} \Phi(kT) \\ \Phi^{*/}(kT) \end{bmatrix} + B_\Phi S(kT) \tag{A.8}$$

$$\textit{where} \qquad A_\Phi = B^*A_V\tilde{B} \qquad \textit{and} \qquad B_\Phi = B^*B_V$$

For simplicity, we assume a full column rank of B_Φ, i.e., the number of sources is equal to the number of recording sites. Moving the LFP terms to the left-hand side, we obtain the relationship between Φ and S.

$$S(kT) = B_\Phi^+\left(\Phi((k+1)T) - A_\Phi\begin{bmatrix} \Phi(kT) \\ \Phi^{*/}(kT) \end{bmatrix}\right) \tag{A.9}$$

Where B_Φ^+ is the pseudo-inverse of B_Φ which fulfill $B_\Phi^+B_\Phi = I_{K\times M}$.

Putting A.8 and A.5 together, we could further write the LFP into a multivariate auto-regressive model:

$$\sum_{i=0}^{2} Z_i\Phi(t+i) + \sum_{j=0}^{1} Z_{*/j}\Phi^{*/}(t+j) = \mathbf{E} \tag{A.10}$$

$$\begin{aligned} \textit{where} \quad Z_2 &= B_S^{-1}B_\Phi^+, \\ Z_1 &= -B_S^{-1}(B_\Phi^+A_{\Phi,:m} + A_{SI}B_\Phi^+), \\ Z_0 &= B_S^{-1}A_{SI}B_\Phi^+A_{\Phi,:m}, \\ Z_{*/1} &= -B_S^{-1}B_\Phi^+A_{\Phi,m+1:}, \\ Z_{*/0} &= B_S^{-1}A_{SI}B_\Phi^+A_{\Phi,m+1:} \end{aligned} \tag{A.11}$$

where $\Phi^{*/}$ span the orthogonal complement space of Φ.

Appendix B

ICA on Ill-condition Scenarios

B.1 Non-Gaussian Brain Signal

Claim: (non-Gaussian brain signal) Sparse input inducts the synaptic activity distribution will not be Gaussian. Here we define sparse as the dynamics region where the activated synapses are far from saturation.

Proof. we use the result of chapter 4.3 in (Tuckwell, 1989). In constraint of sparse input, the response of a group of unsaturated synapses could be described as Stein's model (chapter 4.1 of (Tuckwell, 1989)). In particular, input is modeled as a jumping process with amplitude as an independent variable drawn from ϕ, and there will be exponential decay with a certain time constant between consecutive jumps. There exist a close form solution given stationary input process ϕ. The characteristic function of membrane potential pdf p is given by:

$$\tilde{p}(\omega,t) = exp\left\{\int_{\omega e^{-t}}^{\omega}\left(\frac{\tilde{\phi}(\omega')-\alpha_i}{\omega'}\right)d\omega'\right\}\tilde{p}_0(\omega e^{-t}), \tag{B.1}$$

where α_i denotes the time constant of the exponential decay of open synapses. In the equation,denotes jump amplitude distribution which is strictly positive for any synapses. $\phi(x) = \delta(x - c_E)$

In the condition of a limited amount of synapses, there is no close-form solution as we noticed. We refer to (Destexhe et al., 1998) for a numerical solution by simulating synaptic transmission as Markov process. Therefore, the distribution of post-synaptic activity is determined by presynaptic inputs.

On the other hand, (Parra & Spence, 2000) proved that non-stationarity justifies higher-order criteria. In particular, assuming signal x is draw from a zero mean stochastic process z P_z modulated by a independent scale s P_s, namely: $x(t) = z(t) \cdot s(t)$, then kurtosis $K[x]$ of long term distribution of x is given by $K[x] = K[z]\frac{E(s^4)}{E(s^2)^2} \geq K[z]$. The equality holds if and only if s is fixed to an arbitrary constant, s.t. $x(t)$ is a stationary process proportional to $z(t)$.

The neuronal input is usually assumed to be Poisson distributed or lognormal distributed. Kurtosis in both case is larger than 3. We could use Kurtosis for a gaussian distribution is 3, but the modulated one is larger than 3. Overall, a neuronal input with nonstationary scaler modulation should be nongaussion with sparser distribution. And as we proved in eq.B.1, the arisen synaptic activity is also non-gaussian.

To summarize, the overall proof can justify widely used non-Gaussian source separation on EEG signals or other imaging methods which have non-stationary inputs, even when the input process could be approximated by non-stationary Gaussian.

B.2 ICA under Partially Synchronized Scenario

Here we look at the convergence of ICA under a partially synchronized scenario. The convergence of independent sources follows the Theorem 8.1 of (Hyvärinen & Oja, 2000). We consider the case where the independent sources $s = [s_1; s_2]$ is affected by a synchronised source s_3, makes $\tilde{s} = [s_1 + \alpha_1 s_3; s_2 + \alpha_2 s_3]$. This resembles occasional strong synchronizations of multiple pathways.

Theorem 8.1 Assume that the input data follows the ICA model with whitened data: $z = VAs$ where V is the whitening matrix and that G is a sufficiently smooth even function. Then the local maxima (resp.minima) of $E\{G(\mathbf{W^T z})\}$ under the constraint $||\mathbf{W}|| = \mathbf{1}$ include those rows of the mixing matrix VA such that the corresponding independent component s_i satisfy

$$E\{s_i g(s_i) - g'(s_i)\} > 0 (resp. < 0) \tag{B.2}$$

where $g(.)$ is the derivative of $G(.)$, and $g'(.)$ is the derivative of $g(.)$.

This theorem shows that any non-quadratic function G could be used to perform ICA.

Denote by $H(w)$ the function to be minimized/maximized, $E\{G(\mathbf{w^T z})\}$. Make $\mathbf{q}$ the orthogonal change of the coordinates. Then the gradient of $\frac{\partial H(\mathbf{q})}{\partial \mathbf{q}} = E\{\mathbf{s} g(\mathbf{q^T s})\}$ and the Hessian as $\frac{\partial^2 H(\mathbf{q})}{\partial \mathbf{q^2}} = E\{\mathbf{s s^T} g'(\mathbf{q^T s})\}$. Without loss of generality, we look at $\tilde{s} = [s_1 + \alpha_1 s_m; s_2 + \alpha_2 s_m; s_3; ...; s_n]$ at the point $\mathbf{q} = \mathbf{e_1}$, where $e_1 = [1, 0, 0..., 0]$. Assume the independent sources $s = [s1, s2, ...]$ fulfills theoremB.2, The gradient and the Hessian at point $\mathbf{q} = \mathbf{e_1}$ is:

$$\frac{\partial H(e_1)}{\partial \mathbf{q}} = e_1 E\{\tilde{s}_1 g(\tilde{s}_1)\} \tag{B.3}$$

and

$$\frac{\partial^2 H(\mathbf{q})}{\partial \mathbf{q}^2} = \begin{bmatrix} E\{\tilde{s}_1^2 g'(\tilde{s}_1)\} & E\{\tilde{s}_2\tilde{s}_1 g'(\tilde{s}_1)\} & & \\ E\{\tilde{s}_1\tilde{s}_2 g'(\tilde{s}_1)\} & E\{\tilde{s}_2^2 g'(\tilde{s}_1)\} & & \\ & & E\{g'(\tilde{s}_1)\} & \\ & & & \ldots \end{bmatrix} \tag{B.4}$$

Making a small perturbation $\epsilon = [\epsilon_1, \epsilon_2, ...]$ we obtain:

$$\begin{aligned} H(e_1+\epsilon) &= H(e_1) + \epsilon^T \frac{\partial H(e_1)}{\partial \mathbf{q}} + \frac{1}{2}\epsilon^T \frac{\partial^2 H(\mathbf{q})}{\partial \mathbf{q}^2}\epsilon + o(||\epsilon||^2) \\ &= H(e_1) + \epsilon_1 E\{\tilde{s}_1 g(\tilde{s}_1)\} \\ &\quad + \frac{1}{2}[E\{\tilde{s}_1^2 g'(\tilde{s}_1)\}\epsilon_1^2 + 2 * E\{\tilde{s}_2\tilde{s}_1 g'(\tilde{s}_1)\}\epsilon_1\epsilon_2 + E\{\tilde{s}_2^2 g'(\tilde{s}_1)\}\epsilon_2^2 \\ &\quad + E\{g'(\tilde{s}_1)\}\sum_{i>2}\epsilon_i^2] + o(||\epsilon||^2) \\ &= H(e_1) + \epsilon_1 E\{\tilde{s}_1 g(\tilde{s}_1)\} \\ &\quad + \frac{1}{2}[E\{\tilde{s}_1^2 g'(\tilde{s}_1)\}\epsilon_1^2 + 2\alpha_1\alpha_2 E\{s_m^2 g'(\tilde{s}_1)\}\epsilon_1\epsilon_2 + E\{s_m^2 g'(\tilde{s}_1)\}\epsilon_2^2 \\ &\quad + E\{g'(\tilde{s}_1)\}\sum_{i>1}\epsilon_i^2] + o(||\epsilon||^2) \end{aligned}$$

because $||e_1+\epsilon|| = 1$ we get $\epsilon_1 = \sqrt{1-\epsilon_2^2-\epsilon_3^2} - 1$. Due to $\sqrt{1-\gamma} = 1 - \gamma/2 + o(\gamma)$, the higher order term could be neglected and so is the term with ϵ_1^2, ϵ_2^2 and $\epsilon_1\epsilon_2$,

$$H(e_1+\epsilon) = H(e_1) + \frac{1}{2}[E\{g'(\tilde{s}_1)\} - E\{\tilde{s}_1 g(\tilde{s}_1)\}]\sum_{i>1}\epsilon_i^2 + o(||\epsilon||^2)$$

Since $\epsilon_i^2 > 0$, here the e_1 should be a extreme point. It turns out to be very similar to the independent case, the only difference is here we look at $\tilde{s}$ instead of s. When the shared signal s_m is small or sparse enough, the distribution of $\tilde{s}$ still assembly the distribution of original s. In this case when the local extreme is deep enough, s.t. $[E\{g'(\tilde{s}_1)\} - E\{\tilde{s}_1 g(\tilde{s}_1)\}] > 0$ or (resp. <0) the extreme point should still be valid.

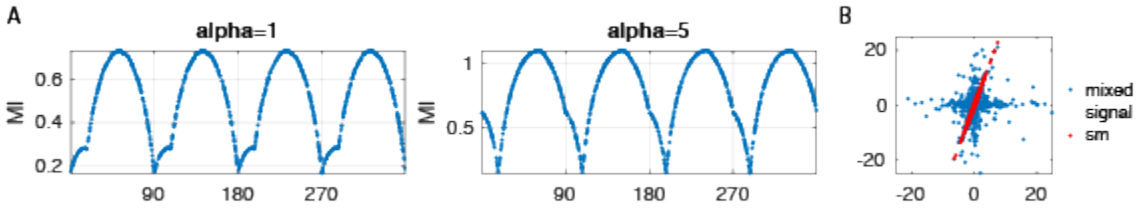

Figure B.1: ICA Convergence under the partially synchronized scenario. A. mutual information with different rotations(in degree). B. data distribution

Here we demonstrate with an example(fig.B.1). In the example, the random sample is drawn from a super-Gaussian distribution as x^3 where $x \sim N(0,1)$(fig.B.1 B). Here we use mutual information as G When the $alpha$ is small, mutual information shows local minimal at $n \times 90, n = 0, ...$ When $alpha$ is too large, the s_m start to dominate the optimization landscape.

B.3 Basic Proofs

B.3.1 Flatness

Theorem: For any unit L2 vector $\vec{x} \in \mathbf{R}^{n\times 1}$, where $\|\vec{x}\|_2 = 1$, then $\sum \vec{x} \leq \sqrt{n}$, with equality when $\vec{x}$ is a flat line with all the entries equal to $\frac{1}{sqrt(n)}$.

Proof: We consider when the vector $\vec{x}$ is not flat, then there exist entries k and n such that $V_{kn} := x_k^2 + x_n^2 = 1 - \sum_{\neq k,n} x_j^2$. We fix all the other entries of $\vec{x}$ and $\sum \vec{x}$ could be written as:

$$\begin{aligned}\sum \vec{x} &= \sum_{\neq k,n} x_j + x_k + x_n, \\ &= \sum_{\neq k,n} x_j + x_k + \sqrt{(V_{kn} - x_k^2)}, \\ &\leq \sum_{\neq k,n} x_j + 2\sqrt{(V_{kn}/2)},\end{aligned}$$

with equality when $x_k \equiv x_n$ using Jensen's inequality. ■

B.4 Reliability Test

Here we briefly summarise the core idea of isctest(Hyvärinen, 2011). Under H0, the mixing matrix $A_k = [\vec{a_{1k}}, ..., \vec{a_{nk}}]$ of the kth session will have the same distribution as $A_0 U_k$, where U_k is a random rotation matrix uniformly distributed in all possible rotation directions, and A_0 is a fixed arbitrary matrix. The test, however, doesn't estimate A_0 or U_k for each mixing matrix A_k. But instead, it defines the similarities of two vectors $\vec{a_{ik}}$ and $\vec{a_{jl}}$ as:

$$\gamma_{ij,kl} = \frac{\left|\alpha_{ik}^T R \alpha_{jl}\right|}{\sqrt{\alpha_{ik}^T R \alpha_{ik}} \sqrt{\alpha_{jl}^T R \alpha_{jl}}} \tag{B.5}$$

where $R = E_0 D_0^- 1 E_0^T$ is the projection into the global dominant eigenspace of all the vectors $\{\vec{a}\}$ over all the sessions, given by:

$$C = \frac{1}{nr} \sum_{ik} \vec{a}_{ik} \vec{a}_{ik}^T \qquad with \qquad C = EDE^T \tag{B.6}$$

the dimension of D_0 and E_0 is fixed as the same n as the dimension of components in each data session. The similarity γ is related to the Mahalanobis similarity. According to Theorem 1 in (Hyvärinen, 2011), under H0, each γ follows the distribution of the absolute value of an element of an orthogonal matrix uniformly distributed in the set $n \times n$ of orthogonal matrices. Then according to Theorem 2 for any entry u in a random matrix $U \in R^{d \times d}$, the transformed variable t:

$$t = \frac{u\sqrt{d-1}}{\sqrt{1-u^2}} \tag{B.7}$$

follows a Student's t-distribution with d-1 degrees of freedom, and u^2 follows a beta distribution with parameters $(\frac{1}{2}, \frac{d-1}{2})$.

Knowing the distribution of t and u^2 under the null hypothesis, a test for picking up components with a controlled false-positive rate (FPR) could be defined. To correct for multiple testing, isctest uses false discovery rate (FDR) proposed by (Benjamini & Hochberg, 1995) and the corrected significance level is given by :

$$\alpha_{FD}^{corr} = \alpha_{FD} \frac{n_\gamma}{m}, \tag{B.8}$$

where n_γ is given by Simes' procedure.

Next, the false positive rate for clusters is estimated to infer the existence of a consistent cluster of components. Isctest uses a Bonferroni correction TO CONTROL THE FPR of the clusters. The corrected threshold α_{FP}^{corr} is given as:

$$\alpha_{FP}^{corr} = \frac{\alpha_{FP}}{m}, \tag{B.9}$$

where the degrees of freedom is $m = \frac{n^2 r(r-1)}{2}$.

B.5 Supplimentary Figures

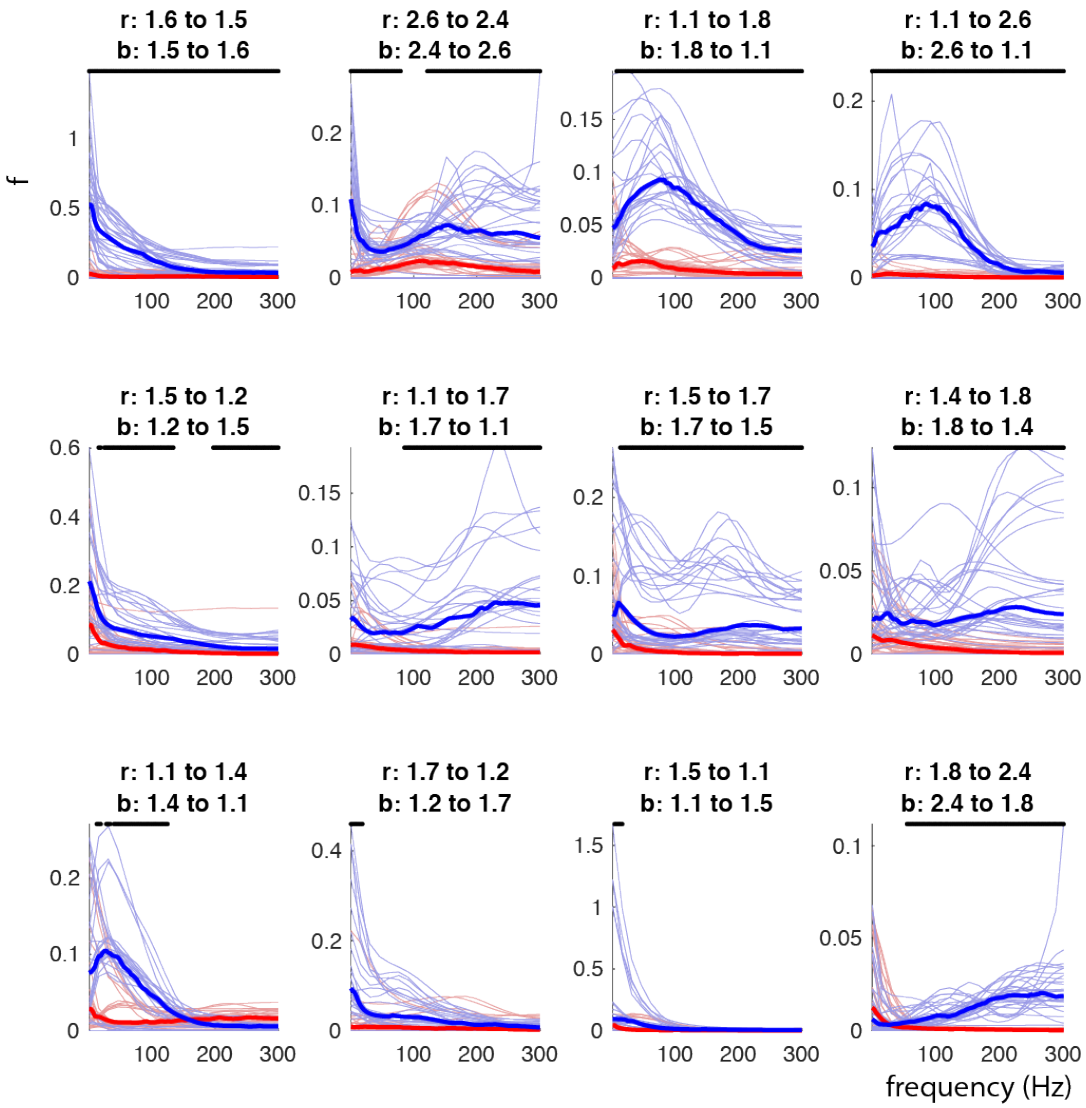

Figure B.2: Frequency domain functional connection between clusters. Black dots indicate the frequency where flow in one direction is significantly dominated (two-sided Wilcoxon signed rank test p<.05 corrected by Bonferroni correction). Component labels are the same as in fig. 2.12

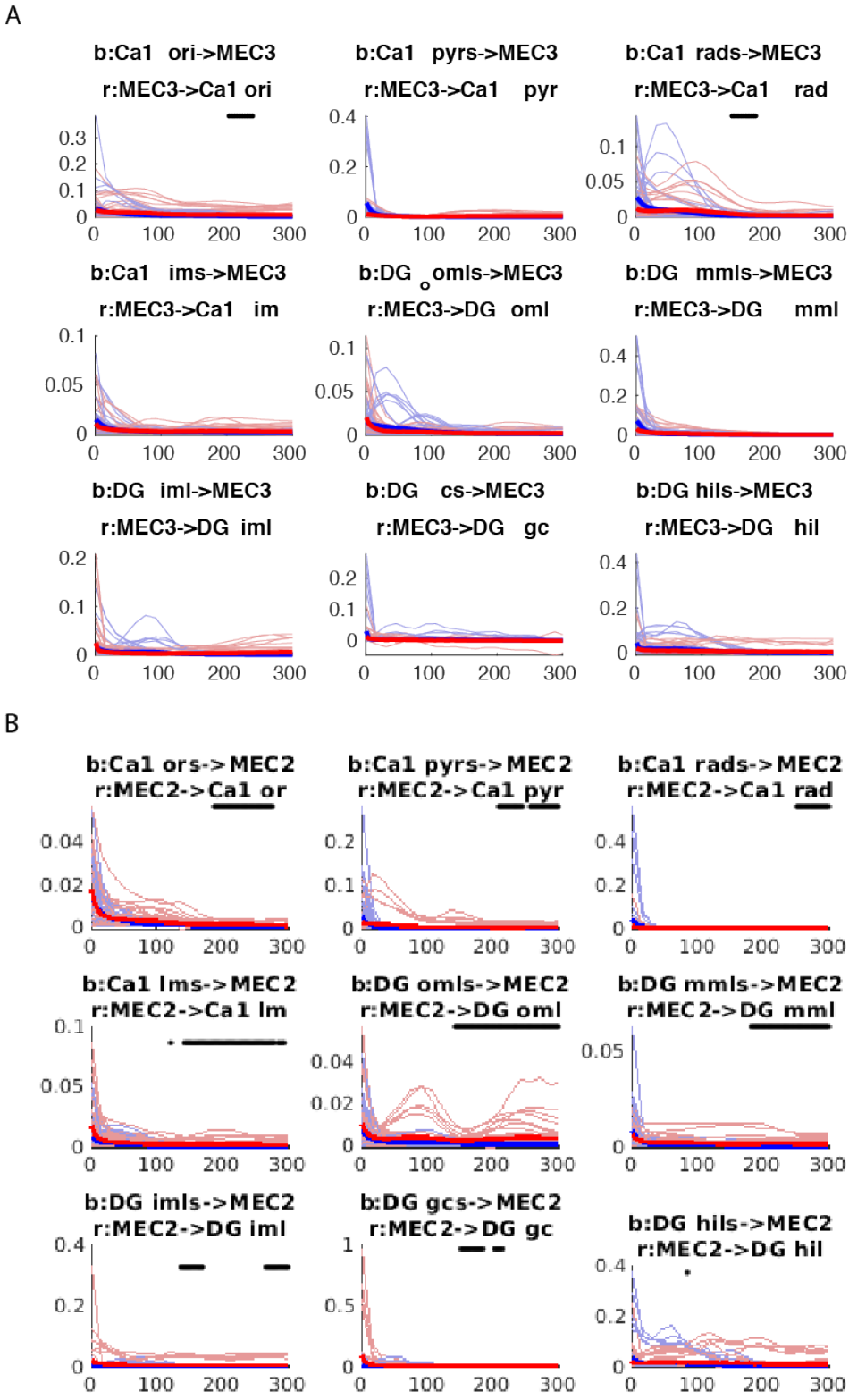

Figure B.3: Frequency domain functional connection between layers. A, frequency domain Granger causality between MEC III LFP and LFP signal from the hippocampus. Black dots indicate the frequency where flow in one direction is significantly dominated (two-sided Wilcoxon signed rank test p<.05 corrected by Bonferroni correction). B. frequency domain Granger causality between MEC III LFP and LFP signals from the hippocampus.

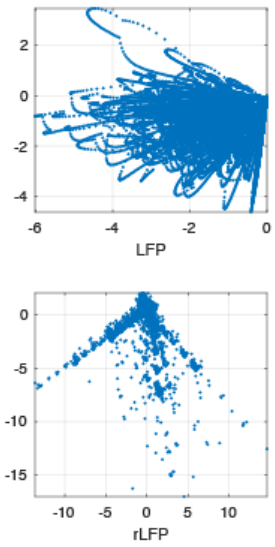

Figure B.4: Example simulation data LFP and rLFP in lower dimension.(projected to their first two principle dimension respectively.)

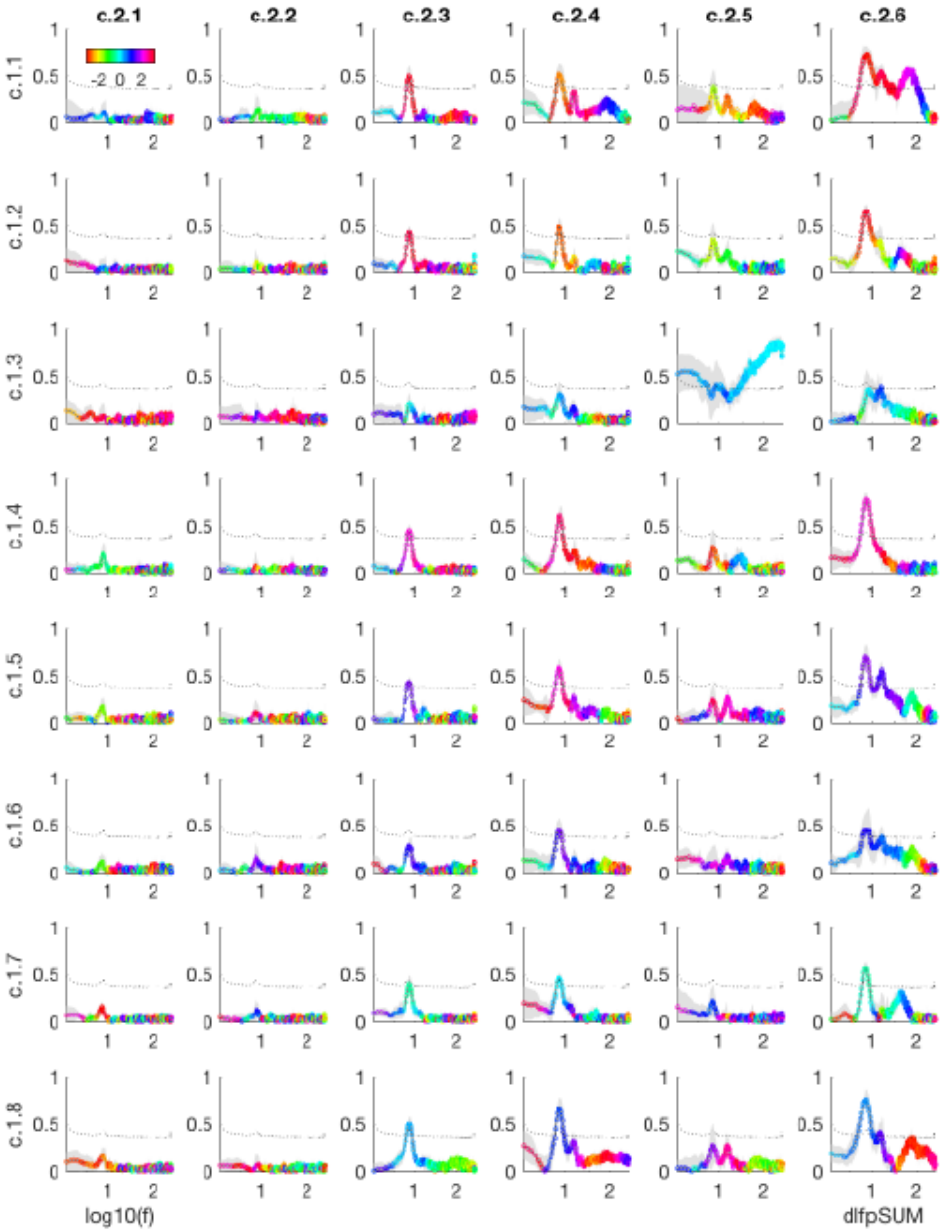

Figure B.5: Coherence between all the dLFP components from Hippocampus and MEC. Component labels are the same as in fig. 2.12

Appendix C

Greens Function

C.1 Comparison of Transmembrane Current Response Simulation

Here we show the comparison of transmembrane current response estimated by NEURON simulation versus Green's function method at each segment during oscillatory input simulation. The simulation model and the response at representative recording sites have been included in figure 3.3 A and B.

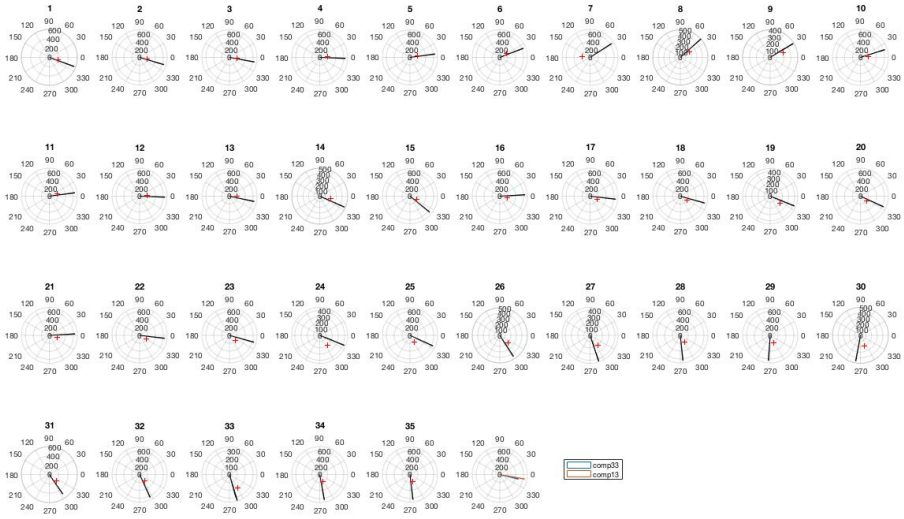

Figure C.1: Comparison of Transmembrane Current Response to Simulation with Oscillatory Inputs by The Demodulated Phase. 1-35: The demodulated phase around input frequency was recorded at the center of each compartment segment. Oscillatory currents are injected at compartment 7. The phase difference at 7 is because we count current injection as transmembrane currents in the forward modeling, but NEURON doesn't. The polar histogram shows the distribution of the signal phase demodulated by the current input. The red cross is the phase estimated by the forward model. The last figure shows the phase difference between demodulated phase and the estimated phase at a neighbor brunch (comp. 13 in red) and a further brunch (comp. 33 in blue). The phase difference at the transmembrane current level is small between the NEURON simulation and the forward modeling. And the phase difference depends on the distance from the injection site to the recording site. The label is the same as in fig. 3.3 A, B. Brunches with: lv.1: $1-5$, lv.2: $6-10$, $r2$: $11-15$, lv.3: $16-20$, black brunch between lv.2 and lv.3: $21-25$, black brunch between $r1$ and $r2$: $26-30$, $r1$: $31-35$.

Appendix D

Green's Function Constrained Complex ICA

D.1 Complex-valued Signal Unmixing

Here we use simulation to assess the performance of complex-valued signal unmixing. Particularly, signal generating process happens in the complex domain, i.e., the mixing matrix $A \in \mathbb{C}^{N_r \times N_s}$ is complex-valued, and so is the source activity $S \in \mathbb{C}^{N_s \times N_t}$, where N_r is the number of recording sites, N_s is the number of independent sources, and the N_t is the number of time samples we recorded. Notice when S only has a real value part or complex value part, then the problem is reduced to real-valued ICA because the complex part of the mixed activity in both cases could be ignored, and the signal would be fully unmixed with unmixing matrices corresponding to the real part of A in the first scenario and complex part of A in the latter scenario, respectively. On the other hand, mixing matrix A with pure real part or purely complex part will follow the same logic. In these scenarios, real-valued ICA is enough to unmix signals, and the algorithm will even benefit from fewer parameters to be estimated. Therefore, here we ask the following questions: how will complex ICA help signal separation? How is the performance depends on the phase of the A matrix? And how does the number of underlying components affect the unmixing?

We set off to address these questions by comparing the performance of complex ICA and simple time domain ICA with simulation as follows:

$$A = A_r + i\eta A_i, \tag{D.1}$$

$$S = S_r + iS_i, \tag{D.2}$$

$$X = AS. \tag{D.3}$$

Where every entry of A_r or A_i is uniformly distributed, i.e., $\sim U[0,1]$. η regulates how much the entry deviates from a zero-phased complex value or real value. We choose this expression to allow for variations in spatial loading amplitude at each

recording site. Here the activity of S, or S_r and S_i, are generated independently as log-normal distribution $\sim Lognormal(0,1)$ (Buzsaki & Mizuseki, 2014). For simplicity, here we set $N_r = N_s$. To compare the results, we set $\eta_A = \frac{A_i}{A_r}$ for the ground truth mixing matrix A and $\eta_{\hat{A}} = \frac{\hat{A}_i}{\hat{A}_r}$ for estimated mixing matrix $\hat{A}$. Both A and $\hat{A}$ are rotated so that the largest loading has zero complex phases for a fair comparison. We use Amari distance to assess the unmixing performance. We repeat 100 random sessions for each condition.

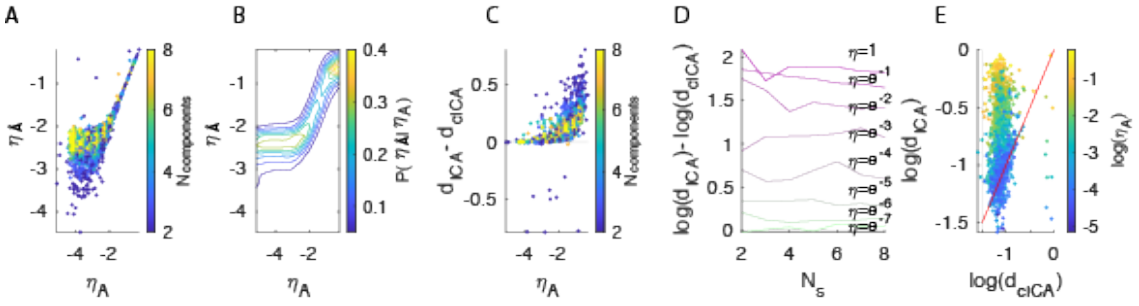

Figure D.1: Complex-valued signal unmixing: comparing cICA and ICA. A. Compare $log(\eta_A)$ with $log(\eta_{\hat{A}})$, color indicates number of components. B. Contour plot shows the distribution of $log(\eta_{\hat{A}})$ against given $log(\eta_A)$. C. the difference of Amari distance plot against $log(\eta_A)$. The color indicates the number of components in separation. D. Performance grouped by initial η measured by the median of difference of Amari distance $log(d_{ICA}) - log(d_{cICA})$. E. Amari distance of cICA and ICA plot against each other. Color indicate $log(\eta_A)$.

Basically, we find the performance depends on the complex to real ratio η_A. When η_A is larger than 10^{-2}, cICA generally unmixes the signals well (fig.D.1B), even when the number of components is large (fig.D.1A). But When η_A is smaller than 10^{-2}, the unmixing fails first in large components simulations. This is because the estimation error accumulates as the number of parameters increases. In the end, the advantage of cICA is diminished with smaller η (fig.D.1 C, D). Starting from $\eta = e^{-7}$, the unmixing performance of cICA is not significantly better than ICA with some component conditions ($n = 2$: $median = -0.0002, p = 0.0900$; $n = 3$, $median = 0.0002, p = 0.2896$ Wilcoxon signed rank test). But in general, even in the low η scenario, where the mixing matrix is very close to pure real value, the separation is generally good ($median = 0.0051$ for all $\eta \leq e^{-7}$).

Next, we ask where the biophysical impulse response patterns sit in the parameter space. Here we give two representative examples. Firstly, we look at the ground truth transfer function pattern of simulation we conducted throughout the thesis (see chapter 2.2.1 and fig.2.2). In the simulation, we stimulate two pathways: the Schaffle collateral path and the perforant path. In the passive membrane scenario, η_A increases monotonically with frequency for both pathways (fig.D.2 A, B). The η_A describes how the currents are spreading along the cable, and it depends

on the position of synapses with regard to the dendritic tree. The η_A is 0.0011 at 4 Hz for the Schaffle collateral path (fig.D.2 A,C) and 0.0030 at 4 Hz for the perforant path (fig.D.2 B,D).

We also examine the transfer function of dendrites with active channels. We use the channel distribution from the same model with the same cell morphology (Grienberger et al., 2017). Here the current is scaled to induce subthreshold inputs, i.e., the synaptic depolarizations are small enough such that no spike is induced. To our surprise, we have much more complex patterns at lower frequencies. But the real part of the spatial profile doesn't change too much (fig.D.2 C, D). This partially explained the complexity of the spatial profile we observed in real data.

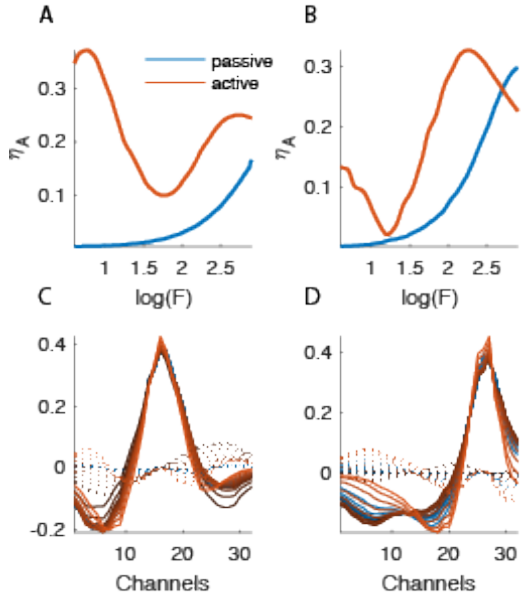

Figure D.2: Ground-truth spatial loading of the simulated data in passive (blue) or active (red) dendrites. A. η_A of Schaffle collateral path components at each frequency plot against frequency. B. η_A of perforant path components at each frequency plot against frequency. C. The spatial profile of the Schaffle collateral path component is plotted by its real (solid line) and complex (dotted line) parts. D. The spatial profile of the perforant path component is plotted by its real (solid line) and complex (dotted line) parts.

D.2 Temporal Domain ICA Result for Optogenetic Stimulation

For the sake of comparison, here we show the components, their stimulus triggered average, and their cross-frequency modulation of $LFP - ICA$ (fig.D.3) and $btLFP - ICA$ (fig.D.4), respectively. The labels are defined in chapter 2.2.3.

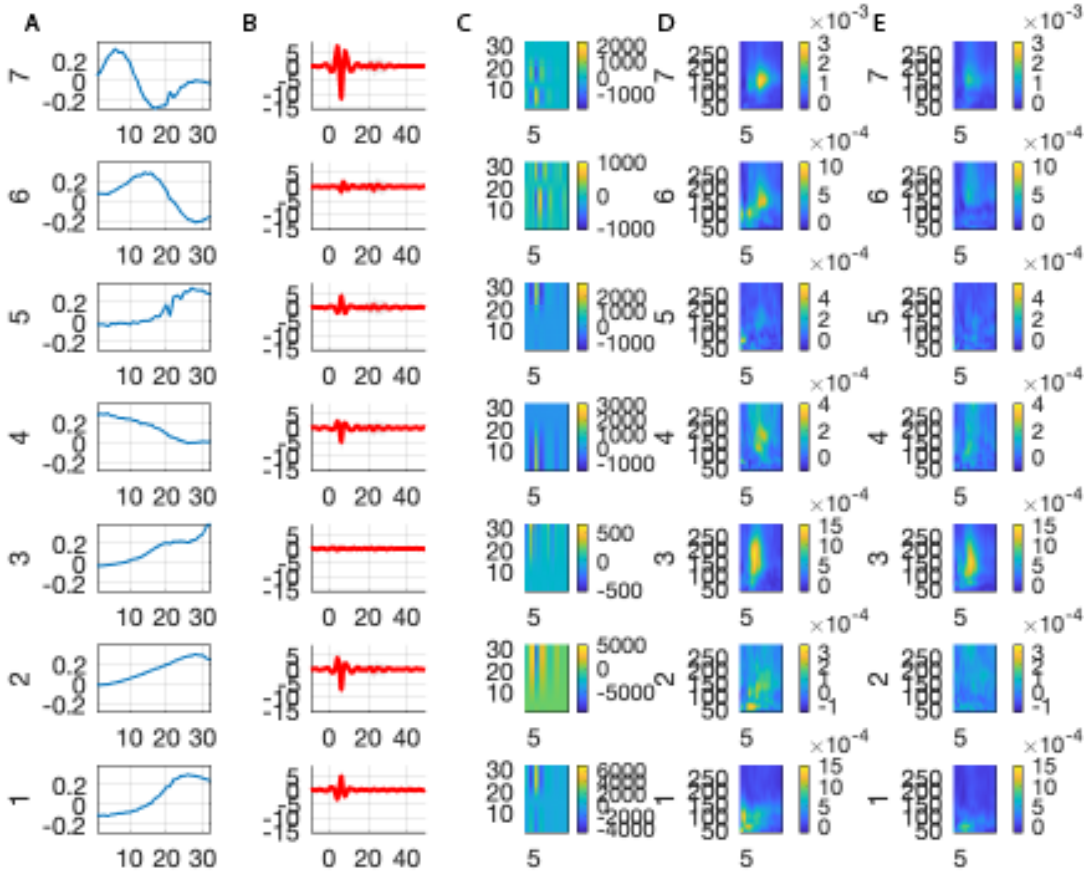

Figure D.3: Comparison to temporal ICA in real data: trained on wide band LFP. a. the initial clusters at step 1. The spatial profile is flipped as the largest loading is positive. b. the final clusters' spatial loading. c. the average activity triggered at contra-lateral CA3 stimulation. The stimuli is given at 0ms. d. The spatial profile of the stimuli triggered average. e,f. Theta gamma modulation in terms of MI. e. before, f. after contra-lateral CA3 stimulation

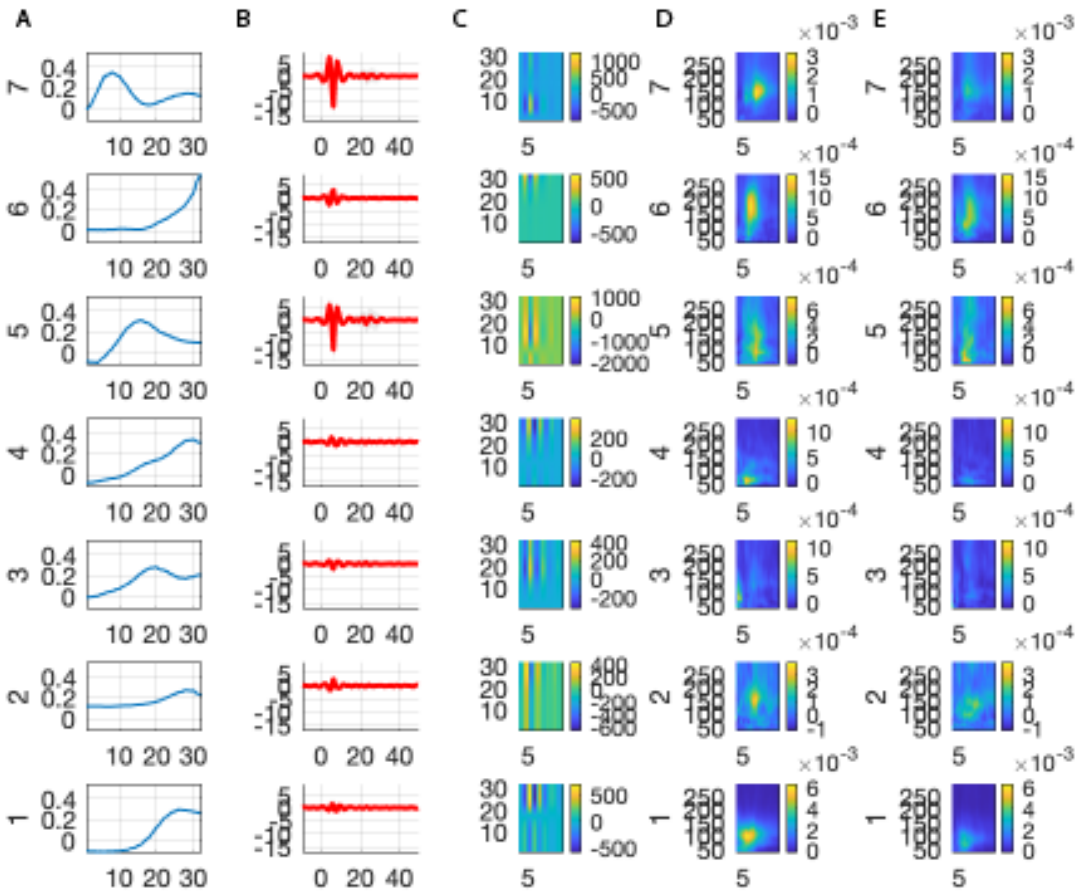

Figure D.4: Comparison to temporal ICA in real data: trained on high pass filtered LFP. a. the initial clusters at step 1. The spatial profile is flipped as the largest loading is positive. b. the final clusters' spatial loading. c. the average activity triggered at contra-lateral CA3 stimulation. The stimuli are given at 0ms. d. The spatial profile of the stimuli triggered average. e,f. Theta gamma modulation in terms of MI. e. before, f. after contra-lateral CA3 stimulation

Appendix E

EMG Removing Toolbox

E.1 Reporting Figures

The *EMG$_r$emoving* toolbox is a MATLAB toolbox for removing high-frequency EMG artifacts from the multichannel extracellular recording with ICA.

Removing EMG signal from LFP recording is generally an overcomplete ICA problem since the number of potential signal sources is much larger than the recording sites. A lower frequency physiological signal is going to affect the separation.

The current version uses spectrum whitening to emphasize the high-frequency EMG tone (*EMG_rm_main.m*). The cleaned signals will be saved in *.lfpd* files and the EMG activity in *.emg*. The EMG signals (*EMG_au*) and the EMG components *AW*. *As* is saved in *FileBase.EMG_rm.mat*.

We generate the following figures to assess the performance of EMG cleaning (fig.E.1 for general information and component profile, fig.E.2 for visualizing EMG removing in short or selected periods, and fig.E.3 for the power spectra of the raw and the denoised LFP signals and EMG signals plotted for all the predefined periods.).

The preprocessing pipeline could be found in an open source EMG denoising toolbox at `https://github.com/YY535/EMG_removing.git`

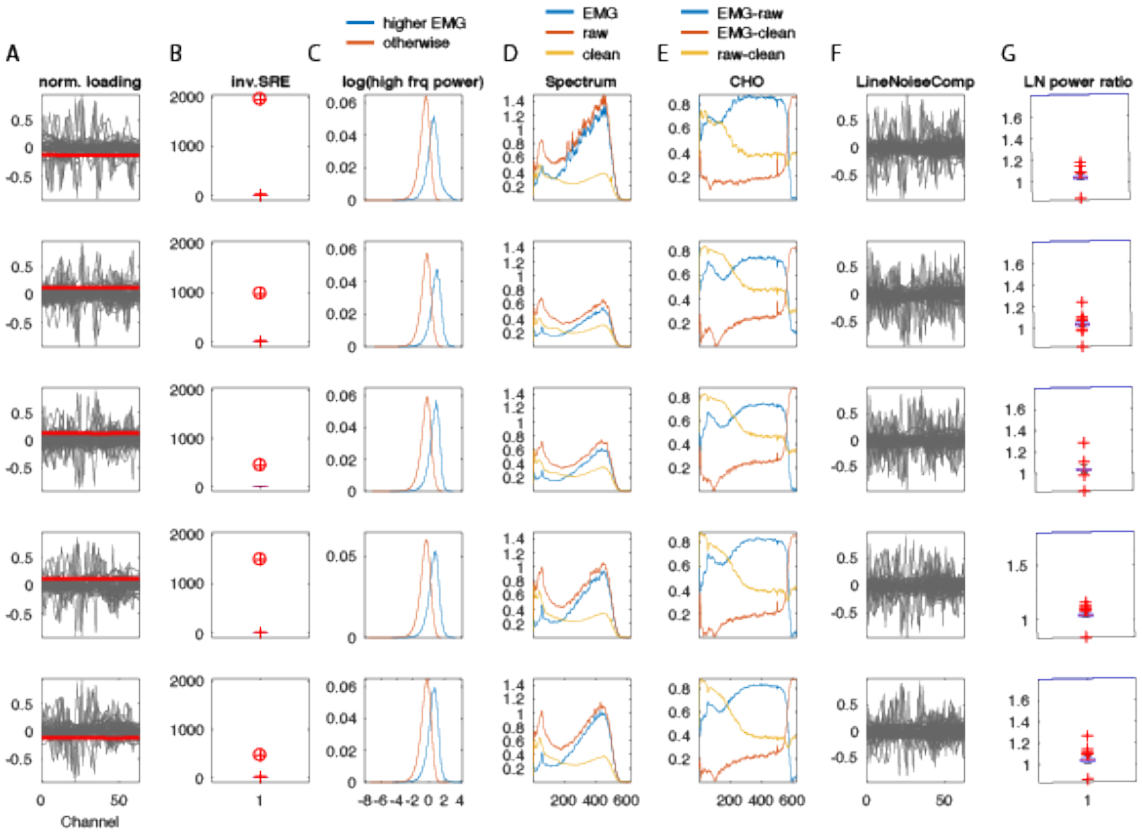

Figure E.1: Example EMG component report by *EMG_rm_report.m*. A. The spatial profile of EMG component (red) is plotted with all the other ICA components (gray). B. the flatness of voltage loading profiles of all ICA components. The circle indicates the selected EMG component. C. High EMG period selection. The distribution of *log* envelope of the high-pass filtered signal, as an alternative measure of high-frequency power, is compared between the selected higher EMG period (blue) and the other periods (red). D. The power spectra for the raw (black) and denoised (red) LFP traces and the removed EMG (green) from the channel $N_{channel} - 3$. E. The coherence between the raw LFP and the EMG traces (black) and between the denoised LFP and the EMG traces (red) from the channel $N_{channel} - 3$. F. The spatial profile of the line noise component (red) is plotted with all the other ICA components (gray). G. The power ratio of power-line frequency F_{line} versus other frequency bands $R_{line} = \frac{E_{i\in\{f_{line}\}}(P_i)}{E_{j\notin\{f_{line}\}}(P_j)}$ (equ.5.9) is plotted for all the components. The power-line frequency F_{line} is defined as $\{f_{line}\} \in [F_{line} \times n - 5, F_{line} \times n + 5]$ Hz, for all $n = 1, ...$ where $F_{line} \times n$ is lower than Nyquist frequency. Notice here none of the components is detected as a power line noise component because none of them reach the given threshold of 1.8.

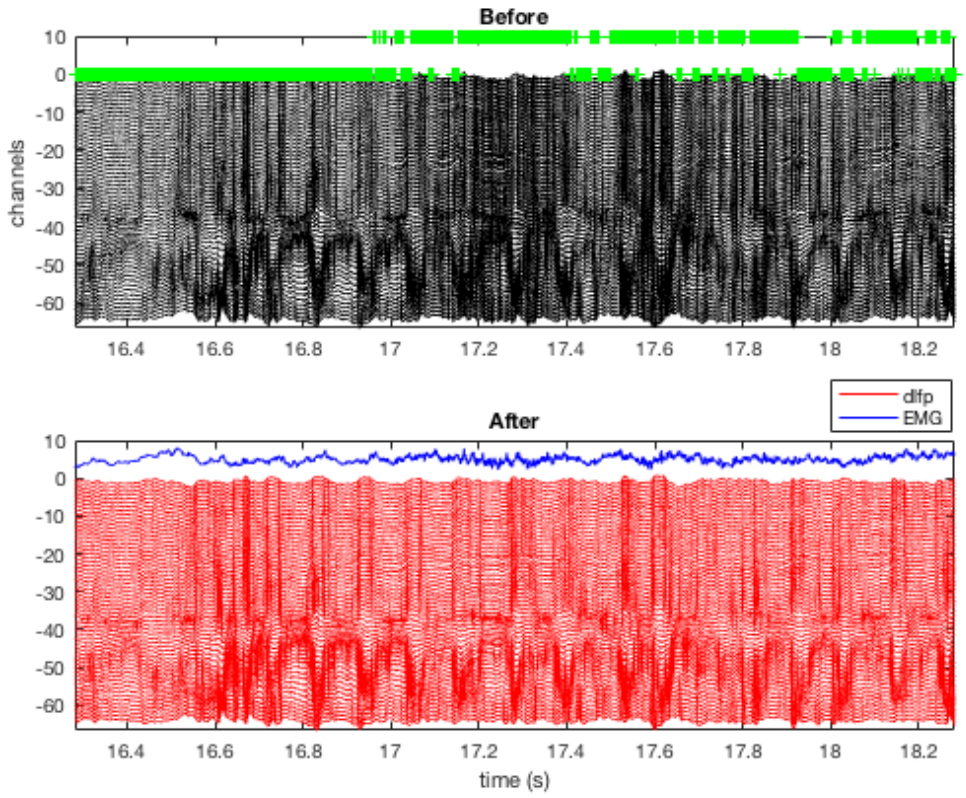

Figure E.2: Example EMG component: view noise by *EMG_rm_viewnoise.m*. Top. raw LFP traces. The green cross larger than 0 indicates the detected high EMG noise period. Bottom. The denoised LFP traces (red) after removing the EMG traces (blue).

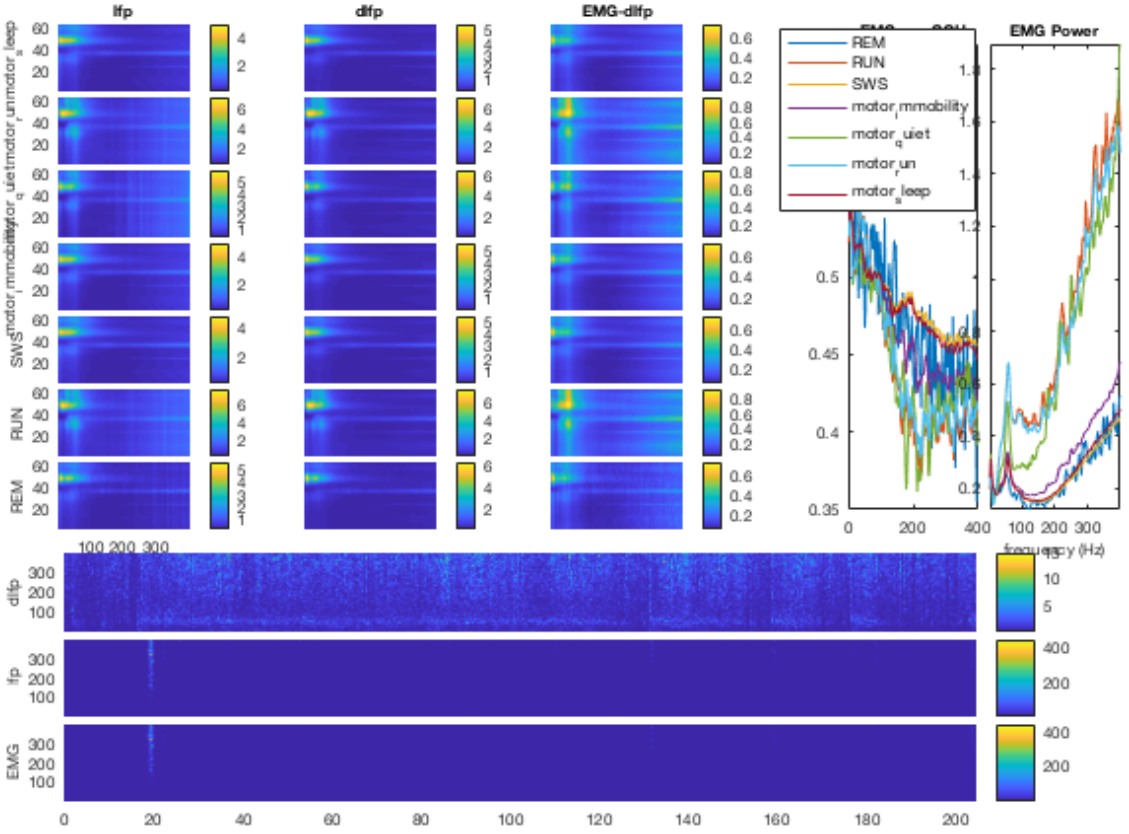

Figure E.3: Example EMG component: view the power spectra of signals in all the predefined states by *EMG_rm_viewspec.m*. A. The power spectra of signals from all the channels in one linear probe for raw (a) and denoised (b) LFP traces and the coherence between EMG activity and denoised data at each channel(c), computed for all the predefined states in each column labeled by state names. B. Left: the same as A. c) plotted for one channel. Right: the power spectra of EMG traces in each state. C. The spectrogram of denoised (dlfp) and raw LFP traces of one channel. We also show the spectrogram of the removed EMG signal.

E.2 Cross-Frequency Coupling of Gamma Bursts

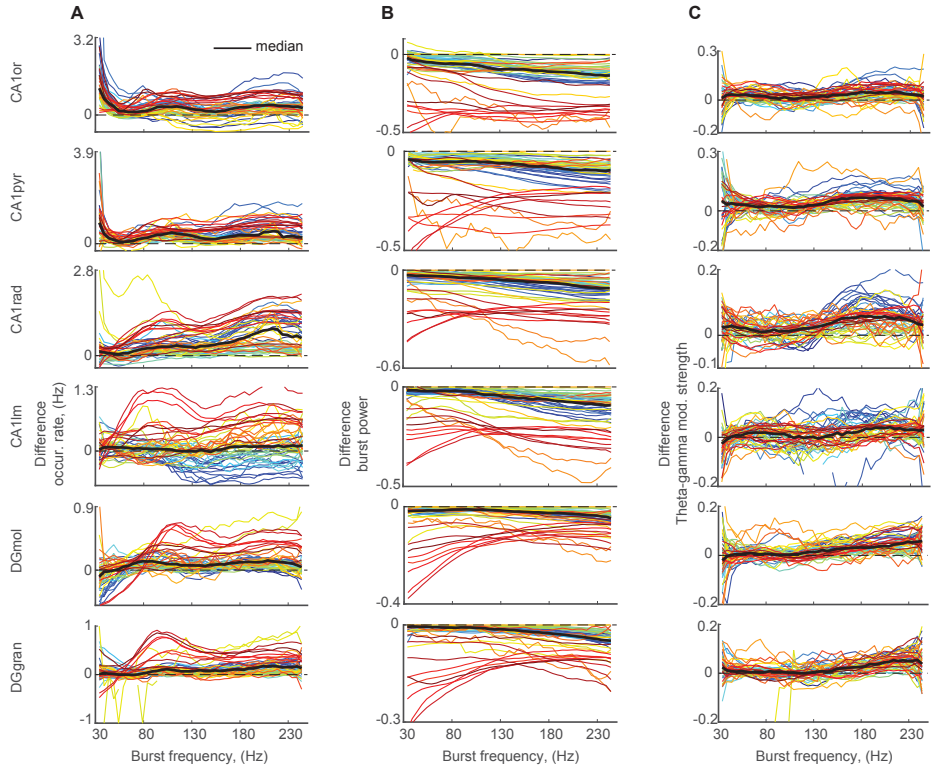

Figure E.4: (A) Difference between the frequency-resolved burst occurrence rate (Hz) profiles computed for the denoised and raw LFP (solid black – the averaged (median) profile, different colors – the raw session-specific profiles). Different rows show data for different hippocampal layers. (B) Same as in (A), but for the difference between the frequency-resolved burst power (a.u.) profiles. (C) Same as in (A), but for the difference between the theta phase modulation strength profiles.

Bibliography

Abbott, L. F. Simple diagrammatic rules for solving dendritic cable problems. *Physica A: Statistical Mechanics and its Applications*, 185(1-4):343–356, 1992.

Abbott, L. F., Farhi, E., and Gutmann, S. The path integral for dendritic trees. *Biological cybernetics*, 66(1):49–60, 1991.

Adali, T., Li, H., Novey, M., and Cardoso, J. Complex ica using nonlinear functions. *IEEE Transactions on Signal Processing*, 56(9):4536–4544, 2008.

Anastassiou, C. A., Perin, R., Markram, H., and Koch, C. Ephaptic coupling of cortical neurons. *Nature neuroscience*, 14(2):217–223, 2011.

Andalman, A. S., Burns, V. M., Lovett-Barron, M., Broxton, M., Poole, B., Yang, S. J., Grosenick, L., Lerner, T. N., Chen, R., Benster, T., et al. Neuronal dynamics regulating brain and behavioral state transitions. *Cell*, 177(4):970–985, 2019.

Andersen, P., Bliss, T., and Skrede, K. K. Lamellar organization of hippocampal excitatory pathways. *Experimental brain research*, 13(2):222–238, 1971.

Anemüller, J., Sejnowski, T. J., and Makeig, S. Complex independent component analysis of frequency-domain electroencephalographic data. *Neural networks*, 16 (9):1311–1323, 2003.

Arnsten, A. F., Wang, M. J., and Paspalas, C. D. Neuromodulation of thought: flexibilities and vulnerabilities in prefrontal cortical network synapses. *Neuron*, 76(1):223–239, 2012.

Artoni, F., Gemignani, A., Sebastiani, L., Bedini, R., Landi, A., and Menicucci, D. Erpicasso: a tool for reliability estimates of independent components in eeg event-related analysis. In *2012 Annual International Conference of the IEEE Engineering in Medicine and Biology Society*, pp. 368–371. IEEE, 2012.

Attiah, M. A., de Vries, J., Richardson, A. G., and Lucas, T. H. A rodent model of dynamic facial reanimation using functional electrical stimulation. *Frontiers in neuroscience*, 11:193, 2017.

Barbati, G., Porcaro, C., Zappasodi, F., Rossini, P. M., and Tecchio, F. Optimization of an independent component analysis approach for artifact identification and removal in magnetoencephalographic signals. *Clinical Neurophysiology*, 115 (5):1220–1232, 2004.

Barbieri, F., Mazzoni, A., Logothetis, N. K., Panzeri, S., and Brunel, N. Stimulus dependence of local field potential spectra: experiment versus theory. *Journal of Neuroscience*, 34(44):14589–14605, 2014.

Barnett, L. and Seth, A. K. The mvgc multivariate granger causality toolbox: a new approach to granger-causal inference. *Journal of neuroscience methods*, 223: 50–68, 2014.

Barnett, L. and Seth, A. K. Granger causality for state-space models. *Physical Review E*, 91(4):040101, 2015.

Barnett, L., Barrett, A. B., and Seth, A. K. Granger causality and transfer entropy are equivalent for gaussian variables. *Physical review letters*, 103(23):238701, 2009.

Barrett, A. B., Barnett, L., and Seth, A. K. Multivariate granger causality and generalized variance. *Physical Review E*, 81(4):041907, 2010.

Bartos, M., Vida, I., and Jonas, P. Synaptic mechanisms of synchronized gamma oscillations in inhibitory interneuron networks. *Nature reviews neuroscience*, 8(1): 45–56, 2007.

Bastos, A. M. and Schoffelen, J.-M. A tutorial review of functional connectivity analysis methods and their interpretational pitfalls. *Frontiers in systems neuroscience*, 9:175, 2016.

Bastos, A. M., Vezoli, J., Bosman, C. A., Schoffelen, J.-M., Oostenveld, R., Dowdall, J. R., De Weerd, P., Kennedy, H., and Fries, P. Visual areas exert feedforward and feedback influences through distinct frequency channels. *Neuron*, 85(2): 390–401, 2015.

Bédard, C., Kröger, H., and Destexhe, A. Modeling extracellular field potentials and the frequency-filtering properties of extracellular space. *Biophysical journal*, 86(3):1829–1842, 2004.

Bell, A. J. and Sejnowski, T. J. An information-maximization approach to blind separation and blind deconvolution. *Neural computation*, 7(6):1129–1159, 1995.

Ben-Ari, Y. Excitatory actions of gaba during development: the nature of the nurture. *Nature Reviews Neuroscience*, 3(9):728–739, 2002.

Benito, N., Fernández-Ruiz, A., Makarov, V. A., Makarova, J., Korovaichuk, A., and Herreras, O. Spatial modules of coherent activity in pathway-specific

lfps in the hippocampus reflect topology and different modes of presynaptic synchronization. *Cerebral cortex*, 24(7):1738–1752, 2014.

Benjamini, Y. and Hochberg, Y. Controlling the false discovery rate: a practical and powerful approach to multiple testing. *Journal of the Royal statistical society: series B (Methodological)*, 57(1):289–300, 1995.

Bi, G.-q. and Poo, M.-m. Synaptic modifications in cultured hippocampal neurons: dependence on spike timing, synaptic strength, and postsynaptic cell type. *Journal of neuroscience*, 18(24):10464–10472, 1998.

Bishop, C. M. *Pattern recognition and machine learning*. springer, 2006.

Bohland, J. W., Wu, C., Barbas, H., Bokil, H., Bota, M., Breiter, H. C., Cline, H. T., Doyle, J. C., Freed, P. J., Greenspan, R. J., et al. A proposal for a coordinated effort for the determination of brainwide neuroanatomical connectivity in model organisms at a mesoscopic scale. *PLoS computational biology*, 5(3):e1000334, 2009.

Borg-Graham, L. J. Interpretations of data and mechanisms for hippocampal pyramidal cell models. *Models of cortical circuits*, pp. 19–138, 1999.

Brandwood, D. A complex gradient operator and its application in adaptive array theory. In *IEE Proceedings H-Microwaves, Optics and Antennas*, volume 130, pp. 11–16. IET, 1983.

Brette, R. and Destexhe, A. *Handbook of Neural Activity Measurement*. Cambridge University Press, 2012. ISBN 9780521516228. URL `https://books.google.de/books?id=YLyGmfVuBsIC`.

Brunton, S. L., Proctor, J. L., and Kutz, J. N. Discovering governing equations from data by sparse identification of nonlinear dynamical systems. *Proceedings of the national academy of sciences*, 113(15):3932–3937, 2016.

Buccino, A. P., Kordovan, M., Ness, T. V., Merkt, B., Häfliger, P. D., Fyhn, M., Cauwenberghs, G., Rotter, S., and Einevoll, G. T. Combining biophysical modeling and deep learning for multielectrode array neuron localization and classification. *Journal of neurophysiology*, 120(3):1212–1232, 2018.

Burt, J. B., Demirtaş, M., Eckner, W. J., Navejar, N. M., Ji, J. L., Martin, W. J., Bernacchia, A., Anticevic, A., and Murray, J. D. Hierarchy of transcriptomic specialization across human cortex captured by structural neuroimaging topography. *Nature neuroscience*, 21(9):1251–1259, 2018.

Butz, E. G. and Cowan, J. D. Transient potentials in dendritic systems of arbitrary geometry. *Biophysical journal*, 14(9):661, 1974.

Buzsáki, G. Large-scale recording of neuronal ensembles. *Nature neuroscience*, 7 (5):446, 2004.

Buzsaki, G. *Rhythms of the Brain*. Oxford university press, 2006.

Buzsáki, G. Hippocampal sharp wave-ripple: A cognitive biomarker for episodic memory and planning. *Hippocampus*, 25(10):1073–1188, 2015.

Buzsaki, G. and Mizuseki, K. The log-dynamic brain: how skewed distributions affect network operations. *Nat Rev Neurosci*, 15(4):264–278, 04 2014. URL `http://dx.doi.org/10.1038/nrn3687`.

Buzsáki, G., Anastassiou, C. A., and Koch, C. The origin of extracellular fields and currents—eeg, ecog, lfp and spikes. *Nature reviews neuroscience*, 13(6):407–420, 2012.

Canolty, R. T., Edwards, E., Dalal, S. S., Soltani, M., Nagarajan, S. S., Kirsch, H. E., Berger, M. S., Barbaro, N. M., and Knight, R. T. High gamma power is phase-locked to theta oscillations in human neocortex. *science*, 313(5793): 1626–1628, 2006.

Cao, B. J. and Abbott, L. F. A new computational method for cable theory problems. *Biophysical journal*, 64(2):303, 1993.

Cao, L., Varga, V., and Chen, Z. S. Uncovering spatial representations from spatiotemporal patterns of rodent hippocampal field potentials. *Cell reports methods*, 1(7):100101, 2021.

Cardoso, J.-F. Infomax and maximum likelihood for blind source separation. *IEEE Signal processing letters*, 4(4):112–114, 1997.

Cardoso, J.-F. Blind signal separation: statistical principles. *Proceedings of the IEEE*, 86(10):2009–2025, 1998.

Cardoso, J.-F. High-order contrasts for independent component analysis. *Neural computation*, 11(1):157–192, 1999.

Carnevale, N. T. and Hines, M. L. *The NEURON Book*. Cambridge University Press, 2006. doi: 10.1017/CBO9780511541612.

Cash, S. and Yuste, R. Linear summation of excitatory inputs by ca1 pyramidal neurons. *Neuron*, 22(2):383–394, 1999.

Caudron, Q., Donnelly, S. R., Brand, S. P., and Timofeeva, Y. Computational convergence of the path integral for real dendritic morphologies. *The Journal of Mathematical Neuroscience*, 2(1):11, 2012.

Cembrowski, M. S. and Spruston, N. Heterogeneity within classical cell types is the rule: lessons from hippocampal pyramidal neurons. *Nature Reviews Neuroscience*, 20(4):193–204, 2019.

Cembrowski, M. S., Phillips, M. G., DiLisio, S. F., Shields, B. C., Winnubst, J., Chandrashekar, J., Bas, E., and Spruston, N. Dissociable structural and functional hippocampal outputs via distinct subiculum cell classes. *Cell*, 173(5):1280–1292, 2018.

Chaudhuri, R., Knoblauch, K., Gariel, M.-A., Kennedy, H., and Wang, X.-J. A large-scale circuit mechanism for hierarchical dynamical processing in the primate cortex. *Neuron*, 88(2):419–431, 2015.

Chaumon, M., Bishop, D. V., and Busch, N. A. A practical guide to the selection of independent components of the electroencephalogram for artifact correction. *Journal of neuroscience methods*, 250:47–63, 2015.

Chelaru, M. I. and Jog, M. S. Spike source localization with tetrodes. *Journal of neuroscience methods*, 142(2):305–315, 2005.

Chen, A. *Fast Kernel Density Independent Component Analysis*, pp. 24–31. Springer Berlin Heidelberg, Berlin, Heidelberg, 2006.

Chen, Y., Bressler, S. L., and Ding, M. Frequency decomposition of conditional granger causality and application to multivariate neural field potential data. *Journal of neuroscience methods*, 150(2):228–237, 2006.

Cichocki, A. and Amari, S.-i. *Adaptive blind signal and image processing: learning algorithms and applications*. John Wiley & Sons, 2002.

Cichocki, A. and Georgiev, P. Blind source separation algorithms with matrix constraints. *IEICE Transactions on Fundamentals of Electronics, Communications and Computer Sciences*, 86(3):522–531, 2003.

Comon, P. Independent component analysis, a new concept? *Signal processing*, 36(3):287–314, 1994.

Cook, E. P., Guest, J. A., Liang, Y., Masse, N. Y., and Colbert, C. M. Dendrite-to-soma input/output function of continuous time-varying signals in hippocampal ca1 pyramidal neurons. *Journal of neurophysiology*, 98(5):2943–2955, 2007.

Coombes, S., Timofeeva, Y., Svensson, C.-M., Lord, G. J., Josić, K., Cox, S. J., and Colbert, C. M. Branching dendrites with resonant membrane: a "sum-over-trips" approach. *Biological Cybernetics*, 97(2):137–149, 2007.

Croft, R. J. and Barry, R. J. Removal of ocular artifact from the eeg: a review. *Neurophysiologie Clinique/Clinical Neurophysiology*, 30(1):5–19, 2000.

Cserpan, D., Meszéna, D., Wittner, L., Tóth, K., Ulbert, I., Somogyvári, Z., and Wójcik, D. K. Revealing the distribution of transmembrane currents along the dendritic tree of a neuron from extracellular recordings. *Elife*, 6:e29384, 2017.

Cunningham, J. P. and Yu, B. M. Dimensionality reduction for large-scale neural recordings. *Nature neuroscience*, 17(11):1500–1509, 2014.

Cuntz, H., Forstner, F., Borst, A., and HÃ€usser, M. One rule to grow them all: A general theory of neuronal branching and its practical application. *PLOS Computational Biology*, 6(8):1–14, 08 2010. doi: 10.1371/journal.pcbi.1000877. URL `https://doi.org/10.1371/journal.pcbi.1000877`.

Dayan, P. and Abbott, L. F. *Theoretical neuroscience: computational and mathematical modeling of neural systems*. Computational Neuroscience Series, 2001.

de Cheveigné, A. and Parra, L. C. Joint decorrelation, a versatile tool for multichannel data analysis. *Neuroimage*, 98:487–505, 2014.

Deco, G. and Jirsa, V. K. Ongoing cortical activity at rest: criticality, multistability, and ghost attractors. *Journal of Neuroscience*, 32(10):3366–3375, 2012.

Deco, G., Ponce-Alvarez, A., Mantini, D., Romani, G. L., Hagmann, P., and Corbetta, M. Resting-state functional connectivity emerges from structurally and dynamically shaped slow linear fluctuations. *Journal of Neuroscience*, 33(27): 11239–11252, 2013.

Deco, G., Ponce-Alvarez, A., Hagmann, P., Romani, G. L., Mantini, D., and Corbetta, M. How local excitation–inhibition ratio impacts the whole brain dynamics. *Journal of Neuroscience*, 34(23):7886–7898, 2014.

Delmas, P. and Brown, D. A. Pathways modulating neural kcnq/m (kv7) potassium channels. *Nature Reviews Neuroscience*, 6(11):850–862, 2005.

Delorme, A., Sejnowski, T., and Makeig, S. Enhanced detection of artifacts in eeg data using higher-order statistics and independent component analysis. *Neuroimage*, 34(4):1443–1449, 2007.

Destexhe, A., Mainen, Z. F., and Sejnowski, T. J. Kinetic models of synaptic transmission. 1998.

Dhamala, M., Rangarajan, G., and Ding, M. Analyzing information flow in brain networks with nonparametric granger causality. *Neuroimage*, 41(2):354–362, 2008.

Dickey, A. S., Suminski, A., Amit, Y., and Hatsopoulos, N. G. Single-unit stability using chronically implanted multielectrode arrays. *Journal of neurophysiology*, 102 (2):1331–1339, 2009.

Donoghue, T., Haller, M., Peterson, E. J., Varma, P., Sebastian, P., Gao, R., Noto, T., Lara, A. H., Wallis, J. D., Knight, R. T., et al. Parameterizing neural power spectra into periodic and aperiodic components. *Nature neuroscience*, 23(12): 1655–1665, 2020.

Druckmann, S., Banitt, Y., Gidon, A. A., Schürmann, F., Markram, H., and Segev, I. A novel multiple objective optimization framework for constraining conductance-based neuron models by experimental data. *Frontiers in neuroscience*, pp. 1, 2007.

Einevoll, G. T., Pettersen, K. H., Devor, A., Ulbert, I., Halgren, E., and Dale, A. M. Laminar population analysis: estimating firing rates and evoked synaptic activity from multielectrode recordings in rat barrel cortex. *Journal of neurophysiology*, 97 (3):2174–2190, 2007.

Einevoll, G. T., Kayser, C., Logothetis, N. K., and Panzeri, S. Modelling and analysis of local field potentials for studying the function of cortical circuits. *Nature Reviews Neuroscience*, 14:770 EP –, 10 2013. URL `https://doi.org/10.1038/nrn3599`.

Fernández-Ruiz, A. and Herreras, O. Identifying the synaptic origin of ongoing neuronal oscillations through spatial discrimination of electric fields. *Frontiers in computational neuroscience*, 7:5, 2013.

Fernández-Ruiz, A., Makarov, V. A., Benito, N., and Herreras, O. Schaffer-specific local field potentials reflect discrete excitatory events at gamma frequency that may fire postsynaptic hippocampal ca1 units. *Journal of Neuroscience*, 32(15): 5165–5176, 2012.

Fernández-Ruiz, A., Muñoz, S., Sancho, M., Makarova, J., Makarov, V. A., and Herreras, O. Cytoarchitectonic and dynamic origins of giant positive local field potentials in the dentate gyrus. *Journal of Neuroscience*, 33(39):15518–15532, 2013.

Fernández-Ruiz, A., Oliva, A., Nagy, G. A., Maurer, A. P., Berényi, A., and Buzsáki, G. Entorhinal-ca3 dual-input control of spike timing in the hippocampus by theta-gamma coupling. *Neuron*, 93(5):1213–1226, 2017.

Fernández-Ruiz, A., Oliva, A., Soula, M., Rocha-Almeida, F., Nagy, G. A., Martin-Vazquez, G., and Buzsáki, G. Gamma rhythm communication between entorhinal cortex and dentate gyrus neuronal assemblies. *Science*, 372(6537), 2021.

Fishell, G. and Kepecs, A. Interneuron types as attractors and controllers. *Annual review of neuroscience*, 43:1, 2020.

Fries, P. Rhythms for cognition: communication through coherence. *Neuron*, 88 (1):220–235, 2015.

Friston, K. J., Fletcher, P., Josephs, O., Holmes, A., Rugg, M., and Turner, R. Event-related fmri: characterizing differential responses. *Neuroimage*, 7(1):30–40, 1998.

Friston, K. J., Harrison, L., and Penny, W. Dynamic causal modelling. *Neuroimage*, 19(4):1273–1302, 2003.

Gajic, Z. *Linear dynamic systems and signals*. Prentice Hall/Pearson Education Upper Saddle River, 2003.

Gallego-Carracedo, C., Perich, M. G., Chowdhury, R. H., Miller, L. E., and Gallego, J. Á. Local field potentials reflect cortical population dynamics in a region-specific and frequency-dependent manner. *Elife*, 11:e73155, 2022.

Gao, R., Peterson, E. J., and Voytek, B. Inferring synaptic excitation/inhibition balance from field potentials. *Neuroimage*, 158:70–78, 2017.

Gao, R., van den Brink, R. L., Pfeffer, T., and Voytek, B. Neuronal timescales are functionally dynamic and shaped by cortical microarchitecture. *Elife*, 9:e61277, 2020.

Gasparini, S., Migliore, M., and Magee, J. C. On the initiation and propagation of dendritic spikes in ca1 pyramidal neurons. *Journal of Neuroscience*, 24(49): 11046–11056, 2004.

Geweke, J. Measurement of linear dependence and feedback between multiple time series. *Journal of the American statistical association*, 77(378):304–313, 1982.

Geweke, J. F. Measures of conditional linear dependence and feedback between time series. *Journal of the American Statistical Association*, 79(388):907–915, 1984.

Głąbska, H., Potworowski, J., Łęski, S., and Wójcik, D. K. Independent components of neural activity carry information on individual populations. *PloS one*, 9 (8):e105071, 2014.

Głąbska, H. T., Norheim, E., Devor, A., Dale, A. M., Einevoll, G. T., and Wójcik, D. K. Generalized laminar population analysis (glpa) for interpretation of multielectrode data from cortex. *Frontiers in neuroinformatics*, 10:1, 2016.

Glymour, C., Zhang, K., and Spirtes, P. Review of causal discovery methods based on graphical models. *Frontiers in genetics*, 10:524, 2019.

Goense, J. B. and Logothetis, N. K. Neurophysiology of the bold fmri signal in awake monkeys. *Current Biology*, 18(9):631–640, 2008.

Gold, C., Henze, D. A., Koch, C., and Buzsaki, G. On the origin of the extracellular action potential waveform: a modeling study. *Journal of neurophysiology*, 95 (5):3113–3128, 2006.

Granger, C. W. Investigating causal relations by econometric models and cross-spectral methods. *Econometrica: journal of the Econometric Society*, pp. 424–438, 1969.

Gratiy, S. L., Devor, A., Einevoll, G. T., and Dale, A. M. On the estimation of population-specific synaptic currents from laminar multielectrode recordings. *Frontiers in neuroinformatics*, 5:32, 2011.

Gratiy, S. L., Halnes, G., Denman, D., Hawrylycz, M. J., Koch, C., Einevoll, G. T., and Anastassiou, C. A. From maxwell's equations to the theory of current-source density analysis. *European Journal of Neuroscience*, 45(8):1013–1023, 2017.

Gratton, G., Coles, M. G., and Donchin, E. A new method for off-line removal of ocular artifact. *Electroencephalography and clinical neurophysiology*, 55(4):468–484, 1983.

Grienberger, C. and Konnerth, A. Imaging calcium in neurons. *Neuron*, 73(5): 862–885, 2012.

Grienberger, C., Milstein, A. D., Bittner, K. C., Romani, S., and Magee, J. C. Inhibitory suppression of heterogeneously tuned excitation enhances spatial coding in CA1 place cells. *Nature Neuroscience*, 20: 417, jan 2017. URL `https://doi.org/10.1038/nn.4486http://10.0.4.14/nn.4486https://www.nature.com/articles/nn.4486{#}supplementary-information`.

Gross, J., Baillet, S., Barnes, G. R., Henson, R. N., Hillebrand, A., Jensen, O., Jerbi, K., Litvak, V., Maess, B., Oostenveld, R., et al. Good practice for conducting and reporting meg research. *Neuroimage*, 65:349–363, 2013.

Hagen, E., Dahmen, D., Stavrinou, M. L., Lindén, H., Tetzlaff, T., Van Albada, S. J., Grün, S., Diesmann, M., and Einevoll, G. T. Hybrid scheme for modeling local field potentials from point-neuron networks. *Cerebral cortex*, pp. 1–36, 2016.

Hagen, E., Næss, S., Ness, T. V., and Einevoll, G. T. Multimodal modeling of neural network activity: Computing lfp, ecog, eeg, and meg signals with lfpy 2.0. *Frontiers in neuroinformatics*, 12:92, 2018.

Hagen, E., Magnusson, S. H., Ness, T. V., Halnes, G., Babu, P. N., Linssen, C., Morrison, A., and Einevoll, G. T. Brain signal predictions from multi-scale networks using a linearized framework. *bioRxiv*, 2022.

Hagmann, P., Cammoun, L., Gigandet, X., Meuli, R., Honey, C. J., Wedeen, V. J., and Sporns, O. Mapping the structural core of human cerebral cortex. *PLoS biology*, 6(7):e159, 2008.

Hansen, J. Y., Shafiei, G., Markello, R. D., Smart, K., Cox, S. M., Nørgaard, M., Beliveau, V., Wu, Y., Gallezot, J.-D., Aumont, É., et al. Mapping neurotransmitter systems to the structural and functional organization of the human neocortex. *Nature neuroscience*, pp. 1–13, 2022.

Harris, J. A., Mihalas, S., Hirokawa, K. E., Whitesell, J. D., Choi, H., Bernard, A., Bohn, P., Caldejon, S., Casal, L., Cho, A., et al. Hierarchical organization of cortical and thalamic connectivity. *Nature*, 575(7781):195–202, 2019.

Hasani, R., Lechner, M., Amini, A., Liebenwein, L., Ray, A., Tschaikowski, M., Teschl, G., and Rus, D. Closed-form continuous-time neural networks. *Nature Machine Intelligence*, pp. 1–12, 2022.

Hasselmo, M. E. and Stern, C. E. Theta rhythm and the encoding and retrieval of space and time. *Neuroimage*, 85:656–666, 2014.

Haufe, S., Nikulin, V. V., and Nolte, G. Alleviating the influence of weak data asymmetries on granger-causal analyses. In *International Conference on Latent Variable Analysis and Signal Separation*, pp. 25–33. Springer, 2012.

Hay, E., Hill, S., Schürmann, F., Markram, H., and Segev, I. Models of neocortical layer 5b pyramidal cells capturing a wide range of dendritic and perisomatic active properties. *PLoS computational biology*, 7(7):e1002107, 2011.

He, B., Astolfi, L., Valdés-Sosa, P. A., Marinazzo, D., Palva, S. O., Bénar, C.-G., Michel, C. M., and Koenig, T. Electrophysiological brain connectivity: theory and implementation. *IEEE Transactions on Biomedical Engineering*, 66(7):2115–2137, 2019.

He, B. J. Scale-free brain activity: past, present, and future. *Trends Cogn Sci*, 18 (9):480–487, Sep 2014. ISSN 1879-307X (Electronic); 1364-6613 (Print); 1364-6613 (Linking). doi: 10.1016/j.tics.2014.04.003.

Herreras, O., Makarova, J., and Makarov, V. New uses of lfps: Pathway-specific threads obtained through spatial discrimination. *Neuroscience*, 310:486–503, 2015.

Hines, M. L. and Carnevale, N. T. Neuron: a tool for neuroscientists. *The neuroscientist*, 7(2):123–135, 2001.

Hipp, J. F. and Siegel, M. Dissociating neuronal gamma-band activity from cranial and ocular muscle activity in eeg. *Frontiers in human neuroscience*, 7:338, 2013.

Hoffman, D. A., Magee, J. C., Colbert, C. M., and Johnston, D. K+ channel regulation of signal propagation in dendrites of hippocampal pyramidal neurons. *Nature*, 387(6636):869–875, 1997.

Holt, G. R. and Koch, C. Electrical interactions via the extracellular potential near cell bodies. *Journal of computational neuroscience*, 6(2):169–184, 1999.

Honey, C. J., Sporns, O., Cammoun, L., Gigandet, X., Thiran, J.-P., Meuli, R., and Hagmann, P. Predicting human resting-state functional connectivity from

structural connectivity. *Proceedings of the National Academy of Sciences*, 106(6): 2035–2040, 2009.

Hu, H., Vervaeke, K., Graham, L. J., and Storm, J. F. Complementary theta resonance filtering by two spatially segregated mechanisms in ca1 hippocampal pyramidal neurons. *Journal of Neuroscience*, 29(46):14472–14483, 2009.

Huang, N. E., Shen, Z., Long, S. R., Wu, M. C., Shih, H. H., Zheng, Q., Yen, N.-C., Tung, C. C., and Liu, H. H. The empirical mode decomposition and the hilbert spectrum for nonlinear and non-stationary time series analysis. *Proceedings of the Royal Society of London. Series A: mathematical, physical and engineering sciences*, 454(1971):903–995, 1998.

Hutcheon, B. and Yarom, Y. Resonance, oscillation and the intrinsic frequency preferences of neurons. *Trends in neurosciences*, 23(5):216–222, 2000.

Huys, Q. J., Ahrens, M. B., and Paninski, L. Efficient estimation of detailed single-neuron models. *J. Neurophysiol.*, 96(2):872–890, Aug 2006.

Hyvarinen, A. Fast and robust fixed-point algorithms for independent component analysis. *IEEE transactions on Neural Networks*, 10(3):626–634, 1999.

Hyvärinen, A. Testing the ica mixing matrix based on inter-subject or inter-session consistency. *NeuroImage*, 58(1):122–136, 2011.

Hyvärinen, A. and Oja, E. Independent component analysis: algorithms and applications. *Neural networks*, 13(4-5):411–430, 2000.

Ito, S., Hansen, M. E., Heiland, R., Lumsdaine, A., Litke, A. M., and Beggs, J. M. Extending transfer entropy improves identification of effective connectivity in a spiking cortical network model. *PloS one*, 6(11):e27431, 2011.

Jaffe, D. B. and Carnevale, N. T. Passive normalization of synaptic integration influenced by dendritic architecture. *Journal of Neurophysiology*, 82(6):3268–3285, 1999. doi: 10.1152/jn.1999.82.6.3268. URL `https://doi.org/10.1152/jn.1999.82.6.3268`. PMID: 10601459.

Jarsky, T., Roxin, A., Kath, W. L., and Spruston, N. Conditional dendritic spike propagation following distal synaptic activation of hippocampal ca1 pyramidal neurons. *Nature neuroscience*, 8(12):1667–1676, 2005.

Jazayeri, M. and Ostojic, S. Interpreting neural computations by examining intrinsic and embedding dimensionality of neural activity. *Current opinion in neurobiology*, 70:113–120, 2021.

Johnson, M. E. and Tenenbein, A. A bivariate distribution family with specified marginals. *Journal of the American Statistical Association*, 76(373):198–201, 1981.

Johnston, D. and Wu, S. M.-S. *Foundations of Cellular Neurophysiology*. The MIT Press, 1994.

Jun, J. J., Steinmetz, N. A., Siegle, J. H., Denman, D. J., Bauza, M., Barbarits, B., Lee, A. K., Anastassiou, C. A., Andrei, A., Aydın, Ç., et al. Fully integrated silicon probes for high-density recording of neural activity. *Nature*, 551(7679): 232–236, 2017.

Jung, T.-P., Makeig, S., Westerfield, M., Townsend, J., Courchesne, E., and Sejnowski, T. J. Removal of eye activity artifacts from visual event-related potentials in normal and clinical subjects. *Clinical Neurophysiology*, 111(10): 1745–1758, 2000.

Karagas, N. E. and Venkatachalam, K. Roles for the endoplasmic reticulum in regulation of neuronal calcium homeostasis. *Cells*, 8(10):1232, 2019.

Keren, N., Peled, N., and Korngreen, A. Constraining compartmental models using multiple voltage recordings and genetic algorithms. *Journal of neurophysiology*, 2005.

Kisilev, P., Zibulevsky, M., and Zeevi, Y. Y. A multiscale framework for blind separation of linearly mixed signals. *The Journal of Machine Learning Research*, 4: 1339–1363, 2003.

Kitamura, T., Pignatelli, M., Suh, J., Kohara, K., Yoshiki, A., Abe, K., and Tonegawa, S. Island cells control temporal association memory. *Science*, 343 (6173):896–901, 2014.

Klein, N., Siegle, J. H., Teichert, T., and Kass, R. E. Cross-population coupling of neural activity based on gaussian process current source densities. *arXiv preprint arXiv:2104.10070*, 2021.

Klyachko, V. A. and Stevens, C. F. Excitatory and feed-forward inhibitory hippocampal synapses work synergistically as an adaptive filter of natural spike trains. *PLOS Biology*, 4(7):null, 06 2006. doi: 10.1371/journal.pbio.0040207. URL `https://doi.org/10.1371/journal.pbio.0040207`.

Koch, C. Cable theory in neurons with active, linearized membranes. *Biological cybernetics*, 50(1):15–33, 1984.

Koch, C. *Biophysics of computation: information processing in single neurons*. Oxford university press, 2004.

Koch, C. and Poggio, T. A simple algorithm for solving the cable equation in dendritic trees of arbitrary geometry. *Journal of neuroscience methods*, 12(4): 303–315, 1985.

Korovaichuk, A., Makarova, J., Makarov, V. A., Benito, N., and Herreras, Ó. Minor contribution of principal excitatory pathways to hippocampal lfps in the anesthetized rat: a combined independent component and current source density study. *Journal of neurophysiology*, 104(1):484–497, 2010.

Krull, E. M., Sakata, S., and Toyoizumi, T. Theta oscillations alternate with high amplitude neocortical population within synchronized states. *Frontiers in neuroscience*, 2019.

Kubo, T., Katayama, N., Karashima, A., and Nakao, M. The 3d position estimation of neurons in the hippocampus based on the multi-site multi-unit recordings with silicon tetrodes. In *2008 30th Annual International Conference of the IEEE Engineering in Medicine and Biology Society*, pp. 5021–5024. IEEE, 2008.

Leão, R. N., Mikulovic, S., Leão, K. E., Munguba, H., Gezelius, H., Enjin, A., Patra, K., Eriksson, A., Loew, L. M., Tort, A. B., et al. Olm interneurons differentially modulate ca3 and entorhinal inputs to hippocampal ca1 neurons. *Nature neuroscience*, 15(11):1524–1530, 2012.

Łęski, S., Kublik, E., Świejkowski, D. A., Wróbel, A., and Wójcik, D. K. Extracting functional components of neural dynamics with independent component analysis and inverse current source density. *Journal of computational neuroscience*, 29(3):459–473, 2010.

Łęski, S., Lindén, H., Tetzlaff, T., Pettersen, K. H., and Einevoll, G. T. Frequency dependence of signal power and spatial reach of the local field potential. *PLoS computational biology*, 9(7):e1003137, 2013.

Li, Y., Wang, P. T., Vaidya, M. P., Flint, R. D., Liu, C. Y., Slutzky, M. W., and Do, A. H. Electromyogram (emg) removal by adding sources of emg (erase)—a novel ica-based algorithm for removing myoelectric artifacts from eeg. *Frontiers in neuroscience*, pp. 1408, 2021.

Lindén, H., Hagen, E., Leski, S., Norheim, E., Pettersen, K., and Einevoll, G. Lfpy: a tool for biophysical simulation of extracellular potentials generated by detailed model neurons. *Frontiers in Neuroinformatics*, 7:41, 2014. ISSN 1662-5196. doi: 10.3389/fninf.2013.00041. URL `http://journal.frontiersin.org/article/10.3389/fninf.2013.00041`.

Liu, Y.-Y., Slotine, J.-J., and Barabási, A.-L. Controllability of complex networks. *nature*, 473(7346):167–173, 2011.

Logothetis, N. K. What we can do and what we cannot do with fmri. *Nature*, 453(7197):869–878, 2008.

Logothetis, N. K., Kayser, C., and Oeltermann, A. In vivo measurement of cortical impedance spectrum in monkeys: implications for signal propagation. *Neuron*, 55(5):809–823, 2007.

Lohani, S., Moberly, A. H., Benisty, H., Landa, B., Jing, M., Li, Y., Higley, M. J., and Cardin, J. A. Spatiotemporally heterogeneous coordination of cholinergic and neocortical activity. *Nature Neuroscience*, pp. 1–8, 2022.

Lopes-dos Santos, V., van de Ven, G. M., Morley, A., Trouche, S., Campo-Urriza, N., and Dupret, D. Parsing hippocampal theta oscillations by nested spectral components during spatial exploration and memory-guided behavior. *Neuron*, 100(4):940–952, 2018.

Losonczy, A. and Magee, J. C. Integrative properties of radial oblique dendrites in hippocampal ca1 pyramidal neurons. *Neuron*, 50(2):291–307, 2006.

Luck, S. J. *An introduction to the event-related potential technique*. MIT press, 2014.

Lueckmann, J.-M., Goncalves, P. J., Bassetto, G., Öcal, K., Nonnenmacher, M., and Macke, J. H. Flexible statistical inference for mechanistic models of neural dynamics. *arXiv preprint arXiv:1711.01861*, 2017.

Lynn, C. W. and Bassett, D. S. The physics of brain network structure, function and control. *Nature Reviews Physics*, 1(5):318–332, 2019.

López-Madrona, V. J., Pérez-Montoyo, E., Álvarez Salvado, E., Moratal, D., Herreras, O., Pereda, E., Mirasso, C. R., and Canals, S. Different theta frameworks coexist in the rat hippocampus and are coordinated during memory-guided and novelty tasks. *eLife*, 9:e57313, jul 2020. ISSN 2050-084X. doi: 10.7554/eLife.57313. URL `https://doi.org/10.7554/eLife.57313`.

Magee, J., Hoffman, D., Colbert, C., and Johnston, D. Electrical and calcium signaling in dendrites of hippocampal pyramidal neurons. *Annual review of physiology*, 60(1):327–346, 1998.

Magee, J. C. Dendritic hyperpolarization-activated currents modify the integrative properties of hippocampal ca1 pyramidal neurons. *Journal of Neuroscience*, 18(19):7613–7624, 1998.

Magee, J. C. Dendritic integration of excitatory synaptic input. *Nature Reviews Neuroscience*, 1(3):181–190, 2000.

Magee, J. C. and Johnston, D. A synaptically controlled, associative signal for hebbian plasticity in hippocampal neurons. *Science*, 275(5297):209–213, 1997.

Majka, P., Bai, S., Bakola, S., Bednarek, S., Chan, J. M., Jermakow, N., Passarelli, L., Reser, D. H., Theodoni, P., Worthy, K. H., et al. Open access resource for cellular-resolution analyses of corticocortical connectivity in the marmoset monkey. *Nature communications*, 11(1):1–14, 2020.

Makarov, V. A., Makarova, J., and Herreras, O. Disentanglement of local field potential sources by independent component analysis. *Journal of computational neuroscience*, 29(3):445–457, 2010.

Makarova, J., Ibarz, J. M., Makarov, V. A., Benito, N., and Herreras, O. Parallel readout of pathway-specific inputs to laminated brain structures. *Frontiers in systems neuroscience*, 5:77, 2011.

Makeig, S., Kothe, C., Mullen, T., Bigdely-Shamlo, N., Zhang, Z., and Kreutz-Delgado, K. Evolving signal processing for brain–computer interfaces. *Proceedings of the IEEE*, 100(Special Centennial Issue):1567–1584, 2012.

Markov, N. T., Ercsey-Ravasz, M., Van Essen, D. C., Knoblauch, K., Toroczkai, Z., and Kennedy, H. Cortical high-density counterstream architectures. *Science*, 342 (6158):1238406, 2013.

Markov, N. T., Ercsey-Ravasz, M. M., Ribeiro Gomes, A., Lamy, C., Magrou, L., Vezoli, J., Misery, P., Falchier, A., Quilodran, R., Gariel, M.-A., et al. A weighted and directed interareal connectivity matrix for macaque cerebral cortex. *Cerebral cortex*, 24(1):17–36, 2014.

Mazzoni, A., Panzeri, S., Logothetis, N. K., and Brunel, N. Encoding of naturalistic stimuli by local field potential spectra in networks of excitatory and inhibitory neurons. *PLoS Comput. Biol.*, 4(12):e1000239, Dec 2008.

McMenamin, B. W., Shackman, A. J., Maxwell, J. S., Bachhuber, D. R., Koppenhaver, A. M., Greischar, L. L., and Davidson, R. J. Validation of ica-based myogenic artifact correction for scalp and source-localized eeg. *Neuroimage*, 49 (3):2416–2432, 2010.

Mechler, F. and Victor, J. D. Dipole characterization of single neurons from their extracellular action potentials. *Journal of Computational Neuroscience*, 32(1):73–100, 02 2012. doi: 10.1007/s10827-011-0341-0. URL `http://www.ncbi.nlm.nih.gov/pmc/articles/PMC3274615/`.

Mechler, F., Victor, J. D., Ohiorhenuan, I., Schmid, A. M., and Hu, Q. Three-dimensional localization of neurons in cortical tetrode recordings. *Journal of neurophysiology*, 106(2):828–848, 2011.

Meinecke, F., Ziehe, A., Kawanabe, M., and Muller, K.-R. A resampling approach to estimate the stability of one-dimensional or multidimensional independent components. *IEEE transactions on biomedical engineering*, 49(12):1514–1525, 2002.

Mejias, J. F., Murray, J. D., Kennedy, H., and Wang, X.-J. Feedforward and feedback frequency-dependent interactions in a large-scale laminar network of the primate cortex. *Science advances*, 2(11):e1601335, 2016.

Migliore, M. and Shepherd, G. M. Emerging rules for the distributions of active dendritic conductances. *Nature Reviews Neuroscience*, 3(5):362–370, 2002.

Mijović, B., De Vos, M., Gligorijević, I., Taelman, J., and Van Huffel, S. Source separation from single-channel recordings by combining empirical-mode decomposition and independent component analysis. *IEEE transactions on biomedical engineering*, 57(9):2188–2196, 2010.

Mikulovic, S., Restrepo, C. E., Siwani, S., Bauer, P., Pupe, S., Tort, A. B., Kullander, K., and Leão, R. N. Ventral hippocampal olm cells control type 2 theta oscillations and response to predator odor. *Nature communications*, 9(1):1–15, 2018.

Min, M.-Y., Asztely, F., Kokaia, M., and Kullmann, D. M. Long-term potentiation and dual-component quantal signaling in the dentate gyrus. *Proceedings of the National Academy of Sciences*, 95(8):4702–4707, 1998.

Mitra, P. P. and Pesaran, B. Analysis of dynamic brain imaging data. *Biophysical journal*, 76(2):691–708, 1999.

Mizuseki, K., Sirota, A., Pastalkova, E., and Buzsáki, G. Theta oscillations provide temporal windows for local circuit computation in the entorhinal-hippocampal loop. *Neuron*, 64(2):267 – 280, 2009. ISSN 0896-6273. doi: http://dx.doi.org/10.1016/j.neuron.2009.08.037. URL `http://www.sciencedirect.com/science/article/pii/S0896627309006734`.

Moca, V. V., Bârzan, H., Nagy-Dăbâcan, A., and Mureșan, R. C. Time-frequency super-resolution with superlets. *Nature communications*, 12(1):1–18, 2021.

Moddemeijer, R. On estimation of entropy and mutual information of continuous distributions. *Signal Processing*, 16(3):233–246, 1989. URL `http://www.cs.rug.nl/~rudy/papers/abstracts/RM8902.html`.

Mognon, A., Jovicich, J., Bruzzone, L., and Buiatti, M. Adjust: An automatic eeg artifact detector based on the joint use of spatial and temporal features. *Psychophysiology*, 48(2):229–240, 2011.

Moran, R., Stephan, K., Kiebel, S., Rombach, N., O'Connor, W., Murphy, K., Reilly, R., and Friston, K. Bayesian estimation of synaptic physiology from the spectral responses of neural masses. *NeuroImage*, 42(1):272–284, 08 2008. doi: 10.1016/j.neuroimage.2008.01.025. URL `http://www.ncbi.nlm.nih.gov/pmc/articles/PMC2644419/`.

Muthukumaraswamy, S. High-frequency brain activity and muscle artifacts in meg/eeg: a review and recommendations. *Frontiers in human neuroscience*, 7:138, 2013.

Næss, S., Halnes, G., Hagen, E., Hagler Jr, D. J., Dale, A. M., Einevoll, G. T., and Ness, T. V. Biophysically detailed forward modeling of the neural origin of eeg and meg signals. *NeuroImage*, 225:117467, 2021.

Ness, T. V., Chintaluri, C., Potworowski, J., Łęski, S., Głąbska, H., Wójcik, D. K., and Einevoll, G. T. Modelling and analysis of electrical potentials recorded in microelectrode arrays (meas). *Neuroinformatics*, 13(4):403–426, 2015.

Nguyen, D. P., Layton, S. P., Hale, G., Gomperts, S. N., Davidson, T. J., Kloosterman, F., and Wilson, M. A. Micro-drive array for chronic in vivo recording: tetrode assembly. *JoVE (Journal of Visualized Experiments)*, (26):e1098, 2009.

Nicholson, C. and Freeman, J. A. Theory of current source-density analysis and determination of conductivity tensor for anuran cerebellum. *Journal of Neurophysiology*, 38(2):356–368, 1975. ISSN 0022-3077. URL `http://jn.physiology.org/content/38/2/356`.

Nicholson, D. A., Trana, R., Katz, Y., Kath, W. L., Spruston, N., and Geinisman, Y. Distance-dependent differences in synapse number and ampa receptor expression in hippocampal ca1 pyramidal neurons. *Neuron*, 50(3):431–442, 2006.

Nolte, G., Ziehe, A., Nikulin, V. V., Schlögl, A., Krämer, N., Brismar, T., and Müller, K.-R. Robustly estimating the flow direction of information in complex physical systems. *Physical review letters*, 100(23):234101, 2008.

Nunez, P. L., Srinivasan, R., et al. *Electric fields of the brain: the neurophysics of EEG*. Oxford University Press, USA, 2006.

Otmakhova, N. A., Otmakhov, N., and Lisman, J. E. Pathway-specific properties of ampa and nmda-mediated transmission in ca1 hippocampal pyramidal cells. *Journal of Neuroscience*, 22(4):1199–1207, 2002.

Otor, Y., Achvat, S., Cermak, N., Benisty, H., Abboud, M., Barak, O., Schiller, Y., Poleg-Polsky, A., and Schiller, J. Dynamic compartmental computations in tuft dendrites of layer 5 neurons during motor behavior. *Science*, 376(6590):267–275, 2022.

O'Hare, J. K., Gonzalez, K. C., Herrlinger, S. A., Hirabayashi, Y., Hewitt, V. L., Blockus, H., Szoboszlay, M., Rolotti, S. V., Geiller, T. C., Negrean, A., et al. Compartment-specific tuning of dendritic feature selectivity by intracellular ca2+ release. *Science*, 375(6586):eabm1670, 2022.

Pakman, A., Huggins, J., Smith, C., and Paninski, L. Fast state-space methods for inferring dendritic synaptic connectivity. *Journal of Computational Neuroscience*, 36(3):415–443, 2014. ISSN 1573-6873. doi: 10.1007/s10827-013-0478-0. URL `http://dx.doi.org/10.1007/s10827-013-0478-0`.

Palmigiano, A., Geisel, T., Wolf, F., and Battaglia, D. Flexible information routing by transient synchrony. *Nature neuroscience*, 20(7):1014–1022, 2017.

Palomero-Gallagher, N. and Zilles, K. Cortical layers: Cyto-, myelo-, receptor- and synaptic architecture in human cortical areas. *Neuroimage*, 197:716–741, 2019.

Pandarinath, C., O'Shea, D. J., Collins, J., Jozefowicz, R., Stavisky, S. D., Kao, J. C., Trautmann, E. M., Kaufman, M. T., Ryu, S. I., Hochberg, L. R., et al. Inferring single-trial neural population dynamics using sequential auto-encoders. *Nature methods*, 15(10):805–815, 2018.

Parra, L. and Spence, C. Convolutive blind separation of non-stationary sources. *IEEE transactions on Speech and Audio Processing*, 8(3):320–327, 2000.

Payne, J. A., Rivera, C., Voipio, J., and Kaila, K. Cation–chloride co-transporters in neuronal communication, development and trauma. *Trends in neurosciences*, 26(4):199–206, 2003.

Penny, W. D., Friston, K. J., Ashburner, J. T., Kiebel, S. J., and Nichols, T. E. *Statistical parametric mapping: the analysis of functional brain images*. Elsevier, 2011.

Pesaran, B., Vinck, M., Einevoll, G. T., Sirota, A., Fries, P., Siegel, M., Truccolo, W., Schroeder, C. E., and Srinivasan, R. Investigating large-scale brain dynamics using field potential recordings: analysis and interpretation. *Nature neuroscience*, 21(7):903–919, 2018.

Peters, J., Janzing, D., and Schölkopf, B. *Elements of causal inference: foundations and learning algorithms*. The MIT Press, 2017.

Pettersen, K. H., Devor, A., Ulbert, I., Dale, A. M., and Einevoll, G. T. Current-source density estimation based on inversion of electrostatic forward solution: Effects of finite extent of neuronal activity and conductivity discontinuities. *Journal of Neuroscience Methods*, 154(1â2):116 – 133, 2006. ISSN 0165-0270. doi: http://dx.doi.org/10.1016/j.jneumeth.2005.12.005. URL `http://www.sciencedirect.com/science/article/pii/S0165027005004541`.

Pettersen, K. H., Lindén, H., Tetzlaff, T., and Einevoll, G. T. Power laws from linear neuronal cable theory: power spectral densities of the soma potential, soma membrane current and single-neuron contribution to the eeg. *PLoS computational biology*, 10(11):e1003928, 2014.

Pinault, D. A novel single-cell staining procedure performed in vivo under electrophysiological control: morpho-functional features of juxtacellularly labeled thalamic cells and other central neurons with biocytin or neurobiotin. *Journal of neuroscience methods*, 65(2):113–136, 1996.

Pinotsis, D. A., Geerts, J., Pinto, L., FitzGerald, T. H., Litvak, V., Auksztulewicz, R., and Friston, K. J. Linking canonical microcircuits and neuronal activity: Dynamic causal modelling of laminar recordings. *Neuroimage*, 146:355–366, 2017.

Plonsey, R. and Heppner, D. B. Considerations of quasi-stationarity in electrophysiological systems. *The Bulletin of mathematical biophysics*, 29(4):657–664, 1967.

Polsky, A., Mel, B. W., and Schiller, J. Computational subunits in thin dendrites of pyramidal cells. *Nature neuroscience*, 7(6):621–627, 2004.

Potworowski, J., Jakuczun, W., Łski, S., and Wójcik, D. Kernel current source density method. *Neural computation*, 24(2):541–575, 2012.

Rall, W. Core conductor theory and cable properties of neurons. *Comprehensive physiology*, pp. 39–97, 2011.

Rao, R. P. and Ballard, D. H. Predictive coding in the visual cortex: a functional interpretation of some extra-classical receptive-field effects. *Nature neuroscience*, 2(1):79–87, 1999.

Reimann, M. W., Anastassiou, C. A., Perin, R., Hill, S. L., Markram, H., and Koch, C. A biophysically detailed model of neocortical local field potentials predicts the critical role of active membrane currents. *Neuron*, 79(2):375–390, 2013.

Rudy, S., Alla, A., Brunton, S. L., and Kutz, J. N. Data-driven identification of parametric partial differential equations. *SIAM Journal on Applied Dynamical Systems*, 18(2):643–660, 2019.

Sabatini, B. L. and Tian, L. Imaging neurotransmitter and neuromodulator dynamics in vivo with genetically encoded indicators. *Neuron*, 108(1):17–32, 2020.

Schmidt-Hieber, C., Jonas, P., and Bischofberger, J. Subthreshold dendritic signal processing and coincidence detection in dentate gyrus granule cells. *Journal of Neuroscience*, 27(31):8430–8441, 2007.

Schneider, M., Broggini, A. C., Dann, B., Tzanou, A., Uran, C., Sheshadri, S., Scherberger, H., and Vinck, M. A mechanism for inter-areal coherence through communication based on connectivity and oscillatory power. *Neuron*, 109(24): 4050–4067, 2021.

Schomburg, E. W., Fernández-Ruiz, A., Mizuseki, K., Berényi, A., Anastassiou, C. A., Koch, C., and Buzsáki, G. Theta phase segregation of input-specific gamma patterns in entorhinal-hippocampal networks. *Neuron*, 84(2):470–485, 2014.

Sejnowski, T. J. Independent component analysis of electroencephalographic data. In *Advances in Neural Information Processing Systems 8: Proceedings of the 1995 Conference*, volume 8, pp. 145. MIT press, 1996.

Seth, A. K., Barrett, A. B., and Barnett, L. Granger causality analysis in neuroscience and neuroimaging. *Journal of Neuroscience*, 35(8):3293–3297, 2015.

Shackman, A. J., McMenamin, B. W., Slagter, H. A., Maxwell, J. S., Greischar, L. L., and Davidson, R. J. Electromyogenic artifacts and electroencephalographic inferences. *Brain topography*, 22(1):7–12, 2009.

Shine, J. M., Breakspear, M., Bell, P. T., Ehgoetz Martens, K. A., Shine, R., Koyejo, O., Sporns, O., and Poldrack, R. A. Human cognition involves the dynamic integration of neural activity and neuromodulatory systems. *Nature neuroscience*, 22(2):289–296, 2019.

Shine, J. M., Müller, E. J., Munn, B., Cabral, J., Moran, R. J., and Breakspear, M. Computational models link cellular mechanisms of neuromodulation to large-scale neural dynamics. *Nature neuroscience*, 24(6):765–776, 2021.

Sirota, A., Montgomery, S., Fujisawa, S., Isomura, Y., Zugaro, M., and Buzsáki, G. Entrainment of neocortical neurons and gamma oscillations by the hippocampal theta rhythm. *Neuron*, 60(4):683–697, 2008.

Song, A. H., Ba, D., and Brown, E. N. Plso: A generative framework for decomposing nonstationary time-series into piecewise stationary oscillatory components. In *Uncertainty in Artificial Intelligence*, pp. 1371–1381. PMLR, 2021.

Song, D., Chan, R. H., Marmarelis, V. Z., Hampson, R. E., Deadwyler, S. A., and Berger, T. W. Nonlinear modeling of neural population dynamics for hippocampal prostheses. *Neural Networks*, 22(9):1340–1351, 2009.

Sporns, O. Contributions and challenges for network models in cognitive neuroscience. *Nature neuroscience*, 17(5):652–660, 2014.

Sporns, O., Tononi, G., and Kötter, R. The human connectome: a structural description of the human brain. *PLoS computational biology*, 1(4):e42, 2005.

Spruston, N. Pyramidal neurons: dendritic structure and synaptic integration. *Nature Reviews Neuroscience*, 9(3):206–221, 2008.

Stark, E., Eichler, R., Roux, L., Fujisawa, S., Rotstein, H. G., and Buzsáki, G. Inhibition-induced theta resonance in cortical circuits. *Neuron*, 80(5):1263–1276, 2013.

Sterratt, D., Graham, B., Gillies, A., and Willshaw, D. *Principles of Computational Modelling in Neuroscience*. Cambridge University Press, 2011a.

Sterratt, D., Graham, B., Gillies, A., and Willshaw, D. *Principles of Computational Modelling in Neuroscience*. Cambridge University Press, 2011b. doi: 10.1017/CBO9780511975899.

Stringer, C., Pachitariu, M., Steinmetz, N., Reddy, C. B., Carandini, M., and Harris, K. D. Spontaneous behaviors drive multidimensional, brainwide activity. *Science*, 364(6437), 2019.

Tanaka, T. and Cichocki, A. Subband decomposition independent component analysis and new performance criteria. In *2004 IEEE International Conference on Acoustics, Speech, and Signal Processing*, volume 5, pp. V–541. IEEE, 2004.

Tang, Q., Burgalossi, A., Ebbesen, C. L., Ray, S., Naumann, R., Schmidt, H., Spicher, D., and Brecht, M. Pyramidal and stellate cell specificity of grid and border representations in layer 2 of medial entorhinal cortex. *Neuron*, 84(6): 1191–1197, 2014.

Tecuatl, C., Wheeler, D. W., Sutton, N., and Ascoli, G. A. Comprehensive estimates of potential synaptic connections in local circuits of the rodent hippocampal formation by axonal-dendritic overlap. *Journal of Neuroscience*, 41(8): 1665–1683, 2021.

Teleńczuk, B., Dehghani, N., Le Van Quyen, M., Cash, S. S., Halgren, E., Hatsopoulos, N. G., and Destexhe, A. Local field potentials primarily reflect inhibitory neuron activity in human and monkey cortex. *Scientific reports*, 7(1): 1–10, 2017.

Timofeeva, Y., Coombes, S., and Michieletto, D. Gap junctions, dendrites and resonances: a recipe for tuning network dynamics. *The Journal of Mathematical Neuroscience*, 3(1):15, 2013.

Tort, A. B., Kramer, M. A., Thorn, C., Gibson, D. J., Kubota, Y., Graybiel, A. M., and Kopell, N. J. Dynamic cross-frequency couplings of local field potential oscillations in rat striatum and hippocampus during performance of a t-maze task. *Proceedings of the National Academy of Sciences*, 105(51):20517–20522, 2008.

Tort, A. B., Komorowski, R., Eichenbaum, H., and Kopell, N. Measuring phase-amplitude coupling between neuronal oscillations of different frequencies. *Journal of neurophysiology*, 104(2):1195–1210, 2010.

Tuckwell, H. C. *Introduction to theoretical neurobiology: linear cable theory and dendritic structure*, volume 1. Cambridge University Press, 1988.

Tuckwell, H. C. *Stochastic Processes in the Neurosciences*. CBMS-NSF regional conference series in applied mathematics 56. Society for Industrial and Applied Mathematics, 1989. ISBN 9780898712322,0898712327. URL `http://gen.lib.rus.ec/book/index.php?md5=7CD7830C8A4668836B4613F0DDC345DF`.

Turi, G. F., Li, W.-K., Chavlis, S., Pandi, I., O'Hare, J., Priestley, J. B., Grosmark, A. D., Liao, Z., Ladow, M., Zhang, J. F., et al. Vasoactive intestinal polypeptide-expressing interneurons in the hippocampus support goal-oriented spatial learning. *Neuron*, 101(6):1150–1165, 2019.

Turner, R. E. and Sahani, M. Time-frequency analysis as probabilistic inference. *IEEE Transactions on Signal Processing*, 62(23):6171–6183, 2014.

Urigüen, J. A. and Garcia-Zapirain, B. Eeg artifact removal—state-of-the-art and guidelines. *Journal of neural engineering*, 12(3):031001, 2015.

Valero, M., Zutshi, I., Yoon, E., and Buzsáki, G. Probing subthreshold dynamics of hippocampal neurons by pulsed optogenetics. *Science*, 375(6580):570–574, 2022.

Van Boxtel, A. Optimal signal bandwidth for the recording of surface emg activity of facial, jaw, oral, and neck muscles. *Psychophysiology*, 38(1):22–34, 2001.

Vinck, M., Huurdeman, L., Bosman, C. A., Fries, P., Battaglia, F. P., Pennartz, C. M., and Tiesinga, P. H. How to detect the granger-causal flow direction in the presence of additive noise? *Neuroimage*, 108:301–318, 2015.

Wang, X.-J. Neurophysiological and computational principles of cortical rhythms in cognition. *Physiological reviews*, 90(3):1195–1268, 2010.

Wang, X.-J. Theory of the multiregional neocortex: Large-scale neural dynamics and distributed cognition. *Annual Review of Neuroscience*, 45:533–560, 2022.

Watson, B. O., Ding, M., and Buzsáki, G. Temporal coupling of field potentials and action potentials in the neocortex. *European Journal of Neuroscience*, 48(7): 2482–2497, 2018.

Whitham, E. M., Pope, K. J., Fitzgibbon, S. P., Lewis, T., Clark, C. R., Loveless, S., Broberg, M., Wallace, A., DeLosAngeles, D., Lillie, P., et al. Scalp electrical recording during paralysis: quantitative evidence that eeg frequencies above 20 hz are contaminated by emg. *Clinical neurophysiology*, 118(8):1877–1888, 2007.

Winterer, J., Maier, N., Wozny, C., Beed, P., Breustedt, J., Evangelista, R., Peng, Y., D'Albis, T., Kempter, R., and Schmitz, D. Excitatory microcircuits within superficial layers of the medial entorhinal cortex. *Cell Reports*, 19(6):1110–1116, 2017.

Wolters, C. H., Anwander, A., Tricoche, X., Weinstein, D., Koch, M. A., and Macleod, R. S. Influence of tissue conductivity anisotropy on eeg/meg field and return current computation in a realistic head model: a simulation and visualization study using high-resolution finite element modeling. *NeuroImage*, 30(3):813–826, 2006.

Wong, K.-F. and Wang, X.-J. A recurrent network mechanism of time integration in perceptual decisions. *Journal of Neuroscience*, 26(4):1314–1328, 2006.

Wybo, W. A., Boccalini, D., Torben-Nielsen, B., and Gewaltig, M.-O. A sparse reformulation of the green's function formalism allows efficient simulations of morphological neuron models. *Neural computation*, 27(12):2587–2622, 2015.

Xi-Lin Li and Adali, T. Complex independent component analysis by entropy bound minimization. *IEEE Transactions on Circuits and Systems I: Regular Papers*, 57(7):1417–1430, July 2010. ISSN 1549-8328. doi: 10.1109/TCSI.2010.2046207.

Yihe, L. and Timofeeva, Y. Response functions for electrically coupled neuronal network: a method of local point matching and its applications. *Biological cybernetics*, 110(2):117–133, 2016.

Zhang, K. and Chan, L.-W. An adaptive method for subband decomposition ica. *Neural computation*, 18(1):191–223, 2006.

Zhang, K., Huang, B., Zhang, J., Glymour, C., and Schölkopf, B. Causal discovery from nonstationary/heterogeneous data: Skeleton estimation and orientation determination. In *IJCAI: Proceedings of the Conference*, volume 2017, pp. 1347. NIH Public Access, 2017.

Eidesstattliche Versicherung

Ich erkläre hiermit an Eides statt, dass ich die vorliegende Dissertation mit dem Thema

Biophysics-based modeling and data analysis of local field potential signal

selbständig verfasst, mich außer der angegebenen keiner weiteren Hilfsmittel bedient und alle Erkenntnisse, die aus dem Schrifttum ganz oder annähernd übernommen sind, als solche kenntlich gemacht und nach ihrer Herkunft unter Bezeichnung der Fundstelle einzeln nachgewiesen habe.

Ich erkläre des Weiteren, dass die hier vorgelegte Dissertation nicht in gleicher oder in ähnlicher Form bei einer anderen Stelle zur Erlangung eines akademischen Grades eingereicht wurde.

Ithaca, 08.01.2024

Ort, Datum

Weiwei Chen

Unterschrift Doktorandin/Doktorand